

# Final Report



Delft University of Technology

Ultimate Unlimited Aerobatic Aircraft  
DSE Group 23



# Final Report

Ultimate Unlimited Aerobatic Aircraft

by

DSE Group 23

Final Report for Design Synthesis Exercise Ultimate Unlimited Aerobatic Aircraft  
at the Delft University of Technology,  
to be handed in by 3rd of July 2018

Student:	Sam van Elsloo	4487060
	Midas Gossye	4460766
	Tobias Haegens	4438663
	Quinty van der Leer	4435931
	Jordy van Leeuwen	4452305
	Emma De Meester	4453190
	Ties Nieuwenhuizen	4148495
	Boris Rowaan	4463757
	Jurian Stougie	4459806
	Gijs Vugts	4465067

Project duration: April 23, 2018 – July 6, 2018

Project Supervisors:	Dr. ir. A. C. in 't Veld,	Principal Tutor
	P. M. G. J. Lancelot MSc,	Coach
	J. Dong MSc,	Coach

Version: 1.1

# Preface

The final step in the Bachelor curriculum of the Aerospace Engineering Faculty at Delft University of Technology is the graduation project known as Design Synthesis Exercise (DSE). Groups of 10 students work full-time on a design project for 10 weeks. This report is the final report of the 2018 TU Delft spring DSE project "The Ultimate Unlimited Aerobatic Aircraft".

Our project objective was "to design the ultimate aerobatic competition aircraft, capable of competing in the FAI Unlimited World Aerobatic Championships." We have worked on an innovative design for a new aerobatic aircraft *StefX* which is able to outperform its current competitors. This report was preceded by the project plan in week one which described the group's overall approach to the technical and management aspects, the baseline report in week three which analysed to top-level requirements in combination with a flowdown in mission and system requirements and the midterm report in week six which explained the results of the analysis and design activities that led to the selected concept for the detailed design phase. The purpose of this report is to explain the detailed design phase and introduce the entire project.

We would like to express our gratitude to all those who provided us with the support needed to complete this report. Firstly, we would like to acknowledge with much appreciation the crucial roles of Dr. Ir. A.C. in 't Veld, P.M.G.J. Lancelot MSc and J. Dong MSc for their valuable feedback and input as tutors of this project. We would like to extend a special gratitude to the aerobatics pilots H.J. van Overvelt and S. De Jaeghere for their help and suggestions. Furthermore, we acknowledge the essential feedback of the British Aerobatics Judges A. Cassidy, N. Buckenham, L. Culpin and E. Marsh on our design choices. We also would like to thank the *Ontwerp Synthese Coördinatie Commissie* for organising this DSE and providing us with the opportunity to work on this project. Finally, we would like to thank M. Haegens for designing the *StefX* logo.

*Group 23*  
Delft, July 2, 2018

# Executive Overview

In this report, the aerobatic aircraft for the unlimited category, a conventional aerobatic aircraft with high lift devices, the *StefX*, is designed in detail.

## Project Introduction

The goal of the project was to design the ultimate unlimited aerobatic aircraft. The mission statement is *To design the ultimate aerobatic competition aircraft, capable of winning in the FAI Unlimited World Aerobatic Championships by ten students in ten weeks.* The EXTRA 330SC is currently the best unlimited aerobatic aircraft. It is dominating the unlimited aerobatic competition. In order to design an aircraft that can beat the EXTRA 330SC, a list of system requirements had been set up. From this list the following requirements were identified as driving requirements:

- STX-SYS-15 The aircraft shall be able to obtain a roll rate of at least  $450^\circ/\text{s}$ .
- STX-SYS-16 The pitch rate shall not be less than  $20^\circ/\text{s}$ .
- STX-SYS-17 The yaw rate shall not be less than  $40^\circ/\text{s}$  while flying at 40 kts in a vertical line up.
- STX-SYS-20 The aircraft shall be able to withstand a  $\pm 10$  G limit load.
- STX-SYS-25 The maximum unit price of the aircraft shall be \$ 325,000.

## Conceptual Design

For the conceptual design, various design options have been explored. This included a conventional aircraft as well as a biplane. It was concluded that the biplane is difficult to judge from the ground. For this reason, only the conventional aircraft had been analysed in more detail. Five different variations on the conventional aircraft have been studied. It was found that the conventional concept with leading edge high lift devices (LEHLD) and flaperons was the best concept. From this point onward, the wing geometry and airfoil were set. The airfoil that is used for *StefX* is the MS15, which is a symmetric airfoil. In addition, the engine had been chosen to be a Lycoming AEIO-580.

## Sizing

After the conceptual design, the aircraft has been designed in more detail. The aircraft is sized to have the best possible performance and to comply with all requirements. In particular, the control surfaces, propeller and landing gear have been designed in more detail.

**Control Surface Sizing** The control surfaces have been sized in accordance with the stability analysis. The stability analysis is dependent on the c.g. of the aircraft, the mass moment of inertia (MMOI), the mass of the different components, and the geometry. From this analysis, a range of possible values for the tail arms and areas as well as XLEMAC was obtained. The judgement on the possible values was based on the determination of the flying and handling qualities. A program was made to simulate the behaviour of *StefX*, such as the angular velocities and accelerations. In combination with the result of the stability analysis, this simulation has been used to size the control surfaces and positions of the wing and tails. The control surface sizes are depicted in Figure 1.

**Propeller** The propeller was designed from scratch. The diameter is based on [22], while the rest of the propeller was designed using the blade element theory (BET). The propeller was sized in order to have a maximum propeller efficiency, which ended up being 91% at its maximum. The optimal twist and pitch at a range of different airspeeds as well as different cord lengths and various airfoils were calculated. The twist angle and pitch for which the propeller efficiency is the highest was chosen.

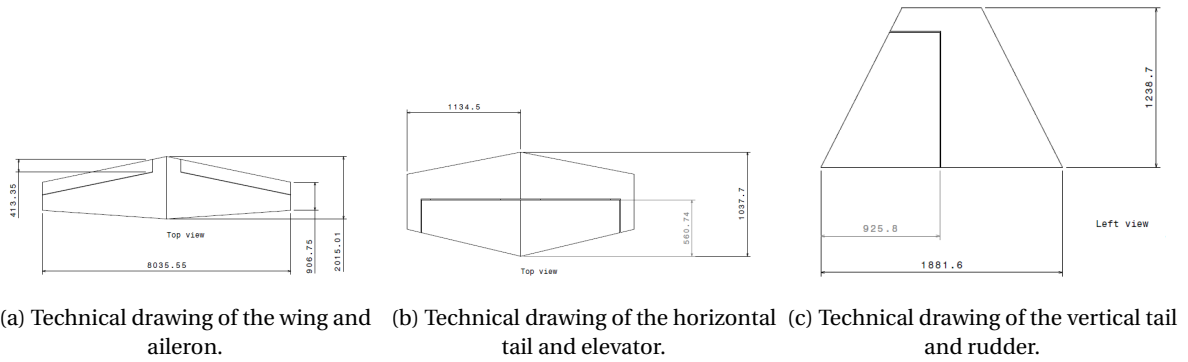


Figure 1: Technical drawings of the control surfaces. The dimensions are in *mm*.

**Landing Gear** The landing gear was sized for ground operations and taxiing such that it would meet the clearance and tip-over requirements described in CS23. The dimensions of the landing gear are depicted in Figure 2.

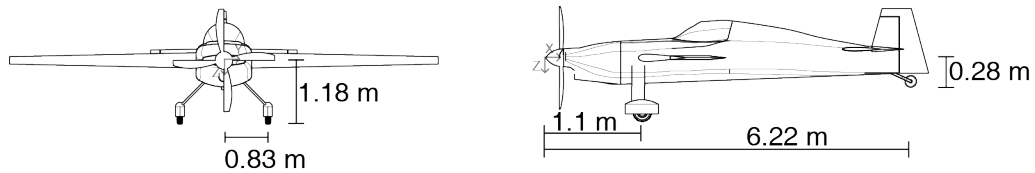


Figure 2: Landing gear dimensions.

## Aerodynamics

In order to simulate the aircraft behaviour, the aerodynamic properties were needed. Moreover, the effect of the HLDs had to be investigated.

**Drag Calculation** A drag estimation of the entire aircraft was performed as input for the control and stability analysis on the *StefX*. The extensively verified and validated DATCOM method is used for this. A total drag coefficient of 0.0569 for an angle of attack of  $5^\circ$  was obtained (lift induced drag included).

**Leading Edge High Lift Devices** Together with the flaperons, the LEHLDs are the innovative part of the *StefX*. This is the feature that distinguishes the *StefX* from other aerobatic aircraft. Many options for LEHLDs were investigated, out of which a system with two slats was selected. An extra slat was needed to allow use of the HLDs with positive as well as negative angles of attack. A sketch of the LEHLD system can be found in Figure 3a and the resulting lift curve is presented in Figure 3b. A total lift coefficient increase of 0.531 can be obtained when the slats are fully deployed. This value was calculated using DATCOM.

The slats can be deployed by using the suction force of the pressure peak on the top part of the wing at high angles of attack. The deployment takes place in about 0.02 s. Further CFD analysis will need to show if the aerodynamic forces are able to push the slat back in when the angle of attack is lowered. In that case, a simple locking mechanism shall be used to let the pilot decide if the slats can deploy at high angles of attack. Otherwise, an actuation system will be installed that will use electric actuators.

**Trailing Edge High Lift Devices** To further decrease the stall speed, trailing edge high lift devices (TEHLDs) were added. The ailerons will also be used as TEHLD, turning it into flaperons. The resulting lift curve slope is presented in Figure 3b. A maximum lift increase of 0.567 is obtained, when the flaperons are fully extended.

**Aerodynamic Properties** To obtain relevant aerodynamic properties, a steady discrete vortex representation of the airfoil was built, after which an unsteady discrete vortex representation of the airfoil was built, concluded with a vortex ring method that was constructed to model the three-dimensional wing, including

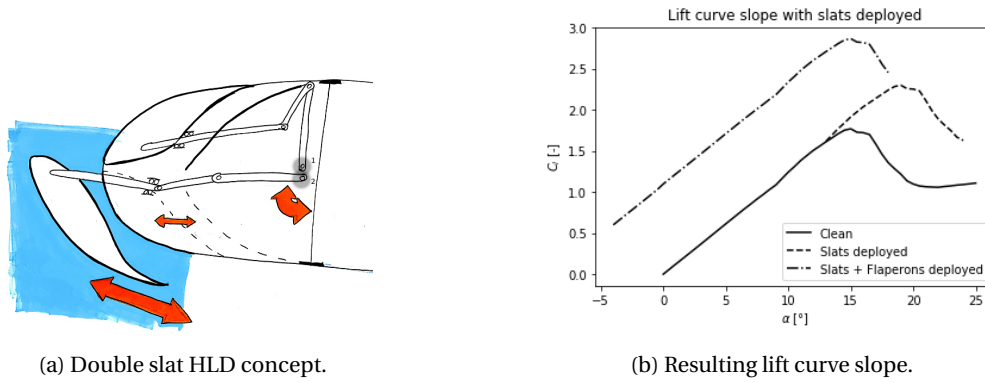


Figure 3: LEHLD double slat concept.

the control surfaces and their balancing horns. These numerical simulations were all based on the well-established [28]. From these inviscid formulations, the aerodynamic properties in Table 1 were obtained.

Parameter	Symbol	Value	Unite
Wing lift curve slope	$C_{L\alpha}$	3.836	$\text{rad}^{-1}$
Span efficiency factor	$e$	0.82	-
Wing lift coefficient derivative w.r.t. aileron deflection	$C_{L\delta_a}$	2.984	$\text{rad}^{-1}$
Wing moment coefficient derivative w.r.t. aileron deflection	$C_{M\delta_a}$	-0.7421	$\text{rad}^{-1}$

Table 1: Aerodynamic properties obtained by vortex ring method.

**Aerodynamic Balancing** From the vortex ring method, the pressure distribution over the full wing was obtained, allowing for straightforward balancing of the control surfaces, based on the required aerodynamic moments about the hinge line by the sizing of the control linkages. It was established that for the aileron, the hingeline should be placed at  $0.77c$  with no horn present; for the elevator, the hingeline should be placed at  $0.6c$  with a horn of  $0.36\text{ m}$  present; for the rudder, the hingeline should be placed at  $0.65c$  with a horn of  $0.26\text{ m}$  present.

## Aircraft Systems

The aircraft systems include everything the pilot will have direct access to, and the systems behind this.

**Stick and Rudder** The stick, rudder pedals and seat have been designed using the DINED database from the TU Delft [32]. It is designed such that every pilot with a length between the 10 and 90 percentile of the dutch population, will be able to fly the aircraft. The stick is designed such that the control force ratio can be adapted upon maintenance. The preferred ratio of the control forces aileron: elevator: rudder is 1:2:3.

**Control Linkages** After the stick and rudder pedals were sized, the control linkages had to be designed. Because the controls are all mechanical, everything is connected to the stick. The ailerons are controlled using pushrods to minimise friction and play. This optimises the feel of the aircraft. The elevator will be controlled using a single pushrod. The rudder will be controlled using two cables. Since the loading will only be in tension, this will result in a direct feel.

**High Lift Device Controls** The flaperons will be controlled by rotating the attachment plate of the pushrods. This changes the neutral position of the ailerons, making them act as flaps. Figure 4 shows this system in the neutral position. The pilot will control the flaperon position by turning the throttle lever. This provides a way to precisely control the position without taking the hands off the throttle or stick.

The LEHLDs are deployed by use of the presence of the suction peak. The LEHLDs without the wing are shown in Figure 5. The deployment of the LEHLDs will take about  $0.02\text{ s}$ . The system is shown graphically in Figure 5. A button will be installed on the throttle lever to deploy and retract the slats. An envelope protection

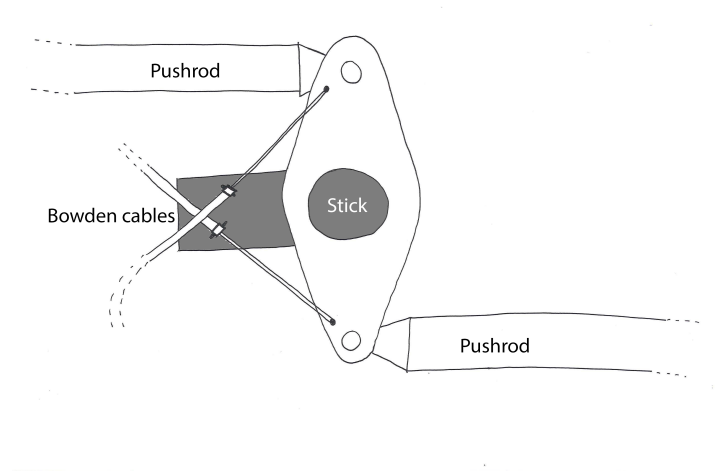


Figure 4: Flaperon actuation system.

system will deploy the correct slat depending on the aircraft angle of attack and will automatically retract or block deployment at a specified speed to avoid damage due to high aerodynamic forces.

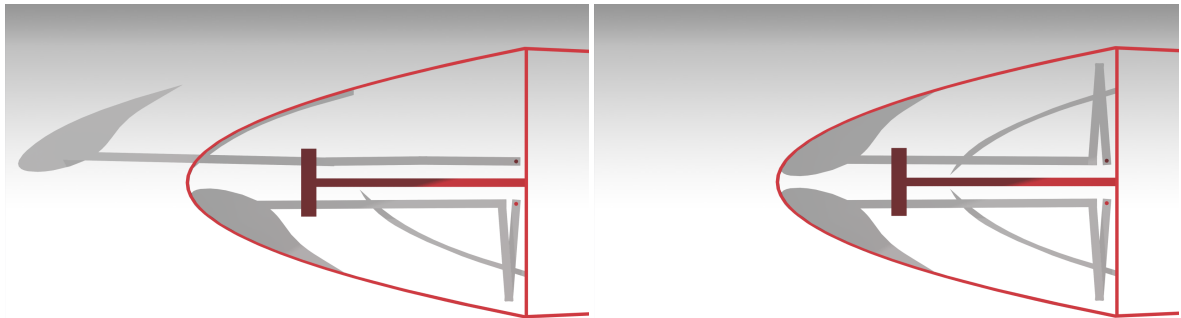


Figure 5: Render of the LEHLDs in both deployed and undeployed position.

**Electrical System** The electrical system includes a 14V alternator, and a 12V battery as a backup in case of failure of the alternator or the engine. The aircraft is equipped with an external power system that provides the capability to start the engine independent from the internal battery.

**Fuel System** The fuel system includes a small acrobatic tank with a flop tube in order to ensure fuel flow to the engine at all attitudes. In addition, a fuel tank with a total capacity of 75 L is feeding into the acrobatic tank using gravity. A valve to prevent feed back is present. Moreover, an electric booster pump is installed in case the engine driven pump fails. The fuselage tanks have enough fuel for 20 minutes of acrobatic flight, and 45 minutes of cruise. For the cruise requirement of 750 km, an additional fuel tank volume of 84 L is included.

## Structural Design

The structure has been designed such that it can sustain the exerted loads. The first step in the structural design was the material selection, followed by the structural analysis. Furthermore, the c.g. and MMOI has been determined. For the production of the *StefX*, a production plan has been made.

**Material Selection** For selecting a material, more information about the possible materials was required. It was determined that Epoxy/ Carbon fibre, uni-directional (UD) prepreg with quasi isotropic (QI) lay-up is the best option for the construction of the fuselage, main wing, horizontal and vertical tail. Its properties can be found in Table 2. For the construction of the landing gear a different material was selected since the Epoxy/

Carbon fibre has a too high Young's Modulus. The material for the landing gear is Epoxy/ S-glass fibre, UD prepreg, QI lay-up, its properties can be found in Table 3.

Property of the material	Value	Unit	Source
Density	$1.58 \cdot 10^3$	kg/m <sup>3</sup>	[14]
Young's modulus	60.1	GPa	[14]
Yield strength	738	MPa	[14]
Elongation	0.35	% strain	[14]
Compressive modulus	60.1	GPa	[14]
Compressive strength	657	MPa	[14]
Shear Modulus	23	GPa	[14]
Shear Strength	60	MPa	<sup>a</sup>
Price	41.6	USD/kg	[14]

Table 2: Properties of the chosen material: Epoxy/Carbon fibre, UD prepreg with QI lay-up.

<sup>a</sup> <http://www.acpsales.com/upload/Mechanical-Properties-of-Carbon-Fiber-Composite-Materials.pdf>

Property of the material	Value	Unit	Source
Density	$1.97 \cdot 10^3$	kg/m <sup>3</sup>	[14]
Young's modulus	21	GPa	[14]
Yield strength	504	MPa	[14]
Elongation	2.6	% strain	[14]
Compressive modulus	21	GPa	[14]
Compressive strength	312	MPa	[14]
Price	19.6	USD/kg	[14]

Table 3: Properties of Epoxy/S-glass fibre, UD prepreg, QI lay-up.

**Structural Analysis** A structural analysis on the major subsystems of the aircraft was performed. The main wing, horizontal and vertical tail were analysed, as well as the fuselage and the landing gear. In order to make sure the structure would not fail, the Tsai-Wu failure criterion was used. This is a failure criterion specially for non-isotropic materials, such as both components used in the structural analysis. For the wing and tails, it was chosen to use a classic wing box as structure. The wing was discretised in spanwise direction into piece with a constant cross section and span. The second moments of area, were calculated for every section. These second moments of area were modelled. This model was verified using SolidWorks. For the stress analysis both the normal and shear stress was evaluated using the method described in Megson [31]. The structure of the aircraft was determined and can be found in Table 4.

	Main wing	Horizontal tail	Vertical tail	units
Thickness spar 1	0.002	0.0015	0.0015	m
Thickness spar 2	0.002	0.0015	0.0015	m
Thickness skin	0.0018	0.0010	0.0010	m
Number of stringers	8, 4, 2	6	6	-
Clamp dimensions	$0.03 \times 0.03$	$0.015 \times 0.015$	$0.015 \times 0.015$	m <sup>2</sup>
Height stringer	0.025	0.015	0.015	m
Width stringer	0.025	0.015	0.015	m
Thickness stringer	0.003	0.003	0.0015	m

Table 4: Results of the structural analysis of the Main Wing, Vertical and Horizontal Tail.

Furthermore, the landing gear struts and fuselage were analysed. The method used for the landing gear is a simplified version of the method that was used for the wing and tails. This method could be simplified since only the bending moment was taken into account, not the shear forces. However, the pure compressive normal load was included. After the stresses were calculated, the required geometry of the landing gear, to prevent structural failure, was calculated. The results can be seen in Table 5.

	Fuselage	Units
$c_{LG}$	0.24	m
$t_{LG}$	0.003	m
$l_{LG}$	0.8	m
$\alpha_{LG}$	35	°
Airfoil	E475	-

Table 5: Geometric properties of the landing gear.

The fuselage of the aircraft was simplified, the simplified model can be seen in Figure 6. It is important to note that due to the fact that to pilot will need to sit in the fuselage, a relatively large cut-out is present. The forces generated by the engine and tails were taken into account, as well as the force introduced by the presence of the pilot. This caused additional stress in the fuselage, which are taken into account in the analysis. The minimum required thickness of the fuselage can be seen in Table 6.

	Fuselage	Units
$b_f$	0.83	m
$t_D$	0.002	m
$t_{ribs}$	0.002	m
$h_{ribs}$	0.08	m
$s_{ribs}$	0.5	m
$l_{fus}$	6.22	m
$l_{sec1}$	1.5	m
$l_{sec2}$	1.5	m
$l_{sec3}$	3.2	m

Table 6: Geometric properties of the fuselage.

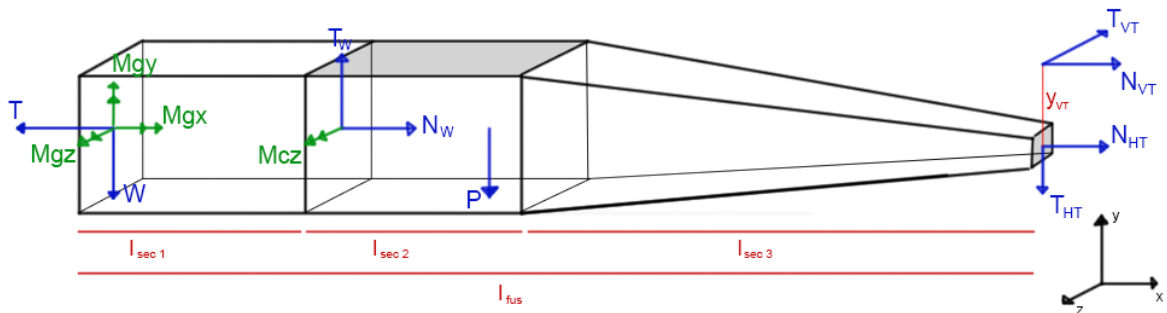


Figure 6: Free body diagram of the fuselage with all the external forces that are taken into account.

**Aeroelasticity** In order to ensure that no aileron reversal would take place, and no significant loss in aileron effectiveness would occur, a basic analysis into aeroelasticity was made. Modelling the wing as having a uniform cross-section, with the wing section at the middle of the half-span being representative of its structural characteristics, and using the data obtained from the vortex panel method, it was established that the aileron reversal speed equalled 854 m/s, far beyond what the aircraft will ever operate at. Indeed, the loss in aileron effectiveness at never exceed speed was shown to only equal 1%.

**c.g. and MMOI** The centre of gravity (c.g.) is important for the flying and handling qualities of the *StefX*. The c.g. was calculated via an iterative process. The c.g. location of each component, as well as the c.g. of the *StefX* itself, are shown in Table 7.

The MMOI was calculated using the method described in [33]. This method uses the masses and c.g. locations of different components of the aircraft. The aircraft was divided in the wing, horizontal tail, vertical tail and fuselage. These components were discretised, and the MMOI was calculated for each of these. The results of this are depicted in Table 8.

	Mass [kg]	x-location from nose [m]	z-location [m]
Aircraft at OEW	557	1.58	0.028
Aircraft with pilot	657	1.68	-0.01
Aircraft at MTOW	714	1.65	-0.009

Table 7: c.g. locations and masses of different configurations of the aircraft.

	Fuselage	Wing	HT	VT	Engine	Fuel	Pilot	Landing Gear	Total
$I_{xx}[kg \cdot m^2]$	6.46	634.89	3.39	10.59	9.55	0.005	4.44	12.6	682.9
$I_{yy}[kg \cdot m^2]$	82.7	34.14	221.1	496.1	304.2	6.92	38.9	23.1	1232
$I_{zz}[kg \cdot m^2]$	83.9	669	217.7	506.13	310.1	6.9	34.43	10.55	1862.9
$I_{xz}[kg \cdot m^2]$	1.3	0.17	-14.8	-11.59	-2.39	-0.19	-12.4	-11.52	-47.79

Table 8: Mass moments of inertia of the most important components as well as the total moments of inertia.

**Production Plan** For an efficient production method, the principles of lean manufacturing will be followed, thus limiting waste of time and resources. Due to the small production numbers, little investment in automation will be made. The select production method for the different subcomponents will therefore be tape laying, which can be done manually.

## Cost

The cost analysis was set up in order to determine the minimum selling price of the *StefX*. This was computed using the break even requirement of eight years. In order to perform a cost analysis, the market has to be explored.

**Market Analysis** The market analysis was based on a market share comparable to the market share of the EXTRA 330SC in the unlimited competition, and the number of aircraft sold in the previous years. To increase the possible market size, the decision was made to design a two seater variant of the *StefX*, besides the single seater *StefX*. The two seater will expand the market, while not having the costs of a new aircraft design. In the end, a total of 240 aircraft in eight years are estimated to be sold. 65 of which are single seaters, and 175 double seaters.

**Unit Price Estimation** The unit price estimation followed a process consisting of two different costs. The first source of cost is the fixed cost, which is only paid once and comes from the design and development of the aircraft. The second source is the variable cost which consists of the material and the manufacturing costs of the aircraft and is paid for every produced aircraft. The cost from all different parts are summarised in Figure 7.

**Operational Cost** The operational cost is estimated with the same method. Here the aircraft is assumed to fly 200 hours per year. It follows that the operational cost per 5 years is \$372,500. These values are based on the costs in the Netherlands, and can differ greatly per country. In the USA for instance, landing fees are often non-existent, and the fuel is cheaper. This would bring the operational cost down to \$201,700. However, the insurance is different for every pilot and depends on the experience, training, and more.

## RAMS

For the reliability, availability, maintainability, and safety (RAMS) analysis the results were as follows. In general aviation there is one accident due to mechanical failure on average every 116,279 flight hours. The majority of the accidents due to mechanical failure are caused by a failure of the power plant. The availability of the aircraft is dependent on maintenance and weather conditions. The ease of the maintenance is taken into account in designing the detailed components. Parts will be categorised based on how likely they are to be replaced. Parts that are replaced often, will be made easy to access and replace. Although all accidents in aerobatics in 2017 were fatal, aerobatic accidents occur rarely. 75% of all accidents and fatalities in general

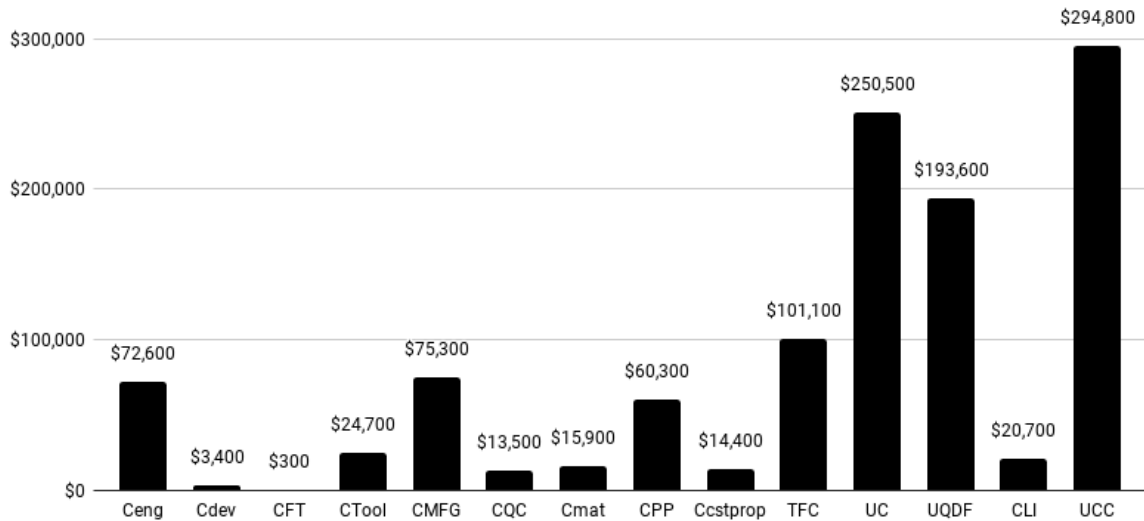


Figure 7: The unit price divided in the different parts.

aviation are caused by pilot error. These statistics are not valid when analysing solely aerobatics, but only limited data is available for accident rates in aerobatics. Therefore, it is concluded that pilot error is the biggest safety hazard. A major advantage in the design is the increased safety because of the lower landing speed due to the high lift devices. In order to maximise the survivability of a crash, a 20 G seat is installed which will take up most energy during a crash.

## Performance

During the design, the aircraft performance was identified to be a driving requirement for the sizing of the aircraft. After all the designing was done the performance of the *StefX* was analysed again, to make sure the aircraft meets the requirements.

**Airfield Performance** The *StefX* has a take-off distance of 77 m until screen height. This take-off will be performed in 5 s. This number applies to an optimal scenario in which not only full thrust is applied but also with all HLD fully deployed. For landing, the *StefX* would need 345 m to go from screen height to a stand still. In addition, when taxiing with a velocity of 5 kts, a turn radius of 7 m can be achieved by the *StefX*.

**Climb and Cruise** The maximum sustained climb angle at different speeds with MTOW can be seen in Figure 8. With 15 kg of fuel aboard the *StefX* can achieve a sustained climb angle of 45°. The cruise speed was determined to be 162 kts. At this speed, the *StefX* is able to fly 1417 km without refuelling.

**Stability** The CAP and the eigenmotions were analysed and found to be within level 1 flying qualities for the CAP and all eigenmotions, except the phugoid and dutch roll. However these eigenmotions were still stable, which was enough to meet the requirements.

**Manoeuvrability** The *StefX* was designed to obtain the required angular rates. The angular velocities that can be obtained are shown in Table 9.

Roll rate	Pitch rate	Yaw rate
463 °/s	66 °/s	87 °/s

Table 9: Rates of the aircraft.

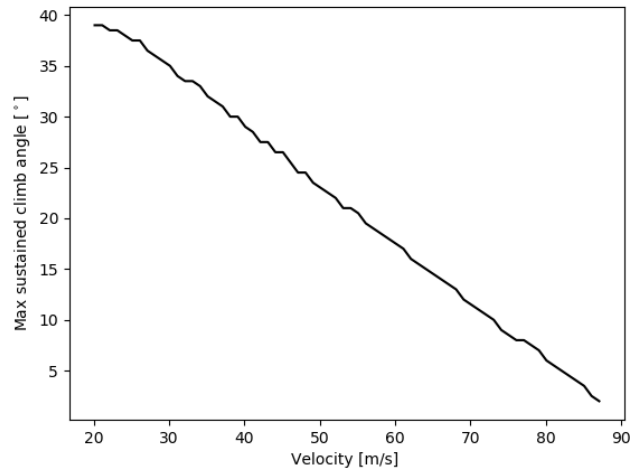
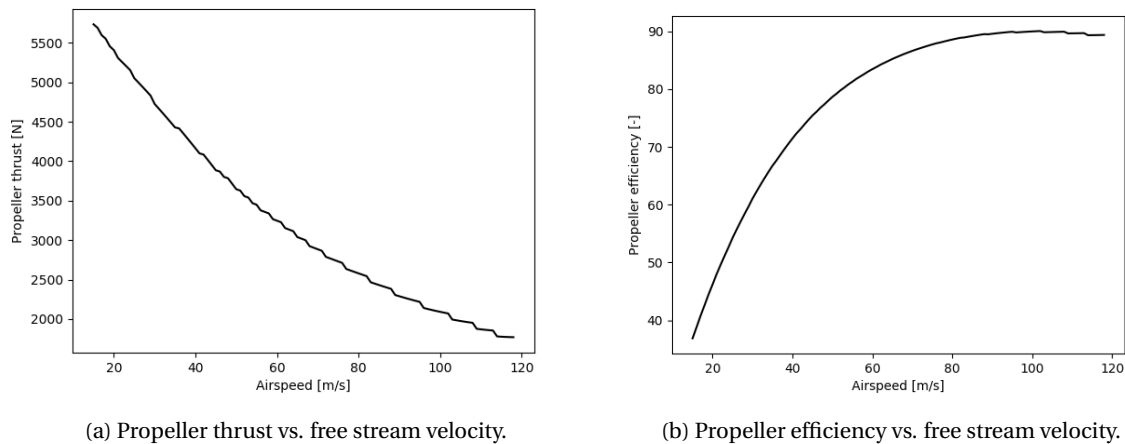


Figure 8: Maximum sustained climb angle at speeds between  $V_{stall}$  and  $V_a$  at MTOW and HLD deployed.



(a) Propeller thrust vs. free stream velocity.

(b) Propeller efficiency vs. free stream velocity.

Figure 9: Comparison of both propeller airfoils.

**Controllability during Stall** To see to what extent the *StefX* is controllable during stall, the airflow due to the propeller was calculated. It was determined what area of the control surfaces are immersed in the propeller slipstream flow as well as the flow velocity. The rudder is always fully immersed in this slipstream, as well as about half of the elevator. However, only 10 % of the ailerons is immersed. Therefore, there is barely any roll control during stall. The air stream from the propeller adds an extra 22 m/s to the free stream velocity.

**Thrust** From the BET analysis of the propeller, the induced airspeed by the propeller was calculated, which was used in the control surface effectiveness. Furthermore, the torque produced and the power needed were calculated. The thrust and efficiency at each velocity for a power needed of 235 kW are shown in Figures 9a and 9b. The torque at maximum power is a constant value of 830 Nm.

## Compliance

After the performance of the *StefX* was determined, all the system requirements were checked for compliance. It was concluded that most of the requirements were already met by the design. None of the requirements were not met. However for STX-SYS-17, STX-SYS-31, STX-SYS-32 and STX-SYS-33, the analysis for meeting the requirement were outside of the scope of this design phase. However, it is likely that that the *StefX* will also meet those requirements, based on reference aircraft.

## Sensitivity Analysis

To check the robustness of the final design a sensitivity analysis was done. For this analysis a change of mass, c.g.-location, decrease in available thrust and decrease of HLD effectiveness was analysed. From this it was concluded that a c.g. location that was moved forward could decrease the *StefX*'s flying capabilities, as well as a mass increase could make the *StefX* not meet the climb rate requirement.

In addition, the effect on the performance of making a two-seater variant of the *StefX* was analysed. The results of this can be found in Table 10

	<i>StefX</i>	Two-seater variant
CAP	3.53	6.1
$\zeta_{shortperiod}$ [-]	0.96	0.11
$T_{caperiodicroll}$ [s]	0.067	0.067
Climb rate [°/s]	45	26
Take-off distance [m]	77	164
Landing distance [m]	345	412
Max Roll rate [°/s]	460	455
Max Yaw rate [°/s]	87	83
Max pitch rate [°/s]	66	64
Sustained pitch rate [°/s]	25	21

Table 10: Effects of making a two-seater variant on the performance of this variant.

## Risk

Both the risks for the following phases of the *StefX* life cycle as well as the individual risks related to the different subsystems of the *StefX* were identified. Where needed, those risks were mitigated. An important additional risk of the *StefX* is the addition of an unconventional dual LEHLD system. It was identified that if the system would not be used correctly during flight, or when the system malfunctions and the pilot does not take the appropriate correcting measures, there is a substantial risk regarding flight safety. Proper documentation and clearly defined operational limits and pilot training should drastically lower the chances of this risk occurring. However, in the event the pilot needs to perform a forced landing without engine power, the lower stall speed due to the deployed HLDs will drastically reduce the amount of kinetic energy during impact with terrain, which in turn will lower the probability sustaining an injury considerably.

## Conclusion

From the analysis it can be concluded that *StefX* will meet all the requirements. The design of the *StefX* meets most of the system requirements. For the three requirements that are not yet met, there is confidence that they will be met in a later stage of the development. The design of *StefX* has been deemed a success and will be able to win the unlimited aerobatic competition in a decade from now.



Figure 10: The *StefX*

# Contents

Preface	ii
Executive Overview	iii
List of Symbols	xv
List of Subscripts	xx
List of Acronyms	xxi
List of Figures	xxii
List of Tables	xxiv
<b>1 Introduction</b>	<b>1</b>
<b>2 Preliminary Design Phase</b>	<b>2</b>
2.1 Functional Analysis . . . . .	2
2.2 Requirements . . . . .	2
2.3 Wing & Power Loading Diagram . . . . .	3
2.4 Initial Sizing. . . . .	3
2.5 Initial Aerodynamic Analysis . . . . .	4
2.6 Initial Stability Analysis . . . . .	5
2.7 Flying and Handling Qualities. . . . .	5
2.8 Initial Cost Analysis . . . . .	5
2.9 Initial Reliability, Availability, Maintainability, and Safety . . . . .	5
2.10 Trade-off . . . . .	6
2.11 Preliminary Design Phase Result . . . . .	6
<b>3 Sizing</b>	<b>7</b>
3.1 Flying and Handling Qualities. . . . .	7
3.2 Control Surface Sizing. . . . .	10
3.3 Propeller . . . . .	15
3.4 Landing Gear . . . . .	18
<b>4 Aerodynamics</b>	<b>20</b>
4.1 Drag Calculation . . . . .	20
4.2 Leading Edge High Lift Devices . . . . .	21
4.3 Trailing Edge High Lift Devices . . . . .	23
4.4 Aerodynamic Properties . . . . .	24
4.5 Aerodynamic Balancing. . . . .	35
<b>5 Aircraft Systems</b>	<b>39</b>
5.1 Stick and Rudder . . . . .	39
5.2 Control Linkages . . . . .	40
5.3 High Lift Device Control and Operation. . . . .	41
5.4 Electrical System . . . . .	43
5.5 Cockpit Layout & Avionics . . . . .	43
5.6 Fuel System . . . . .	44
5.7 Safety . . . . .	45
<b>6 Structural Design</b>	<b>47</b>
6.1 Material Selection. . . . .	47
6.2 Structural Analysis . . . . .	48
6.3 Aeroelasticity . . . . .	61
6.4 Structural Design of the Seat . . . . .	63
6.5 Centre of Gravity and Mass Moment of Inertia . . . . .	64

6.6	Production Plan . . . . .	66
<b>7</b>	<b>Cost</b>	<b>69</b>
7.1	Market Analysis . . . . .	69
7.2	Unit Price Estimation . . . . .	69
7.3	Operational Cost . . . . .	70
<b>8</b>	<b>Reliability, Availability, Maintainability, and Safety</b>	<b>72</b>
8.1	Reliability . . . . .	72
8.2	Availability . . . . .	72
8.3	Maintainability . . . . .	73
8.4	Safety . . . . .	73
8.5	Sustainable Development Strategy . . . . .	74
<b>9</b>	<b>Performance</b>	<b>76</b>
9.1	Regulatory V-speeds . . . . .	76
9.2	Airfield Performance . . . . .	76
9.3	Climb and Cruise . . . . .	78
9.4	Flying and Handling . . . . .	79
9.5	Manoeuvrability . . . . .	80
9.6	Control Effectiveness during Stall . . . . .	80
9.7	Propulsion . . . . .	81
9.8	Gyroscopic Effects . . . . .	82
<b>10</b>	<b>Compliance</b>	<b>86</b>
<b>11</b>	<b>Sensitivity Analysis</b>	<b>89</b>
11.1	Effect on Flying Qualities . . . . .	89
11.2	Effect on Performance . . . . .	89
11.3	Effect of a Two-seater Variant . . . . .	90
<b>12</b>	<b>Risk</b>	<b>91</b>
12.1	Technical Budget Management . . . . .	91
12.2	Post-DSE risks . . . . .	91
12.3	Subsystem Risk . . . . .	91
<b>13</b>	<b>Recommendations</b>	<b>94</b>
<b>14</b>	<b>Conclusion</b>	<b>96</b>
	<b>Bibliography</b>	<b>97</b>
<b>A</b>	<b>FFBD, FBS and Project Design &amp; Development Diagram</b>	<b>100</b>
<b>B</b>	<b>Technical Drawings</b>	<b>105</b>

# List of Symbols

$a$	Ratio axial propeller induced velocity over airspeed	[-]
$a_{mass}$	Linear distribution of mass along the span of the wing	[kg/m]
$A$	Aspect ratio	[-]
$A1$	Coefficient to determine wing mass distribution	[kgm <sup>2</sup> ]
$A_{enclosed}$	Enclosed area	[m <sup>2</sup> ]
$A_{str}$	Area of the stringer	[m <sup>2</sup> ]
$b$	Span	[m]
$b_f$	Width and height of the fuselage	[m]
$b_{str}$	Width of stringer	[m]
$B1$	Coefficient to determine wing mass distribution	[kgm <sup>2</sup> ]
$B_i$	Idealised boom with skin	[m <sup>2</sup> ]
$B_r$	Boom area	[m <sup>2</sup> ]
$c$	Chord	[m]
$c_{LG}$	Chord of the landing gear	[m]
$\bar{c}$	Average chord	[m]
$C1$	Coefficient to determine wing mass distribution	[kgm]
$C_{AP}$	Annual maintenance cost	[\$]
$C_{ctail}$	Cornering stiffness coefficient	[-]
$C_{cstprop}$	Propeller cost	[\$]
$C_{dev}$	Development support cost	[\$]
$C_{eng}$	Engineering cost	[\$]
$C_{fuel}$	Annual fuel cost	[\$]
$C_{HR}$	Hourly operating cost	[\$]
$C_{ins}$	Annual insurance cost	[\$]
$C_{insp}$	Annual inspection cost	[\$]
$C_{over}$	Overhauling cost	[\$]
$CPI_{2012}$	Conversion rate from 2012 to 2018	[-]
$C_{stor}$	Annual storing cost	[\$]
$C_{tool}$	Tooling cost	[\$]
$C_l$	Wing lift coefficient 2D	[-]
$C_{D_0}$	Zero lift drag coefficient	[-]
$C_{FT}$	Flight testing cost	[\$]
$C_f$	Turbulent flat-plate skin friction coefficient	[-]
$C_l$	Airfoil lift coefficient	[-]
$C_L$	Wing lift coefficient	[-]
$C_\ell$	Rolling moments coefficient	[-]
$C_{LI}$	Liability insurance cost	[\$]
$C_m$	Pitching moment coefficient	[-]
$C_{mat}$	Materials cost	[\$]
$C_{MFG}$	Manufacturing cost	[\$]
$C_n$	Yawing moment coefficient	[-]
$C_{PP}$	Power plant cost	[\$]
$C_{QC}$	Quality control cost	[\$]
$C_{Year}$	Annual operating cost	[\$]
$C_X$	Aerodynamic force coefficient in x-direction	[-]
$C_Y$	Aerodynamic force coefficient in y-direction	[-]
$C_{5Y}$	5 yearly operating cost	[\$]
$d$	Diameter	[m]
$D$	Drag	[N]
$D$	Propeller diameter	[m]
$D_p$	Diameter of the propeller	[m]

$e$	Oswald span efficiency factor	[-]
$F$	Force	[N]
$F_{CERT}$	Certification constant	[-]
$F_{CF}$	Constant for complex flap system	[-]
$F_{Comp}$	Constant for use of composites	[-]
$FF$	Fuel usage	[Gallons/hour]
$F_{flaperons}$	Weight of flaperons as fraction of the wing weight	[-]
$F_{fs}$	Weight of front spar as fraction of the wing weight	[-]
$F_{ij}$	Shear force in section ij	[N]
$F_{lehd}$	Weight of the leading edge HLD's as fraction of the wing weight	[-]
$F_{Press}$	Constant for use of a pressurized cabin	[-]
$F_{ribs}$	Weight of the ribs as fractions of the wing weight	[-]
$F_{skin}$	Weight of the skin as fraction of the wing weight	[-]
$F_Q$	Torque force	[N]
$G$	Shear modulus	[Pa]
$h$	Altitude	[m]
$h_f$	Altitude of flare	[m]
$h_{ribs}$	Height of the fuselage ribs	[m]
$h_{str}$	Height of stringer	[m]
$H_{eng}$	Hours spend by engineering	[hours]
$H_{FM}$	Ratio man-hours to flight hours	[-]
$H_{mfg}$	Hours spend by manufacturers	[hours]
$H_{tool}$	Hours spend by making tools	[hours]
$i$	Number of station of the wing	[-]
$I$	Mass moment of inertia	[kg · m <sup>2</sup> ]
$I_{uu}$	Angle transformation of second moment of area about the x-axis	[m <sup>4</sup> ]
$I_{uv}$	Angle transformation of second product moment of area	[m <sup>4</sup> ]
$I_{vv}$	Angle transformation of second moment of area about the y-axis	[m <sup>4</sup> ]
$I_{xx}$	Second moment of area about the x-axis	[m <sup>4</sup> ]
$I_{x'x'}$	Second moment of area about the x-axis transformed to the x'-axis	[m <sup>4</sup> ]
$I_{xy}$	Second product moment of area	[m <sup>4</sup> ]
$I_{yy}$	Second moment of area about the y-axis	[m <sup>4</sup> ]
$I_{y'y'}$	Second moment of area about the y-axis transformed to the y'-axis	[m <sup>4</sup> ]
$J$	Advancement ratio	[-]
$J$	Torsion constant	[m <sup>4</sup> ]
$K$	Non-dimensional radius of gyration	[-]
$l_{fus}$	Length of the fuselage	[m]
$l_{LG}$	Length of the landing gear	[m]
$l_P$	Distance from nose to pilot c.g.	[m]
$l_{sec1}$	Length of section 1 of the fuselage	[m]
$l_{sec2}$	Length of section 2 of the fuselage	[m]
$l_{sec3}$	Length of section 3 of the fuselage	[m]
$l_{wheelbase}$	Wheel base	[m]
$L$	Lift	[N]
$L$	Airfoil thickness location parameter	[-]
$L'$	Lift per unit span	[N/m]
$L_i$	Length of section	[m]
$m$	Aircraft mass	[kg]
$m_i$	Mass of local station	[kg]
$m_{pm}$	Mass of lumped point mass	[kg]
$M$	Mach number	[-]
$M$	Moment	[N · m]
$M_{ac}$	Moment about the aerodynamic center	[N · m]
$M_g$	Gyroscopic moment	[Nm]
$M_x$	Moments about the x-axis	[N · m]

$M_y$	Moments about the y-axis	[N · m]
$\mathbf{n}$	Unit normal vector	[-]
$n$	Load factor	[-]
$n$	Rotational speed of propeller	[rad/s]
$N_B$	Number of blades	[-]
$N_{HT}$	Normal force component of the horizontal stabiliser	[N]
$N_P$	Number of aircraft to be made in 5 years	[-]
$N_{PP}$	Number of engines	[-]
$N_{tail}$	Normal force on the tail wheel	[N]
$N_{VT}$	Normal force on the vertical stabiliser	[N]
$p$	Angular velocity about x-axis	[rad/s]
$P$	Power needed	[W]
$P$	Weight of the pilot	[kg]
$P_i$	Axial loading in idealised boom i	[Pa]
$P_{BHP}$	Engine power	[BHP]
$\mathbf{q}$	Induced velocity vector	[m/s]
$q$	Angular velocity about y-axis	[rad/s]
$q$	Dynamic pressure	[kg m <sup>-1</sup> s <sup>-2</sup> ]
$q_{ij}$	Shear flow in section ij	[N/m]
$q_{ijfinal}$	Total shear flow over section ij	[N/m]
$q_{iN}$	Shear flow due to the normal force in section ij	[N/m]
$q_{iT}$	Shear flow due to the tangent force in section ij	[N/m]
$q_{s,0}$	Correcting shear flow	[N/m]
$q_{s,0N}$	Correcting shear flow due to normal shear force	[N/m]
$q_{s,0T}$	Correcting shear flow due to tangent shear force	[N/m]
$q_{torque}$	Shear flow due to torque	[N/m]
$Q$	Torque	[Nm]
$Q_{FLGT}$	Flight hours per year	[Hours]
$\mathbf{r}$	Distance vector	[m]
$r$	Angular velocity about z-axis	[rad/s]
$r$	Local propeller radius	[m]
$R$	Aerodynamic interference correlation factor	unit
$R$	Radius	[m]
$R_{Hub}$	Hub radius	[m]
$R_{ENG}$	Hourly rate of an engineer	[\$]
$R_{FUEL}$	Hourly rate of fuel	[\$]
$R_{MFG}$	Hourly rate of a manufacturer	[\$]
$R_{TOOL}$	Hourly rate of making tools	[\$]
$R_{MF}$	Hourly rate of maintenance	[\$]
$R_{STOR}$	Monthly rate of storage	[\$]
$Re$	Reynolds number	[-]
$R_f$	Radius of flare motion	[m]
$R_{l.s.}$	Lifting surface correction factor	[-]
$s$	Arc length	[m]
$s_i$	Arc length of section	[m]
$s_{ribs}$	Spacing of the fuselage ribs	[m]
$S$	Surface area	[m <sup>2</sup> ]
$S_x$	Shear force in x-direction	[N]
$S_y$	Shear force in y-direction	[N]
$t$	Local thickness	[m]
$(t/c)$	Thickness to chord ratio	[-]
$t_D$	Skin thickness of the fuselage	[m]
$t_{LG}$	Skin thickness of the airfoil	[m]
$t_{ribs}$	Thickness of the fuselage ribs	[m]
$T$	Thrust	[N]
$T_{HT}$	Tangential force acting on the horizontal stabiliser	[N]
$T_{VT}$	Tangential force acting on the vertical stabiliser	[N]

$T_W$	Tangential force acting on the wing	[N]
$TFC$	Total Fixed Cost	[\$]
$u$	Linear velocity along x-axis	[m/s]
$UC$	Unit cost	[\$]
$UC_{pre}$	Preliminary unit cost	[\$]
$UC_{QDF}$	Unit cost with quality discount function	[\$]
$v$	Linear velocity along y-axis	[m/s]
$\mathbf{V}$	Velocity vector	[m/s]
$V$	Airspeed	[m s <sup>-1</sup> ]
$V_0$	Free stream airspeed	[m s <sup>-1</sup> ]
$V_E$	Airspeed seen by propeller blade	[m s <sup>-1</sup> ]
$V_R$	Combined airspeed of blade rotation and $V_0$	[m s <sup>-1</sup> ]
$V_H$	Maximum level speed	[KTAS]
$V_{LOF}$	Lift-off speed	[m/s]
$V_R$	Rotation speed	[m/s]
$V_r$	Aileron reversal speed	[m/s]
$V_{s0}$	Stall speed in landing configuration	[m/s]
$V_{s1}$	Stall speed obtained in a specified configuration	[m/s]
$w$	Linear velocity along z-axis	[m/s]
$w$	induced velocity by the propeller	[m s <sup>-1</sup> ]
$W$	Aircraft weight	[N]
$W_{airframe}$	Weight of the airframe	[lbs]
$W_E$	Engine weight	[kg]
$\mathbf{x}$	Position vector	[m]
$x$	Distance	[m]
$x_c$	Horizontal distance from the centroid to the origin	[m]
$\hat{\mathbf{y}}$	Unit vector in $y$ -direction	[-]
$y_c$	Vertical distance from the centroid to the origin	[m]
$y_{VT}$	The moment arm from the centre of the fuselage to the centre of pressure	[m]
$\alpha$	Angle of attack	[rad]
$\alpha_{LG}$	Angle with the vertical axis of the landing gear	[°]
$\beta$	Angle of sideslip	[rad]
$\beta$	Pitch of the propeller blade	[rad]
$\delta$	Deflection	[rad]
$\epsilon$	Downwash angle	[rad]
$\epsilon$	Distance to shear centre from the aerodynamic centre	[m]
$\gamma$	Flight path angle	[rad]
$\mathbf{\Gamma}$	Circulation vector	[m/s <sup>2</sup> ]
$\Gamma$	Circulation	[m <sup>2</sup> /s]
$\eta_{max}$	Maximum lifting efficiency based on leading edge ratio to airfoil thickness ratio	[-]
$\eta_\delta$	Empirical factor taking into account changes in flap deflection	[-]
$\kappa$	Surface roughness factor	[in]
$\lambda$	Eigen value	[-]
$\Lambda$	Sweep angle	[rad]
$\Lambda_{local}$	Local sweep due to taper	[rad]
$\mu_b$	Relative density, asymmetric motions	[-]
$\mu_c$	Relative density, symmetric motions	[-]
$\rho$	Density	[kg/m <sup>3</sup> ]
$\sigma$	Sidewash angle	[rad]
$\sigma_1$	Normal stress in direction 1	[Pa]
$\sigma_2$	Normal stress in direction 2	[Pa]
$\sigma_3$	Normal stress in direction 3	[Pa]
$\sigma_{1c}$	Maximum compressive normal stress in direction 1	[Pa]
$\sigma_{2c}$	Maximum compressive normal stress in direction 2	[Pa]
$\sigma_{3c}$	Maximum compressive normal stress in direction 3	[Pa]

$\sigma_{1t}$	Maximum tensile normal stress in direction 1	[Pa]
$\sigma_{2t}$	Maximum tensile normal stress in direction 2	[Pa]
$\sigma_{3t}$	Maximum tensile normal stress in direction 3	[Pa]
$\sigma_j/\sigma_i$	Stress ratio	[-]
$\sigma_z$	Normal stress in z-direction	[Pa]
$\sigma'_z$	Normal stress in z-direction corrected for taper	[Pa]
$\omega$	Undamped natural frequency	[rad/s]
$\omega$	Angular rate	[rad/s]
$\dot{\omega}$	Angular acceleration	[rad/s <sup>2</sup> ]
$\Omega$	Axis system rotation	[rad/s]
$\phi$	Roll angle	[rad]
$\phi$	Transformation angle	[rad]
$\Phi$	Velocity potential	[m <sup>2</sup> /s]
$\tau$	Tangential unit vector	[-]
$\tau_{12}$	Maximum shear stress on plane 1 in direction 2	[Pa]
$\tau_{13}$	Maximum shear stress on plane 1 in direction 3	[Pa]
$\tau_{23}$	Maximum shear stress on plane 2 in direction 3	[Pa]
$\tau_{ij}$	Shear stress in section ij	[Pa]
$\theta$	Pitch angle	[rad]
$\theta$	Twist angle	[rad]
✓	Requirement has been met	[-]
✱	Requirement cannot be checked for compliance	[-]

# List of Subscripts

<i>a</i>	Aileron
<i>B<sub>te</sub></i>	Maximum body frontal area
<i>c.g.</i>	Centre of gravity
<i>e</i>	Elevator
<i>eq</i>	equivalent
<i>f</i>	flap
<i>fus</i>	Fuselage
<i>gear</i>	Landing gear
<i>HT</i>	Horizontal tail
<i>i</i>	Induced
<i>l</i>	Local
<i>l</i>	Lower
<i>misc</i>	Miscellaneous
<i>p</i>	Propeller
<i>pm</i>	Point mass
<i>r</i>	Rudder
<i>ref</i>	Reference
<i>req</i>	Required
<i>s</i>	Slat
<i>s</i>	Slipstream of propeller
<i>sp</i>	Short period
<i>t</i>	Tangential
<i>TB</i>	Tail-body
<i>u</i>	Upper
<i>VT</i>	Vertical tail
<i>w</i>	Wing
<i>wet</i>	Wetted
<i>WB</i>	Wing-body
$\infty$	Freestream

# List of Acronyms

a.c.	Aerodynamic Center
AVL	Athena Vortex Lattice
BET	Blade Element Theory
CAP	Control Anticipation Parameter
CFD	Computational Fluid Dynamics
c.g.	Centre of gravity
CHT	Cylinder Head Temperature
CS23	Certification Specification 23
CIVA	Commission Internationale de Voltige Aérienne
EGT	Exhaust Gas Temperature
ELT	Emergency Locator Transmitter
EOM	Equations of Motion
FAI	Fédération Aéronautique Internationale
FBS	Functional Breakdown Structure
FFBD	Functional Flow Block Diagram
GAAD	General Aviation Aircraft Design
GPS	Global Positioning System
ID	IDentification number
LEHLD	Leading Edge High Lift Device
MMOI	Mass Moment of Inertia
N.A.	Not Applicable
PFD	Primary Flight Display
s.c.	Shear Centre
TBD	To be determined
TRL	Technology Readiness Level

# List of Figures

1	Technical drawings of the control surfaces. The dimensions are in <i>mm</i> . . . . .	iv
2	Landing gear dimensions. . . . .	iv
3	LEHLD double slat concept. . . . .	v
4	Flaperon actuation system. . . . .	vi
5	Render of the LEHLDs in both deployed and undeployed position. . . . .	vi
6	Free body diagram of the fuselage with all the external forces that are taken into account. . . . .	viii
7	The unit price divided in the different parts. . . . .	x
8	Maximum sustained climb angle at speeds between $V_{stall}$ and $V_a$ at MTOW and HLD deployed. . . . .	xi
9	Comparison of both propeller airfoils. . . . .	xi
10	The <i>StefX</i> . . . . .	xii
2.1	Highest level in the design option tree. V1.0 . . . . .	3
3.1	Equivalence of Cooper–Harper rating scale with levels of flying qualities [13]. . . . .	7
3.2	Free body diagram in the <i>yz</i> plane. . . . .	12
3.3	Free body diagram in the <i>xz</i> plane. . . . .	12
3.4	Free body diagram in the <i>xy</i> plane. . . . .	12
3.5	Local flow for a strip wing [38]. . . . .	12
3.6	Technical drawings of the control surfaces. The dimensions are in <i>mm</i> . . . . .	16
3.7	The airfoil geometry from the propeller.[22] . . . . .	17
3.8	Comparison of both propeller airfoils. . . . .	18
3.9	Constraints for the landing gear, to prevent tip over. [49] . . . . .	18
3.10	Landing gear dimensions. . . . .	19
4.1	LEHLD concepts. . . . .	22
4.3	$\alpha - C_l$ curve with the slat system. . . . .	23
4.4	Induced velocity of a discrete vortex [28, p. 231]. Note that the positive <i>y</i> -axis points into the paper. . . . .	25
4.5	Example panel distribution over airfoil [45, p.29]. Note that although in this Figure a thick airfoil is used, it was assumed for this simulation that the airfoil could be modelled as thin, i.e. all panels are only placed on the mean camber line. . . . .	26
4.6	Coordinate system chosen for the unsteady airfoil analysis [28, p. 387]. Note that the positive <i>y</i> -axis points into the paper. . . . .	28
4.7	Wake shedding from a forward moving airfoil [28, p. 387]. . . . .	29
4.8	Mesh creation [28, p. 341]. . . . .	31
4.9	Mesh creation [28, p. 344]. . . . .	31
4.10	Straight vortex line segment and point <i>P</i> [28, p. 254]. . . . .	32
4.11	Construction of the unit normal vector to a panel [28, p. 254]. . . . .	32
4.12	Aerodynamic polars of the main wing. . . . .	34
4.13	Pressure distribution over wing, with flaperons extended upwards at a deflection angle of $10^\circ$ , at an angle of attack of $10^\circ$ , at a freestream velocity of 80 m/s. . . . .	35
4.14	Aerodynamic hinge moment of the control surfaces. . . . .	37
4.15	Pressure distribution over wing, with flaperons extended upwards at a deflection angle of $10^\circ$ , at an angle of attack of $10^\circ$ , at a freestream velocity of 80 m/s. Note that the wing is looked at from behind, i.e. the leading edge is located at positive <i>x</i> . . . . .	38
5.1	Control linkage layout. . . . .	40
5.2	LEHLD deployment . . . . .	42
5.3	Flaperon actuation system. . . . .	42
5.4	LEHLD pilot interface (throttle lever, pilot's view) . . . . .	43
5.5	Electrical system diagram. . . . .	44
5.6	Proposed cockpit layout. . . . .	45

5.7	Example of a flop tube. . . . .	46
6.1	Z-stringer axis transformation. . . . .	49
6.2	Effect of normal stress due to taper. . . . .	52
6.3	Schematic representation of a wing box. . . . .	53
6.4	Effect of normal stress due to taper. . . . .	54
6.5	Normal stress distribution for Top side of the wing. Unit of the colour scheme is given in 10 MPa. . . . .	55
6.6	Normal stress distribution for bottom side of the wing. Unit of the colour scheme is given in 10 MPa. . . . .	56
6.7	Tsai-Wu Failure criterion for Top side of the wing. . . . .	57
6.8	Tsai-Wu Failure criterion for bottom side of the wing. . . . .	58
6.9	Steel truss structured fuselage of the EXTRA 300. . . . .	59
6.10	Cross section of the fuselage with four booms. . . . .	59
6.11	Free body diagram of the fuselage with all the external forces that are taken into account. . . . .	59
6.12	Sketches used to calculate the shear flows in the cut out section. . . . .	60
6.13	The axial loading induced due to shear in boom 3 in detail. . . . .	60
6.14	A 3D plot showing the F values at all points of a simplification of the fuselage skin. . . . .	61
6.15	A 3D plot showing a stresses due to normal stresses in the fuselage with red depicting compression and purple tension. The colour scale has an unit of 100 MPa. . . . .	61
6.16	Cross section of landing gear strut with E475 airfoil shape and foam filling. . . . .	61
6.17	Simplified model of the wing [31, p. 809]. . . . .	63
6.18	Aileron effectiveness as function of speed. . . . .	63
6.19	Stress-strain curve of a elastomeric foam. . . . .	64
6.20	Coordinate system for c.g. location, as well as the c.g. locations for OEW and MTOW. . . . .	64
6.21	Hand lay up of prepreg composite sheets [46]. . . . .	67
6.22	Work flow diagram of the manufacturing procedure of carbon components [39]. . . . .	67
6.23	Work flow diagram of the assembly procedure of the sub-components [46]. . . . .	68
7.1	The unit price divided in the different parts. . . . .	70
9.1	The <i>StefX</i> take-off trajectory. . . . .	77
9.2	The <i>StefX</i> landing trajectory. . . . .	78
9.3	Maximum sustained climb angle at speeds between $V_{stall}$ and $V_a$ at MTOW and HLD deployed. . . . .	79
9.4	Roll rate for $\delta_a = 30^\circ$ at 1 s. . . . .	80
9.5	Pitch rate for $\delta_e = -25^\circ$ at 1 s. . . . .	81
9.6	Yaw rate for $\delta_r = 25^\circ$ at 1 s. . . . .	81
9.7	Comparison of both propeller airfoils. . . . .	83
9.8	Induced velocities at the hub and tip of the propeller. . . . .	83
9.9	Gyroscopic time responses . . . . .	85
A.1	Project Development Diagram. . . . .	100
A.2	Function Flow Block Diagram. . . . .	101
A.3	Functional Breakdown Structure. . . . .	102
A.4	Functional Breakdown Structure of mission. . . . .	103
A.5	Post-DSE Gantt Chart . . . . .	104

# List of Tables

1	Aerodynamic properties obtained by vortex ring method. . . . .	v
2	Properties of the chosen material: Epoxy/Carbon fibre, UD prepreg with QI lay-up. . . . .	vii
3	Properties of Epoxy/S-glass fibre, UD prepreg, QI lay-up. . . . .	vii
4	Results of the structural analysis of the Main Wing, Vertical and Horizontal Tail. . . . .	vii
5	Geometric properties of the landing gear. . . . .	viii
6	Geometric properties of the fuselage. . . . .	viii
7	c.g. locations and masses of different configurations of the aircraft. . . . .	ix
8	Mass moments of inertia of the most important components as well as the total moments of inertia. . . . .	ix
9	Rates of the aircraft. . . . .	x
10	Effects of making a two-seater variant on the performance of this variant. . . . .	xii
2.1	Trade-off summary table. . . . .	6
2.2	Design parameters which will not change during the detailed design phase. . . . .	6
3.1	Final sizing values for the stability derivatives. . . . .	8
3.2	Longitudinal stability derivatives formulas. . . . .	8
3.3	Lateral stability derivatives formulas. . . . .	9
3.4	Geometric values for control surfaces. . . . .	15
4.1	Drag Calculation using DATCOM, for a velocity of $94 \text{ m s}^{-1}$ and angle of attack of $5^\circ$ . . . . .	20
4.2	Verification DATCOM [11] zero lift drag coefficient with midterm values calculated using Gudmundsson [22]. . . . .	21
4.3	Slat deployment time due to suction peak force. . . . .	22
4.4	Results of the slat optimisation for the geometric average chord location. . . . .	22
4.5	Aerodynamic properties obtained by vortex ring method. . . . .	33
5.1	Results of the control linkage analysis. . . . .	41
5.2	Slat actuation mechanism sizing inside wing. . . . .	41
5.3	Cockpit equipment list. . . . .	46
6.1	Specific properties of Aluminium 7075 T6 and Epoxy/Carbon fiber, uni-directional prepreg with quasi isotropic lay-up. . . . .	48
6.2	Properties of the chosen material: Epoxy/Carbon fiber, uni-directional prepreg with quasi isotropic lay-up. . . . .	48
6.3	Properties of Epoxy/S-glass fibre, UD prepreg, QI lay-up. . . . .	48
6.4	Results of the structural analysis of the Main Wing, Vertical and Horizontal Tail. . . . .	59
6.5	Geometric properties of the fuselage. . . . .	62
6.6	Geometric properties of the landing gear. . . . .	62
6.7	Properties of three elastomeric foams. . . . .	64
6.8	C.g. locations and masses of each component of the aircraft. . . . .	65
6.9	Local mass moments of inertia of the horizontal and vertical tail. . . . .	66
6.10	Mass moments of inertia of the most important components as well as the total moments of inertia. . . . .	66
7.1	Number of EXTRA 300 and 330 aircraft build until January 2018 [34]. . . . .	69
7.2	Unit cost estimation and operational cost estimation. . . . .	71
8.1	Carbon footprint, energy and water usage for the production of the <i>StefX</i> . . . . .	75
9.1	<i>StefX</i> V-speeds . . . . .	76
9.2	Summary of the <i>StefX</i> take-off performance. . . . .	77
9.3	Summary of <i>StefX</i> take-off performance. . . . .	77

---

9.4	Summary of the <i>StefX</i> climb performance. . . . .	78
9.5	Fuel volumes, range and endurance . . . . .	79
9.6	Level of flying qualities . . . . .	79
9.7	Control surface immersed in propeller slipstream during stall with comparison to full control surface areas. . . . .	82
11.1	Effects of change in mass and c.g. location on the flying qualities of the <i>StefX</i> . . . . .	89
11.2	Effects of change in parameters to the performance of the <i>StefX</i> . . . . .	90
11.3	Effects of making a two-seater variant on the performance of this variant . . . . .	90
12.1	Technical budgets as determined at the start of the project. . . . .	91
12.2	List of possible technical risks before mitigation. . . . .	92
12.3	Technical risk map before mitigation. . . . .	92
12.4	Risk mitigation strategies. . . . .	93
12.5	Technical risk map after mitigation. . . . .	93
12.6	Deployable HLDs risks. . . . .	93



# Chapter 1

## Introduction

Aerobatics is a jury sport in which pilots perform all kind of manoeuvres putting the aircraft in unusual attitudes such as flying vertical, upside down or even backwards for a short period of time. All these manoeuvres are performed within the so-called performance zone, a virtual box of 1x1x1 km. Full control and precision in the manoeuvres is key to win competitions. The World Championships for aerobatics are conducted under the supervision of the FAI Aerobatics Commission (CIVA), at which the best pilots perform in this thrilling and highly dynamic event. The powered aerobatics are divided into five categories, based on the level of difficulty of the performed aerobatic manoeuvres. The EXTRA 330SC, first produced in 2009, currently dominates the highest competition category, the Unlimited category.

The goal of this project is to design an aircraft that is able to outperform the current generation of Unlimited category aerobatic aircraft. The customer mentioned power to weight ratio, manoeuvrability, easy and precision of control and energy management as important parameters in which the aircraft should be better than its competition. Besides, the aircraft should be strong, light weight, capable of high-G manoeuvres and should possess excellent handling qualities that allow for very precise control of the aircraft. It should be able to outperform the current aircraft in this category [27]. The following mission statement was set-up in the beginning of the project: “To design the ultimate aerobatic competition aircraft, capable of winning in the FAI Unlimited World Aerobatic Championships by ten students in ten weeks.”

The purpose of this report is to present the design of the Ultimate Unlimited Aerobatic Aircraft called the *StefX* and the phases leading up to this detailed design. The final result and its performance is presented as well as the complete methodology used to design every subsystem of the *StefX*. Besides the technical analysis, a business case was developed by means of a market analysis and a risk analysis.

The structure of the report is as follows. Chapter 2 describes the phases leading up to the detailed design of the *StefX*. In Chapter 3, the dimensions of the aircraft were sized including the control surfaces. Chapter 4 covers the aerodynamic analysis in which the innovative use of leading edge high lift devices are explained. The aircraft systems like the control system, control linkages and the electrical system are described in Chapter 5. Next, the structural design of the aircraft and the production plan are explained in Chapter 6. Chapter 7 holds the market analysis and the cost estimation. The RAMS analysis and risk analysis are described in Chapter 8 and Chapter 12 respectively. The complete performance of the aircraft is explained in Chapter 9. The compliance with the requirements and the sensitivity analysis are covered in Chapter 10 and Chapter 11 respectively. Finally, the recommendations and conclusion are presented.

# Chapter 2

## Preliminary Design Phase

This chapter explains the progress made in the first half of the project to design the next Ultimate Unlimited Aerobatic Aircraft. It started with setting up requirements and concept generation. From there, five concepts were selected which were thoroughly analysed for an extensive trade-off. The winner of the trade-off was designed in detail in the second half of the project and is explained in the other parts this report.

### 2.1 Functional Analysis

As described in the midterm report, the Functional Flow Block Diagram (FFBD) shows the logical order of functions the aircraft has to perform. It contains a number of blocks describing these functions connected by arrows. Functions may be performed in parallel (AND junction) or optional functional paths may exist (OR junction). This diagram was used to identify aircraft systems and parts to be designed during the final design phase and the phases after. It also helped to identify areas where innovation could occur. Based on all families of manoeuvres represented in the FFBD (block 4.6.2.4.1 - block 4.6.2.4.8) [10], it was for example identified that lowering the stall speed can improve the performance for certain stall related manoeuvres and it also helps to stay within the box. It was decided to investigate the option of adding HLDs both at the trailing and leading edge. The Functional Breakdown Structure (FBS) gives a clear overview of all of the functions that the aircraft needs to perform. The functions are represented in a hierarchical manner. This diagram is used in a similar manner as the FFBD. The FBS and FFBD can be found in Appendix A.

### 2.2 Requirements

The customer provided a list of ten requirements that the *StefX* will need to meet. Other requirements follow from the different stakeholders. Eight different stakeholders were identified:

- Pilots.
- Fédération Aéronautique Internationale (FAI).
- Spectators.
- Governments.
- Airports.
- Economic owners of the aircraft.
- Suppliers.
- Manufacturers.

The final method which was used to come up with requirements, was the requirements discovery tree. The discovery tree was split up into two parts, the functional requirements, which are derived from the functional analysis and the different constraints for designing the *StefX*. From all these methods of generating requirements a list of system requirements was derived. No killer requirements were identified. There are 5 driving requirements:

- STX-SYS-15: The aircraft shall be able to obtain a roll rate of at least 450 °/s.
- STX-SYS-16: The pitch rate shall not be less than 20 °/s
- STX-SYS-17: The yaw rate shall not be less than 40 °/s while flying at 40 kts in a vertical line up.
- STX-SYS-20: The aircraft shall be able to withstand  $\pm 10$  G
- STX-SYS-25: The maximum unit price of the aircraft shall be \$ 325,000.

### Design Options

To choose the concept that will lead to the best design, an extensive trade-off was performed. Before this extensive trade-off could be done, some of the concepts needed to be eliminated, to ensure that each concept in the trade-off could be analysed properly. The biplane concepts were eliminated, as judges and pilots stated that it was hard to see from the ground, which would lead to less points from judges for manoeuvres, and

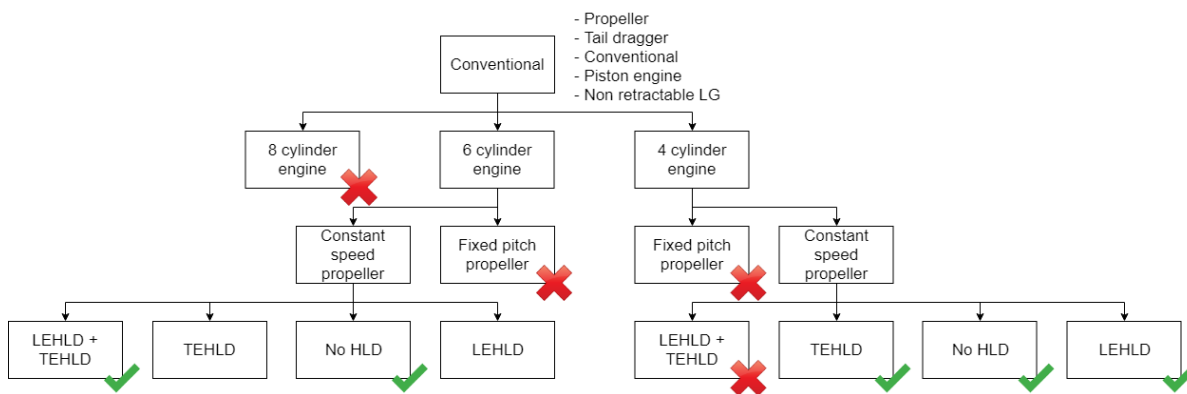


Figure 2.1: Highest level in the design option tree. V1.0

thus it would be hard to reach the objective of the *StefX* to win the Unlimited Aerobatic Competition. The five concept that were chosen after the Design Option Tree for the trade-off are:

- Concept 1: Conventional aircraft
- Concept 2: Conventional aircraft with High Lift Devices (HLD)
- Concept 3: Lightweight aircraft
- Concept 4: Lightweight aircraft with flaperons
- Concept 5: Lightweight aircraft with leading edge HLD's

Concept 1 was also used as a benchmark, to check if the more innovative concepts 2 till 5 will lead to an increase in performance. The Lightweight aircraft concepts also have a conventional configuration. The Design Option Tree had a branch with a 4 cylinder engine on which these lightweight concepts are based. This type of engine has less power but also less weight. The trade-off is based on 6 different criteria. The weights for the criteria were determined using a Quality Function Deployment (QFD) diagram.

## 2.3 Wing & Power Loading Diagram

Seven requirements were used with respect to the stall speed, landing and take-off distance, cruise speed, climb rate and gradient and a sustained level turn. From the resulting wing & power loading diagram, the design point was chosen. These models were verified by using the same model for the EXTRA 330SC; the design point was indeed in the allowable design space. The wing and power loading obtained from this analysis was  $W/S=740 \text{ N/m}^2$  for concept 1, 2 and 3. For concept 4  $W/S=600 \text{ N/m}^2$  and for concept 5  $W/S=900 \text{ N/m}^2$ . The higher maximum lift coefficient of the concepts with HLD's were used to decrease the stall speed.

## 2.4 Initial Sizing

**Airfoil selection** After the wing and power loading were obtained, an airfoil needed to be selected. For the airfoil selection, five different airfoils which would generate a sudden and severe collapse in lift when stalling were simulated with XFOIL. The airfoil that was selected was the MS15, which outperformed the other airfoils in almost everything. This airfoil is also used on the EXTRA 330SC. For the horizontal and vertical tail, the same airfoils as used in the EXTRA 330 SC will be used, being the NACA0009 airfoil that will be used for the horizontal tail, and the Wortmann FX 71-L-150/30 airfoil that will be used for the vertical tail.

**Power Unit Sizing** For the selection of the power unit a list of viable engines was generated, for which the power to weight ratio and engine overhaul time of each engine was compared. For concepts 1 and 2 the six cylinder AEIO-580 engine was selected and for concepts 3, 4 and 5 the four cylinder AEIO 390. Concepts 1 and 2 will have a propeller diameter in between 1.92 and 2.19 m, for the other concepts the diameter will be in between 1.73 and 1.98 m.

**Fuselage sizing** The sizing was based on the engine bay from the selected engine, cabin dimensions based on the dimensions for the 95th percentile Dutch males and the fuel tank size. A simplified model of the fuselage was used to determine the wetted area. The fuselage sizing will be used for the drag estimation and empennage sizing.

**Wing planform** For the different concepts different wing plan-form were determined based on the design point, the estimated MTOW and reference aircraft. For all concepts, the quarter chord sweep was set to  $0^\circ$  and the taper ratio was set to 0.45.

**Empennage sizing** The tail arm and location of the leading edge of the root of the main wing were estimated based on the EXTRA 330SC. The initial tail sizing is based on this tail arm. The design decision was made to put the rudder completely after the trailing edge of the elevator. Like this, no parts of the elevator have to be removed to allow for full rudder deflection.

**Control Surfaces and High Lift Device Sizing** Based on the EXTRA 330SC, the aileron spanned over the full wing, with a chord length of the control surface over the wing chord of  $(c_f/c)_e = (c_f/c)_r = 0.5$ . Additionally, it was assumed that for the conventional concepts, the ailerons will deflect for  $\pm 30^\circ$ , but that the lightweight concepts will only deflect for  $\pm 25^\circ$ . For the elevator and rudder, it is assumed that the control surface spans the whole of the horizontal respectively vertical tail.

For the Leading Edge High Lift Devices on concept 2 and 5, it was assumed that the leading edge HLD (LEHLD) would span 10% of the chord, and the ratio of the slat span to exposed wing span would equal 95%. For the flaperons, used on concept 2 and 4, the same dimensions as for the ailerons will be used.

**Landing gear** A conventional landing gear (tail dragger configuration) was selected since the lower structural weight and drag outweigh the decreased ease and safety of landings and take-offs. The tire diameter of the main wheels for all the concepts is 17".

**Weight estimation** After all the sizing was finished, a weight estimation could be performed. The weight estimation was done by iterating between a Class I and Class II estimation. It was estimated that concept 1 will have a MTOW of 841 kg, concept 2 890 kg, and concept 3, 4 and 5 will weigh 665, 713 and 663 kg respectively. This means that the lightweight concepts are estimated to be heavier than the maximum MTOW determined previously to have the same power to weight ratio as concepts 1 and 2. For validation, the class II weight estimation was performed for five other aerobatic aircraft. An error of 10% to 20% has been identified.

**Structural analysis** The structural analysis is performed to make sure that each concept has a design that is structurally feasible. A material database was established and it was chosen to use Epoxy resin, carbon fibre, woven fabric pre-preg Quasi Isotropic lay-up as the material for all parts of the aircraft due to its high tensile strength and low density. A simplified model was used to determine the weight of the wing structure including the webs, spar caps and ribs.

## 2.5 Initial Aerodynamic Analysis

**Drag** The drag analysis was done to obtain data needed for the lift analysis, as well for the calculation of the stability derivatives. The method of analysing the drag was obtained from [22], which is based on statistical data as well as formulas from for example [42]. For the analysis a distinction was made between skin friction drag, lift induced drag and miscellaneous drag. The total drag was computed, based on the determined geometry, to be 2076 N for concept 1 and 2, and 1727 N for the lightweight concepts 3, 4 and 5.

**Aerodynamics** To determine the aerodynamic properties the DATCOM methods were used, which require the initial geometry of each concept, and is based on statistical data. The DATCOM method is a method that is already extensively verified and validated. The aerodynamic properties that were found will be used for the determination of the stability derivatives, as well as the determination of the flying and handling qualities of each concept.

**Control Surface Analysis** To analyse the manoeuvrability of the aircraft, the aerodynamic properties of the control surfaces were needed. To obtain this information, again XFOIL was used. The elevator, aileron and rudder effectiveness were determined. A similar analysis was performed for the HLD's.

## 2.6 Initial Stability Analysis

**Stability Derivatives** The formulas for calculating the longitudinal stability derivatives were obtained from [44, page. 187] and were verified by calculating these stability derivatives for the Ryan Navion aircraft. The lateral stability derivatives were calculated by using equations for the wing and vertical tail contribution of these derivatives. All the lateral derivatives were also verified by comparing the values with the Ryan Navion aircraft. This was done for validation of the method, as this aircraft is one of the few aircraft of which all the stability derivatives were calculated in [37], while having a comparable geometry compared with the concepts.

**Loading Diagram and Stability Margin** The loading diagrams were made, based on the assumption that the fuel is added before the pilot enters the aircraft, to determine the c.g. excursion. With this c.g. excursion the x-plots, also known as scissor plots were made.

## 2.7 Flying and Handling Qualities

To quantify the behaviour and handling of an aircraft the flying and handling qualities rating scale was used. The five eigenmodes of the concepts have been evaluated with these flying quality levels based on their natural frequency and damping ratio. Finally, the Control Anticipation Parameter (CAP) was used as well. A low CAP means that the aircraft reacts really sluggishly and a too high CAP means that the aircraft is too responsive and abrupt.

**Manoeuvrability** The pitch and roll were obtained by using the equations of motion. Further more, the elevator control force and the stick force gradient, which effectively measures the change in elevator control force for a deviation from the trim condition into a pull up manoeuvre, were determined. The calculated values for the roll rate have been identified as unrealistic since when validated with the EXTRA 330SC, likely due to the simplifications made in the model.

**Responsiveness** For the responsiveness, the instantaneous accelerations and decelerations in pitch and roll were determined for each concept. Compared to the EXTRA 330SC, all but concept five score better in terms of responsiveness. The radius of the pitch motion was evaluated as well.

**Pull-up and Vertical Climb Performance** It was noted that almost all concepts perform better than the EXTRA 330SC: for the lightweight configurations this can be attributed to their lower inertia's, increasing the number of rolls that can be performed in the same altitude difference, whereas for the conventional configurations an increase in performance was made possible due to larger wings but reduced mass (concept 1), or the use of high-lift devices that lowered the stall speed (concept 2).

## 2.8 Initial Cost Analysis

There was also a cost analysis made, to check the economic feasibility of each concept. A market analysis was performed to check the break-even user requirement of 8 years. In this period, it is estimated that 50 single-seater versions will be sold and another 100 double-seaters. This double-seater will be an adaption of the single-seater design, as is often done by aerobatic aircraft manufacturers. The conventional concepts were estimated at a unit price of about \$315,000 and an operating cost per hour of \$370. The three lightweight concepts were estimated at a unit price of roughly \$270,000 and an operating cost per hour of \$290.

## 2.9 Initial Reliability, Availability, Maintainability, and Safety

In general aviation there is one accident due to mechanical failure on average every 116,279 flight hours. The majority of the accidents due to mechanical failure are caused by a failure of the power plant. The availability of the aircraft is dependent on maintenance and weather conditions. The ease of the maintenance will be taken into account in designing the detailed components. 75% of all accidents and fatalities in general aviation are caused by pilot error. Even though these statistics from General Aviation are not suitable for an accurate analysis for aerobatics, no better data for aerobatics was found. It is concluded that pilot error is the biggest safety hazard.

## 2.10 Trade-off

With all the different criteria analysed and scored, the trade-off was performed. The total score can be seen in Table 2.1.

	Pilot rating (feel of the aircraft)	Reponsiveness (Accelerations)	Manoeuvrability (Angular velocities)	Energy loss (Vertical climb)	RAMS + Risk	Cost	Total Score
Weight	20%	25%	20%	25%	5%	5%	100%
Concept 1	40.91%	68.00%	4.29%	62.50%	50.00%	44.22%	46%
Concept 2	39.39%	74.00%	0.00%	100.00%	48.33%	41.67%	56%
Concept 3	31.82%	72.00%	37.14%	62.50%	0.00%	100.00%	52%
Concept 4	36.36%	100.00%	50.00%	62.50%	0.00%	98.45%	63%
Concept 5	0.00%	45.00%	34.29%	37.50%	0.00%	98.45%	32%

Table 2.1: Trade-off summary table.

As can be seen in Table 2.1 concept 2 and 4 had the highest score. While analysing the risk and feasibility of each concept, it was determined that the lightweight concepts would not meet their required maximum weight in order to have a similar power to weight ratio as the EXTRA 330SC and the conventional concepts. The weight of these concepts should have been reduced by at least 150 kg in order to meet to sustained climb at 45° requirement. Thus were the three lightweight concepts discarded from the trade-off. That meant that concept 2 was the winner of the Trade-off. The *StefX* will become a conventional aircraft with flaperons and Leading Edge High Lift Devices (LE HLD's). The sensitivity of a change in trade-off criteria was determined to assess the robustness of the chosen design. A change in the criteria weights and a change in the requirements were also examined. At this stage, it was estimated that the *StefX* will be able to win the unlimited world championships aerobatics.

## 2.11 Preliminary Design Phase Result

The result of the trade-off and preliminary design phase was the conventional aircraft with leading edge high lift devices and flaperons and will be further developed in the detailed design phase . The 6 cylinder off-the-shelf piston engine AEIO-580 engine by Lycoming will be used for the aircraft. The parameters of the design that were established during the design analysis for the trade-off and will not change during the detailed design phase are presented in Table 2.2.

Parameter	Wing	Horizontal Tail	Vertical Tail
$S$ [m <sup>2</sup> ]	11.74	-	-
$b$ [m]	8.04	-	-
$\lambda$ [-]	0.45	0.529	0.33
$\Lambda_{0.25c}$ [rad]	0.0	0.0	0.0
$AR$ [-]	5.5	2.86	0.99
$c_r$ [m]	2.015	-	-
$c_t$ [m]	0.906	-	-
$t/c$ [-]	0.15	-	-
$C_{l_{max}}$ [-]	1.83	-	-
$C_{l_\alpha}$ [rad]	6.52	5.86	6.37

Table 2.2: Design parameters which will not change during the detailed design phase.

# Chapter 3

## Sizing

This chapter discusses the sizing of the lifting surfaces, propeller and landing gear. Section 3.1 discusses how the flying and handling qualities were measured as well as how the eigenmotions were analysed. The outcome of these analyses was list of acceptable values for the XLEMAC, tail areas and tail surfaces. Section 3.2, discusses the simulation that was build to measure and size for manoeuvrability. In addition, it explains how the results from Section 3.1 are used to size the control surfaces. The result from this section are the control surfaces sizes, tail arms and tail areas as well as XLEMAC. In Section 3.3 the propeller is designed and analysed. The results of this will be used for the gyroscopic effects discussed in Section 9.8 and the aerodynamics in Chapter 4. Finally, Section 3.4 discusses the landing gear sizing.

This chapter only focuses on the sizing, the actual performance of the *StefX* is discussed in Chapter 9. Various sections of this chapter use the aircraft weight as well as the mass moments of inertia. These input values can be found in Section 6.5.

### 3.1 Flying and Handling Qualities

One of the costumer requirements is that the aircraft should have very well harmonised and precise control characteristics. This costumer requirement is partly covered in the system requirements STX-SYS-44 until STX-SYS-50. These requirements are about the level of flying and handling qualities concerning the eigenmotions and the control anticipation parameter (CAP). The flying and handling quality levels are based on the Cooper–Harper handling qualities rating scale. The pilot rating can be translated into levels of flying qualities. The conversion can be seen in Figure 3.1. The Cooper–Harper handling qualities rating scale has been developed in order to have a concise rating for the interpretation of pilot opinion. The rating scale links the aircraft characteristics with the workload on the pilot. The maximum rating is level 1, the minimum is level 10. A pilot rating of 1 means a very low workload on the pilot and excellent aircraft characteristics. For a level 10 pilot rating, there are major deficiencies and loss of control is likely. Most of the eigenmotions have to be of level 1 quality according to the requirements. This section discusses the exact requirements on the eigenmotions and CAP extracted from the system requirements in Subsection 3.1.3. Moreover, this subsection discusses how the eigenmotions are analysed. Subsection 3.1.2 discusses the stability derivatives needed for the eigenmotion analysis.

Level of flying qualities	Level 1			Level 2			Level 3			Below Level 3		
Cooper–Harper rating scale	1	2	3	4	5	6	7	8	9	10		

Figure 3.1: Equivalence of Cooper–Harper rating scale with levels of flying qualities [13].

#### 3.1.1 Design iteration

To ensure the *StefX* would meet requirements STX-SYS-44 till STX-SYS-50, the XLEMAC,  $S_{HT}$ ,  $S_{VT}$  and the distance between the horizontal tail and the nose (while the distance between the two stabilizers were kept constant) were iterated. For this iteration a python script was made, that used checked for all different combinations of values if the aircraft would be meeting the requirements. The values that were selected, to meet all the requirements, are presented in Table 3.1

#### 3.1.2 Stability

For the analyses of the eigenmotion, the stability derivatives had to be determined. The stability derivatives are divided in longitudinal and lateral stability derivatives. The longitudinal stability derivatives were determined for the equations of motions as defined in Table 3.2 [44, p.100].

The stability derivatives present in the asymmetric equations of motions are calculated as presented in Table 3.3 [44]. The calculation of these derivatives were split up in the contribution of the vertical tail and the

Variable	Value
XLEMAC [m]	1.1
$S_{HT}$ [m <sup>2</sup> ]	1.8
$S_{VT}$ [m <sup>2</sup> ]	1.55
$X_h$ [m]	4.8

Table 3.1: Final sizing values for the stability derivatives.

Coefficient	Formula [44]	Value
$C_{X_0}$	$\frac{W}{\frac{1}{2}\rho V^2 S} \sin \gamma_0$	0.0026
$C_{X_u}$	$-2C_L \tan \gamma_0$	-0.005
$C_{X_\alpha}$	$C_L * \left(1 - \frac{2C_{L\alpha}}{\pi A e}\right)$	0.035
$C_{Z_0}$	$\frac{-W}{\frac{1}{2}\rho V^2 S} \cos \gamma_0$	-0.110
$C_{Z_u}$	$-2C_L$	-0.22
$C_{Z_\alpha}$	$-C_{L\alpha}$	-4.6532
$C_{Z_{\dot{\alpha}}}$	$-(C_{N_\alpha})_h \left(\frac{V_h}{V}\right)^2 \frac{\delta \epsilon}{\delta \alpha} \frac{S_{HT}}{S} \frac{l_{HT}}{\bar{c}}$	-0.751
$C_{Z_q}$	$-2 \left(\frac{V_h}{V}\right)^2 \frac{S_{HT}}{S} \frac{l_{HT}}{\bar{c}}$	-0.575
$C_{m_u}$	0	0
$C_{m_\alpha}$	$(C_{N_\alpha}) \frac{X_{cg} - X_w}{\bar{c}} - (C_{N_{alpha}}) \left(1 - \frac{\delta \epsilon}{\delta \alpha}\right) \left(\frac{V_h}{V}\right)^2 \frac{S_{HT} l_{HT}}{S \bar{c}}$	0.32
$C_{m_{\dot{\alpha}}}$	$-(C_{N_\alpha})_h \left(\frac{V_h}{V}\right)^2 \frac{S_{HT} l_{HT}^2}{S \bar{c}^2} \frac{\delta \epsilon}{\delta \alpha}$	-1.65
$C_{m_q}$	$-1.1 (C_{N_\alpha})_h \left(\frac{V_h}{V}\right)^2 \frac{S_{HT} l_{HT}^2}{S \bar{c}^2}$	-2.25

Table 3.2: Longitudinal stability derivatives formulas.

contribution of the wings. As there was no possibility to calculate the fuselage contribution to the derivatives without an experiment or the use of CFD, and for the comparison between models only a certain level of accuracy is required, the fuselage contribution was neglected.

### 3.1.3 Eigenmotions

In this section the different requirements for the eigenmotions are elaborated upon. Furthermore, the method for the analyses of the eigenmotions is discussed. The characteristic equations of the eigenmotions are obtained from the symmetric and asymmetric EOM [44].

**Short-Period Motion** The equation of motion for the Short-Period Motion can be simplified, by assuming that the velocity is constant, as well as an initial pitch angle of zero.

For the short-period motion to be of level 1 quality, it is given that  $\zeta$  should be between 0.35 and 1.40 [13]. The design will become unacceptable if  $\zeta$  is smaller than 0.25.

The damping ratio of the *StefX* is determined on 0.96.

**Phugoid** For the Phugoid, the damping ratio  $\zeta$  shall be at least 0.04 to meet level 1 requirements. For the Phugoid a quadratic equation can be found as well, by assuming that the change in pitch angle and angle of

Coefficient	Wing	Vertical tail	Total value
$C_{Y\beta}$	-	$(C_{Y\beta})_v = C_{Y_{va}} \left(1 - \frac{d\sigma}{d\beta}\right) \left(\frac{V_v}{V}\right)^2 \frac{S_{VT}}{S}$ [44]	-0.21
$C_{\ell\beta}$	$(C_{\ell\beta})_w = C_L \cdot (C_{\ell\beta c_L})_A$ [35]	$(C_{\ell\beta})_v = (C_{Y\beta})_v \left(\frac{z_{VT} - z_{c.g.}}{b} \cos \alpha_0 - \frac{x_{VT} - x_{c.g.}}{b} \sin \alpha_0\right)$ [44]	-0.007
$C_{n\beta}$	$(C_{n\beta})_w = C_L^2 \frac{1}{4\pi A}$ [41]	$(C_{n\beta})_v = -(C_{Y\beta})_v \left(\frac{l_{VT}}{b}\right)$ [44]	0.11
$C_{\ell p}$	$(C_{\ell p})_w = \frac{(C_{L\alpha} + C_{D0})c_r b}{24S} (1 + 3\lambda)$	-	-0.48
$C_{n_p}$	$(C_{n_p})_w = \frac{(\Delta C_{np})_1}{C_L} C_L + \frac{(\Delta C_{np})_2}{(C_{D0})_\alpha} (C_{D0})_\alpha$ [9]	$(C_{n_p})_v = -2 \frac{l_{VT}}{b} \frac{z}{b} (C_{Y\beta})_v$ [9]	-0.22
$C_{Y_r}$	-	$(C_{Y_r})_v = 2 C_{Y_{va}} \left(\frac{V_v}{V}\right)^2 \frac{S_{VT} l_{VT}}{S b}$ [44]	0.248
$C_{\ell_r}$	$(C_{\ell_r})_w = C_L \left(\frac{\bar{y}_{l_r}}{b/2}\right)^2$ [41]	$(C_{\ell_r})_v = (C_{Y_r})_v \left(\frac{z_{VT} - z_{c.g.}}{b} \cos \alpha_0 - \frac{x_{VT} - x_{c.g.}}{b} \sin \alpha_0\right)$ [44]	0.039
$C_{n_r}$	$(C_{n_r})_w = -\frac{C_L^2}{\pi A} \left(\frac{\bar{y}_{N_r}}{b/2}\right)^2$ [41]	$(C_{n_r})_v = (C_{Y_r})_v \left(\frac{l_{VT}}{b}\right)$ [44]	-0.13

Table 3.3: Lateral stability derivatives formulas.

attack is so slow that  $\dot{\alpha}$  and  $\dot{q}$  are zero. The characteristic equation for the phugoid is presented in Equation (3.1).

$$A\lambda_c^2 + B\lambda_c + C = 0 \quad (3.1)$$

Where:

$$\begin{aligned} A &= 2\mu_c (C_{Z_\alpha} C_{m_q} - 2\mu_c C_{m_\alpha}) \\ B &= 2\mu_c (C_{X_u} C_{m_\alpha} - C_{m_u} C_{X_\alpha}) + C_{m_q} (C_{Z_u} C_{X_\alpha} - C_{X_u} C_{Z_\alpha}) \\ C &= C_{Z_0} (C_{m_u} C_{Z_\alpha} - C_{Z_u} C_{m_\alpha}) \end{aligned}$$

The damping ratio for the phugoid of the *StefX* is calculated to be 0.0035, which also means that the phugoid is a stable eigenmotion.

**Aperiodic Roll** According to [13], a time constant of less than 1.0 s is rated level 1. For the Aperiodic Roll it assumed that, as this eigenmotion is short, only roll motion needs to be taken into account. Because of this, the equations for the lateral force and the yawing moment can be omitted, as well as the side-slip and yaw-rate terms, which leads to Equation (3.2).

$$(C_{\ell_p} - 4\mu_b K_X^2 \lambda_b) \frac{pb}{2V} = 0 \quad (3.2)$$

The time constant of the aperiodic roll will be 0.067 s.

**Dutch Roll** For the Dutch roll flying qualities not only the damping ratio  $\zeta_d$  and natural frequency  $\omega_d$  are important, but also the product of the two. For a level 1 rating  $\zeta_d$  should at least be 0.19,  $\omega_d$  at least 1.0 and the product of the two 0.35. For the Dutch Roll, the roll is neglected, this will omit the roll angle and roll rate terms. When calculating the eigenvalues this will lead to Equation (3.3).

$$A\lambda_b^2 + B\lambda_b + C = 0 \quad (3.3)$$

Where:

$$\begin{aligned} A &= -2\mu_b K_Z^2 \\ B &= \frac{1}{2} C_{n_r} \\ C &= -C_{n\beta} \end{aligned}$$

The damping constant of the dutch roll was calculated to be 0.06, which also means that the dutch roll is a stable eigenmotion.

**Spiral Motion** As the spiral motion is slow, it is acceptable to be an unstable motion, as the pilot has quite some time to intervene, however it is important that the amplitude of the motion does not increase too fast. For this reason, the doubling time ( $T_2$ ) should at least be 12 s for a level 1 rating. As the Spiral motion is in general a motion that is slow, all the accelerations can be neglected. The eigenvalue can be calculated by Equation (3.4).

$$\lambda_b = \frac{2C_L(C_{\ell_\beta}C_{n_r} - C_{n_\beta}C_{\ell_r})}{C_{\ell_p}(C_{Y_\beta}C_{n_r} + 4\mu_b C_{n_\beta}) - C_{n_p}(C_{Y_\beta}C_{\ell_r} + 4\mu_b C_{\ell_\beta})} \quad (3.4)$$

The doubling time is determined to be 137 s for the *StefX*.

**Control Anticipation Parameter** The damping and frequency of the short period are of great importance. However, Birlle [8] states that

"For aircraft having high inertia or low static stability, the angular pitching acceleration accompanying small adjustments to flight path may fall below the threshold of perception"

This means that the anticipatory nature of the response may become insignificant, causing bad handling qualities [13]. To deal with this, Birlle came up with the CAP. The definition of CAP is "The amount of instantaneous angular pitching acceleration per unit of steady-state normal acceleration [8]". The CAP gives an indication of the strength of the anticipation signal received by the pilot. It can also be seen as the answer to the question "Does the nose follow the stick?". A low CAP value means a sluggish response; the aircraft is not closely coupled and the aircraft overshoots. If the CAP value is too high, pilots will say that the response is abrupt and too sensitive. The way the CAP is calculated is shown in Equation (3.5) [43].

$$CAP = \frac{\omega_{n_{sp}}^2}{n_\alpha} \quad n_\alpha = \frac{C_{L_\alpha} \bar{q} S}{W} \quad (3.5)$$

The CAP values for a level 1, category A aircraft, have to be between 0.28  $1/s^2$  and 3.6  $1/s^2$ . The CAP of the *StefX* is 3.53  $1/s^2$  which is on the high side of level 1, which is actually desirable for aerobatic aircraft, as this means the *StefX* will be responsive.

To validate the calculations of the flying qualities, the stability derivatives as well as the flying qualities of the EXTRA 330SC were calculated. For the mass moment of inertia, the same calculations as explained in Section 6.5 were used. As the EXTRA 330SC was found to have level 1 flying qualities for all eigenmotions, except the dutch roll, which is still stable. This were the expected results, and therefor the calculations are deemed validated.

## 3.2 Control Surface Sizing

In order to optimise the size of the control surfaces for the desired performance, a dynamic flight model of the aircraft was made. This model is explained in Subsection 3.2.1. The simulation was used to analyse the performance of the aircraft as well to optimise for it. The way the simulation is used for the performance optimisation is discussed in Subsection 3.2.2.

### 3.2.1 Simulation

In order to optimise the size of the control surfaces for the desired performance, a dynamic flight model of the aircraft was made. A widely used flight dynamic model is a linearised model. But this model, which uses stability derivatives, is only valid for small variations of the angles of attack and sideslip and is therefore not able to simulate the full flight envelope of an aerobatic aircraft. The approach used to set up the flight dynamics of the aircraft is based on aerodynamic models for the separate aircraft components. These have been divided into the wing, horizontal tail and vertical tail. Each component is modelled to determine its contribution to the total forces and moments. The program simulates the aircraft response to various control surface inputs. Although the full 6-DOF equations were set up, the simulation was split-up in 3 sub-simulations simulating the aircraft in a 3-DOF frame. Every sub-simulation looks at one rotation about an axis and the forces in the other axes. The two remaining angular velocities and the remaining force were assumed to be zero. In this way, the p,q and r-motion can be analysed independently.

### Nonlinear Equations of Motion

The nonlinear equations were set up in the body frame. This reference frame is a right handed frame with its centre at the aircraft c.g. with the positive  $x$ -axis through the nose and the positive  $y$ -axis through the right wing. The aerodynamic forces are acting in the aerodynamic reference frame. This frame has its origin in the aircraft c.g. with the positive  $x$ -axis in the direction of the aerodynamic velocity. In order to come up with the equations of motion, a free body diagram was made as shown in Figures 3.4, 3.4 and 3.2. These free body diagrams show the assumed direction of the lift and drag coefficients in the aerodynamic frame. The aerodynamic forces had to be transformed to the body frame. This was done by transforming the lift and drag coefficients to the body frame. The transformation has been done by use of the transformation matrix shown in Equation (3.6) and the free body diagrams. The equations for the normal force, tangential force and side force coefficient for the wing, horizontal and vertical tail in the body frame are given in Equations (3.7) - (3.15). For these equations it has been assumed that there is no tangential or normal force of the drag and lift due to side slip on the wing and horizontal tail. Similarly, the angle of attack has no influence on the forces on the vertical tail.

$$\mathbb{T}_{Ab} = \begin{bmatrix} \cos \alpha \cos \beta & -\sin \beta & -\sin \alpha \cos \beta \\ \cos \alpha \sin \beta & -\cos \beta & -\sin \alpha \sin \beta \\ \sin \alpha & 0 & \cos \alpha \end{bmatrix} \quad (3.6)$$

$$C_{X_w} = -C_D \cos(\alpha_{c.g.} + \Delta\alpha_l) + C_L \sin(\alpha_{c.g.} + \Delta\alpha_l) \quad (3.7)$$

$$C_{Z_w} = -C_L \cos(\alpha_{c.g.} + \Delta\alpha_l) - C_D \sin(\alpha_{c.g.} + \Delta\alpha_l) \quad (3.8)$$

$$C_{Y_w} = 0 \quad (3.9)$$

$$C_{X_{HT}} = -C_{D_{HT}} \cos(\alpha_{c.g.} + \Delta\alpha_l) + C_{L_{HT}} \sin(\alpha_{c.g.} + \Delta\alpha_l) \quad (3.10)$$

$$C_{Z_{HT}} = -C_{L_{HT}} \cos(\alpha_{c.g.} + \Delta\alpha_l) - C_{D_{HT}} \sin(\alpha_{c.g.} + \Delta\alpha_l) \quad (3.11)$$

$$C_{Y_{HT}} = 0 \quad (3.12)$$

$$C_{X_{VT}} = -C_{D_{VT}} \cos(\beta_{c.g.} + \Delta\beta_l) - C_{L_{VT}} \sin(\beta_{c.g.} + \Delta\beta_l) \quad (3.13)$$

$$C_{Z_{VT}} = 0 \quad (3.14)$$

$$C_{Y_{VT}} = -C_{D_{VT}} \sin(\beta_{c.g.} + \Delta\beta_l) + C_{L_{VT}} \cos(\beta_{c.g.} + \Delta\beta_l) \quad (3.15)$$

To effectively compute the contribution of each lifting surface to the EOM, strip theory is applied similarly as in [38]. The wing and horizontal and vertical tail were discretised in  $n$  strips of equal width over the span resulting in areas  $\Delta S$  such that  $\sum_i^n \Delta S_i = S$ . For each strip, the local angle of attack, sideslip and velocity had to be determined as visualised in Figure 3.5. The tangential and normal coefficients were determined for each strip of the components. The coefficients were translated into forces by multiplying by  $1/2\rho V^2 S$ , where  $V$  differs per strip. The tangential and normal force were used for setting up the equations of motion. The sum of the forces in  $x_b$ ,  $y_b$  and  $z_b$  are given in Equations (3.16), (3.17) and (3.18). The sum of the moments are given in Equations (3.19), (3.20) and (3.21).

$$\sum F_{x_b} = T_{prop} + \sum F_{x_w} + \sum F_{x_{HT}} + \sum F_{x_{VT}} + F_{x_{gear,fus}} - W \sin \theta \quad (3.16)$$

$$\sum F_{y_b} = \sum F_{y_w} + \sum F_{y_{HT}} + \sum F_{y_{VT}} + W \sin \phi \cos \theta \quad (3.17)$$

$$\sum F_{z_b} = \sum F_{z_w} + \sum F_{z_{HT}} + W \cos \theta \cos \phi \quad (3.18)$$

$$\sum M_{x_b} = \sum F_{z_{w_i}} \cdot y_i + \sum F_{z_{HT_i}} \cdot y_i + F_{y_{VT}} \cdot (z_{VT} - z_{c.g.}) \quad (3.19)$$

$$\sum M_{y_b} = \sum F_{z_{w_i}} \cdot (x_{c.p.} - x_{c.g.}) + \sum F_{z_{HT_i}} \cdot (x_{HT} - x_{c.g.}) \quad (3.20)$$

$$\sum M_{z_b} = -\sum F_{x_{w_i}} \cdot y_i - \sum F_{x_{HT_i}} \cdot y_i + F_{y_{VT}} \cdot (x_{VT} - x_{c.g.}) \quad (3.21)$$

### Updating Velocities and Attitude

At the beginning of each run, the velocities, accelerations and aircraft attitude have to be specified. For the first run, these parameters are such that the aircraft is trimmed. For every following run, these parameters

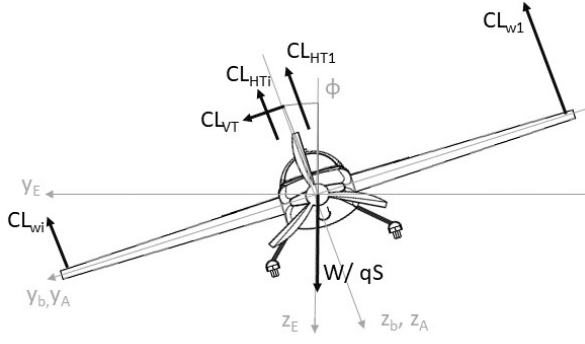


Figure 3.2: Free body diagram in the yz plane.

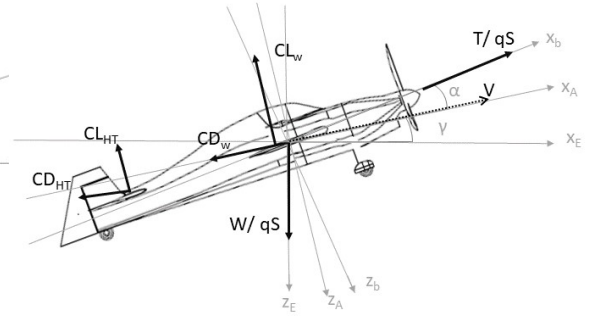


Figure 3.3: Free body diagram in the xz plane.

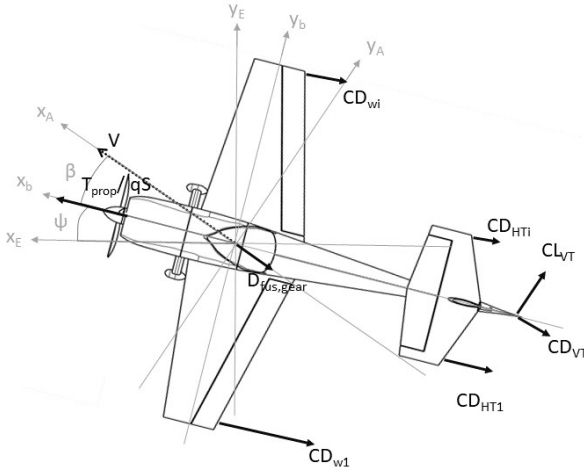


Figure 3.4: Free body diagram in the xy plane.

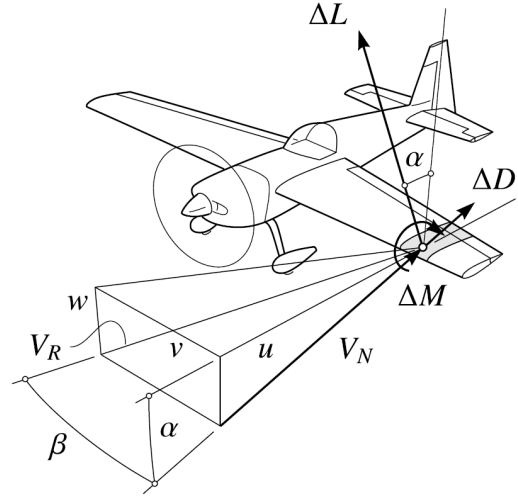


Figure 3.5: Local flow for a strip wing [38].

had to be updated. The parameters for run  $i$  were determined at the end of the previous run. At the end of each run the axial and angular accelerations were calculated as described by Equations (3.22) - (3.25) [6] [23]. The start velocities for the current run are calculated such that  $u_i = u_{i-1} + \dot{u}_{i-1} \cdot dt$ .

$$\dot{u} = \frac{F_x}{m} - qw + rv \quad \dot{v} = \frac{F_y}{m} - ru + pw \quad \dot{w} = \frac{F_z}{m} - pv + qu \quad (3.22)$$

$$\dot{p} = \frac{I_{zz}}{I^*} M_x + \frac{I_{xz}}{I^*} M_z + \frac{(I_{xx} - I_{yy} + I_{zz}) I_{xz}}{I^*} pq + \frac{(I_{yy} - I_{zz}) I_{zz} - I_{xz}^2}{I^*} qr \quad (3.23)$$

$$\dot{q} = \frac{M_y}{I_{yy}} + \frac{I_{xz}}{I_{yy}} (r^2 - p^2) + \frac{I_{zz} - I_{xx}}{I_{yy}} pr \quad (3.24)$$

$$\dot{r} = \frac{I_{xz}}{I^*} M_x + \frac{I_{xx}}{I^*} M_z + \frac{(I_{xx} - I_{yy}) I_{xx} + I_{xz}^2}{I^*} pq + \frac{(-I_{xx} + I_{yy} - I_{zz}) I_{xz}}{I^*} pr \quad (3.25)$$

The changes in Euler angles can be calculated by Equations (3.26) - (3.28) [6]. The current attitude was calculated in a similar manner as the velocity was calculated.

$$\dot{\phi} = p + \sin \phi \tan \phi q + \cos \phi \tan \theta r \quad (3.26)$$

$$\dot{\theta} = \cos \phi q - \sin \phi r \quad (3.27)$$

$$\dot{\psi} = \frac{\sin \phi}{\cos \theta} q + \frac{\cos \phi}{\cos \theta} r \quad (3.28)$$

In addition to the accelerations, velocities and attitude, the aerodynamic angles  $\alpha$  and  $\beta$  have to be updated. These angles describe the orientation of the nose with respect to the velocity as can clearly be seen in Figure 3.5. The angle of attack and sideslip angle can be calculated by Equation (3.29) [6].

$$\alpha = \arctan\left(\frac{w}{u}\right) \qquad \beta = \arctan\left(\frac{v}{u}\right) \qquad (3.29)$$

### Aerodynamic Models

As mentioned before, each strip sees a different angle of attack, sideslip angle and velocity. This means that these parameters have to be determined for each strip. These local angles and velocities depend on the movement of the aircraft c.g. as well as geometry, aerodynamic angles and angular rotations. In addition, the lift and drag polars have to be known for the wing, horizontal and vertical tail for different control surface deflections.

**Local Angle of Attack** The angle of attack of the wing and horizontal tail strips differ with roll and pitch rate. Furthermore, the angle of attack on these strips is dependent on tip vortexes. The vertical tail also experiences a downwash. The sum of these local changes in angle of attack is the  $\Delta\alpha_l$  used in Equations (3.7) - (3.15). The angle of attack has to be corrected if the aircraft is rolling. A roll motion causes a decrease in local angle of attack for the up-going-wing and an increase in the local angle of attack for the down-going-wing. This effect is described by Equation (3.30) [44]. The further the strip away in  $y$  direction from the c.g, the higher the change in angle of attack due to a rolling motion.

$$\Delta\alpha_{roll} = \frac{p \cdot y_i}{V} \qquad (3.30)$$

If the aircraft is pitching, the horizontal tail wing experience a different angle of attack of attack than the wing. The further away the horizontal tail from the c.g., the higher the change in angle of attack. The change in angle of attack due to a pitching motion is shown in Equation (3.31) [44].

$$\Delta\alpha_{pitch} = \frac{q \cdot x_i}{V} \qquad (3.31)$$

Moreover, the wing introduces a positive vertical component to the airflow, also known as down-wash which results in a lower local angle of attack experienced by the horizontal stabiliser. This down-wash angle is computed by Equation (3.32).

$$\epsilon = \frac{2C_l}{\pi A e} \qquad (3.32)$$

Since the  $C_l$  can vary between different stations of the wing, a relation for the down-wash angle based on the distance to the x-axis is set-up in order to accurately introduce the down-wash for the stations of the horizontal stabiliser. The total change in angle of attack locally experienced is given by Equation (3.33).

$$\Delta\alpha_l = \Delta\alpha_{roll} + \Delta\alpha_{pitch} - \epsilon \qquad (3.33)$$

**Local Sideslip Angle** The difference in sideslip angle seen by the vertical tail with respect to the c.g. comes from a yaw rate and a sidewash angle. The higher the yaw rate, the larger the local sideslip angle at the strip. In addition, the local sideslip angle due to a r-motion differs with the distance in  $x$ . The local change in sidewash angle due to a yawing motion is given by Equation (3.34) [44].

$$\Delta\beta_{yaw} = \frac{r \cdot x_i}{V} \qquad (3.34)$$

**Advanced roll evaluation** Since the roll rate was set as a user requirement, a more extensive analysis was performed in order to make the simulation more accurate. The horizontal tail was discretized for the roll simulation in a similar way to the main wing and the NACA009 airfoil data was used. In this way, the 3D effects and the downwash were determined in a more accurate way. In order to account for the 3D tip vortexes that occur, the local angle of attack is reduced by the tip vortex induced angle of attack. This is a function of the aspect ratio and is given by Equation 3.35.

$$\Delta\alpha_{tip-vortex} = \frac{C_l}{\pi A e} \qquad (3.35)$$

**Lift and Drag Polar** XFOIL has simulated the aerodynamics for the three different airfoils for an angle of attack of  $0^\circ$  to  $25^\circ$  with a control surface chord from  $0.01c$  to  $0.5c$  and a control surface deflection from  $0^\circ$  to  $\pm 30^\circ$ . The data on the resulting aerodynamic coefficients  $C_l$ ,  $C_d$  and  $C_p$  are imported as look-up tables into the flight dynamics model. By use of interpolation, it was possible to find every possible combination of angle of attack, control surface length and control surface deflection. With the local angle of attack computed, the resulting forces on each section were calculated by use of Equations (3.7) - (3.15).

**Trim Condition** In order to be able to properly simulate the behaviour of the aircraft to a control surface input, the simulation should start from a steady state trim condition. The analysis on the performance of the aircraft due to a control input is based on the change to the equilibrium position of the aircraft. If the aircraft is not trimmed, the results of a control input can not be accurately analysed since the aircraft was already accelerating in one or more of the six degrees of freedom before the control input. For a steady state, the resulting forces and moments about the aircraft c.g. are zero such that the aircraft is not accelerating. To satisfy this criteria in the longitudinal direction of the aircraft, the thrust should be set equal to the total drag including the component of the weight along the  $x_b$ -axis. For the lateral direction, the sideslip angle and rudder deflection should be set to zero. To balance the forces along the  $z_b$ -axis, the lift generated by the wing and horizontal tail should be equal to the component of the weight of the aircraft. The sum of moments about the  $x$ -axis is zero when the ailerons have zero deflection. For the moments about the  $z$ -axis to be zero, there should be no sideslip or rudder deflection. Finally, the sum of moments about the  $y$ -axis must be zero by balancing the lift generated by the wing and the arm it makes to the c.g. and the lift generated by the horizontal tail and its responding arm to the c.g.

Since the lift generated by the wing and the horizontal tail depend on the variables airspeed, the angle of attack and the control surface deflection, these two degrees of freedom are coupled. To be able to both satisfy the moment equilibrium around the  $y$ -axis and the force equilibrium in the  $z$ -direction, an optimisation procedure was built into the simulation which was used to minimise  $F_z$  and  $M_y$  for a given airspeed by changing both the angle of attack  $\alpha$  and the elevator deflection  $\delta_e$ . This ensures that the aircraft is not accelerating in the  $z$ -direction nor around the  $y$ -axis.

The trim procedure sets the control surface deflections as described above and determines the angle of attack at which the aircraft must be flying. Finally, the flight path angle  $\gamma$ , which is defined as  $\theta - \alpha$ , is set to zero since the aircraft is flying straight and level in the trim condition. This trim procedure was called every time the simulation started with a different airspeed as input.

The behaviour of the aircraft when starting from a non steady state condition was analysed. It was found that the aircraft would stabilise after a dozen seconds, depending on the power level and initial airspeed, to a steady climb or descent. It was determined that the aircraft is stable in pitch, yaw and roll.

**Verification and Validation of the Simulation** The simulation has been verified in different ways. First of all, the eigenmotions of the *StefX* have been simulated. The response of the aircraft has been compared to the period and doubling time calculated in Subsection 3.1.2. The differences between the results were acceptable, taking into account the assumptions made for the two methods. Furthermore, the maximum achievable angular rates and accelerations were analytically verified. This was done by use of a similar method as done in the midterm report [3]. The trimming of the aircraft in the simulation has been verified manually. To check if the aircraft was indeed trimmed, the pitch rate,  $\theta$  and  $\alpha$  were graphically presented. It was verified that the pitch rate,  $\dot{\theta}$  and  $\dot{\alpha}$  were zero and that  $\theta = \alpha$ , which is the definition of the trim condition. The discretization has been verified by comparing the sum of the areas of each element to the total wing area for an increasing number of stations, which was accurate up to three decimals. The lift generated by the discretized surface has been verified by simulation this wing in a steady condition and comparing the determined lift to a simple lift calculation for the wing as a whole. The difference found was smaller than 1%. Finally, the effect of discretizing the horizontal tail was evaluated in the accurate roll simulation. It was found that this had very little influence on the result since the elevator deflects in the same direction over the entire span, in contrast to the aileron which deflects in the opposite direction left and right of the fuselage. It was therefore concluded that the simplification to not discretize the horizontal tail for evaluating pitch and yaw was valid.

### 3.2.2 Control Surface Optimisation

The stability analysis as described in Section 3.1 has determined the allowable design space for the tail size and the horizontal and vertical tail arms to have the eigenmotions and the Control Anticipation Parameter in level 1 flying qualities. The exact values of these parameters were determined by simulating the performance

of the aircraft over the full range of the allowable design space. This was done in combination with different control surface sizes to accurately measure the behaviour of the aircraft to a control surface input. The simulation was run with different input values for the control surfaces and tail size to find the combination that met the requirements on performance which were setup in the beginning of the project.

The ailerons will have a constant chord length over the entire span of the wing. This results in an increasing aileron chord over local wing chord when moving from the root chord towards to tip chord. This increasing percentage of local chord allows for more effective aileron authority. The larger the moment arm of the ailerons becomes when moving towards the tip of the wings, the larger the change in lift. This creates a larger moment for the same aileron deflection which is beneficial for the roll acceleration and deceleration, allowing for the aircraft to be better manoeuvrable. However, this system does add additional complexity to the design of the wing box structure inside the wing compared to an aileron design which would have a constant percentage of chord over the local wing chord. The rudder and elevators will have a constant percentage of control surface chord over local lifting surface chord. This choice has been made to simplify the structure inside the empennage, which is in accordance with reference aircraft.

### 3.2.3 Results

By use of the flight simulation and the optimisation procedure described in Subsection 3.2.2, the area and location of the control surfaces have been determined. The parameters describing the location and geometry of the control surfaces are shown in Table 3.4. In addition, the technical drawings of the control surfaces are shown in Figure 3.6

Geometry parameter	Value
<b>Main wing</b>	
XLEMAC	1.10 m
Aileron span	3.66 m
Aileron chord	0.41 m
<b>Horizontal tail</b>	
Horizontal tail arm	5.00 m
Surface area	1.80 m <sup>2</sup>
Span	2.27 m
Elevator span	2.27 m
Elevator cord	0.5 c
<b>Vertical tail</b>	
Vertical tail arm	5.56 m
Surface area	1.55 m <sup>2</sup>
Span	1.24 m
Rudder span	1.24 m
Rudder cord	0.45 c

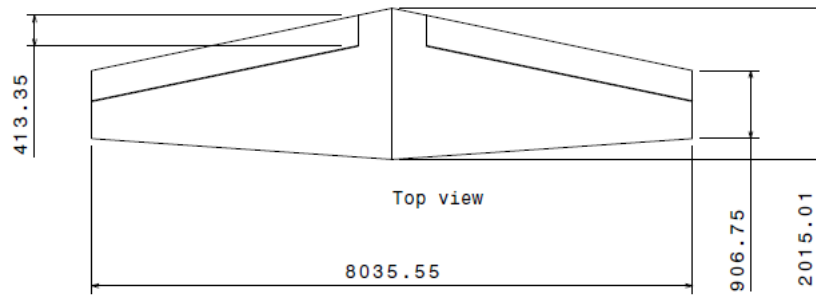
Table 3.4: Geometric values for control surfaces.

## 3.3 Propeller

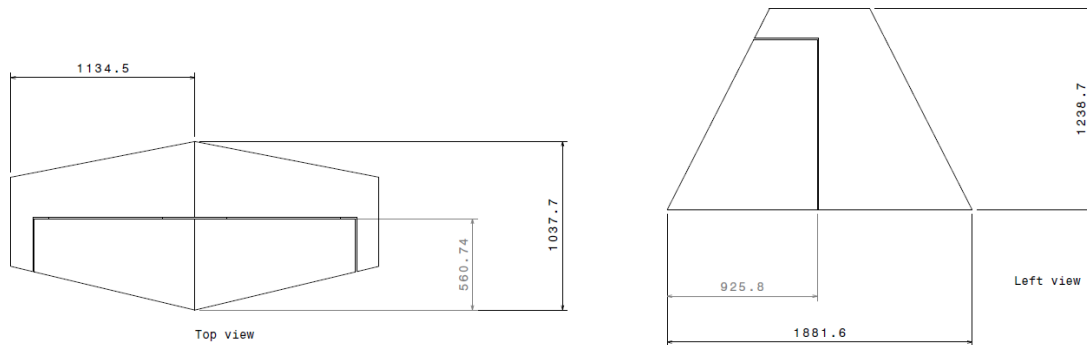
The propeller was designed in order to create sufficient thrust for a 45° sustained climb. In order to realise this, a propeller efficiency of 87% was needed. This is the requirement the propeller was sized for. The results of the propeller are explained in Section 9.7

**Blade Element Theory** The blade element theory (BET) depends on dividing the blade of the propeller up into sections in order to calculate the performance of the propeller. The BET will calculate the performance of the entire propeller by Equation (3.36) to describe the thrust, Equation (3.37) to determine the torque produced by the propeller, and Equation (3.38) to determine the power needed from the engine. In order to design the best performing propeller, a Python program is made optimising every part of the propeller.

$$T = N_B \int_{R_{Hub}}^R dT \quad (3.36)$$



(a) Technical drawing of the wing and aileron.



(b) Technical drawing of the horizontal tail and elevator.

(c) Technical drawing of the vertical tail and rudder.

Figure 3.6: Technical drawings of the control surfaces. The dimensions are in *mm*.

$$Q = N_B \int_{R_{Hub}}^R r \cdot dF_Q \quad (3.37)$$

$$P = N_B \int_{R_{Hub}}^R \Omega r \cdot dF_Q \quad (3.38)$$

The thrust and torque force produced by the propeller can be determined from Figure 3.7 where the lift and drag can be calculated by Equations (3.39) and (3.40).

$$dL = C_l \frac{1}{2} \rho V_E^2 c(r) \Delta r \quad (3.39)$$

$$dD = C_d \frac{1}{2} \rho V_E^2 c(r) \Delta r \quad (3.40)$$

In order for this to be possible,  $\alpha$  has to be calculated in order to determine the lift and drag coefficient. The angle of attack is determined by subtracting  $\phi$  and  $\alpha_i$  from  $\beta$ , and adding  $\alpha_{ZL}$ .

All the angles can be calculated from the turning speed of the propeller, and the forward velocity of the aircraft.  $\beta$  is the pitch of the propeller blade and will be an input to the program.  $\phi$  is the angle the total velocity makes with the rotational velocity. This can be calculated easily as both speeds are known.  $\alpha_i$  is a more difficult angle to determine. This angle describes the change in velocity from the induced velocity. This angle will be calculated by an iterative process using the Newton method. This uses the Rankine-Froude momentum theory to get an equation including the induced velocity and the thrust. This formula determined for a single element is shown in Equation (3.41)

$$dT = 4\rho\pi r dr (V_0 + w)w[22] \quad (3.41)$$

This is then converted with the BET formula for thrust in order to create a formula dependent on only  $w$ , the blade geometry, the aerodynamic coefficients, and the rotational and free stream velocity. This formula is then differentiated in order to start the iterative process according to the formula depicted in Equation (3.42).

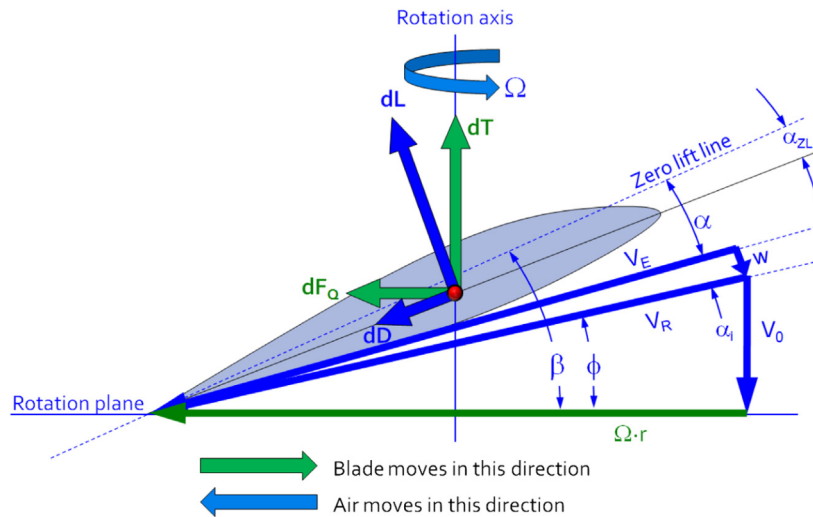


Figure 3.7: The airfoil geometry from the propeller.[22]

$$w_1 = w_0 - \frac{f(w)}{f'(w)} \quad (3.42)$$

This is then iterated until the values of  $w_1$  and  $w_0$  are less than 0.001 apart for every blade element. With  $w$  known,  $\alpha_i$  can be calculated from geometry as well as  $V_E$ . Now that the thrust, torque, and power needed can be calculated, optimal values for the blade geometry can be determined as well as a selection for the airfoil can be done. First, the efficiency of both airfoils at their optimal total twist, and their optimal pitch angle per velocity, can be plotted against the efficiency. The efficiency is calculated according to the formula shown in Equation (3.43). Here,  $J$  stands for the advancement ratio, and is determined by Equation (3.44).

$$\eta_p = J \frac{C_T}{C_P} \quad (3.43)$$

$$J = \frac{V_0}{n \cdot D} \quad (3.44)$$

For the efficiency, the power coefficient and the thrust coefficient have to be determined. This can be done by the following formulas depicted in Equations (3.45) and (3.46)

$$C_P = \frac{P}{\rho n^3 D^5} \quad (3.45)$$

$$C_T = \frac{T}{\rho n^2 D^4} \quad (3.46)$$

**Optimisation of the Efficiency** With the propeller efficiency as the foundation, the propeller was optimised. A higher speed is beneficial, together with a larger hub. In order to stay realistic, the hub diameter is set at 40 cm and the speed is set at the maximum manoeuvring speed of 83 m/s. The angular velocity was set at 2700 RPM in order to maximise the engine power output. These parameters were set in order to optimise the efficiency. From this, the optimal propeller twist can be calculated. This is for both airfoils a total twist of 33.6°. The pitch position where this maximum efficiency occurs does change with the airspeed. Therefore, for every speed, a range of pitches is run through at every analysis.

**Airfoil Selection** Two airfoils were selected. One is the Clark Y<sup>1</sup> airfoil and the ONERA HOR07<sup>2</sup>. These airfoils are selected because they were previously used on propellers. The propeller airfoils have a steep slope and a high minimum angle of attack. The Clark Y and the ONERA airfoils were chosen to investigate the difference in slope and maximum lift coefficient. Both airfoils have their maximum lift coefficient at roughly the same angle of attack. However, the ONERA airfoil has a maximum lift coefficient at 1.71 while the Clark airfoil

<sup>1</sup><http://airfoiltools.com/airfoil/details?airfoil=clarky-il>

<sup>2</sup><http://airfoiltools.com/airfoil/details?airfoil=hor07-il>

has its top at 1.52. Furthermore, the Clark airfoil has its minimum  $C_l$  at a lower angle of attack, giving an even shallower slope. Both airfoils were compared at their optimal twist and pitch at different speeds. The results are given in Figures 3.8a and 3.8b. As can be seen, the ONERA airfoil is better in both fields within the operating range of the aircraft. However, the values are not that much better for the airfoil. This means that searching for another airfoil with an even higher maximum  $C_l$ , or an even steeper slope will not be time efficient. Therefore, the ONERA HOR07 is selected for the propeller blades.

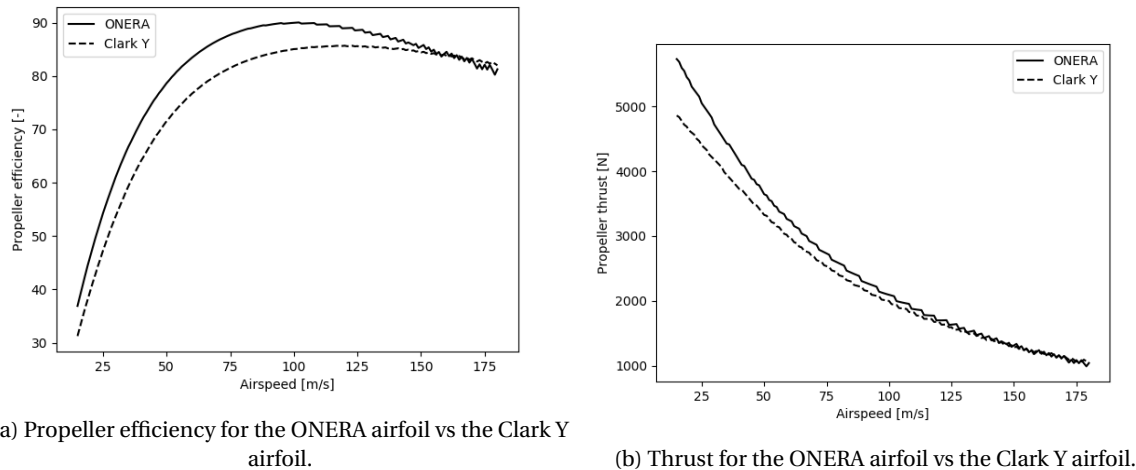


Figure 3.8: Comparison of both propeller airfoils.

**Blade Geometry** The chord of the airfoil was examined. The chord will start at the broadest width and linearly decrease. This is more efficient than using a curved decrease. Furthermore, a diameter of 1.90 m is selected from an empirical relation from Raymer as found in [22]. This compares the number of blades against the needed diameter. A four bladed propeller was chosen. In order to keep generating enough thrust, the chord of the propeller decreases from 14 cm to 10 cm. The BET is then run through different twists in order to determine the highest efficiency at each total twist from 15° to 45°. The optimal twist is achieved at 33.6°, following a linear twist.

### 3.4 Landing Gear

The landing gear sizing is important for the aircraft during taxiing, take-off and landing. The most important requirements for the landing gear is that it has to withstand the loads during operation, and that the aircraft will not tip over while standing on the ground.

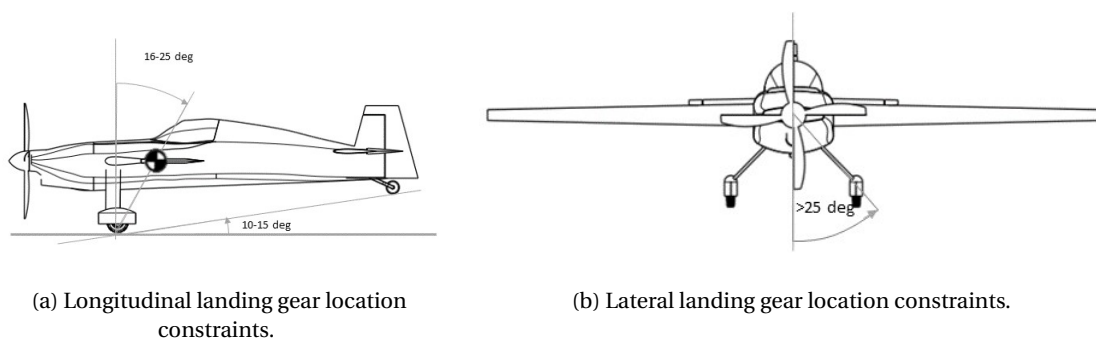


Figure 3.9: Constraints for the landing gear, to prevent tip over. [49]

The main landing gear should be placed in such a way that the angle of the line between the main landing gear and the most forward c.g. is at least 16° and between the main landing gear and the most aft c.g. is at

most  $25^\circ$ , as can be seen in Figure 3.9a. The tail down angle should be in between  $10^\circ$  and  $15^\circ$ . To certify the aircraft for CS 23, the minimum propeller clearance should be at least 23 cm.

The size of the landing gear will be minimised in the sizing of the aircraft, as a larger landing gear will increase the drag of the aircraft as well as the mass. First the vertical length of the main landing gear is set to the length of the propeller with the minimum propeller clearance added. The  $x$ -location of the main landing gear will be set to the firewall  $x$ -position, as the firewall will be the place where the loads of the landing gear are introduced to the fuselage.

As the firewall is located 1.1 m from the nose, the main landing gear will also be located at 1.1 m from the nose. For the height of the main landing gear, the length of the propeller blade was taken (95 cm) and the 23 cm from the ground clearance requirement of CS23 was added. With the  $x$  and  $z$ -position of the main landing gear determined and the c.g. location determined in Section 6.5, the current chosen landing gear position could be checked if it meets the tip over requirements. As all the possible c.g. locations during operations lay between  $16^\circ$  and  $25^\circ$ , the c.g. location of the main landing gear location does not need to be changed. The distance in  $y$ -direction from the centre of the aircraft will be 83 cm to ensure the aircraft will not tip over during turning while taxiing. For the sizing of the tail wheel a tail down angle of  $10^\circ$  was used. All the relevant dimensions of the landing gear can be found in Figure 3.10.

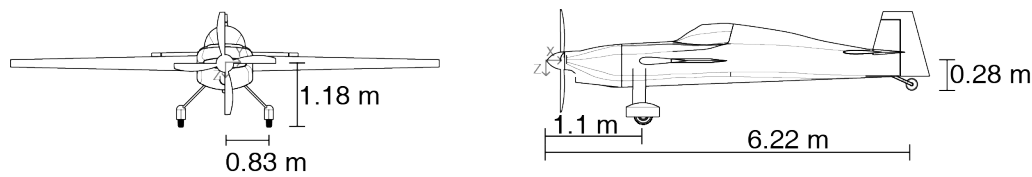


Figure 3.10: Landing gear dimensions.

In order to select the tires, the static load on each tire should be determined. The static load on the front tires will be 3.125 N each, and the static load on the tail tire will be 750 N. According to [42], to ensure the *StefX* will be able to land on grass landing strips the main landing gear tires will need to be 5.00-5 size tires. The tail landing gear tire will be a 5 inch solid rubber tail wheel. For the main landing gear tires the Goodyear Flight Special II 5.00-5 tires are selected, as they are rated for loads up to 5.600 N. This tire is also rated for ground operations of speeds up to 54 m/s [12].

# Chapter 4

## Aerodynamics

In this chapter, the aerodynamics of the *StefX* is further analysed. In Section 4.1, a more elaborated drag estimation is performed. In Section 4.2, the leading edge high lift device system is designed and in Section 4.4 the aerodynamic properties of the aircraft are determined using an aerodynamic model.

### 4.1 Drag Calculation

A python program is written to estimate the drag of the *StefX* aircraft. For this final design, a more elaborate and detailed method was used compared to the midterm, although both methods are very similar. The DATCOM method is now followed for a more accurate method that has also been extensively verified and validated by wind tunnel and flight test data of different aircraft [11]. An overview of the different calculation steps can be found in Table 4.1.

The DATCOM method uses graphs to obtain certain parameters. Based on a selection of data points, these graphs are interpolated to be used in python as long as the input data falls within the range of data points used. Equation (4.1) shows an example of an equation presented in DATCOM for the zero lift drag coefficient of a lifting surface. This equation is therefore used for the wing, horizontal and vertical tail. The  $(t/c)$  is the average ratio for the airfoil. This is calculated by taking the average value of the coordinates of the upper part of the airfoil and doubling it since the *StefX* has symmetrical airfoils. The factor  $L$  takes into account the location of the maximum thickness and  $R_{l.s.}$  the Mach number and sweep at location of the maximum thickness.

$$C_{D_{0,l.s.}} = C_f (1 + L(t/c) + 100(t/c)^4) R_{l.s.} \frac{S_{wet}}{S_{ref}} \quad (4.1)$$

Output	Input	Reference	Results			
			Wing	HT	VT	Fuselage
$Re$	$\rho, V, \bar{c}, \kappa$	[11, p. 4.1.5.1-27]	$9 \cdot 10^6$	$5 \cdot 10^6$	$8 \cdot 10^6$	$38 \cdot 10^6$
$C_f$	$Re$	[11, p. 4.1.5.1-26]	0.0030	0.0034	0.0031	0.0025
$R_{l.s.}$	$M, \Lambda_{(t/c)_{max}}$	[11, p. 4.1.5.1-28b]	1.07	1.07	1.07	N.A.
$C_{D_{0,l.s.}}$	$C_f, S_{ref}, S_{wet}, R_{l.s.}, (t/c), L$	[11, p. 4.1.5.1-a]	0.0076	0.0013	0.001	N.A.
$C_{D_{0,fus}}$	$l_{fus}, d_{eq}, S_{wet}, S_{Bf}$	[11, p. 4.2.3.1-a]	N.A.	N.A.	N.A.	0.0047
$C_{D_i}$	$C_L, A, e, \alpha$	[11, p. 4.1.5.2-c]	0.012	0.0063	0	N.A.
Entire Aircraft						
$C_{D_{tot}}$	$C_{D_0}, C_{D_i}, C_{D_{misc}}, R_{WB}, R_{TB}$	[11, p. 4.5.3.1-a]	0.0569			

Table 4.1: Drag Calculation using DATCOM, for a velocity of  $94 \text{ ms}^{-1}$  and angle of attack of  $5^\circ$ .

**Verification and Validation** The drag calculation is verified with the estimates obtained during the midterm using the General Aviation Aircraft Design book (GAAD) by Gudmundsson [22]. In Table 4.2, it can be seen that the estimations do differ. Investigating both methods in more detail, reveals that there is almost no difference in the calculated skin friction coefficients. The big difference was found in the form factor that takes into account the geometric shape of the lifting surfaces. Both methods use  $(t/c)$  as input for their form factor, see Equation (4.1). In Gudmundsson [22], it wasn't specified which value to take, so the maximum  $(t/c)$  was used. In DATCOM however, it was specified to use the average value, which is about half of the maximum. This explains the difference for the  $C_{D_0}$  of the lifting surfaces. Using the average  $(t/c)$  for Gudmundsson as well, made the difference less big and therefore the current drag calculations have been verified.

It must furthermore be noted that the DATCOM method is verified and validated on its own.

	Wing		HT		VT		Fuselage	
	DATCOM	GAAD	DATCOM	GAAD	DATCOM	GAAD	DATCOM	GAAD
$C_{D_0}$	0.00791	0.0107	0.00188	0.00206	0.000756	0.000988	0.00497	0.0052

Table 4.2: Verification DATCOM [11] zero lift drag coefficient with midterm values calculated using Gudmundsson [22].

## 4.2 Leading Edge High Lift Devices

The trade-off showed that LEHLDs were expected to improve the aircraft performance. In this final design phase, the type of LEHLD will be selected and designed.

### 4.2.1 Leading Edge Flap

Since a symmetrical LEHLD that can be deployed equally in both directions is required, a leading edge flap is the most straightforward solution. The drawback of this flap is the creation of the so called flap knuckle that is prone to separation [47]. Since these flaps are only used on (thin airfoil) military jets, an XFOIL analysis is performed to see if an acceptable increase in maximum lift coefficient can be obtained in this case. First a python program was written that uses Euler transformations to modify the airfoil coordinate file for a deployed flap and to make the flap knuckle smooth. Different analysis are performed for varying hinge locations, flap lengths and deployment angles. Some small gains in lift coefficient were obtained, but all of them were less than 0.1. This is however not considered sufficient, so the option of a leading edge flap was ruled out.

### 4.2.2 Slats

Slats are LEHLDs with an airfoil shape that are deployed in front of the main airfoil. Usually, a gap is present in between the slat and the airfoil. The effect of deploying slats is an increase in  $C_{L_{max}}$  and stall angle of attack, thus a lower stall speed can be obtained. Due to their presence in front of the airfoil, they reduce the suction peak and adverse pressure gradient on the main airfoil and create a fresh boundary layer on both components. As a result, the flow separation is postponed and higher lift coefficient can be obtained by further increasing the angle of attack.

**The StefX Slat System** Due to the many advantages slats have, an effort has been made to find a system that could use slats both in normal as in inverted flight. Due to their asymmetric shape, no system could be designed to use a single slat for both flight attitudes. Therefore, two slats will be used, one for normal and one for inverted flight. As a consequence, the leading edge of the main airfoil no longer has an aerodynamic shape if one slat is extended, which is detrimental for the lift generation. This problem can be solved by installing a plate behind the slat. This plate will have the same shape as the outer part of the main wing that has been removed, and will take the place of the slat sealing the gap and restoring the main airfoil shape. For simplicity reasons, this plate will be installed on the same rod as the slat, so it will automatically be deployed together with the slat.

**Slat Deployment** Since slats postpone stall to higher angles of attack, they are deployed when the aircraft is flying at an angle of attack close to the maximum lift angle of attack. In clean configuration, a large negative pressure peak will be present at the front of the airfoil. This suction peak can be used to pull the slats out in deployed position. Using XFOIL, the average negative pressure coefficient on the slat can be calculated and used to estimate the force pulling the slat out, see Equation (4.2). It is assumed that this force is constant during the deployment of the slat. Based on the mass estimation of the LEHLD system, the acceleration and deployment time can be found using basic kinematic equations.

$$P_{\text{slat}} = C_p \frac{1}{2} \rho V^2 S_{\text{slat}} \quad (4.2)$$

The results of this automatic deployment can be found in Table 4.3.

**Slat Retraction** Once the slats are no longer needed or wanted, the pilot can retract them. The calculation of the force needed to retract the slats is outside the scope of this project. It is however expected that by lowering the angle of attack, the dynamic pressure acting on the airfoil will push the slats back in. The transition phase

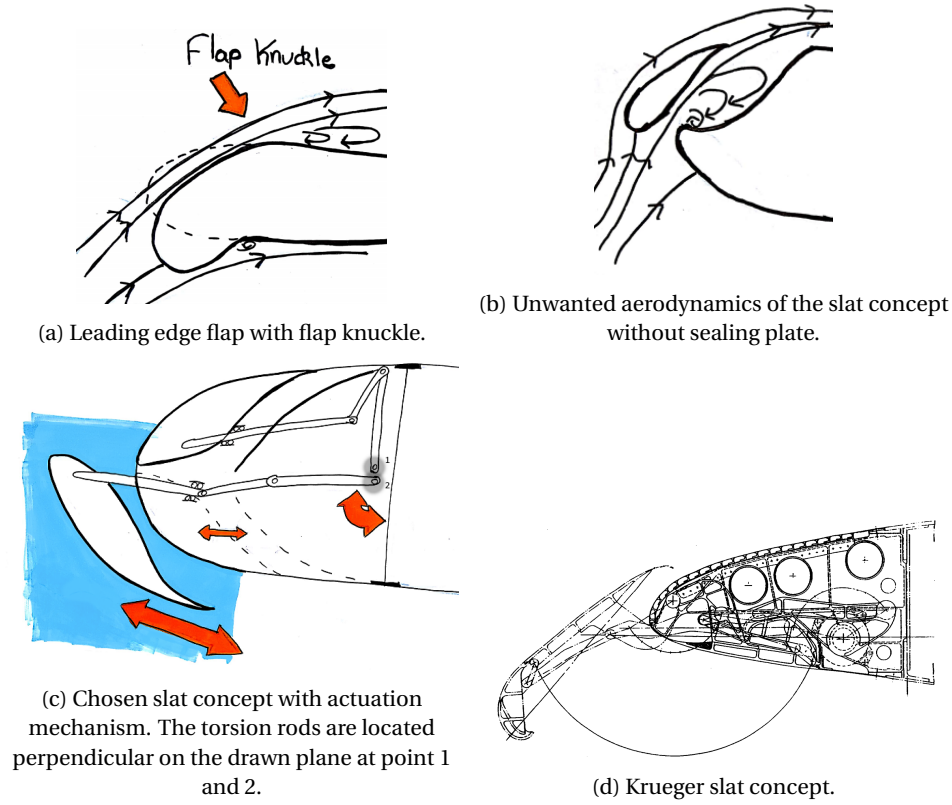


Figure 4.1: LEHLD concepts.

$\alpha$ [°]	$Re$ [-]	$C_{p_{avg}}$ [-]	$F_{slat}$ [N]	$t_{deploy}$ [s]
15.0	$2 \cdot 10^6$	-5.12	-6127.15	0.02

Table 4.3: Slat deployment time due to suction peak force.

and altered pressure distribution due to the slats, can only be accurately modelled using CFD. Therefore, in further development of the *StefX*, a more detailed analysis of the aerodynamic forces working on the slat system should be performed, investigating the need and sizing of the actuation system.

**Slat Optimisation** The lift increase that is obtained by using slats can be calculated using Equation (4.3) from DATCOM.  $c_{l_{\delta_{max}}}$  is the theoretical maximum lifting effectiveness and depends on the ratio of slat chord to wing chord.  $\eta_{max}$  and  $\eta_{\delta}$  are effectiveness parameters that take into account the airfoil parameters and the changes in slat deflection. Finally,  $\delta_s$  is the slat deflection and  $\frac{c'}{c}$  the ratio of the new chord (with slats deployed) and the original airfoil chord.

$$\Delta c_{l_{max}} = c_{l_{\delta_{max}}} \eta_{max} \eta_{\delta} \delta_s \frac{c'}{c} \quad (4.3)$$

Equation (4.3) was used to optimise three slat parameters: deflection angle, chord and deployment distance. This was done using a python program. The deciding factor turned out to be the mechanism to deploy the slats and the limitations imposed by DATCOM. Increasing all of the above mentioned parameters improved the lift coefficient, but increasing these values led to problems in the sizing of the deployment mechanism and the preferred location of the front spar, as determined by the structures group in Chapter 6. The results can be found in Table 4.4 and the newly obtained  $\alpha - C_l$  curve can be found in Figure 4.3.

$\Delta c_{l_{max}}$ [-]	$\frac{c'}{c}$ [-]	$\delta_s$ [°]	Deployed distance [m]
0.531	0.15	25.0	0.0825

Table 4.4: Results of the slat optimisation for the geometric average chord location.

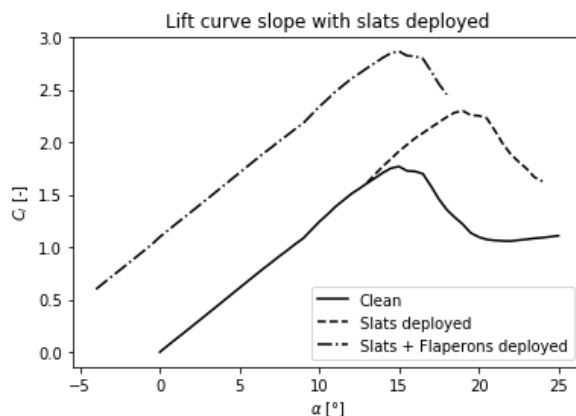


Figure 4.3:  $\alpha - C_L$  curve with the slat system.

**Slat Control System** Independent of the chosen actuation system, a method for the pilot to control the slats will be designed. Since the slats only have 2 positions, fully deployed or fully retracted, it is decided to control them with a simple switch. This also reduces the work load of the pilot, since he only needs to push the switch and not move his hand and arm to a different position in the cockpit. Therefore, this switch will be placed on the throttle lever, which will also be used for flaperon control by a turning movement. The pilot can control the stick with his right hand while having full control over the HLDs and throttle with his left hand. Since the entire system is actuated electrically, the possibility exists to install a simple envelope protection system for the actuation. At high velocity, the forces on the slat will become high, with risk of damaging them. Therefore, a velocity limit will be determined in a following design phase. The envelope protection system will be coupled to the velocity indicator and if the velocity limit is crossed, the pilot will not be able to deploy the slats. Furthermore, if the slats are still deployed when the pilot reaches this speed (if he forgot to retract them for example), the system will automatically retract the slat to avoid damage. Also, the envelope protection system will be used to assist the pilot in deploying the correct slat. Based on the G force acting on the *StefX*, as indicated by the accelerometer, the envelope protection system will deploy the correct slat for the specific G force. Finally, an indication light will be put on the cockpit panel showing the retracted/deployed position of the slats.

**Verification and Validation** The code has been verified using unit and system tests. For the unit tests, small parts of the code are run separately to check if their output is correct. These small parts are for example the part that calculates the area of the slat based on the airfoil coordinate file. Furthermore, a worked out example of DATCOM [11, p.6.1.1.3-6] was plugged into the section that calculates the lift increase due to slats. An accuracy of 100% was obtained in the calculation, verifying the program. The calculated lift coefficient increase of 0.612 is validated in DATCOM with a test value of 0.56.

### 4.2.3 Krueger Flaps

Another commonly used LEHLD system are Krueger flaps. They are commonly used on commercial airliners. Krueger flaps are deployed on the bottom half of the airfoil and can therefore easily be installed on the top half as well for the inverted flight condition of the *StefX*. They are however not as effective as slats and only work for a limited angle of attack range, which ruled them out as LEHLD option [36]. There does exist an experimental Krueger Slat concept, which is a Krueger flap that deploys from the bottom part to the top part of the airfoil such that it acts as a slat [36]. This system has the effectiveness advantage of a slat and the symmetrical storage and deployment advantage of the Krueger flap. This concept can be seen in Figure 4.2d. Since a working slat system was found, the complexity of the Krueger slat actuation mechanism and concerns about aerodynamic behaviour and sudden drag increase during deployment ruled this option out.

## 4.3 Trailing Edge High Lift Devices

In the Midterm report [3], the chosen concept also uses flaperons as HLD. A flaperon is an aileron that also functions as a flap. The effect of using ailerons as flaps on the  $C_{L_{max}}$  can be compared with the effect of plain

flaps. The plain flap is a simple high lift surface that only moves through rotation without translation, just as a classic aileron as used on aerobatic aircraft. The advantage of using such a simple flaperon is that it is by itself completely symmetric and can therefore be used both in normal and inverted flight. The max deflection of an aileron on the *SteifX* is 30°. As the flaperon still needs to be able to provide roll, the deflection used to increase  $C_{l_{max}}$  is limited to approximately 15°. This has a big impact on the performance of the flaperon compared to the plain flap, as a plain flap can normally extend even further than 30°. The aileron occupies an average of around 27% of the chord. Using this parameter, the  $\Delta C_{l_{max}}$  is calculated with [11] using Equation (4.4). This yields  $\Delta C_{l_{max}}$  of approximately 0.567.  $k_1$ ,  $k_2$  and  $k_3$  are factors that take into account the flap-chord-to-airfoil-chord ratio, flap deflection and motion. The results are also shown in Figure 4.3

$$\Delta C_{l_{max}} = k_1 k_2 k_3 (C_{l_{max}})_{base} \quad (4.4)$$

## 4.4 Aerodynamic Properties

With the zero-lift drag coefficient determined in Section 4.1, it becomes possible to construct a drag polar of the aircraft. It should be noted that several freely available tools, such as XFLR5 and AVL, already provide the option of analysing the 3D aerodynamic performance of a wing. However, their use is often limited. First and foremost, neither offers an easy way to assess the aerodynamic balancing of the control surfaces, even though this was the primary objective of the aerodynamic analysis that was to be performed. On a secondary note, XFLR5 does not provide the option of unsteady flow simulation, and the flight dynamics module of AVL provides merely a fully linearised model of the aerodynamic performance. When the aerodynamic analysis was initiated, it was the ambition to use the aerodynamic calculations of an unsteady solver to simulate the full flight envelope of the aircraft. For these reasons, solvers such as XFLR5 and AVL were discarded. Solvers that did have these capabilities were unfeasible for various other reasons, such as financially expensive, computationally expensive (e.g. ANSYS) or generally not suitable for design routines (e.g. X-Plane does not allow for easy aerodynamic balancing).

To perform the aerodynamic balancing, multiple aerodynamic models were built, each with increasing complexity, so as to provide ways of verifying the more complicated models. Additionally, unsteady models were built to show how the steady models can be extended to treat unsteady flow, after which the extension to simulate the full flight dynamics of the aircraft is trivial; once the pressure distribution over the aircraft are known, it is merely a matter of computing forces and moments and analysing the required kinetics and kinematics.

All models have been built on the assumptions of incompressible, inviscid and irrotational flow, such that a velocity potential exists. The first of these assumptions is accurate as only low Mach numbers are achieved; the latter two are far more significant simplifications and mean that results above angles of attack of 15°, or when the deflections of the control surfaces are large, should be treated with great care<sup>1</sup>. Nonetheless, it still provides a first-order estimate of the aerodynamic characteristics, which is determined to be sufficiently accurate at this stage of the design.

Finally, all models have been built based on [28], which provides step-by-step procedures for various potential flow solving methods. As [28] is a well-established reference in terms of numerical aerodynamic computations, it is assumed that the methods described in [28] have been extensively validated already.

### 4.4.1 Steady Airfoil Simulation

**Background** In general, for steady, incompressible, inviscid and irrotational flow, a velocity potential exists, that is, there exists a function  $\Phi$  such that

$$\nabla^2 \Phi = 0 \quad (4.5)$$

This is a linear second order differential equation, and thus if the functions  $\Phi_1, \Phi_2, \dots, \Phi_n$  are each solutions to (4.5), then it also holds that

$$\nabla^2 \left( \sum_{i=1}^n \Phi_i \right) = 0 \quad (4.6)$$

<sup>1</sup>The airfoil of the main wing is known to stall at an angle of attack of 15°.

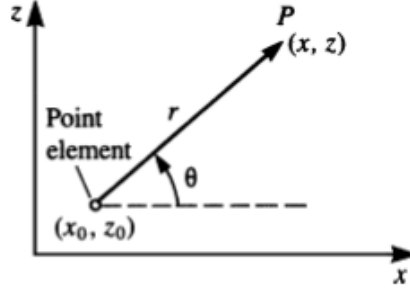


Figure 4.4: Induced velocity of a discrete vortex [28, p. 231]. Note that the positive  $y$ -axis points into the paper.

This property can be used to construct a boundary element method. One can construct  $n$  solutions  $\Phi_1, \Phi_2, \dots, \Phi_n$ , where the unknown weights  $a_i$  of these solutions must satisfy

$$\nabla^2 \Phi = \nabla^2 \left( \sum_{i=1}^n a_i \Phi_i + \Phi_\infty \right) = 0 \quad (4.7)$$

where  $\Phi_\infty$  is the velocity potential of the freestream velocity. If  $\Phi_1, \Phi_2, \dots, \Phi_n$  are all solutions to (4.5), then this means that  $n$  equations are required to establish a determined system of equations. This can be done by setting up the boundary condition that the flow must be tangential to the surface at the surface. In other words, the dot product between the velocity (equal to  $\mathbf{V} = \nabla \Phi$ ) and the vector normal to the surface must be 0, i.e.  $\nabla \Phi \cdot \mathbf{n} = 0$  (equivalent to a Neumann boundary condition). By selecting  $n$  points on the surface where this holds, a system of  $n$  equations can be established, resulting in a determined system of equations of the form

$$\left( \sum_{i=1}^n a_i \nabla \Phi_i \right) \cdot \mathbf{n}_j = -\nabla \Phi_\infty \cdot \mathbf{n}_j \quad \text{for } 1 \leq j \leq n \quad (4.8)$$

which can be solved for the weights  $a_i$ .

**Discrete Vortex Representation** To simulate the airfoil in a steady environment, the discrete vortex representation was used, as mentioned in [28]. A discrete vortex is shown in Figure 4.4. Let the vortex strength equal  $\Gamma_j$ ; with the vortex pointing in counterclockwise direction in the  $xz$ -plane, this means that the discrete vortex may be represented as

$$\boldsymbol{\Gamma}_j = \begin{bmatrix} 0 \\ -\Gamma_j \\ 0 \end{bmatrix} = -\Gamma_j \hat{\mathbf{y}} \quad (4.9)$$

Furthermore, if  $\mathbf{r}_{P_i}$  is the vector connecting point  $P$  to the discrete vortex, then the induced velocity at  $P$  due to  $i$  is given by

$$\mathbf{Q}_{P_j} = \Gamma_j \mathbf{q}_{P_j} = -\Gamma_j \mathbf{r}_{P_j} \times \hat{\mathbf{y}} \quad (4.10)$$

**Mesh Creation** To create a mesh on which the Equation (4.8) may be solved, the airfoil was assumed to be thin, and divided in panels. Near the leading and trailing edge, high gradients in  $\Gamma_i$  are to be expected, and thus rather than using an uniform panel distribution, the distribution shown in Figure 4.5 is used. Thus, a simple method to create  $n$  panels would be to first create  $n+1$   $\theta_i$ , linearly spaced between 0 and  $\pi$ ; the corresponding  $x_i$  are then computed by

$$x_i = 0.5 - 0.5 \cos \theta_i, \quad 1 \leq i \leq n+1 \quad (4.11)$$

The corresponding  $z_i$ -coordinate then follows straightforwardly from the airfoil camber line (as a symmetric airfoil is used, it is zero everywhere). The panels could then be created, with panel  $i$  being associated with  $(x_i, y_i, z_i)$  and  $(x_{i+1}, y_{i+1}, z_{i+1})$ . The vortices were placed at the quarter-point of each panel, and the control

points, the points where Equation (4.7) was to be satisfied, were located at the three-quarter-points of the panels; this guarantees that the Kutta-condition (the circulation is zero at the trailing edge) is satisfied [28].

To take into account the presence of control surfaces, above methodology was adopted to take flaps into account; if the flap takes up a fraction  $c_f/c$  of the chord, and  $n$  panels were to be created in total,  $c_f/c \cdot n$  would be allocated to the flap, and the remainder to the main airfoil itself; the  $\theta_i$  and  $x_i$  were then created for the main airfoil and the flap separately, and combined afterwards. The panels associated with the flap were then transformed over an angle  $\delta_f$  over the hingeline, located at  $(x_{\text{hingeline}}, 0, z(x_{\text{hingeline}}))$ , by use of

$$\mathbf{x}_{\text{transformed}} = \begin{bmatrix} \cos \delta_f & 0 & \sin \delta_f \\ 0 & 1 & 0 \\ -\sin \delta_f & 0 & \cos \delta_f \end{bmatrix} (\mathbf{x}_i - \mathbf{x}_{\text{hingeline}}) + \mathbf{x}_{\text{hingeline}} \quad (4.12)$$

With the mesh created, the linear system of algebraic equations may be set up. From Equations (4.8) and (4.10), it follows that the system will be of the form

$$A \begin{bmatrix} \Gamma_1 \\ \vdots \\ \Gamma_n \end{bmatrix} = \mathbf{b} \quad (4.13)$$

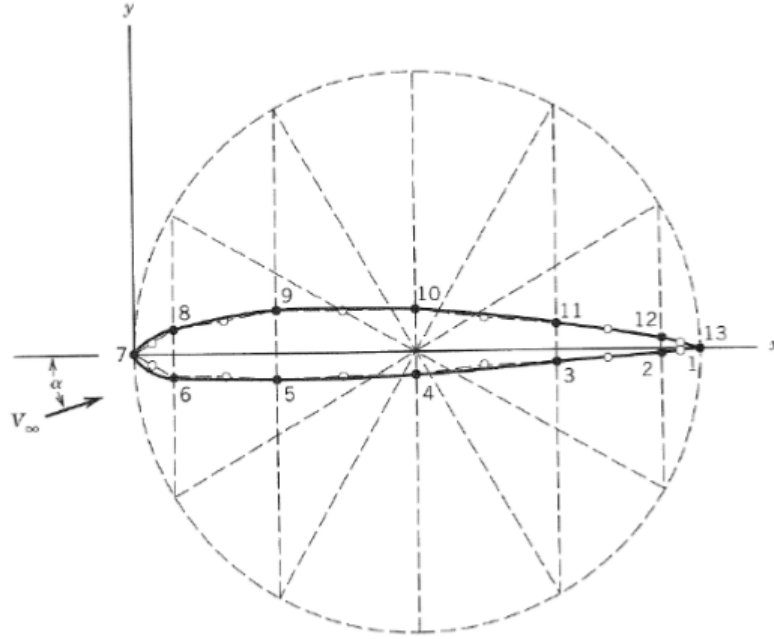


Figure 4.5: Example panel distribution over airfoil [45, p.29]. Note that although in this Figure a thick airfoil is used, it was assumed for this simulation that the airfoil could be modelled as thin, i.e. all panels are only placed on the mean camber line.

**Matrix Construction** The left-hand side matrix of Equation (4.13) can straightforwardly be set up. With  $\mathbf{q}_{ij}$  given by Equation (4.10), and  $\mathbf{n}_i$  denoting unit vector normal to panel  $i$ , the left-hand side matrix is given by

$$A = \begin{bmatrix} \mathbf{q}_{11} \cdot \mathbf{n}_1 & \mathbf{q}_{12} \cdot \mathbf{n}_1 & \mathbf{q}_{13} \cdot \mathbf{n}_1 & \dots & \mathbf{q}_{1n} \cdot \mathbf{n}_1 \\ \mathbf{q}_{21} \cdot \mathbf{n}_2 & \mathbf{q}_{22} \cdot \mathbf{n}_2 & \mathbf{q}_{23} \cdot \mathbf{n}_2 & \dots & \mathbf{q}_{2n} \cdot \mathbf{n}_2 \\ \mathbf{q}_{31} \cdot \mathbf{n}_3 & \mathbf{q}_{32} \cdot \mathbf{n}_3 & \mathbf{q}_{33} \cdot \mathbf{n}_3 & \dots & \mathbf{q}_{3n} \cdot \mathbf{n}_3 \\ \vdots & \vdots & \vdots & \ddots & \vdots \\ \mathbf{q}_{n1} \cdot \mathbf{n}_n & \mathbf{q}_{n2} \cdot \mathbf{n}_n & \mathbf{q}_{n3} \cdot \mathbf{n}_n & \dots & \mathbf{q}_{nn} \cdot \mathbf{n}_n \end{bmatrix} \quad (4.14)$$

**Vector Construction** Constructing the right-hand side vector of Equation (4.13) is trivial as well, and is simply equal to

$$b = \begin{bmatrix} \mathbf{V}_\infty \cdot \mathbf{n}_1 \\ \mathbf{V}_\infty \cdot \mathbf{n}_2 \\ \mathbf{V}_\infty \cdot \mathbf{n}_3 \\ \vdots \\ \mathbf{V}_\infty \cdot \mathbf{n}_n \end{bmatrix} \quad (4.15)$$

**Results** The  $\Gamma_i$  may now straightforwardly be found by simply solving Equation (4.13). By the Kutta-Joukowski theorem, the lift per unit span differential over each panel is given by

$$\Delta L'_i = \rho V_\infty \Gamma_i \quad (4.16)$$

such that the lift coefficient of the complete airfoil is given by

$$C_l = \frac{2 \sum_{i=1}^n \Gamma_i}{V_\infty} \quad (4.17)$$

Meanwhile, the pressure difference over each panel is given by

$$\Delta p_j = \rho V_\infty \frac{\Gamma_i}{x_{i+1} - x_i} \quad (4.18)$$

From the simulation, a lift curve slope of  $6.27 \text{ rad}^{-1}$  was obtained if  $n = 200$  panels were used; this is close to the expected value of  $2\pi \text{ rad}^{-1} - 1$  with the difference being due to discretisation errors. For a flap length of  $c_f/c = 0.25$ , and the hingeline located at  $x_{\text{hingeline}} = 0.75c$ , the change of lift coefficient with change in deflection angle equalled  $3.56 \text{ rad}^{-1}$ .

**Verification** The program was also run with an airfoil of which the camberline shape is

$$z(x) = 0.4 \cdot \frac{x}{c} \left[ 1 - \frac{x}{c} \right] \quad (4.19)$$

of which the exact solution of the lift coefficient is known to equal 1.275 for  $\alpha = 0$  [28]. It was established that the discrete vortex model converges to this value as  $N$  is increased, and thus the code is verified to work correctly. Furthermore, [28] is a well-established source with regards to numerical methods for aerodynamics, validating the model made.

#### 4.4.2 Unsteady airfoil simulation

To model the airfoil in an unsteady flow, only few modifications need to be made to the aforementioned method. First, a coordinate system must be established; the coordinate system as shown in Figure 4.6 shall be used. The  $XYZ$ -frame represents an inertial frame of reference, whereas the  $xyz$ -frame moves along with the leading edge of the airfoil, with the  $x$ -axis aligned with the chordline of the airfoil of which the flap is not deflected. The rotation about the  $T$ -axis is given by the angle  $\theta$ , and the  $z$ -coordinate of the airfoil is a function of both  $x$  and  $t$ ; it will be assumed however that the shape of the airfoil is constant over time and that any flap deflections are instantaneous.

Several amendments need to be made to the theory behind the steady discrete vortex model. Recall the Neumann boundary condition applied to the velocity potential, equation (4.7); it must hold that

$$(\nabla\Phi + \mathbf{v}) \cdot \mathbf{n} = 0 \quad (4.20)$$

where  $\mathbf{v}$  is the velocity of the undisturbed flow at the surface. This velocity is equal to

$$\mathbf{v} = -\mathbf{V}_0 - \mathbf{v}_{rel} - \boldsymbol{\Omega} \times \mathbf{r} \quad (4.21)$$

as the velocity of the undisturbed flow at the surface points in opposite direction of the velocity of the surface itself, and where  $\mathbf{V}_0$  is the velocity of the origin of the  $xyz$ -frame,  $\mathbf{v}_{rel}$  the relative velocity of the airfoil within the  $xyz$ -frame (e.g. due to a flap deflection, where  $\boldsymbol{\Omega}$  is the angular velocity vector of the  $xyz$ -frame with

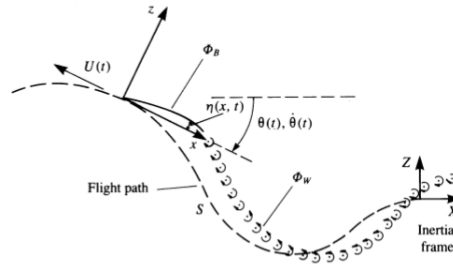


Figure 4.6: Coordinate system chosen for the unsteady airfoil analysis [28, p. 387]. Note that the positive  $y$ -axis points into the paper.

respect to the  $XYZ$ -frame, and  $\mathbf{r}$  is the position of the point within the  $xyz$ -frame. Assuming the airfoil is rigid,  $\mathbf{v}_{rel} = \mathbf{0}$ .

In addition to this change to the vector that appears on the right-hand side of the equation, it should be noted that as the airfoil moves forward in space, vortices will be shed from the trailing edge<sup>2</sup>, as shown in Figure 4.7; these vortices all contribute to the velocity potential as well. The strength of the leading wake vortex is unknown; however, once calculated, it will remain constant due to the Helmholtz theorem, which states that there is no vortex decay [28]. Thus, if only one discrete vortex is added to the wake with each time-step, only one additional unknown is introduced per timestep. Nonetheless, this means that currently, Equation (4.7) only offers  $n$  equations, even though there will be  $n + 1$  unknowns. Thus, an additional equation is required. This comes from Kelvin's theorem, which states that the time rate of change of the circulation of a fluid is zero, i.e.  $d\Gamma/dt = 0$ . Thus, let  $i$  denote the current timestep, let  $\Gamma_W$  denote the circulation of the wake, and let  $\Gamma_{W_i}$  denote the discrete vortex shed from the trailing edge at this timestep. As mentioned, the vortices aft of the leading wake vortex are already constant in time, in other words, all  $\Gamma_{W_j}$ ,  $j < i$ , are constant in time. Let  $\Gamma(t_i)$  denote the circulation of the airfoil itself, i.e. the sum of the circulations of the vortices that are actually on the airfoil itself,

$$\Gamma(t_i) = \sum_{j=1}^n \Gamma_j(t_i) \quad (4.22)$$

Mathematically, this means that

$$\frac{d\Gamma(t_i)}{dt} + \frac{d\Gamma_W}{dt} = \frac{\Gamma(t_i) - \Gamma(t_{i-1})}{\Delta t} + \frac{\Gamma_{W_i}}{\Delta t} = 0 \quad (4.23)$$

Finally, it should be noted that in Equation (4.20),  $\nabla\Phi$  now also includes the induced velocity of the wake vortices; at a time  $t_i$ , the induced velocity due to the vortices  $\Gamma_j$ ,  $1 \leq j < i$  is known and can be computed as all  $\Gamma_j$ ,  $1 \leq j < i$  are known at that point in time. This means that the induced velocity due to those wake vortices may straightforwardly be computed by Equation (4.10) and can be subtracted from the right-hand-side vector. In other words, the following system of Equations is obtained for an arbitrary  $i$ ,  $i \geq 1$ :

$$\nabla \left( \sum_{j=1}^n (\phi_j) + \Phi_{W_i} \right) \cdot \mathbf{n}_k = \left( \mathbf{V}_0 + \boldsymbol{\Omega} \times \mathbf{r}_k - \nabla \sum_{j=1}^{i-1} \Phi_{W_j} \right) \cdot \mathbf{n}_k \quad (4.24)$$

$$\sum_{j=1}^n \Gamma_j(t_i) + \Gamma_{W_i} = \sum_{j=1}^n \Gamma_j(t_{i-1}) \quad (4.25)$$

$$A \begin{bmatrix} \Gamma_1 \\ \Gamma_2 \\ \vdots \\ \Gamma_n \\ \Gamma_{W_i} \end{bmatrix} = \mathbf{b} \quad (4.26)$$

**Mesh Creation** The mesh has been created in exactly the same fashion as for the steady discrete vortex representation. The leading wake vortex has been placed 0.25 of the distance covered by the trailing edge during the timestep  $\Delta t$  aft of the trailing edge, and its position remains unchanged everafter<sup>3</sup>.

<sup>2</sup>Note: the wake of an airfoil is only shed if the circulation varies with time, due to Kelvin's condition. This is the reason why for the steady solver, no wake had to be modelled. However, for the unsteady solver, it can obviously not be assumed that the circulation of the airfoil is constant with time.

<sup>3</sup>It should be noted that technically speaking, the position should be updated throughout time, and wake roll-up should be computed, as the vortices should move along with the flow field as the circulation vector should be parallel to the velocity. However, this has not

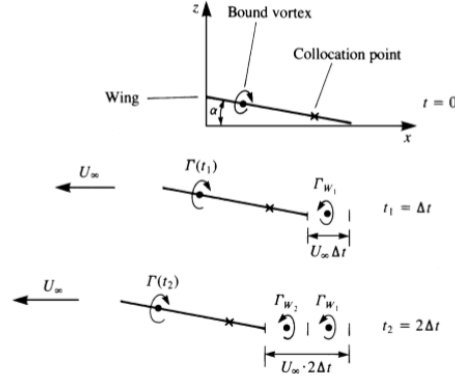


Figure 4.7: Wake shedding from a forward moving airfoil [28, p. 387].

**Matrix Construction** The matrix on the left-hand side of Equation (4.26) may be constructed in a very similar fashion to how it was constructed for the steady discrete vortex representation. Let  $\mathbf{q}_{iw}$  denote the induced velocity due to a unit vortex located the leading wake vortex, then the left-hand side matrix is given by

$$A = \begin{bmatrix} \mathbf{q}_{11} \cdot \mathbf{n}_1 & \mathbf{q}_{12} \cdot \mathbf{n}_1 & \dots & \mathbf{q}_{1n} \cdot \mathbf{n}_1 & \mathbf{q}_{1p} \cdot \mathbf{n}_1 \\ \mathbf{q}_{21} \cdot \mathbf{n}_2 & \mathbf{q}_{22} \cdot \mathbf{n}_2 & \dots & \mathbf{q}_{2n} \cdot \mathbf{n}_2 & \mathbf{q}_{2p} \cdot \mathbf{n}_2 \\ \vdots & \vdots & \vdots & \ddots & \vdots \\ \mathbf{q}_{n1} \cdot \mathbf{n}_n & \mathbf{q}_{n2} \cdot \mathbf{n}_n & \dots & \mathbf{q}_{nn} \cdot \mathbf{n}_n & \mathbf{q}_{np} \cdot \mathbf{n}_n \\ 1 & 1 & \dots & 1 & 1 \end{bmatrix} \quad (4.27)$$

**Vector Construction** The right-hand-side vector can be computed rather straightforwardly as well, and is equal to

$$b = \begin{bmatrix} (\mathbf{V}_0 + \boldsymbol{\Omega} \times \mathbf{r}_1 - Q_{1W}) \cdot \mathbf{n}_1 \\ (\mathbf{V}_0 + \boldsymbol{\Omega} \times \mathbf{r}_2 - Q_{2W}) \cdot \mathbf{n}_2 \\ \vdots \\ (\mathbf{V}_0 + \boldsymbol{\Omega} \times \mathbf{r}_n - Q_{nW}) \cdot \mathbf{n}_n \\ \sum_{j=1}^n \Gamma_j(t_{i-1}) \end{bmatrix} \quad (4.28)$$

where  $\mathbf{Q}_{iW}$  represents the induced velocity due to all wake points except the leading wake vortex.

**Results** The unknown vortex strengths can now straightforwardly be computed by solving Equation (4.26). However, the pressure difference is now more complicated to compute, due to the unsteadiness of the flow. The pressure difference is now given by

$$\Delta p = p_l - p_u = \rho \left[ \left( \frac{Q_t^2}{2} \right)_u - \left( \frac{Q_t^2}{2} \right)_l + \left( \frac{\partial \Phi}{\partial t} \right)_u - \left( \frac{\partial \Phi}{\partial t} \right)_l \right] \quad (4.29)$$

Here, the tangential velocity  $Q_t$  at control point  $j$  equals simply

$$(\mathbf{V}_0 + \boldsymbol{\Omega} \times \mathbf{r}_j - Q_{jW}) \cdot \boldsymbol{\tau}_j \pm \frac{\partial \Phi}{\partial \tau_j} \quad (4.30)$$

Here,

$$\frac{\partial \Phi}{\partial \tau_j} = \gamma_2 \approx \frac{\Gamma_j}{2(x_{j+1} - x_j)} \quad (4.31)$$

---

been implemented at this stage due to the little added accuracy compared to the increased computational effort.

The time derivatives of the velocity potential in tangential direction are simply

$$\frac{\partial \Phi_j}{\partial t} = \frac{\partial}{\partial t} \sum_{k=1}^j \frac{\Gamma_k}{2} \quad (4.32)$$

Substituting Equations (4.30), (4.31) and (4.32) into Equation (4.29) yields

$$\Delta p_j = \rho \left[ (\mathbf{V}_0 + \boldsymbol{\Omega} \times \mathbf{r}_j - \mathbf{Q}_{jW}) \cdot \boldsymbol{\tau}_j \frac{\Gamma_j}{x_{j+1} - x_j} + \frac{\partial}{\partial t} \sum_{k=1}^j \Gamma_k \right] \quad (4.33)$$

With the pressure distribution over the airfoil known, it becomes trivial to compute the lift and drag coefficient.

**Verification** Above method was verified by running the simulation for many timesteps, at constant  $\mathbf{V}_0$  and zero  $\boldsymbol{\Omega}$ ; it was established that the resulting solution converged to the same solution as obtained in the steady solver, as expected, verifying the working of the code. Additionally, the results for certain motions (e.g. sudden acceleration of a flat plate) were compared to results shown in [28], further verifying the working of the code.

### 4.4.3 Steady Wing Simulation

To be able to perform the aerodynamic balancing on a three-dimensional wing, a steady wing simulation was built, relying on vortex panels to represent the circulation distribution over the airfoil. The general process behind this is very similar to the steady airfoil simulation: a left-hand-side matrix of influence coefficients is set up, containing the influence of panel  $j$  to control point  $i$ , and a right-hand-side vector is established based on the normal velocity of the freestream at control point  $i$ . The only real difference is naturally in how the mesh is generated and how the influence coefficients are computed.

It should be noted that in the simulation, the presence of the fuselage has been neglected. Similarly, for the vertical tail, in reality, there is only ‘side’ of the wing. However, although it is relatively straightforward to only simulate one side of the wing on its own, it is then difficult to implement it such that no tip vortices are present on the inboard side of the wing. As a result, it was chosen to model the vertical tail as if it had another side to it. Finally, it was proven to be too challenging to model an aileron that would remain constant in absolute length (such that the relative chord-length varies over the span), and as such it was chosen to instead use the average relative chord-wise length the aileron to model the aileron (this was not an issue for the elevator or rudder, as they had fixed relative chord-wise lengths).

**Mesh Generation** The chosen mesh is shown in Figure 4.8. The wing is discretised in several panels, with counter  $i$  in chordwise direction and counter  $j$  in spanwise direction, each with their own bound vortex, each with vortex strength  $\Gamma_{i,j}$ . The leading bound vortex is placed at the quarter-chord of each panel, whereas the trailing bound vortex is placed a quarter-chord behind the panel. The control point is chose to be at the three-quarter-chord of the panel, such that the Kutta-condition is satisfied. Free wake vortices are also added; these have the same strength as the trailing edge bound vortices, and are there to ensure that the trailing vortices extend up to infinity.

To generate the mesh,  $N$  panels were created in spanwise direction, and  $M$  panels were created in chord-wise direction, such that there are  $K = N \cdot M$  panels in total, as shown in Figure 4.9, uniformly distributed in both directions.

The possibility to add flaps and horns was included. The implementation of this was relatively simplistic, and similar to Equation (4.12): for each spanwise position, the location of the hingeline along the chordwise direction was computed, after which Equation (4.12) was applied to points that would be part of the aileron or horn.

**Matrix Construction** The induced velocity  $\mathbf{q}_{km}$  for a unit vortex strength at control point  $k$  due to panel  $m$  can be straightforwardly computed. For a finite constant-strength vortex line segment, running between points  $\mathbf{x}_1$  and  $\mathbf{x}_2$  the induced velocity at point  $P$ , located at  $\mathbf{x}_P$  (see Figure 4.10), may be computed as

$$\mathbf{q} = \frac{\Gamma}{4\pi} \frac{\mathbf{r}_1 \times \mathbf{r}_2}{|\mathbf{r}_1 \times \mathbf{r}_2|^2} \mathbf{r}_0 \cdot \left( \frac{\mathbf{r}_1}{r_1} - \frac{\mathbf{r}_2}{r_2} \right) \quad (4.34)$$

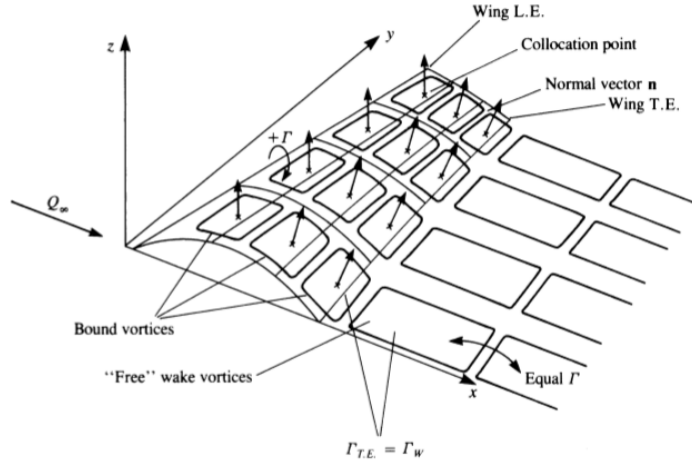


Figure 4.8: Mesh creation [28, p. 341].

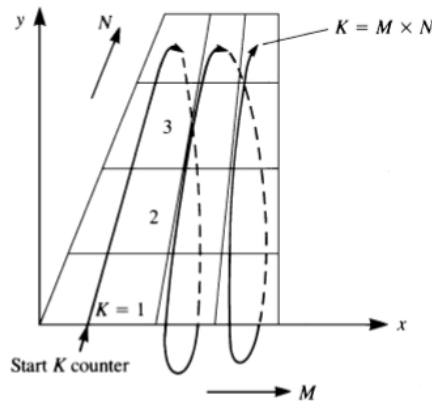


Figure 4.9: Mesh creation [28, p. 344].

with  $\mathbf{r}_1 = \mathbf{x}_p - \mathbf{x}_1$ ,  $\mathbf{r}_2 = \mathbf{x}_p - \mathbf{x}_2$  and  $\mathbf{r}_0 = \mathbf{x}_2 - \mathbf{x}_1$ . A vortex ring is simply a combination of four constant-strength vortex line segments, and thus  $\mathbf{q}_{km}$  may easily be obtained from Equation (4.34). Then, the left-hand-side matrix is simply given by

$$A = \begin{bmatrix} \mathbf{q}_{11} \cdot \mathbf{n}_1 & \mathbf{q}_{12} \cdot \mathbf{n}_1 & \mathbf{q}_{13} \cdot \mathbf{n}_1 & \dots & \mathbf{q}_{1K} \cdot \mathbf{n}_1 \\ \mathbf{q}_{21} \cdot \mathbf{n}_2 & \mathbf{q}_{22} \cdot \mathbf{n}_2 & \mathbf{q}_{23} \cdot \mathbf{n}_2 & \dots & \mathbf{q}_{2K} \cdot \mathbf{n}_2 \\ \mathbf{q}_{31} \cdot \mathbf{n}_3 & \mathbf{q}_{32} \cdot \mathbf{n}_3 & \mathbf{q}_{33} \cdot \mathbf{n}_3 & \dots & \mathbf{q}_{3K} \cdot \mathbf{n}_3 \\ \vdots & \vdots & \vdots & \ddots & \vdots \\ \mathbf{q}_{K1} \cdot \mathbf{n}_K & \mathbf{q}_{K2} \cdot \mathbf{n}_K & \mathbf{q}_{K3} \cdot \mathbf{n}_K & \dots & \mathbf{q}_{KK} \cdot \mathbf{n}_K \end{bmatrix} \quad (4.35)$$

Here,  $\mathbf{n}_k$  follows from Figure 4.11, and is given by

$$\mathbf{n}_k = \frac{\mathbf{A}_k \times \mathbf{B}_k}{|\mathbf{A}_k \times \mathbf{B}_k|} \quad (4.36)$$

where  $\mathbf{A}_k$  and  $\mathbf{B}_k$  are the diagonals of the panel.

**Vector Construction** Constructing the right-hand side vector is the same as before, and is simply equal to

$$b = \begin{bmatrix} \mathbf{V}_\infty \cdot \mathbf{n}_1 \\ \mathbf{V}_\infty \cdot \mathbf{n}_2 \\ \mathbf{V}_\infty \cdot \mathbf{n}_3 \\ \vdots \\ \mathbf{V}_\infty \cdot \mathbf{n}_n \end{bmatrix} \quad (4.37)$$

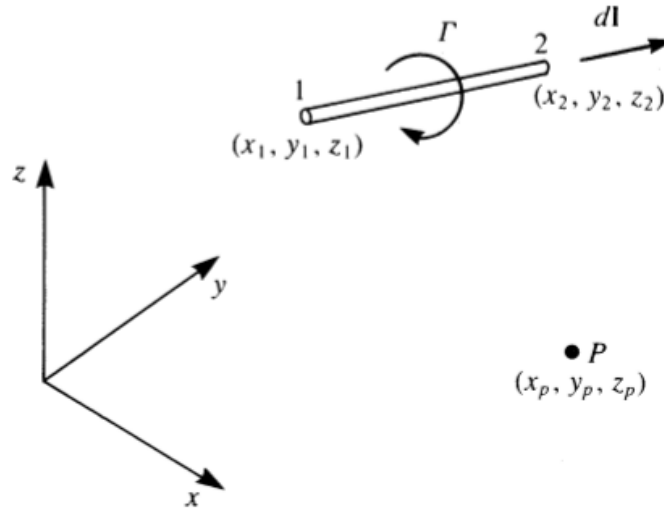
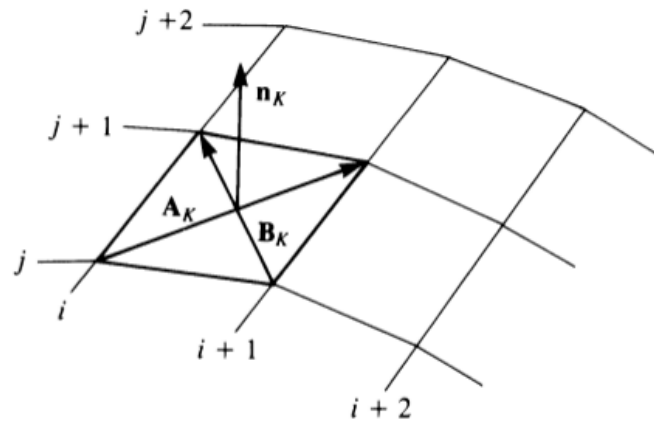
Figure 4.10: Straight vortex line segment and point  $P$  [28, p. 254].

Figure 4.11: Construction of the unit normal vector to a panel [28, p. 254].

**Secondary computations** The system may now straightforwardly be solved for the missing circulation strengths  $\Gamma_{i,j}$ . The lift distribution over the panels then follows from

$$\Delta L_{ij} = \rho V_{\infty} (\Gamma_{i,j} - \Gamma_{i-1,j}) \Delta y_{ij}, \quad i > 1 \quad (4.38)$$

where  $\Delta L_{ij}$  is the lift generated by panel  $ij$ , and when  $i = 1$  (thus at the leading edge)

$$\Delta L_{ij} = \rho V_{\infty} \Gamma_{i,j} \Delta y_{ij}, \quad i = 1 \quad (4.39)$$

The pressure difference distribution is then simply

$$\Delta p_{ij} = \frac{\Delta L_{ij}}{\Delta S_{ij}} \quad (4.40)$$

where  $\Delta p_{ij}$  is the difference between the pressure over the lower and upper surface,  $\Delta S_{ij}$  is the area of panel  $ij$  and  $\Delta y_{ij}$  the width of panel  $ij$ . The drag coefficient can be computed by

$$\Delta D_{ij} = -\rho w_{ind_{ij}} (\Gamma_{i,j} - \Gamma_{i-1,j}) \Delta y_{ij}, \quad i > 1 \quad (4.41)$$

$$\Delta D_{ij} = -\rho w_{ind_{ij}} \Gamma_{i,j} \Delta y_{ij}, \quad i = 1 \quad (4.42)$$

Here,  $w_{ind_{ij}}$  is the induced downwash at panel  $ij$  due to the trailing vortices. The total lift and drag are simply the sum of the contributions of the individual panels. The lift and drag coefficients are then straightforwardly

found by dividing by  $qS$ , with  $q$  the dynamic pressure and  $S$  the reference area of the wing. As the wing was assumed to be thin, naturally no distinction can be made between a pressure on the lower and upper surface; therefore, merely the *difference* in pressure coefficient over the wing may be computed, given by

$$\Delta c_p = \frac{\Delta p_{ij}}{p_\infty} \quad (4.43)$$

The wing moment coefficient could be obtained from this pressure distribution; the force acting on each panel can be computed by

$$\mathbf{F}_{ij} = \Delta p_{ij} \mathbf{n}_{ij} \quad (4.44)$$

The moment about the quarter-chord can then be computed by

$$\mathbf{M}_{ij} = (\mathbf{x}_{ij} - \mathbf{x}_{\text{quarter-chord}}) \times \mathbf{F}_{ij} \quad (4.45)$$

The total moment about the quarter-chord is then simply found by summing the individual contributions of the panels. The moment coefficient is found by dividing by  $qS\bar{c}$ , with  $\bar{c}$  the mean aerodynamic chord.

**Results** From the secondary computations, several relevant parameters may be obtained. First, the  $C_L - \alpha$ ,  $C_D - \alpha$  and  $C_D - C_L$  polars of the main wing have been plotted in Figure 4.12a-4.12c; these have been constructed using  $N = 160$  panels in spanwise direction, and  $M = 2$  panels in chordwise direction (note that it essentially becomes a simple horseshoe vortex model), as the spanwise lift distribution is naturally of significantly more relevance than the chordwise lift distribution. Furthermore, in Figure 4.12d, the variation of the induced angle of attack  $\alpha_i$  over the wing is shown, with  $\alpha_i = \arctan w_i/V_\infty$ , where  $w_i$  is the induced downwash at the leading edge due to the trailing vortices. The results have been compared with the results obtained by XFLR5; this will be described in more detail in the verification of the code.

Furthermore, a plot of the pressure distribution is shown in Figure 4.13, constructed with the flaperons extended upwards at a deflection of  $10^\circ$ , at an angle of attack of  $10^\circ$ , at a freestream velocity of 80 m/s and with  $N = 40$  panels in spanwise direction, and  $M = 20$  panels in chordwise direction.

From the aerodynamic polars, it was possible to compute two relevant parameters. First, the wing lift curve slope equals  $C_{L\alpha_w} = 3.836 \text{ rad}^{-1}$ ; secondly, the span efficiency factor  $e$  could be computed from the lift and drag coefficient at a given angle of attack, as

$$e = \frac{C_L^2}{\pi A C_D} \quad (4.46)$$

Computing this at an angle of attack of  $10^\circ$ <sup>4</sup>, for which  $C_L = 0.670$  and  $C_D = 0.0301$ , such that

$$e = \frac{0.670^2}{\pi \cdot 5.8 \cdot 0.0301} = 0.82 \quad (4.47)$$

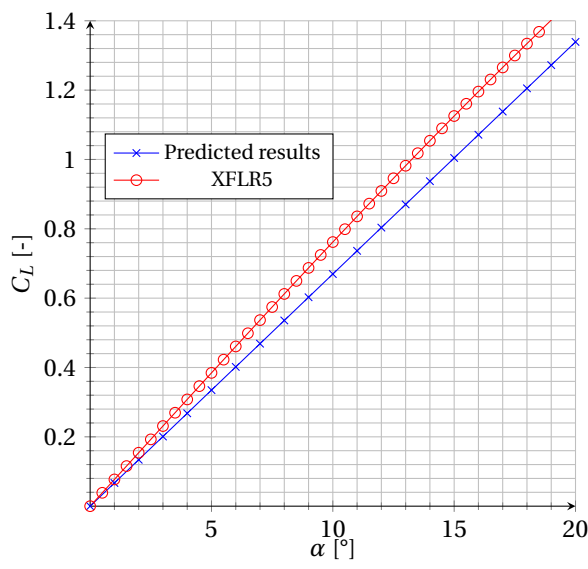
This compares well with the value that was estimated in [3], where it was estimated it would equal 0.79. Furthermore, the wing lift coefficient derivative w.r.t. aileron deflection was easily computed by computing the lift coefficient for a fixed  $\alpha$  at two different  $\delta_a$  and computing the slope;  $C_{M\delta_a}$  was similarly easily obtained.

An overview of the obtained aerodynamic properties is shown in Table 4.5.

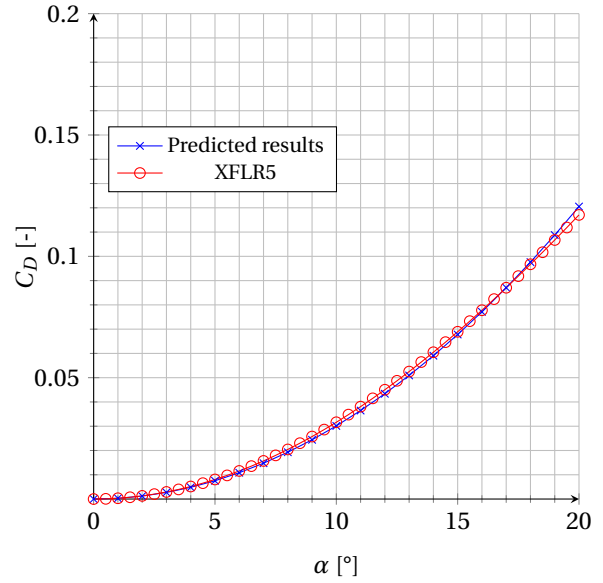
Parameter	Symbol	Value	Unit
Wing lift curve slope	$C_{L\alpha}$	3.836	$\text{rad}^{-1}$
Span efficiency factor	$e$	0.82	-
Wing lift coefficient derivative w.r.t. aileron deflection	$C_{L\delta_a}$	2.984	$\text{rad}^{-1}$
Wing moment coefficient derivative w.r.t. aileron deflection	$C_{M\delta_a}$	-0.7421	$\text{rad}^{-1}$

Table 4.5: Aerodynamic properties obtained by vortex ring method.

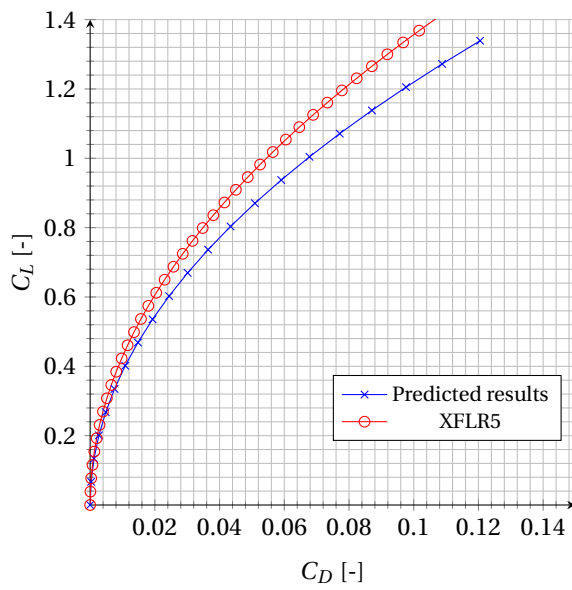
<sup>4</sup>It should be noted that this computation is independent from angle of attack.



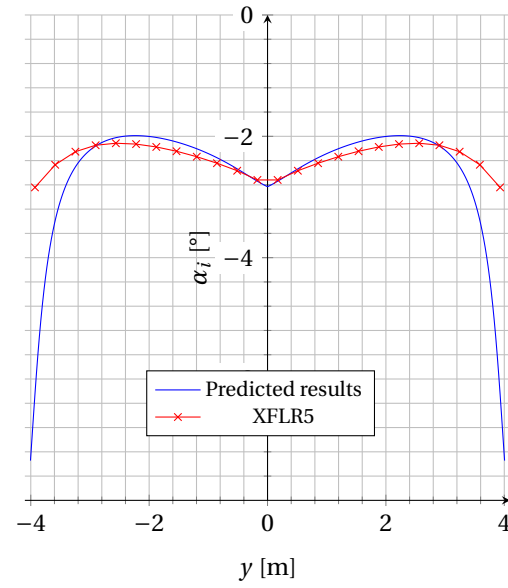
(a) Predicted  $C_L - \alpha$  of the main wing.



(b) Predicted  $C_D - \alpha$  of the main wing.



(c) Predicted  $C_D - C_L$  of the main wing.



(d) Predicted induced angle of attack variation over the span of the main wing.

Figure 4.12: Aerodynamic polars of the main wing.

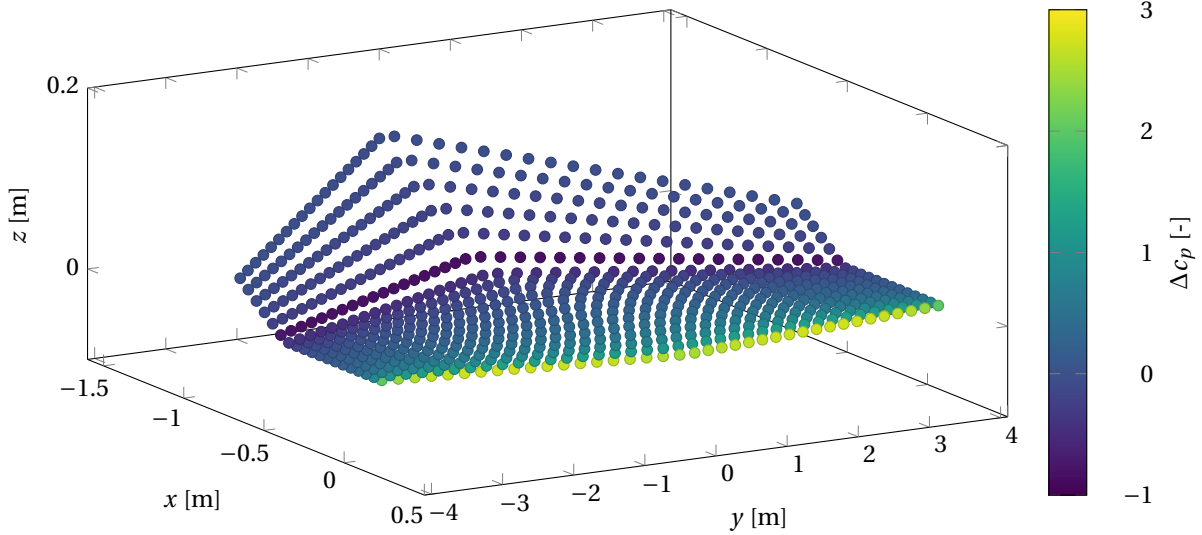


Figure 4.13: Pressure distribution over wing, with flaperons extended upwards at a deflection angle of  $10^\circ$ , at an angle of attack of  $10^\circ$ , at a freestream velocity of 80 m/s.

**Verification** The code was verified in various ways. First, many unit tests were performed in checking the calculations performed. The mesh generation and computations listed above are often simple steps that can, for simple cases, be checked by hand. Secondly, the code was verified by creating a wing with an aspect ratio of 100; the wing lift curve slope should then get close to  $2\pi$ . It was established that this is indeed the case. Thirdly, the code was verified by comparison with XFLR5 (using the inviscid 3D panel method), of which the results are shown in Figure 4.12. A very close match can be seen between the predicted results using the custom-built vortex panel method, and the results predicted by XFLR5. The only noticeable difference is in the lift coefficient and the induced angle of attack near the wing tips. These can arguably be attributed to the fact that a relatively coarse mesh was used for the XFLR5 results, namely on 24 panels in spanwise direction.

## 4.5 Aerodynamic Balancing

With the pressure distribution over the wing known, it was possible to do the aerodynamic balancing of the control surfaces in a relatively simple way, based on the control surface sizes described in Section 3.2.3 and with the desired hinge moments as will be described in Section 5.2. The general method can be described as follows: the force acting on each panel can be computed by

$$\mathbf{F}_{ij} = \Delta p_{ij} \mathbf{n}_{ij} \quad (4.48)$$

If the panel is part of the control surface, then the moment generated by this panel about the hingeline is simply given by

$$\mathbf{M}_{ij} = (\mathbf{x}_{ij} - \mathbf{x}_{\text{hingeline}}) \times \mathbf{F}_{ij} \quad (4.49)$$

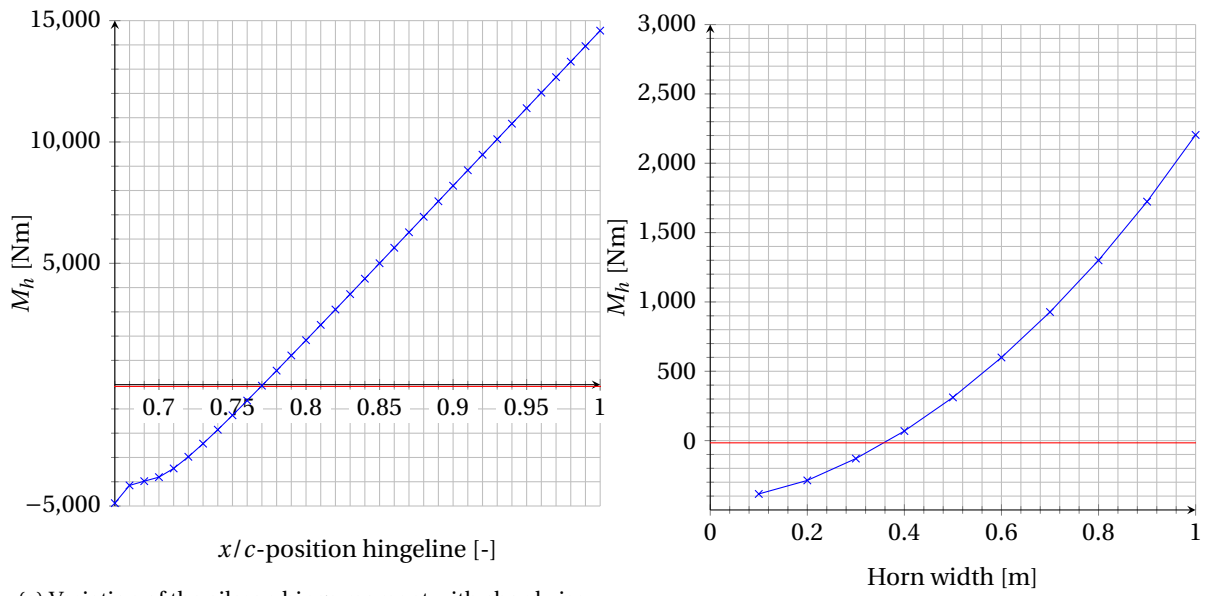
The total moment about the hingeline is then simply found by summing the individual contributions of the panels that are part of the control surface. The aerodynamic balancing can then straightforwardly be performed. All balancing has been performed at manoeuvring speed, at zero angle of attack, at standard sea-level conditions.

**Aileron** For the aileron, the variable that could be used for tuning of the aerodynamic moment was the position of the hingeline. It should be noted once more that it was found too challenging to write a program that allowed for an aileron that is constant in absolute length rather than constant in relative length. Thus, the aileron was modelled as having constant relative length, equal to the average aileron chord, equal to 33%. The hingeline was similarly assumed to be located at the same relative chord-position. The magnitude of the moment of the hingeline should equal about 72 Nm, as determined in Section 5.2, with the aerodynamic moment still being negative obviously. The aerodynamic moment acting on the hingeline as function of relative hingeline position is shown in Figure 4.14a. This led to a hingeline position of approximately  $x/c =$

0.763. However, this is arguably too far aft as it would probably mean the leading edge of the airfoil rise beyond the trailing edge of the main airfoil, which would likely result in unpredictable aerodynamic effects. Therefore, at further stages in the development of *StefX*, spades should be considered, such that the hingeline can shift further forward.

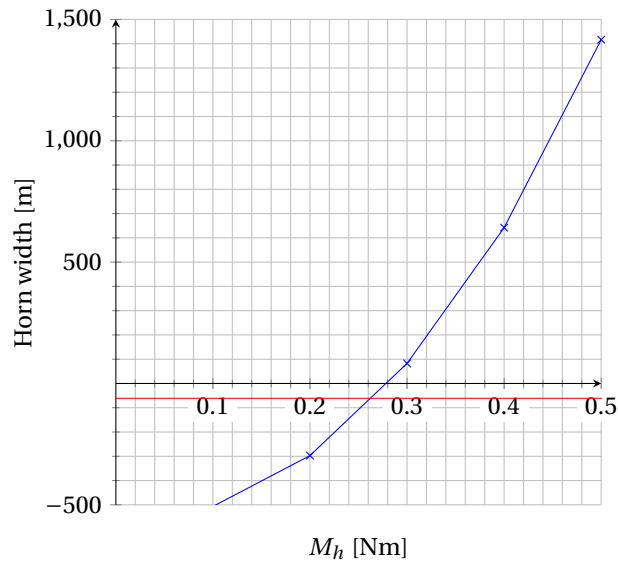
**Elevator** For the elevator, it was chosen to fix the hingeline to be  $0.1c$  aft of the leading edge of the elevator, and the variable that could be used for tuning the aerodynamic moment was the size of the horn. The effect of the horn width on the aerodynamic hinge moment is shown in Figure 4.14b. With the required moment equalling  $-16\text{ Nm}$ , it can be established that a horn width of approximately  $0.36\text{ m}$  ensures proper aerodynamic balancing of the elevator. As a means of visualisation, the pressure distribution over the horizontal tail, at an angle of attack of  $10^\circ$  with a downward elevator deflection of  $30^\circ$  has been plotted in Figure 4.15.

**Rudder** For the rudder, the exact same calculations were performed as for the elevator. Once again, the hingeline was placed  $0.1c$  aft of the leading edge of the rudder, and the horn size was altered to obtain desirable aerodynamic moments. The aerodynamic moment about the hingeline as function of horn size is depicted in Figure 4.14c. With the required moment equalling  $-62\text{ Nm}$ , it can be established that a horn width of approximately  $0.26\text{ m}$  ensures proper aerodynamic balancing of the rudder.



(a) Variation of the aileron hinge moment with chordwise hingeline position.

(b) Variation of the elevator hinge moment with horn width.



(c) Variation of the rudder hinge moment with horn width.

Figure 4.14: Aerodynamic hinge moment of the control surfaces.

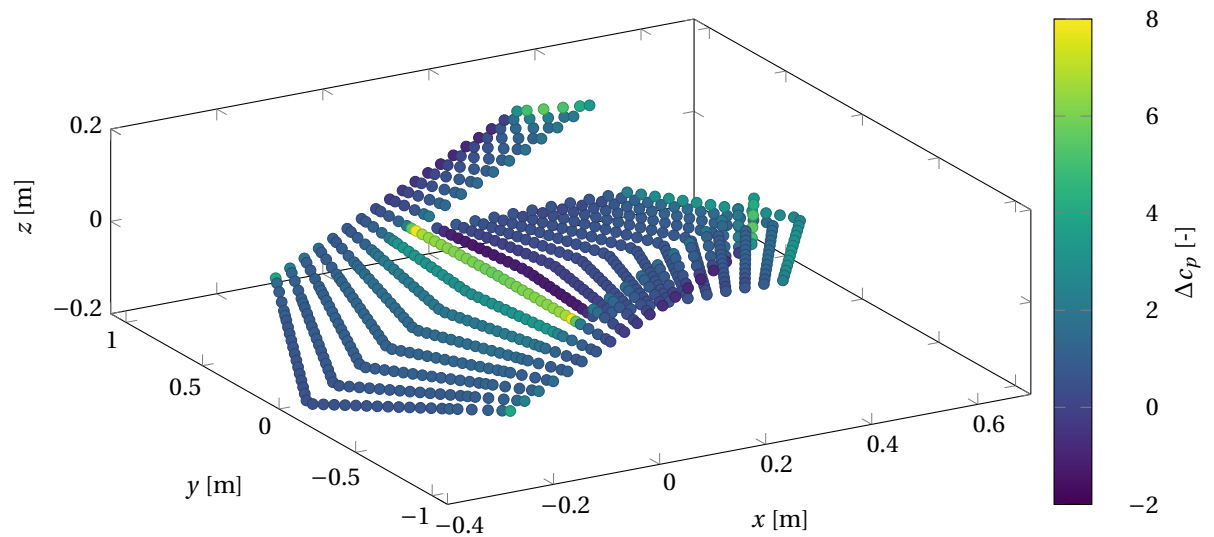


Figure 4.15: Pressure distribution over wing, with flaperons extended upwards at a deflection angle of  $10^\circ$ , at an angle of attack of  $10^\circ$ , at a freestream velocity of 80 m/s. Note that the wing is looked at from behind, i.e. the leading edge is located at positive  $x$ .

# Chapter 5

## Aircraft Systems

This Chapter describes all the aspects which the pilot has direct control over and their systems. In Section 5.1 the control methods and the seat is described. In Section 5.2 the linkages of the control surfaces and the maximum forces are calculated. In Section 5.3 the controls of the high lift devices are designed. In Section 5.4 the electrical system is described. In Section 5.5 the layout of the cockpit instruments is designed. Lastly, in Section 5.6 the fuel system of the *StefX* is designed.

### 5.1 Stick and Rudder

In order for the aircraft to be able to be controlled comfortably, the stick has to be designed in such a way that the forces are of a preset magnitude ratio. However, after looking for different sources and asking multiple pilots, the results were that the desired force distribution differs. For this reason, the decision was made to have the stick forces be adjustable. The stick will be attached to the floor of the fuselage. This will act as its hinge point. The rods will be attached to this, which are able to be moved during maintenance. This way, the customer can change the control force ratio of the stick to their liking. Upon delivery, the ratio of aileron force:elevator force:rudder force will be 1:2:3. The rudder force will stay the same, but the aileron and elevator force are adaptable by moving the attachment point on the stick up and down to tweak the relative forces.

**Stick and Seat** The stick and seat are sized using DINED [32] in order to make sure as many people can fit in the aircraft, the 5 percentile will be used as the minimum limit, and 95 percentile will be used as the maximum limit. The seat is designed in such a way that the minimum upper leg will be able to have their lower back on the back of the seat, while their knee cavity is still over the edge of the seat (457 mm). The seat is as broad as the maximum hip breath (447 mm), and as high as the maximum shoulder height (664 mm). Furthermore, the stick length above the seat is the medium elbow height plus the handle (252 mm). Also, the seat will incorporate a small indent at the right side of the pilot so the stick can be pulled back to the right lower corner without the seat blocking the elbow. The seat itself will be at a 15° inclination, while the back support is at an angle of 10° relative to the seat. The neutral position of the stick is at the middle of the control area. The basic control area is sized for the 50 percentile person. This area ranges from the abdominal depth (270 mm) to the far left corner for the arm length, with the left boundary at half of the forearm length past the left shoulder. This results in an area of 786 mm width by 373.6 mm length. This area can be adapted by moving the attachment points of the aileron and elevator on the stick. The stick will enter the cockpit from the tip of the seat, and curve towards the pilot with a radius of 1.29 m. A curve has been chosen because it gives more clearance than a straight line. When designing this seat it was made sure that it would be possible to escape the aircraft by parachute. An additional safety feature is the crash capability of the seat. The seat must collapse at 20 G while not deforming at 10 G. this is done with a honeycomb system which will collapse and create a crumple zone in order to take up some of the energy otherwise transferred to the pilot.

#### 20G Seat

$$F_{crit} = \frac{n^2 \pi E_s I}{l^2} \quad (5.1)$$

$$U = \int_0^{\epsilon_{max}} \sigma^* d\epsilon \quad (5.2)$$

$$E_{kin} = 0.5 m v^2 \quad (5.3)$$

**Rudder Pedals** The rudder pedals will be able to displace a total of 20 cm, and will be interlinked. The pedals will have a heel stand in order to be able to keep the feet on the pedals without giving inputs. The rudders will be mechanically movable to adjust for the length of the pilot. The pedals will also include toebrakes for the wheels. The pedals will be sized using the maximum foot size (279 - 106 mm).

## 5.2 Control Linkages

For precise control in all manoeuvres it is important for the linkages between the pilot and the control surfaces to be as direct and friction-free as possible. Small aircraft usually use cables and pulleys, but this introduces friction and play; friction from the contact of the cable with the pulley and play because of the limited stiffness of the components. For the rudder this is not a problem since there can be one cable in a straight line from each pedal to the rudder, which leaves only the stretch in the cable as play. This play is negligible for steel cable. For the aileron and elevator, however, the cables are replaced with pushrods. Since pushrods can be loaded in compression as well as tension, a single pushrod can be used for each surface instead of 2 cables, which improves the control feel. To ensure the most direct control feel possible, all rotating parts are mounted using ball bearings, which virtually removes any friction. The total layout of the system can be seen in Figure 5.1.

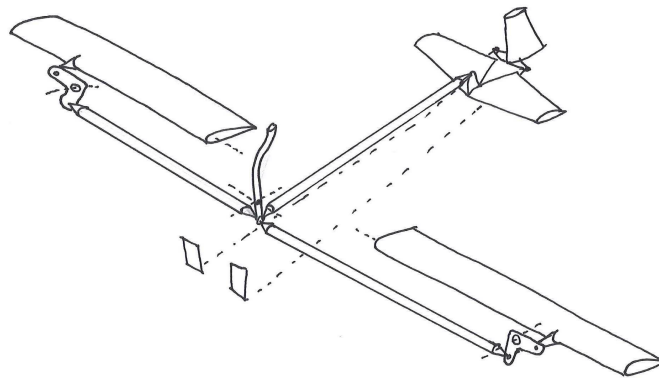


Figure 5.1: Control linkage layout.

**Hinge moment calculation** For the aerodynamic balancing in Section 4.5 as well as for the sizing of the pushrods and cables, it is necessary to determine the forces and moments in the system. For the roll force exerted by the pilot on the control stick, [15] specifies a maximum of 20 lbf for level 1 flying qualities. Combining this value with the desired 1:2:3 ratio for pitch:roll:yaw, this leads to the values for maximum force shown in Table 5.1. Using the stick length and deflections from Section 5.1, the maximum angular stick deflection was found to be 11.6° for pitch and 12.4° for roll. This means the hinge moments on the stick will be larger than the hinge moments on the control surfaces, which can deflect 30°. This factor is 2.6 for pitch and 2.4 for roll. Using these factors, the maximum hinge moments in Table 5.1 were found.

**Pushrod sizing** To determine the size needed for the pushrods, the forces need to be calculated. These were obtained using the maximum forces found above combined with the stick length (from the hinge to the pilot's hand) and pedal movement. To account for different settings of the adjustable control surfaces as well as different pilots' handling of the aircraft, a safety factor of 5 was used in sizing the pushrods. It was found that the critical failure mode of the pushrods is buckling. This is as expected, as the pushrods are long slender cylinders. Therefore, the rods were sized based on the minimum buckling strength to withstand the forces determined above. Euler's formula for the critical buckling load of pin-ended columns was used:

$$P_{cr} = \frac{\pi^2 EI}{L^2} \quad (5.4)$$

Using this analysis, it was chosen to use carbon fibre as the material for the pushrods. To validate the use of Euler's formula for carbon composite tubes, results from literature were used. Research on this exact subject [7] found that this method is still extremely accurate, even for these complex materials. For safety and ease of manufacturing, the aileron and elevator pushrods have the same diameter and thickness. This was sized using the aileron, as it experiences higher loads. The results of the analysis on control surfaces can be found in Table 5.1.

	Value	Unit
Aileron max stick force	89	N
Elevator max stick force	46	N
Rudder max pedal force	133	N
Aileron max hinge moment	73	Nm
Elevator max hinge moment	16	Nm
Rudder max hinge moment	46	Nm
Force on aileron pushrod	254	N
Force on elevator pushrod	127	N
Force in rudder cables	267	N
Pushrod diameter	30	mm
Pushrod wall thickness	3	mm
Rudder cable diameter	5	mm

Table 5.1: Results of the control linkage analysis.

### 5.3 High Lift Device Control and Operation

The High Lift Devices (HLDs) will be controlled in different ways. Both the Leading Edge High Lift Devices (LEHLDs) and flaperons will be controlled using electrical actuators, however, the cockpit control is different.

**LEHLDs** If the CFD analysis shows that no actuation system is required for deployment and retraction, a simple locking mechanism will be installed in the wing. The mechanism will lock the slats either in deployed or retracted position. This gives the pilot full control over the slat deployment and will avoid unwanted deployment or retraction during certain aerobatic manoeuvres that would generate sufficient suction or pressure force on the slat. If an actuation system would be required, the slats will be connected to linear electric actuators. To have equal forces and no moments in the plane of the wings on the slat, a torsion bar will be used to transfer the loads. The slats will deploy along a linear path. The circular movement of the torsion bar will be transformed to a linear movement using an interconnected rod, as can be seen in Figure 4.2c. Note that the rod directly connected to the slat is forced in a linear path. Since the available space in the wing is limited and three bars are needed to transform the rotary movement of the torsion rod to a linear movement, the length of all three bars was optimised such that the longest linear deflection can be obtained and the entire mechanism will fit into the leading edge of the wing. Due to the presence of the horn at the tip of the wing, it was assumed that the furthest linkage is at the location where the chord is 1.14m. This is thus the location where the entire system is designed to fit. The dimensions can be found in Table 5.2. A technical drawing of the slat system can be found in Appendix B. The actuation system has been taken into account in the electrical block diagram, as can be seen in Figure 5.5.

Rotary rod [m]	Middle rod [m]	Slat rod [m]	Torsion rod deflection [°]
0.078	0.104	0.111	86.3

Table 5.2: Slat actuation mechanism sizing inside wing.

A similar system is present in the fuselage to transform the linear movement of the actuator to a rotary movement of the torsion bar. The sizing of this system will depend on the deployment and retracting force needed. The forces to be delivered by the actuators inside the cockpit can be obtained using the principle of work. Based on the selected actuator force, the displacement needed can be found. Obtaining this data needed for sizing is however outside the scope of this project.

**Flaperons** To facilitate deployment of the flaperons, a slight alteration is made to the attachment of the pushrods to the stick. This alteration is shown in Figure 5.3. When the cables are in their neutral position, the aircraft behaves as usual since the pushrod attachments are at the height of the stick. When a cable is pulled however, the attachment plate rotates around the stick which moves both pushrods either in- or outward, thus extending the ailerons both up or both down, making them act as flaps. In this deflected position, aileron control is unaltered; moving the stick still moves one aileron up and the other down. What has changed is the neutral position of both.

Since the forces on the flaperons are considerable, these cables will be controlled by an electric actuator.

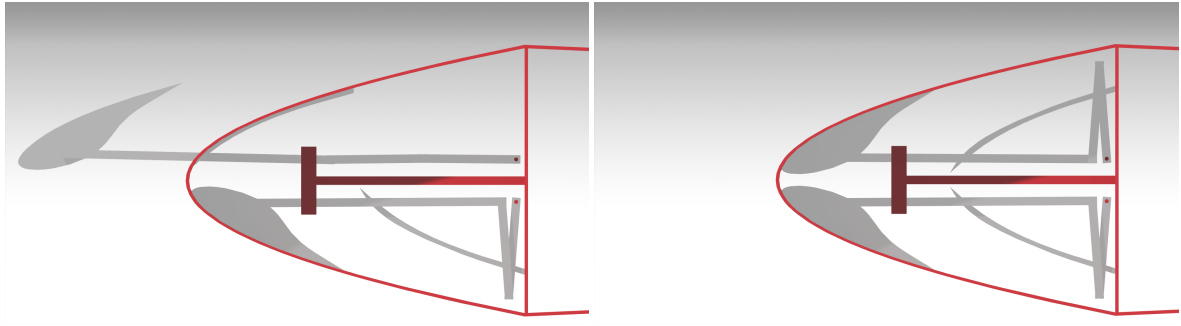


Figure 5.2: LEHLD deployment

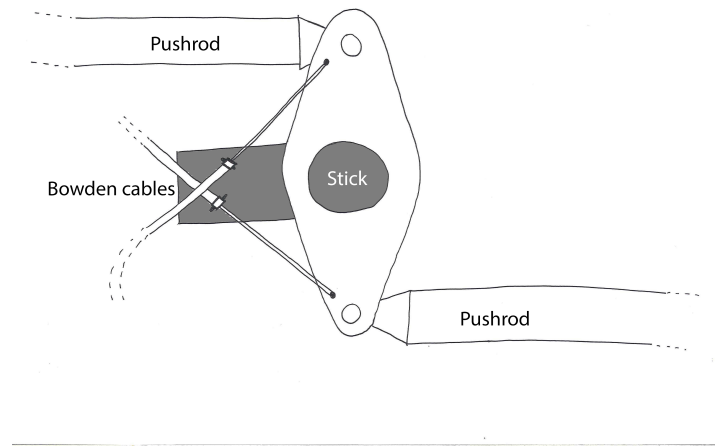


Figure 5.3: Flaperon actuation system.

**Operation** For aerobatic pilots, the use of HLDs is a new concept. Therefore an effort was made to make the operation as easy as possible. To determine the optimal way of activating the HLDs, their possible use cases were determined:

- Lower the stall speed for:
  - Level-off manoeuvres
  - Wider range of speeds
  - Take-off
  - (Emergency) Landing
- More aggressive pitch manoeuvres
- Stall on demand

Furthermore, it was determined that actuation of the lower slat (as seen by the airflow) is never desirable. Additionally, partial deflection of the LEHLDs is not useful in any case. Therefore, it was chosen to actuate the LEHLDs using a simple toggle button, which will be placed on the throttle to be actuated by the pilots thumb. A simple logic system will then determine which slat to deploy or retract, as well as whether the airspeed is low enough for actuation. This system will then also automatically retract the slats when the airspeed gets too high. For the flaperons, it can be useful to extend them partially or in reverse direction, partially to obtain a slight lift increase and in reverse direction to force the aircraft into a stall. To obtain this level of control without taking the hands off the throttle or the stick, it was chosen to control the flaperons by turning the throttle lever about the axis of the pilots lower arm. To prevent unwanted deployment, a slight break-out force will be implemented on the neutral position. To improve the comfort of the pilot, this neutral position will be a 45° angle. The system is shown in Figure 5.4.

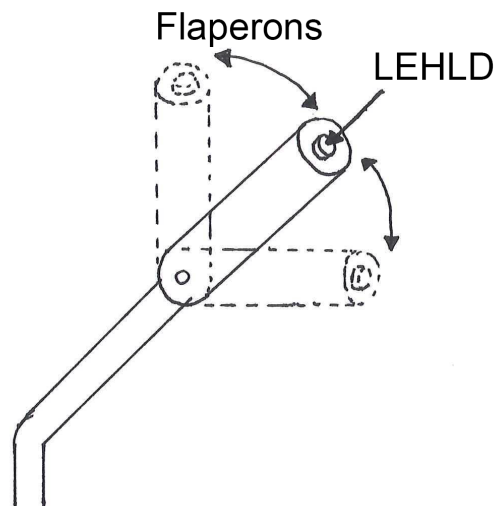


Figure 5.4: LEHLD pilot interface (throttle lever, pilot's view)

## 5.4 Electrical System

The electrical power of the aircraft is generated by a 14V alternator and a voltage regulator that regulates the voltage to 12V. The alternator will be driven by the engine. A 12V battery is installed behind the firewall to supply power to the critical systems in the event of an alternator failure in flight, possibly resulting from an engine failure. The aircraft is equipped with an external power system that provides the capability to start the engine independent from the internal battery. All the electrical circuits will be protected by circuit breakers which are installed in the cockpit. All switches and circuit breakers will be properly labelled and manufactured according to aeronautical regulations.

## 5.5 Cockpit Layout & Avionics

The equipment that the pilot will interact with apart from the flight controls, the avionics and other cockpit instruments, provide the pilot with key flight parameter as well as navigation and communication capability. In Figure 5.6 the proposed cockpit layout is shown. All of the equipment proposed is tabulated in Table 5.3 together with the estimated cost and mass.

On the top row, apart from the usual airspeed indicator and altimeter, a small PFD with airspeed and altitude tapes as well as attitude and skid/slip information and magnetic heading is installed. This provides the pilot with the approximate airspeed and altitude at a quick glance, as well as precise digital readouts when desired. A precise timer/clock is also installed for timed manoeuvres and to keep track of total flight time. Above the 3 main instruments, a digital bar graph G-meter that displays the current G-factor is installed with clear indications if the aircraft is approaching its maximum rated load factor. On the second row, a second G-meter that displays the value with dials, and also keeps track of both the maximum positive and negative load factor is installed. Next to the ARESTI card holder, two slip/skid indicators are installed which provide information to get a perfect coordinated turn both in normal and inverted flight. An analogue magnetic compass is also present as a backup to the electronic PFD. To the right, a sophisticated engine monitoring system is installed which monitors the CHT and EGT of each cylinder, as well as displaying Manifold Pressure, RPM, fuel flow, fuel quantity and battery voltage and charge/discharge current. This makes it really easy for the pilot to spot abnormal behaviour of the engine and monitor the fuel and electrical system. On the bottom row, the transponder and VHF radio are placed, together with the ELT control panel. Above it, the start/magneto key switch, master and alternator switch and toggle switches for lights, fuel pump, smoke system and avionics are installed.

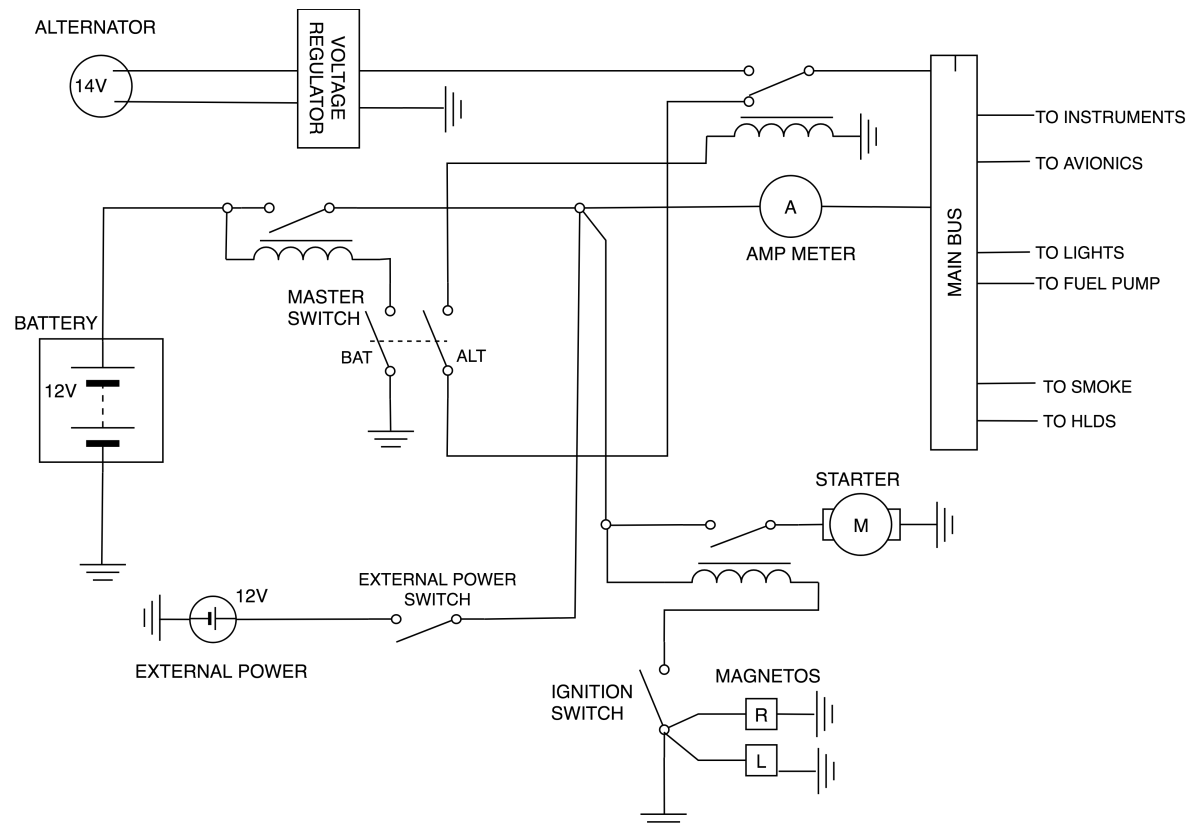


Figure 5.5: Electrical system diagram.

## 5.6 Fuel System

For aerobatic aircraft, the fuel system is slightly more complex than for regular general aviation aircraft. This is caused by two factors: the fuel system has to function in inverted flight as well as upright, and fuel tanks in wings cannot be used during aerobatic flight. This latter factor is caused by both a higher moment of inertia with fuel present in the wings, which is detrimental for rolling performance. Additionally, high roll rate manoeuvres would cause excessive stress on the outboard walls of wing fuel tanks. Therefore, fuselage fuel tanks are installed for aerobatic flight, while wing tanks are added to ensure sufficient range during ferry flight. To ensure fuel flow in all circumstances, several features are added:

- In the bottom of the fuselage an "acro tank" is added.
- A "flop tube" is installed in the acro tank.
- An electric booster fuel pump is added as a redundancy to the engine-driven fuel pump.

The acro tank is a small fuel tank which is gravity-fed from the main tanks. A valve in the feed hose prevents flow back into the main tanks. The acro tank is therefore always full as long as there is fuel in the main tanks. The flop tube is pictured in Figure 5.7. It is a flexible hose with a weight added to the end, which means the end moves with the fuel in inverted and even sideways flight, thus preventing any air to be sucked into the engine. The electric fuel pump supplies the engine with enough fuel for take-off power in case of a fuel pump failure in the engine-driven pump.

For the volumes of the tanks, the requirements for endurance in aerobatic flight and range in cruise, STX-SYS-13 and STX-SYS-14 were considered. For the aerobatic endurance requirement, full power fuel consumption was assumed for the entirety of the flight. According to [16], this is 142 lbs/hr, or 64.4 kg/hr in metric units. Combining this with the density of Avgas, the minimum fuselage fuel tank volume to reach the requirement is 50 L, including 5 L for warm-up, taxi and take-off. However, the fuselage is large enough to accommodate a larger tank, which improves the aerobatic endurance. This also reduces the risk of not meeting reserve fuel requirements in all countries, or if these requirements are changed in the future. Therefore, a fuselage tank of 75 L was chosen, as this allows for 20 minutes of aerobatic flight after take-off, with enough fuel at the end to cruise for 45 minutes.

For minimum volume of the wing tanks, the "economy cruise" engine setting from [16] was used. At this



Figure 5.6: Proposed cockpit layout.

setting, the fuel consumption is 14.0 Gal/hr, or 53 L/hr in metric units, and the power produced is 192 bhp. To find the range, the cruise speed has to be calculated. Since this is steady level flight, the condition to be found is one where the thrust produced equals the drag. Since the both thrust and drag are dependent on airspeed, finding the cruise speed is an iterative process. For the thrust, the calculations presented in 3.3 were used. For the drag, the value for  $C_{D_0}$  from 4.1 was used and combined with Equation 5.5 to obtain the total drag.

$$C_{D_i} = \frac{C_L^2}{\pi e A} \quad (5.5)$$

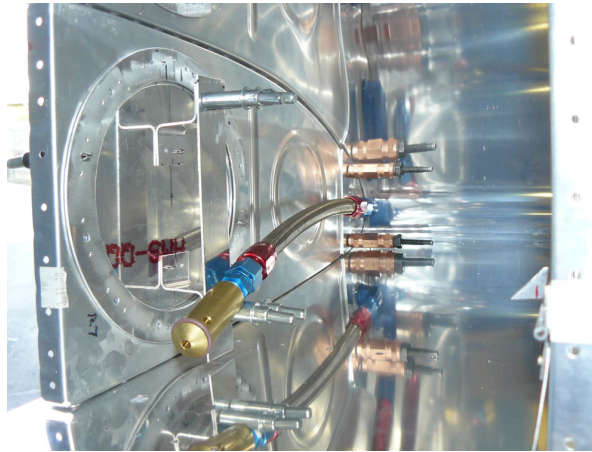
This iterative process resulted in a cruise speed of 83.3 m/s (161 kts). At this velocity, it takes 2.5 hours to reach the required 750 km cruise range. Using the 53 L/hr fuel consumption, this results in 132.5 L of fuel required for cruise. Adding the required fuel for 30 minutes at cruising altitude, the minimum fuel amount is 159 L. Taking into account the fuel in the fuselage tanks, the wing tanks need to hold at least 84 L of fuel. This requirement would be met by extending the wing tanks up to the first rib, which would give a volume of approximately 100 L. However, since it does not add a significant amount of weight, it was decided to let the tanks extend to the 2nd rib. The volume of the wing box for this length was calculated to be 230 L. Taking into account a 10 % margin to isolate the fuel from the carbon composite, this leaves 207 L. This extra fuel capacity allows for more comfortable cross-country flying, as fewer landings are needed to reach the destination. Additionally, the volume of these tanks is expected to decrease in the detailed design phase, and will be monitored throughout this phase. Having this extra volume means the risk of not meeting requirement STX-SYS-14 is almost nonexistent.

The emissions of 1 kg AVGAS 100LL is 3.17 kg  $\text{CO}_2$  [17]. With the cruise fuel flow of 53 L/h, this comes down to an emission of 121 kg  $\text{CO}_2$  per hour in cruise. This complies with the CS23 requirements of fuel emissions [5].

## 5.7 Safety

As a safety measurement, it is also very important that the pilot can egress the aircraft by parachute if necessary. When it would go wrong, the pilot has not much time to exit the aircraft. It is therefore of utmost importance that he can do so quickly. Therefore, the canopy will be equipped with handle to eject the canopy in flight. Furthermore, the seat belts will also be equipped with a quick release system. Both of the above

Item	Estimated cost [US\$]	Estimated mass [kg]
Airspeed indicator	540.00	0.25
Altimeter (hPa and InHg)	1,500.00	0.37
Compass	192.00	0.15
ELT	1,000.00	1.27
Engine monitor (E.I. MVP-50P)	6,000.00	0.86
G-meter (+/- 10 G analog dial with limit indicators)	460.00	0.30
G-meter (digital bargraph display)	500.00	0.25
GPS (Garmin Aero 695)	750.00	0.25
Garmin G5 Electronic flight instrument	2,149.00	0.38
Dual slip indicator (normal and inverted)	120.00	0.10
Timer (E.I. SC-5)	285.00	0.29
Transponder (Trig TT21)	1,325.00	0.46
Trim indicator (elevator)	100.00	0.15
VHF radio (Trig TY91)	2,000.00	0.44

Table 5.3: Cockpit equipment list.<sup>a</sup><sup>a</sup> <https://www.aircraftspruce.com/>Figure 5.7: Example of a flop tube. <sup>a</sup><sup>a</sup> <http://smilinpete.com/wp/?p=1034>

mentioned systems will give the pilot the chance to bail out of the aircraft and use his parachute to get safely back to the ground.

# Chapter 6

## Structural Design

In this chapter, the overall structural design of the *StefX* will be discussed. The materials used for the design were selected in Section 6.1. In Section 6.2, a structural analysis of the main wing was carried out and the resulting structure was iterated until an optimised configuration was obtained. The structural analysis methods used are based on Aircraft Structures for Engineering Students [31].

### 6.1 Material Selection

One of the first steps of the structural analysis of the *StefX* is the selection of the most suitable material. Before the best material can be determined, the most important properties need to be identified. The next step is to establish which materials are used in the aerospace industry and compare them on the aforementioned properties.

#### 6.1.1 Material Properties

The most relevant material properties need to be identified in order to find the most suitable material for the *StefX*. The *StefX* needs to have a mass as low as possible and needs to be very stiff, since this will limit the aeroelastic effects. It does not suffice to only look at the density, yield strength and E-modulus of the material, instead the material with the highest specific yield strength will be chosen. The same holds for the specific E-modulus and Shear-modulus of the material. If two or more materials have the same specific properties, but one is more sustainable than the other, the most sustainable option will be chosen.

#### 6.1.2 Aerospace Materials

In the aerospace industry lots of different materials are used, the most widely used are aluminum alloys, but also composites such as Glare, Carbon fiber epoxy, sandwich panels, titanium alloys and many more are used<sup>1</sup>. Each material has its own advantages and disadvantages. Titanium can resist heat up to a way higher temperatures than composites and aluminium alloys. However since only the wing boxes, the fuselage and the landing gear are being designed in this design phase, only composites and aluminium alloys are considered.

##### Aluminium Alloys

There are many different aluminium alloys that can be considered for use in aviation, however the most suitable and most used are the Al 7000 series. The aluminium alloy with the most desirable qualities is the Al 7075 T6. The properties of this material can be seen in Table 6.1

##### Composites

CES Edupack has a large database for composite materials. It is important to note that for the comparison quasi isotropic material properties will be used. The material used in the final design phase will also be assumed to be quasi isotropic. There are different possibilities for the fibres and for the resins. The two most commonly used fibres are carbon fibres and fibreglass. Fibreglass composites have a lower yield stress and are more ductile compared to carbon fibres. As a result it was chosen to use carbon fibre composites in the design. It was also determined that an epoxy resin would result in the best material for the design. The material properties for the epoxy/carbon fiber, uni-directional prepreg with quasi isotropic lay-up can be found in Table 6.1.

---

<sup>1</sup> <http://www.machinedesign.com/materials/basics-aerospace-materials-aluminum-and-composites>

Specific Property	Al7075 T6	Epoxy/Carbon	unit
Specific Yield-Strength	0.187	0.467	MPa · m <sup>3</sup> /kg
Specific E-modulus	26.86	38.0	MPa · m <sup>3</sup> /kg
Specific G-modulus	9.89	14.6	MPa · m <sup>3</sup> /kg
Price	4.03	41.6	USD/kg
End-of-life	40.5 – 44.7 % recyclable	Downcycle	-

Table 6.1: Specific properties of Aluminium 7075 T6 and Epoxy/Carbon fiber, uni-directional prepreg with quasi isotropic lay-up.

As can be seen, the specific properties of the carbon fibre composite are higher than those of the most suitable aluminium alloy as can be seen in Table 6.1. As a result *Epoxy/Carbon fiber, uni-directional prepreg with quasi isotropic lay-up* will be used in the final design of the *StefX*. A more elaborate overview of the properties of the chosen material can be seen in Table 6.2.

Property of the material	Value	Unit	Source
Density	$1.58 \cdot 10^3$	kg/m <sup>3</sup>	[14]
Young's modulus	60.1	GPa	[14]
Yield strength	738	MPa	[14]
Elongation	0.35	% strain	[14]
Compressive modulus	60.1	GPa	[14]
Compressive strength	657	MPa	[14]
Shear Modulus	23	GPa	[14]
Shear Strength	60	MPa	<sup>a</sup>
Price	41.6	USD/kg	[14]

Table 6.2: Properties of the chosen material: Epoxy/Carbon fiber, uni-directional prepreg with quasi isotropic lay-up.

<sup>a</sup> <http://www.acpsales.com/upload/Mechanical-Properties-of-Carbon-Fiber-Composite-Materials.pdf>

However, when performing the structural analysis of the landing gear strut, the high stiffness of the epoxy/carbon fibre was an issue, since it would not provide adequate damping when the aircraft would hit the ground at a relatively high vertical speed. As a result a more ductile material was chosen for this part of the aircraft. In general aluminium alloys are more ductile than carbon fibre, thus the Aluminium 7075 T6 alloy was considered, however, since the landing gear is a small part of the aircraft when compared to the wings or to the fuselage, it would be better from an economic point of view to not use an alloy if possible, since this will increase the equipment cost or the part should be made externally. Fortunately there are sufficient composites that are more ductile than the epoxy/carbon fibre and can be manufactured without the special equipment needed to manufacture metal parts. From CES Edupack, it was determined that the epoxy/S-glass fibre, UD prepreg, QI lay-up had more suitable qualities for the use as landing gear legs compared to the epoxy/carbon fibre. The properties of this material can be seen in Table 6.3.

Property of the material	Value	Unit	Source
Density	$1.97 \cdot 10^3$	kg/m <sup>3</sup>	[14]
Young's modulus	21	GPa	[14]
Yield strength	504	MPa	[14]
Elongation	2.6	% strain	[14]
Compressive modulus	21	GPa	[14]
Compressive strength	312	MPa	[14]
Price	19.6	USD/kg	[14]

Table 6.3: Properties of Epoxy/S-glass fibre, UD prepreg, QI lay-up.

## 6.2 Structural Analysis

In this section the method used to perform the structural analysis of the wing box of the main wing, horizontal tail and vertical tail is explained, as well as the method used for the fuselage and landing gear. First the

structural analysis of the wing box of the main wing and of than later wing boxes of the horizontal and vertical tail is discussed in Subsection 6.2.1.

### 6.2.1 Structural Analysis of the Wing

There are two kinds of stresses acting on the wing box of the *StefX*, the first one is normal stress and is generated by the bending moment caused by the normal and the tangent force of the wing surface. The second type is shear stress caused by torsion and due to the normal and tangent force acting as shear forces. In order to have a thorough structural analysis the effect of both stresses will need to be analysed. It was chosen that a classic wing box was the best option for the *StefX*.

#### Moment of Inertia of the Wing

In order to obtain a stiff wing box structure capable of withstanding high loads, which will result in large normal and shear stresses, the second moment of area of the wing box sections must be sufficiently large. In order to achieve this, a basic wing box design layout was chosen with 2 spars, a thick enough skin to carry the shear stresses and stringers to increase the moment of inertia. With the basic layout known, the moment of inertia of each section can be analysed based on the dimensions of the wing profile, number and dimensions of the stringers and locations and thicknesses of the two spars.

First, the base inertia's for the Z-stringers, spars and skins were calculated using Equations (6.1) and (6.2). In order to take into account the rotation of the Z-stringers when they are placed on a curved surface like the top side of the skin, an axis transformation is performed (See Figure 6.1) using Equations (6.4), (6.5) and (6.6). Since the wing box cross section is symmetrical about the horizontal axis,  $I_{xy}$  of the entire wing box will be zero. All of the separate inertia's are then referenced to the centroid of the wing box using the parallel axis theorem (6.3).

$$I_{xx} = \frac{b_{str} \cdot h_{str}^3}{12} + A_s tr \cdot y_c^2 \quad (6.1)$$

$$I_{yy} = \frac{b_{str}^3 \cdot h_{str}}{12} + A_s tr \cdot x_c^2 \quad (6.2)$$

$$\begin{aligned} I_{x'x'} &= I_{xx} + A \cdot y_c^2 \\ I_{y'y'} &= I_{yy} + A \cdot x_c^2 \end{aligned} \quad (6.3)$$

$$I_{uu} = \frac{I_{xx} + I_{yy}}{2} + \frac{I_{xx} - I_{yy}}{2} \cos(2\phi) - I_{xy} \sin(2\phi) \quad (6.4)$$

$$I_{vv} = \frac{I_{xx} + I_{yy}}{2} - \frac{I_{xx} - I_{yy}}{2} \cos(2\phi) + I_{xy} \sin(2\phi) \quad (6.5)$$

$$I_{uv} = \frac{I_{xx} - I_{yy}}{2} \sin(2\phi) + I_{xy} \cos(2\phi) \quad (6.6)$$

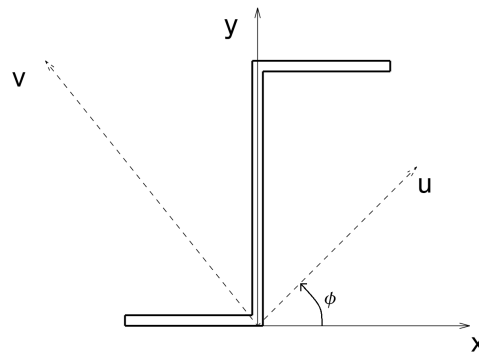


Figure 6.1: Z-stringer axis transformation.

The moment of inertia calculations were verified by drawing a simplified wingbox model in CATIA and using the built in inertia measuring tool. The value from CATIA only deviated 2 % from the calculations, making it safe to assume the method used is valid.

### Wing Loading

To calculate all the stresses in the wing, it is necessary to know for every span-wise location all the forces and moments that act on that specific point. All the calculations are based on the aerodynamic properties of full aileron deflection at never exceed speed as this would be the most extreme load case. It is chosen to calculate all the forces and moments that act on the wing around the 25% chord-wise location as all the aerodynamic wing properties from Chapter 4 are calculated around that point.

The forces and moment calculations are performed by dividing the wing up in span-wise direction with equal spacing into a number of sections. The surface area  $S_i$  of the sections is calculated by multiplying the spacing distance with the average chord length  $c_i$  of that specific section. Together with the aerodynamic coefficients  $c_t, c_n, c_m$  from Chapter 4 and the manoeuvring conditions from Chapter 9 the normal, tangential and moment forces for each section are calculated using Equation (6.7). These equations cannot be used for the entire wing span however, as it is assumed that the wing does not produce any forces or moments anymore once it goes into the fuselage.

$$\delta N_{W_j} = \frac{C_n \rho V^2 S_j}{2} \quad (6.7a)$$

$$\delta T_{W_j} = \frac{C_t \rho V^2 S_j}{2} \quad (6.7b)$$

$$\delta M_{W_j} = \frac{C_m \rho V^2 S_j c_j}{2} \quad (6.7c)$$

To calculate all the specific forces and moments at one specific location, all the forces and moments of the previous sections have to be summed up as shown in Equation (6.8) where  $z$  equals the spanwise location.

$$N_{W_i} = \sum_{j=0}^i \delta N_{W_j} \quad (6.8a)$$

$$T_{W_i} = \sum_{j=0}^i \delta T_{W_j} \quad (6.8b)$$

$$M_{W_i} = \sum_{j=0}^i \delta M_{W_j} \quad (6.8c)$$

To calculate the bending moment due to the tangential and normal forces for a specific spanwise location, the lift of each section outboard of that point is multiplied with the moment arm from the centre of that section to the point the moment is calculated around  $r_j$ .

$$M_{N_i} = \sum_{j=0}^i \delta N_{W_j} \cdot r_j \quad (6.9a)$$

$$M_{T_i} = \sum_{j=0}^i \delta T_{W_j} \cdot r_j \quad (6.9b)$$

As the aerodynamic forces are not able to produce 20G at never exceed speed, the tangential forces of both wings at root are multiplied by a factor such that they are 20 times the MTOW. The formula to calculate this equation is shown in Equation (6.10) This factor is also multiplied with the normal forces and the moment in order to simulate a 20G load case.

$$F_{20G} = \frac{20 \cdot g \cdot MTOW}{2T_{W_r}} \quad (6.10)$$

### Stress Calculation of the Wing

The two principal stress acting on the wing box should be analysed for a complete structural analysis. First the normal stress was determined. This stress is caused by the bending moment that is a result of the normal and tangent force acting on the wing box. As a result the general equation for bending can be used in order to

determine this. There are no pure tensile or compressive loads acting on the wing box, and will thus not cause any normal stress. The general equation for bending can be seen in Equation (6.11). Due to the symmetry of our wing box, the term  $I_{xy}$  is equal to zero and this simplifies the equation extensively. The moments of inertia found in Subsection 6.2.1 can be plugged in to this equation and this will result in the normal stress distribution over the a cross section of the wing. Needless to say,  $\sigma_{zs}$  must not exceed the yield strength of the material found in Table 6.2. However, due to the fact that the structure is experiencing both normal and shear stress, a more strict criterion is set and is elaborated on in Subsection 6.2.1.

$$\sigma_z = -\frac{M_y I_{xx} - M_x I_{xy}}{I_{xx} I_{yy} - (I_{xy})^2} x - \frac{M_x I_{yy} - M_y I_{xy}}{I_{xx} I_{yy} - (I_{xy})^2} y \quad (6.11)$$

$$\sigma_z = -\frac{M_y}{I_{yy}} x - \frac{M_x}{I_{xx}} y \quad (6.12)$$

The second stress acting on the wing box cross section is shear stress. The method to determine the shear flow is more extensive. In the final stage of these calculations the shear stress will be calculated from the shear stress. The shear flow is caused by both the torque acting on the wing as by the shear forces. First, the shear flow caused by the shear forces will be analysed. After that, the shear flow caused by the torque will be calculated. The combination of both will result in the final shear flow distribution. Both the normal and tangent forces are causing a shear flow. Due to symmetry it can be determined that the tangent force acts through the shear centre. As a result the tangent force will not induce any torque, with resulting torque on the cross-section.

To start off, an imaginary cut needed to be made somewhere in the cross section, preferable at the axis of symmetry. This will allow the cross section to be analysed as an open section. As a corrective measure the correcting shear flow will need to be calculated. The cut was chosen to be at the crossing of the chord line and the most forward spar, this point is referred to as point 1 in Figure 6.3. Then the base shear flow for each section could be evaluated, as can be seen in Equation (6.13). This further simplifies to Equation (6.14) due to symmetry. The subscripts  $ij$  denote respectively the beginning and end points of every part of the cross section. The cross section is divided into 5 section that can be seen in Figure 6.3. Note that  $q_{ij}$  will need to be evaluated for all sections of the cross section.

$$q_{ij} = -\frac{S_x I_{xx} - S_y I_{xy}}{I_{xx} I_{yy} - (I_{xy})^2} \left( \int_0^{s_i} t \cdot x \cdot ds + \sum_{r=1}^n B_r \cdot x_r \right) - \frac{S_y I_{yy} - S_x I_{xy}}{I_{xx} I_{yy} - (I_{xy})^2} \left( \int_0^{s_i} t \cdot y \cdot ds + \sum_{r=1}^n B_r \cdot x_r \right) \quad (6.13)$$

$$q_{ij} = -\frac{S_x}{I_{yy}} \left( \int_0^{s_i} t \cdot x \cdot ds + \sum_{r=1}^n B_r \cdot x_r \right) - \frac{S_y}{I_{xx}} \left( \int_0^{s_i} t \cdot y \cdot ds + \sum_{r=1}^n B_r \cdot x_r \right) \quad (6.14)$$

However, when determining the location of the shear centre, only the shear flow caused by the normal force will need to be taken into account. Subsequently, a distinction will be made between the shear flow caused by the normal force and by the tangent force. This will be named  $q_{ijN}$  and  $q_{ijT}$  respectively. Both shear flows were calculated. Now, for the moment caused by the shear flow around the aerodynamic centre, only  $q_{ijN}$  needs to be evaluated. The forces caused by the shear flow can be determined using Equation 6.15. In order to compute the moment,  $M_{ac}$ , the force  $F_{ij}$  will need to be multiplied by the distance between the force vector and the aerodynamic centre. This moment,  $M_{ac}$  will allow to calculate the location of the shear centre, see Equation (6.16), which can later be used to determine the twist of the wing box in Subsection 6.2.1.

$$F_{ij} = \int_0^l q_{ijL} ds \quad (6.15)$$

$$e = \frac{M_{ac}}{S_y} \quad (6.16)$$

The following step is to calculated the correcting shear flow using Equation (6.17), which than further simplifies to Equation (6.18), since our material properties, such as G, do not differ. The correcting shear flow will be need to be calculated for both  $q_{ijN}$  and  $q_{ijT}$ . This will result in respectively  $q_{s,0N}$  and  $q_{s,0T}$ .

$$q_{s,0} = - \frac{\oint \frac{q_{ij}}{t} ds}{\oint \frac{ds}{t}} \quad (6.17)$$

$$q_{s,0} = - \frac{\oint \frac{q_{ij}}{t} ds}{\oint \frac{ds}{t}} \quad (6.18)$$

Additionally to the shear flow caused by the normal and tangent forces, there is also a shear flow caused by the torque action on the wing. This can simply be calculated using Equation (6.19).

$$q_{torque} = \frac{M}{2A_{enclosed}} \quad (6.19)$$

The final shear flow is the sum of all previously computed shear flows, which results in  $q_{final_{ij}}$ , the final shear flow acting on a section on a part of the wing box, and is expressed in Equation (6.20).

$$q_{ij_{final}} = q_{torque} + q_{i_{jN}} + q_{i_{jT}} + q_{s,0N} + q_{s,0T} \quad (6.20)$$

In Equation 6.20,  $q_{ij_{final}}$  is the shear flow at a certain location along section  $ij$ . However, this still needs to be converted to the actual shear stress acting on the cross section. This can simply be done by dividing the the final shear flow over the local thickness, as can be seen in Equation 6.21.

$$\tau_{ij} = \frac{q_{ij_{final}}}{t} \quad (6.21)$$

Now the final shear stress is calculated and can be used for the failure analysis using the Tsai-Wu failure criterion. Due to the way the failure criterion is set up, the actual shear stress is dissolved in too shear stress in  $x$ -direction and  $y$ -direction, using the axis system introduced in Figure 6.3. The dissolved  $\tau_{ij}$  terms in  $x$  and  $y$ -direction will be respectively be referred to as  $\tau_{ijx}$  and  $\tau_{ijy}$ .

The wing is discretised in spanwise direction into smaller sections. For each of these sections the aforementioned analysis is performed. All spanwise sections have a slightly different geometry due to the fact the aileron has a constant chord and will this cause the geometry to change spanwise. The number of stringers also varies along the cross-section. If the structural analysis determines the structure is oversized past a certain span, one or multiple stringers can be removed. This will reduce the weight of the structure. The effect of the taper was also investigated, and the correction factor is shown in Equation 6.22. The symbols are explained in Figure 6.2. However, due to the fact that the largest local sweep,  $\Lambda_{local}$ , is less then  $15^\circ$  the small angle assumption is valid, and will result in a deviation less then 2 %.

$$\sigma'_z = \frac{\sigma_z}{\cos(\Lambda_{local})} \quad (6.22)$$

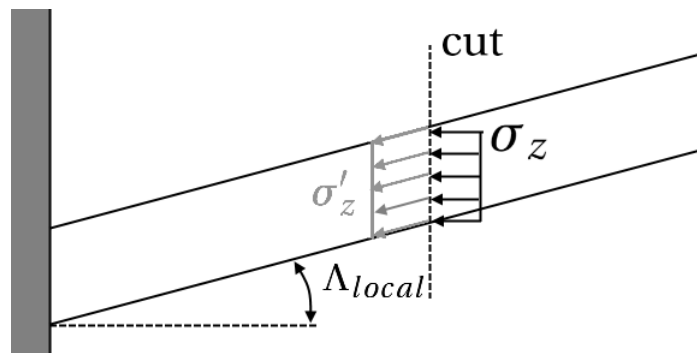


Figure 6.2: Effect of normal stress due to taper.

### Torsion

The rate of twist is determined relatively easy and can be seen in Equation (6.23). The integrals are again evaluated for all sections, as can be seen in Figure 6.3 The resultant torque acting on a section is determined with Equation (6.24).

$$\frac{d\theta}{dz} = \frac{T}{4 \cdot A_{enclosed}^2 G} \oint \frac{ds}{t} \tag{6.23}$$

$$\text{with } T = M + \epsilon \cdot L \tag{6.24}$$

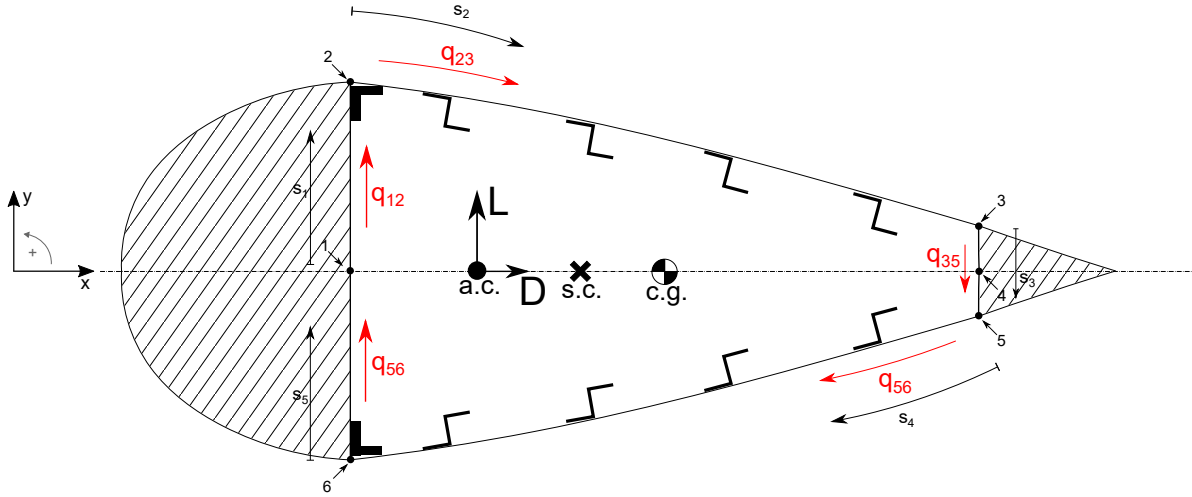


Figure 6.3: Schematic representation of a wing box.

### Tsai-Wu Failure Criterion

In order to make sure the loads acting on the aircraft will not cause structural failure, it needs to be checked with the Tsai-Wu failure criterion for non-isotropic materials. This failure criterion holds for composites, such as the one used in the design of the *StefX*. The failure criterion can be found in Equation (6.25). For a material that is in-plane quasi isotropic, the  $F$ -terms can be calculated using Equations (6.26). This  $F$ -value shall be smaller than zero, if not, failure occurs. A conservative approximation of  $F_{12}$  is shown in Equation (6.27) according to [29]. The nomenclature used for the stresses acting on an arbitrary body are graphically explained in Figure 6.4.

$$F = F_{11}\sigma_1^2 + F_{22}(\sigma_2^2 + \sigma_3^2) + (2F_{22} - F_{44})\sigma_2\sigma_3 + 2F_{12}\sigma_1(\sigma_3 + \sigma_2) + F_1(\sigma_1 + \sigma_2) + F_2\sigma_3 + F_{44}\tau_{23}^2 + F_{66}(\tau_{13}^2 + \tau_{12}^2) \tag{6.25}$$

$$F_{11} = \frac{1}{\sigma_{1t}\sigma_{1c}} \tag{6.26a}$$

$$F_{22} = \frac{1}{\sigma_{2t}\sigma_{2c}} \tag{6.26b}$$

$$F_1 = \frac{1}{\sigma_{1t}} - \frac{1}{\sigma_{1c}} \tag{6.26c}$$

$$F_2 = \frac{1}{\sigma_{2t}} - \frac{1}{\sigma_{2c}} \tag{6.26d}$$

$$F_{44} = \frac{1}{\tau_{23}^2} \tag{6.26e}$$

$$F_{66} = \frac{1}{\tau_{12}^2} \tag{6.26f}$$

$$F_{12} = \frac{-1}{2} \sqrt{F_{11}F_{22}} \tag{6.27}$$

### Stress Distribution of the Main Wing

In Figures 6.5 and 6.6 the normal stress distribution can be seen respectively on the top and bottom side of the wing. If a data point is green it indicates (barely) no normal stress is present. If a data point has a red colour, it is under tension, and a blue or purple colour when it is under compression. In the aforementioned

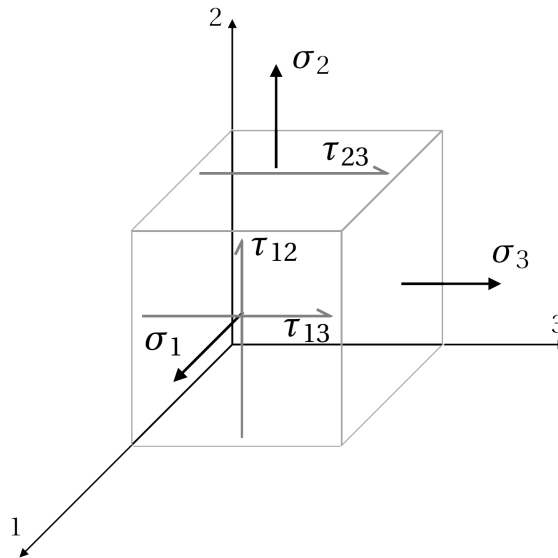


Figure 6.4: Effect of normal stress due to taper.

figures it can be seen that no data point reaches the maximum compressive or tensile stress as can be found in Table 6.2. This is due to the fact that the shear stress is the most determining for the design of the wing box.

In Figures 6.7 and 6.8 the F-value for the Tsai-Wu failure criterion is plotted. As discussed in Subsubsection 6.2.1, this F-value may not be greater than 1. If the data point has a yellow colour, the associated F-value is close to zero, meaning there are barely any stresses acting on this point. If the data point is dark blue, the associated F-value will be larger than 0.6. It can be seen that nowhere across the top or bottom skin of the wing, the F-value will reach the maximum allowed value of 1. In fact the F-value never exceeds 0.6. It was chosen to implement such a large safety factor, because stress concentrations will occur and are not yet analysed in this stage of the design.

### Horizontal and Vertical Tail

The same method as explained above can be used for both the horizontal and vertical tail. The geometry of these structures will be different but the method applied will be the same.

### Results of Structural Analysis of the Main Wing, Vertical and Horizontal Tail

Using the above explained methods, the structure of the aircraft was determined. The results can be found in Table 6.4.

## 6.2.2 Structural Analysis of the Fuselage

After the wings, the fuselage is statistically the second most heavy structural component of an aerobatic aircraft. In almost all aerobatic aircraft, including the EXTRA 330SC, the loads of the fuselage are carried by a steel truss structure as shown in Figure 6.9<sup>2</sup>. Although this is a proven concept, the design of *StefX* has an innovative monocoque fuselage. This means that, contrary to the EXTRA 330SC where the steel structure carries all the loads and the plastic shell provides the aerodynamic properties, in the design of *StefX* the skin will be made of carbon composites and will carry all the loads. This results in a large weight reduction, improving the performance of *StefX*.

The structural analysis of the fuselage is done by structural idealisation. For the structural idealisation it is assumed that the cross section of the fuselage consists out of four booms as seen in Figure 6.10. For the sizing of the fuselage a cylinder with a certain ratio and taper was assumed. However, to simplify the calculations without under-designing the fuselage, the cross section of the fuselage is assumed to be a square within that circle as seen in the figure. Another simplification is to divide the fuselage in three sections as shown in Figure

<sup>2</sup>URL url<https://grabcad.com/library/extra-300-fuselage-2>

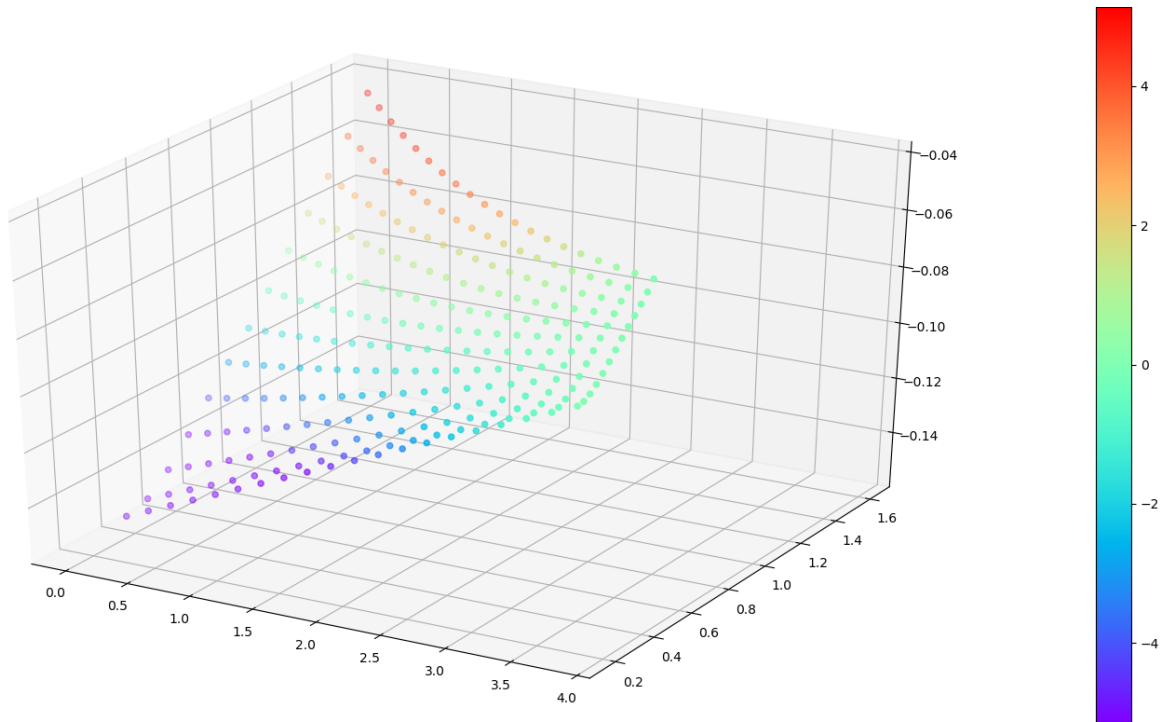


Figure 6.5: Normal stress distribution for Top side of the wing. Unit of the colour scheme is given in 10 MPa.

6.11. The first section is a simple closed box structure with fixed dimensions, the second section has a cut-out and still has fixed dimensions, and the third section is closed box structure with taper. Again, to avoid under estimation of the stresses the dimensions of the first and the second section are set to be equal to the dimensions at the end of the second section of the initial sizing of the fuselage.

### Moment of Inertia of the Fuselage

To calculate the area moment of inertia for a structurally idealised structure, first the boom areas have to be calculated using Equation (6.28) [31]. This equation simplifies as  $\sigma_j/\sigma_i$  equals 1, because the double symmetric geometry of the cross-section. Then, using only the Steiner term of Equations (6.1) and (6.2) the moment of inertia is calculated as the location of the centroid is already known due to symmetry. At the cut-out the moment inertia is held constant with the value of the full box as it is assumed that the access material will be located at the edge of the cut-out. At the taper a new moment of inertia is calculated at each new cross-section of the simulation, however any other effects due to taper can be neglected due to the small angle approximation ( $10^\circ$ ).

$$B_i = \frac{t_D b_f}{6} \left( 2 + \frac{\sigma_j}{\sigma_i} \right) \quad (6.28)$$

### Loading of the Fuselage

The loading of the fuselage is quite complicated with the free body diagram drawn in Figure 6.11. To analyse the stresses in the fuselage, the fuselage was divided into two sections, with a cut made right at the starting point of the cut-out between the first and the second section. It was assumed that the deflection at this point is zero, because the centre of gravity is located less than 20 cm from this location. The forces and moments introduced into the fuselage are the forces of the engine, including the thrust  $T$ , the weight  $W$  and the gyroscopic moments  $M_{gy}$ ,  $M_{gx}$ ,  $M_{gz}$ . Furthermore the wing exerts a tangential force,  $T_W$  and a normal force,  $N_W$ , together with a moment  $M_{cz}$ . The horizontal stabilisers exert a substantial tangential force,  $T_{HT}$ , and normal force,  $N_{HT}$ , on the fuselage. Lastly the tangential force of the vertical tail plain,  $T_{VT}$ , introduces a torsion force on the fuselage due to the offset  $y_{VT}$ . Although there are obviously other forces and moments acting on the fuselage, for example the normal force of the vertical tail, it is chosen to exclude these from the free body diagram because of their relatively small magnitude and to keep the calculations clear.

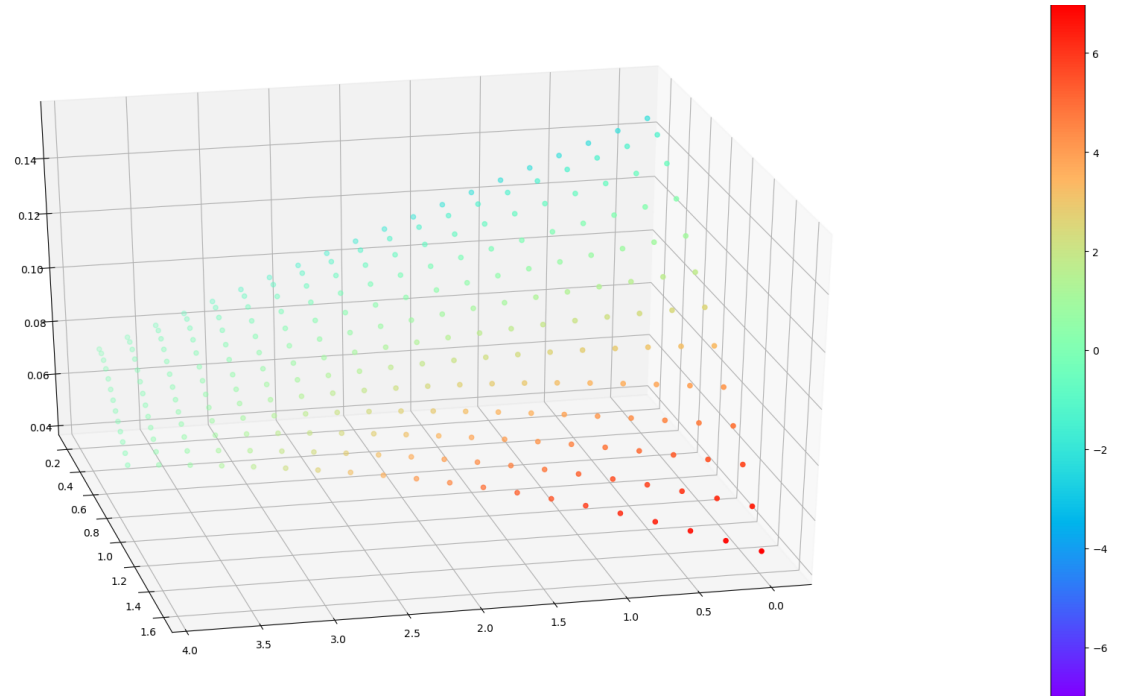


Figure 6.6: Normal stress distribution for bottom side of the wing. Unit of the colour scheme is given in 10 MPa.

In order to calculate the normal and shear stresses the moments and the axial loading needs to be calculated at each point along the length of the fuselage. As mentioned before the fuselage is divided in two section for the structural analysis. All the loads are calculated for the most demanding circumstances, thus for full control surface deflection and maximum power settings. For the first part the force and moment equations are given by Equation (6.29):

$$\sum F_x = -T \quad (6.29a)$$

$$\sum M_y = M_{gy} \quad (6.29b)$$

$$\sum M_x = M_{gx} \quad (6.29c)$$

$$\sum M_z = W_E \cdot x + M_{gz} \quad (6.29d)$$

For the second and the third section the axial and bending loading can be calculated with the same equations as shown in Equation (6.30):

$$\sum F_x = N_{VT} + N_{HT} \quad (6.30a)$$

$$\sum M_y = (l_{fus} - x) \cdot T_{VT} \quad (6.30b)$$

$$\sum M_x = y_{VT} \cdot T_{VT} \quad (6.30c)$$

$$\sum M_z = -(l_{fus} - x) \cdot T_{HT} - y_{VT} \cdot N_{VT} - (l_p - x) \cdot P \quad (6.30d)$$

### Stress Calculation of the Fuselage

Similar to the wing both normal and shear stresses act on the fuselage. One substantial difference is that there is no shear flow due to shear forces, but only due to torque, as the cross-section has two axis of symmetry. To analyse the stresses in the fuselage, first the stresses in the cut out section have to be analysed, as a cut out induce loading through the whole structure.

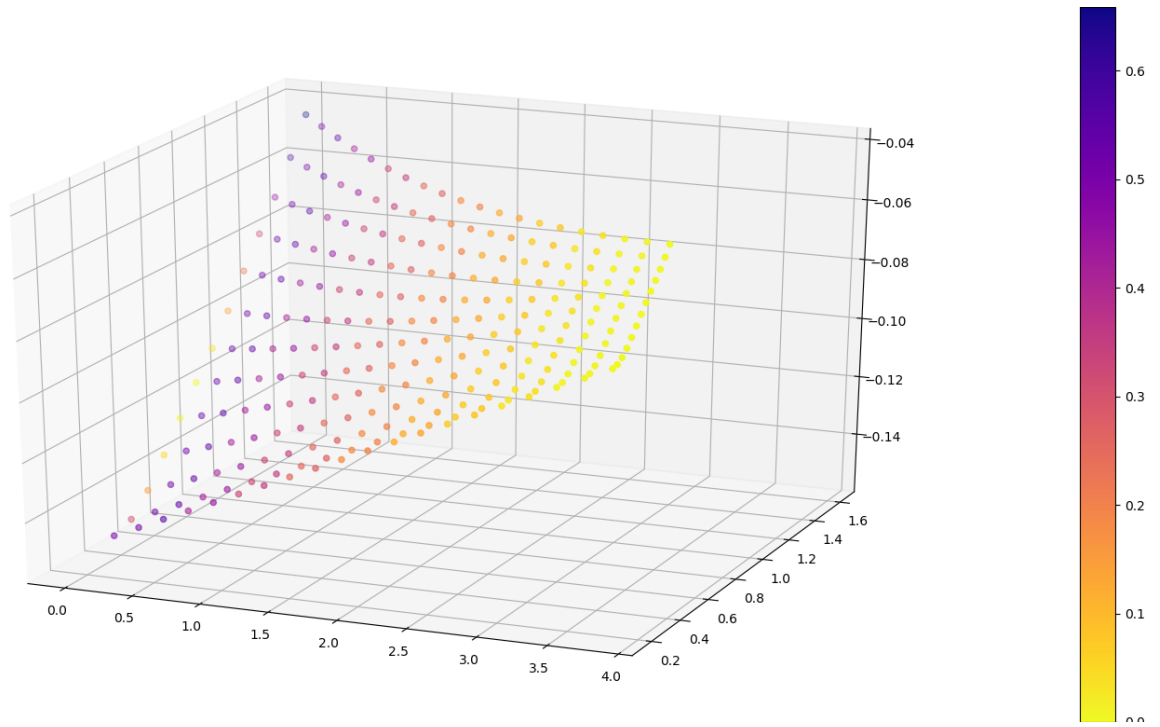


Figure 6.7: Tsai-Wu Failure criterion for Top side of the wing.

**Cut out** In this paragraph all the shear and normal stresses due to the fuselage are calculated. To calculate the forces through the cut out [31] is used. The cut out section will behave exactly the same as the non cut out sections under bending. However, as open section behave substantially worse under torsion than closed sections beams, for the cut out section this effect also has to be taken into account. To calculate the stresses induced due to the cut out, first the shear flow is calculated the same way as if there had been no cut out via Equation (6.19), resulting in a shear flow as shown in Figure (6.12a). However, as there actually is a cut out, the shear flow in the other panels have to counter act the shear flow in such a way that the net shear flow in the removed panel is zero, as shown in Figure (6.12b). To calculate those shear flows the force and moment equilibrium is used as shown in Equation (6.31). From these equations it is obtained that all the shear flows have to same magnitude and sign as defined in Figure (6.12b). The final shear flows are found by super imposing the correcting shear flows over the initial shear flows, effectively doubling the shear flow in the vertical walls and removing those in the horizontal walls.

$$\sum F \rightarrow: b_f \cdot q'_{34} = b_f \cdot q'_{12} \quad (6.31a)$$

$$\sum F \uparrow +: b_f \cdot q'_{14} = b_f \cdot q'_{23} \quad (6.31b)$$

$$\sum M_1: 0 = b_f^2 \cdot q'_{34} - b_f^2 \cdot q'_{23} \quad (6.31c)$$

The discontinuities introduced in shear flow are induced in the booms. To calculate resulting axial stresses due to the correcting shear flow Equation (6.32) is used. As the shear flow in wall 43 is the same as in wall 12, the axial load in boom 2 is also equal to  $P_3$ . However, where boom 3 was in tension, boom 2 will be in compression. The same method is used to calculate the other axial forces.

$$P_3 = \frac{(q'_{34} + q'_{23}) \cdot l_{sec2}}{2} \quad (6.32)$$

**Stresses in non cut out sections** The bending stresses, for both cut out and non cut out sections, are calculated with Equation (6.11). The shear flows for the non cut out sections are calculated with Equation (6.19). The compression and tension due to the thrust and normal forces is calculated with Equation (6.33). To calculate the shear flow induced by the cut out in the non cut out sections Equation (6.34) is used, with (6.34d) for the first section and (6.34e) for the third section. Superimposing those stresses yielded the final stresses

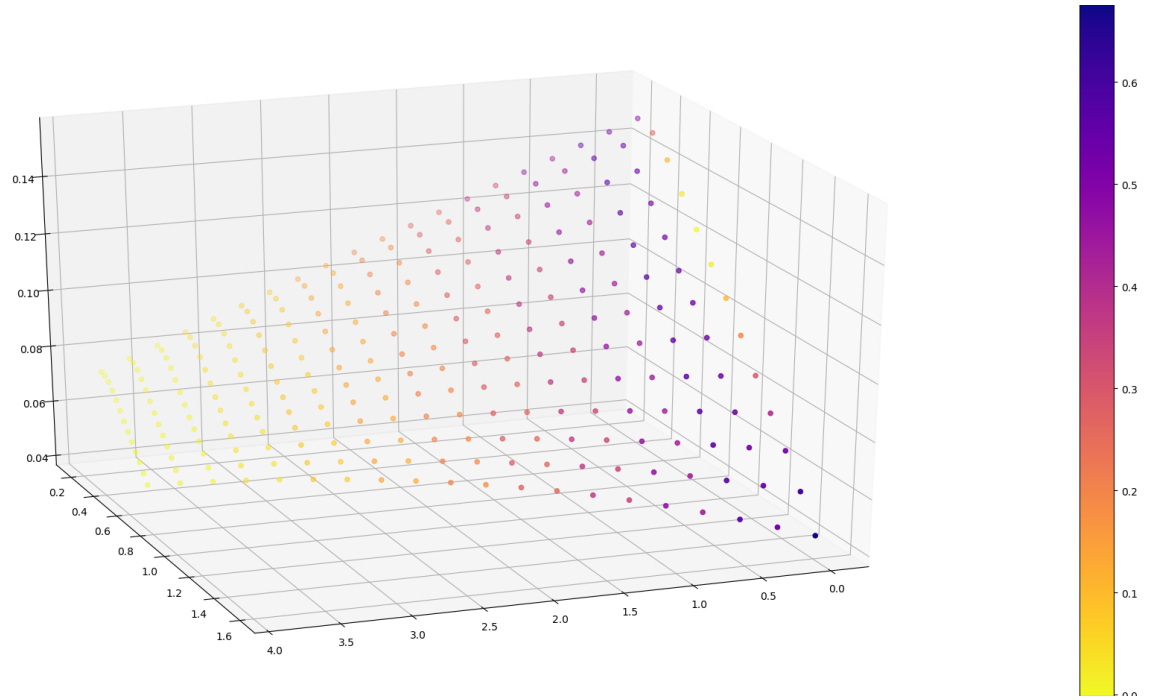


Figure 6.8: Tsai-Wu Failure criterion for bottom side of the wing.

for the whole structure. To couple the shear stresses to the normal stresses the Tsai-Wu failure criterion is used as explained in Section 6.2.1.

$$\sigma_z = \frac{F}{A} \quad (6.33)$$

$$\sum F \rightarrow: b_f \cdot q_{12}'' = b_f \cdot q_{34}'' \quad (6.34a)$$

$$\sum F \uparrow +: b_f \cdot q_{23}'' = b_f \cdot q_{14}'' \quad (6.34b)$$

$$\sum M_4: b_f \cdot q_{12}'' = b_f \cdot q_{23}'' \quad (6.34c)$$

$$l_{sec1} \cdot q_{34} + l_{sec1} \cdot q_{14} = P \quad (6.34d)$$

$$l_{sec3} \cdot q_{34} + l_{sec3} \cdot q_{14} = P \quad (6.34e)$$

**Results of the structural analysis** Based on multiple iterations the final geometrical parameters for the fuselage are given in Table 6.5. Because of the structural advantages of a monocoque fuselage the weight is severely reduced with respect to the steel truss structure of the EXTRA 330SC, as the skin only has to be 2 mm thick. It is chosen to keep the thickness constant through the whole fuselage in order to not further complicate the manufacturing process. In order to secure structural stability ribs are added to the fuselage at a 0.5 meter spacing. Those ribs do not close off the entire cross section of the fuselage as all the components still have to be able to run through the fuselage. Therefore the ribs will have an height of approximately 8 cm, leaving enough room for all the components to pass through.

The results of the structural analysis of the fuselage are shown in Figure 6.14 and 6.15. In Figure 6.14 the F values of the Tsai-Wu criterion, as explained in 6.2.1, are plotted. As explained earlier, those values should be below 1 to avoid failure. From the figure can be noted that is value is in the majority of the structure not even close to 1. This is done on purpose in order to maintain a sufficiently large safety factor for the extensive number of assumptions made while doing this analysis. In Figure 6.15 all the normal stresses due to the forces of Figure 6.11 are given. This plot is made to give a better insight and to verify the loading paths induced by the forces and moments. From this analysis it can be concluded that this fuselage design is strong enough to handle all loads and is also significantly lighter than the steel truss fuselage of the EXTRA, even if contingencies due to joints and mounts are taken into account.

	Main wing	Horizontal tail	Vertical tail	units
$A$	5.5	2.86	0.99	-
$\lambda$	0.45	0.529	0.33	-
$b$	4.018	1.134	0.619	m
Location $\Lambda_0$	25	55	50	% of chord
Location spar 1 at root	18	18	18	% of chord
Location spar 1 at tip	18	18	18	% of chord
Location spar 2 at root	80	55	50	% of chord
Location spar 2 at tip	55	55	50	% of chord
Root Chord	2.015	1.038	1.882	m
Thickness spar 1	0.002	0.0015	0.0015	m
Thickness spar 2	0.002	0.0015	0.0015	m
Thickness skin	0.0018	0.0010	0.0010	m
Number of stringers	8, 4, 2	6	6	-
Clamp dimensions	$0.03 \times 0.03$	$0.015 \times 0.015$	$0.015 \times 0.015$	$m^2$
Height stringer	0.025	0.015	0.015	m
Width stringer	0.025	0.015	0.015	m
Thickness stringer	0.003	0.003	0.0015	m

Table 6.4: Results of the structural analysis of the Main Wing, Vertical and Horizontal Tail.

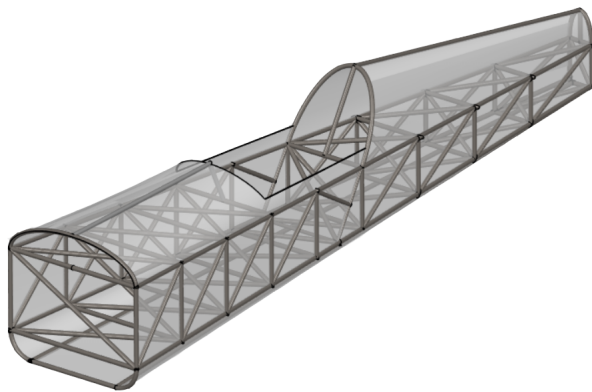


Figure 6.9: Steel truss structured fuselage of the EXTRA 300.

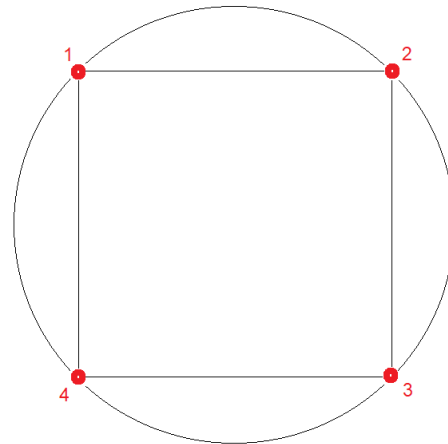


Figure 6.10: Cross section of the fuselage with four booms.

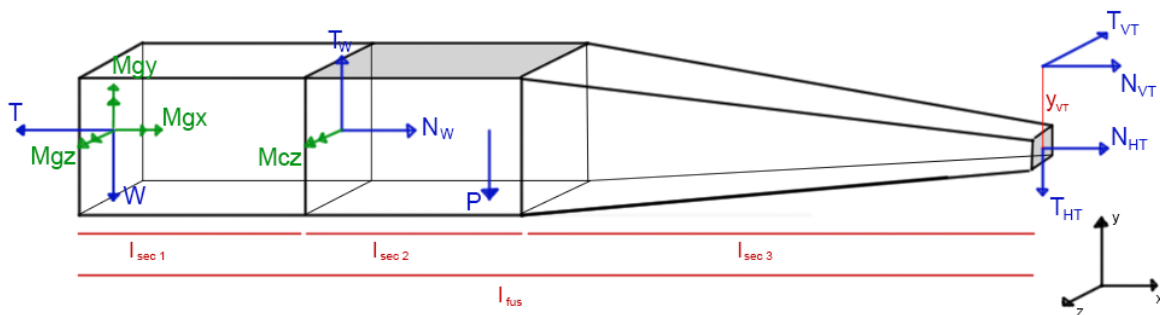


Figure 6.11: Free body diagram of the fuselage with all the external forces that are taken into account.

### Structural Analysis of the Landing Gear

In this section a simple structural analysis of the landing gear struts is performed. The landing gear is produced from a glass-fibre based composite (Epoxy/S-glass fiber) instead of a carbon based composite, because of its better ability to store energy. The shape of the struts is that of the E475 airfoil. This airfoil is selected

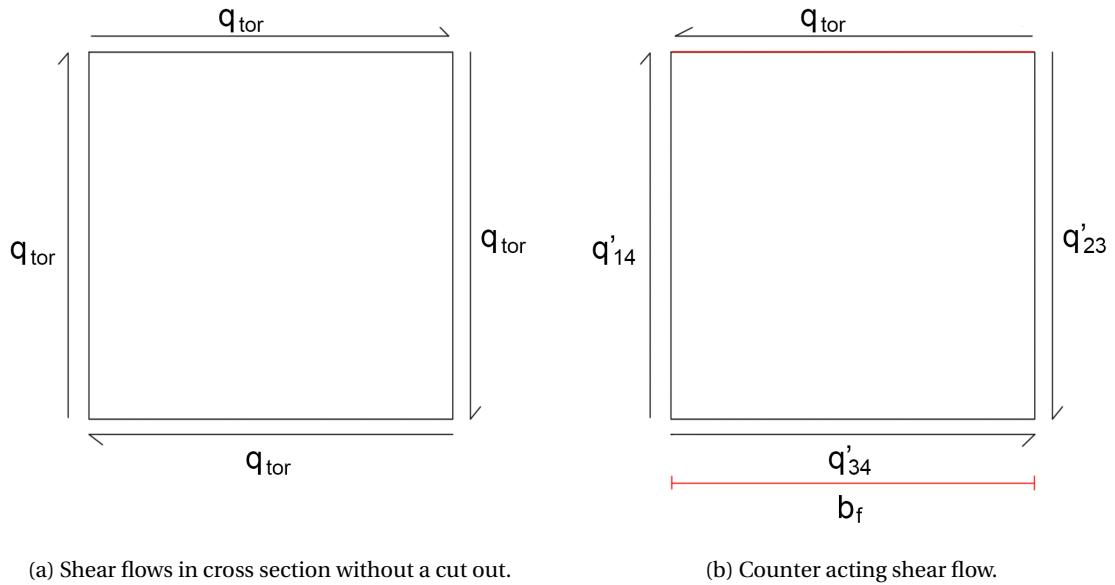


Figure 6.12: Sketches used to calculate the shear flows in the cut out section.

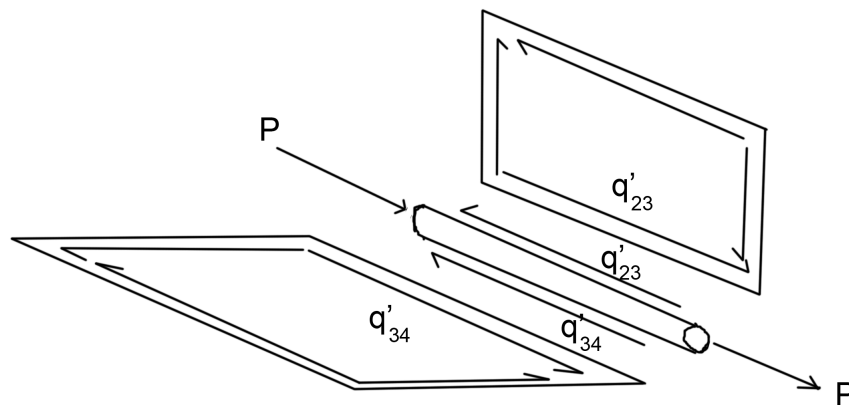


Figure 6.13: The axial loading induced due to shear in boom 3 in detail.

for its low drag characteristics. The calculations for the moment of inertia is the same as the calculation of the moment of inertia performed for the skin of the wingbox in Section 6.2.1. For the landing gear struts the only load carrying part of the structure is the skin as can be seen in Figure 6.16. The strut is filled with foam to prevent out of plain buckling. As there are no spars present, the calculation of the moment of inertia of the skin spans from the leading edge till the trailing edge.

For the loading case of the landing gear the moment of impact while landing is analysed. For this moment a single vertical force is assumed that has ten times to magnitude of the weight of the aircraft. This is to account for a hard landing in which one of the landing gears touches down earlier than the other due to roll. This means that one landing gear strut should be able to carry ten times the maximum take off weight of the aircraft. This force introduces a bending loading and a compression loading. It is assumed that the torsion due to shear is negligible compared to the bending moment. If the skin is strong enough withstand the bending moment, it is also strong enough to withstand the induced shear.

As it is assumed the shear forces are negligible, the only stresses that have to be calculated are the bending stresses and the stresses due to compression. The calculation of the bending stresses is the same as the one performed for the wing in Section 6.2.1 and the compression stresses are calculated the same way as for the fuselage in Section 6.2.2. Comparing those results with the material properties given in Section 6.1.1 it is

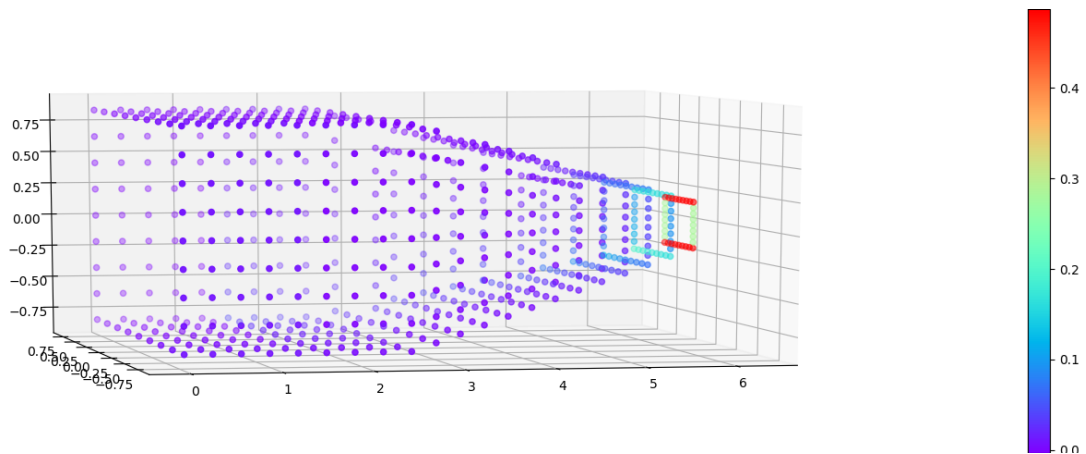


Figure 6.14: A 3D plot showing the F values at all points of a simplification of the fuselage skin.

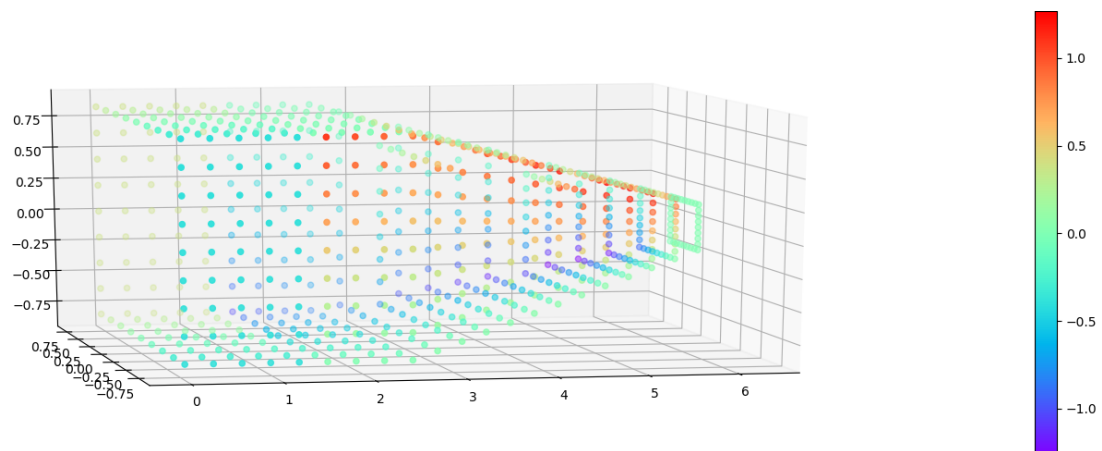


Figure 6.15: A 3D plot showing a stresses due to normal stresses in the fuselage with red depicting compression and purple tension. The colour scale has a unit of 100 MPa.

apparent that the strong enough by a large margin. The final geometry for the landing gear struts is found in Table 6.6.

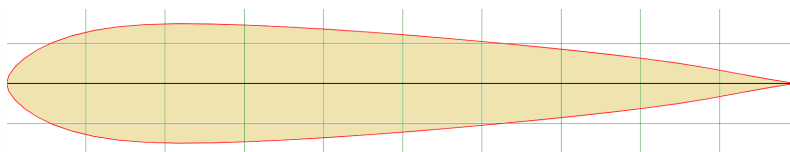


Figure 6.16: Cross section of landing gear strut with E475 airfoil shape and foam filling.

## 6.3 Aeroelasticity

In aerobatic flight, it goes without saying that the wing needs to be rigid such that the aileron does not lose significant performance due to twist, or would even experience aileron reversal. To analyse this, a simple model of the wing is made, as shown in Figure 6.17 [31]. For sake of simplicity, it will be assumed that the wing section at the middle of the half-span is representative of the entire wing with respect to its structural characteristics. All aerodynamic properties have been obtained from the aerodynamic simulation described in Section 4.4.

First, the aileron reversal speed,  $V_r$ , may be computed; this is the velocity at which the downward deflected aileron causes a downgoing force. This speed may be derived as follows [31]: an aileron deflection  $\delta_a$  (defined as  $\xi$  in Figure 6.17) causes a twist  $\theta$ ; the increment in lift and moment due to an aileron deflection

	Fuselage	Units
$b_f$	0.83	m
$t_D$	0.002	m
$t_{ribs}$	0.002	m
$h_{ribs}$	0.08	m
$s_{ribs}$	0.5	m
$l_{fus}$	6.22	m
$l_{sec1}$	1.5	m
$l_{sec2}$	1.5	m
$l_{sec3}$	3.2	m

Table 6.5: Geometric properties of the fuselage.

	Fuselage	Units
$c_{LG}$	0.24	m
$t_{LG}$	0.003	m
$l_{LG}$	0.8	m
$\alpha_{LG}$	35	°
Airfoil	E475	-

Table 6.6: Geometric properties of the landing gear.

thus equal

$$\Delta L = (C_{L_\alpha} \theta + C_{L_{\delta_a}} \delta_a) \frac{1}{2} \rho V^2 S \quad (6.35)$$

$$\Delta M = C_{M_{\delta_a}} \delta_a \frac{1}{2} \rho V^2 S c \quad (6.36)$$

From the aerodynamic simulation of Section 4.4, it followed that  $C_{L_\alpha} = 3.836 \text{ rad}^{-1}$ ,  $C_{L_{\delta_a}} = 2.984 \text{ rad}^{-1}$  and  $C_{M_{\delta_a}} = -0.7421 \text{ rad}^{-1}$ . The torque generated about the shear center is equal to

$$\Delta T = K\theta = \frac{1}{2} \rho V^2 S [(C_{L_\alpha} \theta + C_{L_{\delta_a}} \delta_a) e c + C_{M_{\delta_a}} \delta_a c] \quad (6.37)$$

where  $ec$  is the distance between the quarter-chord and the shear center, and  $K$  is the torsional rigidity of the wing, given by  $GJ$ . The shear modulus  $G$  is equal to 23 GPa as follows from Table 6.2, and  $J$ , the torsional constant, may be approximated as

$$J = I_{xx} + I_{yy}$$

Evaluating this at the midpoint of the half-span results in a  $J = 3.409 \times 10^{-4} \text{ m}^4$ . Writing Equation (6.37) as function of  $\theta$  yields

$$\theta = \frac{\frac{1}{2} \rho V^2 S [C_{L_{\delta_a}} e c + C_{M_{\delta_a}} c] \delta_a}{GJ - \frac{1}{2} \rho V^2 S e c C_{L_\alpha}} \quad (6.38)$$

This may be substituted in Equation (6.35) to obtain

$$\Delta L = \frac{1}{2} \rho V^2 S \left[ \frac{\frac{1}{2} \rho V^2 S c C_{M_{\delta_a}} C_{L_\alpha} + GJ C_{L_{\delta_a}}}{K - \frac{1}{2} \rho V^2 S e c C_{L_\alpha}} \right] \quad (6.39)$$

Aileron reversal happens when  $\Delta L = 0$ , in other words, when

$$\frac{1}{2} \rho V^2 S c C_{M_{\delta_a}} C_{L_\alpha} + GJ C_{L_{\delta_a}} = 0 \quad (6.40)$$

Solving for  $V$  yields the aileron reversal speed  $V_r$ :

$$V_r = \sqrt{\frac{-GJ C_{L_{\delta_a}}}{\frac{1}{2} \rho S c C_{M_{\delta_a}} C_{L_\alpha}}} = 854 \text{ m/s} \quad (6.41)$$

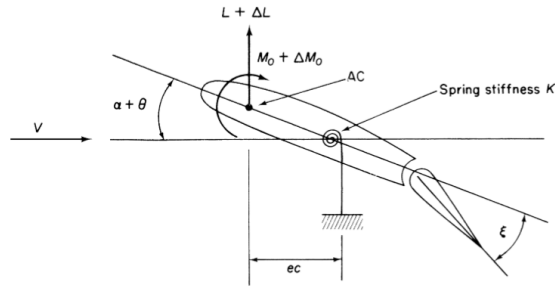


Figure 6.17: Simplified model of the wing [31, p. 809].

This confirms that aileron reversal is essentially negligible; the high value can be explained due to the high torsional stiffness that was required of the structure anyway, as extensively computed in the foregoing sections.

Nonetheless, it is interesting to examine the aileron effectiveness as function of speed. If  $\Delta L_R$  is the lift increase of a pure rigid wing due to an aileron deflection, i.e.

$$\Delta L_R = C_{L\delta_a} \delta_a \frac{1}{2} \rho V^2 S \quad (6.42)$$

then the aileron effectiveness is given by

$$\text{Aileron effectiveness} = \frac{\Delta L}{\Delta L_R} = \frac{\frac{1}{2} \rho V^2 S c (C_{M\delta_a} C_{L\alpha}) + GJ C_{L\delta_a}}{[GJ - \frac{1}{2} \rho V^2 S e c C_{L\alpha}] C_{L\delta_a}} \quad (6.43)$$

where  $ec$ , the distance between the shear center and the quarter-chord, equals 16.7 cm for the middle section of the wing half-span. The aileron effectiveness as function of speed is plotted in Figure 6.18. As clearly visible, loss of aileron effectiveness is no issue at all; at most a 1% decrease in aileron effectiveness is achieved near the never exceed speed.

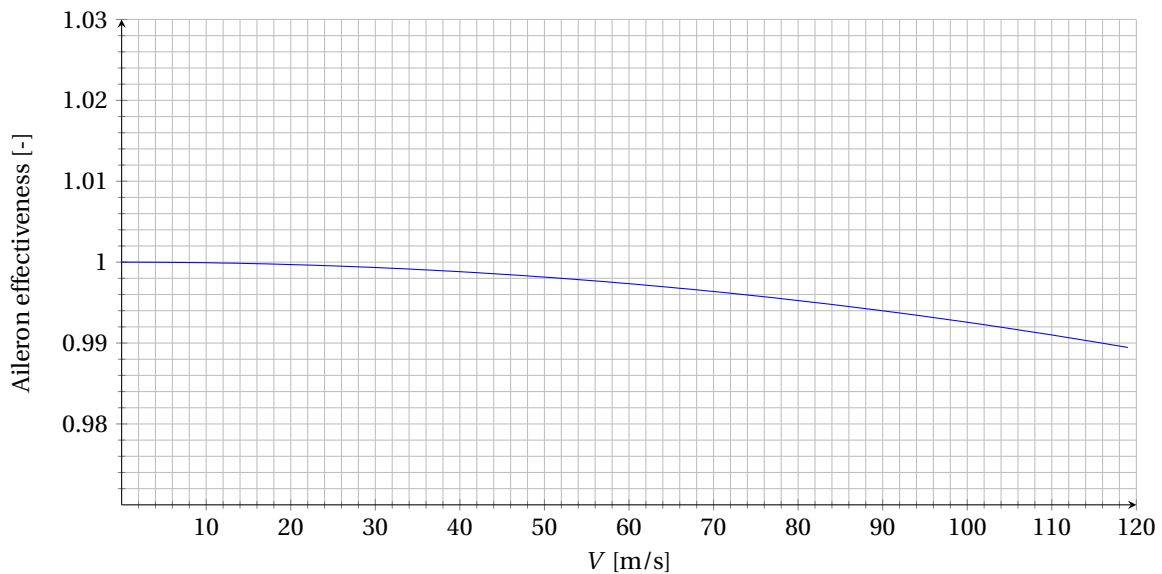


Figure 6.18: Aileron effectiveness as function of speed.

## 6.4 Structural Design of the Seat

One of the requirements is that the seat needs to be able to withstand a loading of 20 G. However, the design challenge is not in designing a seat that can withstand the load, but making the seat absorb energy if the loading is exceeding the 10 G limit. The materials selected earlier are not usable for the design of this part, since they are not ideal for absorbing energy. This is why in the next subsection possible materials are investigated.

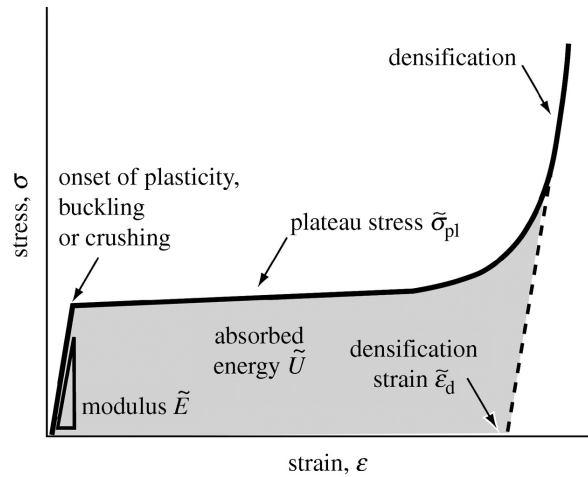


Figure 6.19: Stress-strain curve of an elastomeric foam.

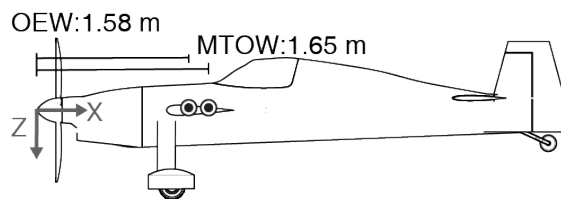


Figure 6.20: Coordinate system for c.g. location, as well as the c.g. locations for OEW and MTOW.

### 6.4.1 Material Selection for the Seat

The option has been investigated to use a polymer foam to absorb the excessive energy. Polymer foams consist of bubbles of gasses that are trapped inside cells that are made of the polymer. A typical stress-strain curve for an elastomeric foam can be seen in Figure 6.19. This curve can be divided into three sections: the elastic phase, the plateau phase and the densification phase. The phase of most interest is the plateau phase, since most energy is absorbed in this region. The elastic phase is ignored for the design of the 20 G seat, since the amount of energy absorbed here can be neglected. It is however found that the amount of foam needed to absorb the energy of the pilot crashing at 20G would be impossible to fit in the cockpit. In future work, other shock absorbing materials and structures (such as honeycomb structures) will be investigated as impact energy absorbers.

Property of the material	Polyurethane	Polystyrene	Polyethylene	Unit	Source
Density	75	22	101	kg/m <sup>3</sup>	[14]
Compressive modulus	0.0296	0.0191	0.11	GPa	[14]
compressive strength	0.03	0.16	1.86	MPa	[14]
Price	7.63	2.78	11.3	USD/kg	[14]

Table 6.7: Properties of three elastomeric foams.

## 6.5 Centre of Gravity and Mass Moment of Inertia

The location of the centre of gravity is important for the handling and performance of the aircraft.

For the determination of the c.g. it was assumed that the  $y$ -location was 0, as the aircraft will be symmetric in the  $XZ$ -plane. For the location on the other axes the aircraft will be subdivided into different components of which each component's mass and location will be iterated. The final location and mass of each component as well as the total location of the c.g. can be found in Table 6.8. For the location of each component the coordinate system in Figure 6.20 was used.

To estimate the mass moment of inertia a method developed in [33] was used. The aircraft was divided into the wing, horizontal and vertical stabiliser; and fuselage. All other parts of the aircraft were assumed to be

	Mass [kg]	$x$ -location from nose [m]	$z$ -location [m]
Wing	88.9	1.79	0
Horizontal tail	15.9	5.2	-0.09
Vertical tail	11.3	6.23	-0.31
Fuselage	40	3	-0.06
Landing gear	35	1.1	0.59
Propeller	30	-0.2	0
Fuel system	10	1.18	0
Flight controls	20	2.435	0.21
Avionics	17	2.035	0
LEHLD	16	1.1	0
Flaperons	14	2.63	0
Aircraft at OEW	557	1.58	0.028
Pilot	100	2.235	-0.22
Aircraft with pilot	657	1.68	-0.01
Fuel	57	1.18	0
Aircraft at MTOW	714	1.65	-0.009

Table 6.8: C.g. locations and masses of each component of the aircraft.

point masses. The fuselage was divided into 16 different stations along the  $x$ -axis, with each station having a mass that was assumed equal to the total mass of the fuselage times the fraction of the local area of the station divided by the sum of all areas. Each station was subdivided into 8 point masses, which are equally spaced around the circumference. The mass of these points was determined with Equation (6.44), where  $s$  is the arc-length over each point mass. After the location and mass of each point was determined, the mass moments of inertia of each point could be calculated with Equation (6.45), with the mass moments of inertia about different axis calculated in the same way, only changing the  $y$  or  $z$  with  $x$ . The total moment of inertia of the fuselage can then be found by summing all the moments of inertia of each point.

$$m_{pm} = m_i \frac{s_{pm}}{\Sigma s} \quad (6.44)$$

$$I_{xx_{pm}} = m_{pm} \left( (y_{cg_{pm}} - y_{cg})^2 + (z_{cg_{pm}} - z_{cg})^2 \right) \quad (6.45)$$

The wing was divided in five stations along the chord and 50 along its span to determine its mass moment of inertia. For the weight distribution, the coefficients  $A1$ ,  $B1$  and  $C1$  were determined with Equations (6.46) till (6.48).

$$A1 = \frac{b^2}{4N_{st}^2} \frac{a_{mass}}{2} + \frac{b}{2N_{st}} C1 \quad (6.46)$$

$$B1 = \frac{3b^2}{2N_{st}^2} \frac{a_{mass}}{4} + \frac{b}{2N_{st}} C1 \quad (6.47)$$

$$C1 = \frac{2}{b} \left( \frac{m_{wing}}{2} - \frac{b^2}{8} a_{mass} \right) \quad (6.48)$$

Where  $a_{mass}$  can be calculated with Equation (6.49)

$$a_{mass} = -m_{wing} \left( \frac{c_r(1-\lambda)}{\frac{\Sigma c_i}{N_{st}}} \right)^2 \quad (6.49)$$

The mass of each point along the wing can be calculated with Equations (6.50) till (6.54)

$$W_{i,1} = \left( F_{lehd} + L_1 F_{skin} + \left( \frac{A_{airfoilsegment1_i}}{A_{airfoil_i}} \right) F_{ribs} \right) (A1 + (B1 - A1)(i - 1)) \quad (6.50)$$

$$W_{i,2} = \left( (L_2 - L_1) F_{skin} + \left( \frac{A_{airfoilsegment2_i}}{A_{airfoil_i}} \right) F_{ribs} + F_{fs} \right) (A1 + (B1 - A1)(i - 1)) \quad (6.51)$$

$$W_{i,3} = \left( (L_3 - L_2) F_{skin} + \left( \frac{A_{airfoilsegment3_i}}{A_{airfoil_i}} \right) F_{ribs} \right) (A1 + (B1 - A1)(i - 1)) \quad (6.52)$$

$$W_{i,4} = \left( (L_4 - L_3) F_{skin} + \left( \frac{A_{airfoilsegment4_i}}{A_{airfoil_i}} \right) F_{ribs} + F_{rs} \right) (A1 + (B1 - A1)(i - 1)) \quad (6.53)$$

$$W_{i,5} = \left( F_{flaperons} + (1 - L_4) F_{skin} + \left( \frac{A_{airfoilsegment5_i}}{A_{airfoil_i}} \right) F_{ribs} + F_{rs} \right) (A1 + (B1 - A1)(i - 1)) \quad (6.54)$$

The total moment of inertia of the wing can then be calculated in the same way, as for the fuselage with Equation (6.45).

The mass moment of inertia of the horizontal and vertical tail were calculated using DATCOM [11]. The results of this can be found in Table 6.9

Output	Input	Reference	Results	
			HT	VT
$\rho$ [kg/m]	$C_a, C_b, C_c, m_{tail}$	[33, p.26]	17.7	5.44
$I$ [kg · m <sup>2</sup> ]	$\rho, C_a, C_b, C_c$	[11, p. 8.1-8]	8.0	3.8
$I_{0X}$ [kg · m <sup>2</sup> ]	$b, c_r, c_t, K_4, K_5, m_{tail}$	[11, p. 8.1-8]	8.4	0.69
$I_{0Y}$ [kg · m <sup>2</sup> ]	HT: $I, K_0, m_{h-tail}$ , VT: $I_{0X}, I_{0Z}$	[11, p. 8.1-7]	1.16	1.24
$I_{0Z}$ [kg · m <sup>2</sup> ]	HT: $I_{0X}, I_{0Y}$ , VT: $I, K_0, m_{v-tail}$	[11, p. 8.1-8]	9.56	0.55

Table 6.9: Local mass moments of inertia of the horizontal and vertical tail.

All the other components of the aircraft were assumed to be point masses. All the mass moments of inertia of each component as well as the total mass moments of inertia are presented in Table 6.10. The results for the mass moments of inertia have been compared to similar sized aircraft in [21] to verify this method. The moments of inertia of the *StefX* are lower than the moments of inertia of the reference aircraft, but still in the same order of magnitude. However this can be explained, as the masses of the reference aircraft are higher, as those aircraft are largely made of wood or aluminium instead of carbon of which the *StefX* will be made of.

## 6.6 Production Plan

In this section a close look is given to the production plan. The production plan entails a description of the manufacturing strategy of the components of the aircraft as described in Section 6.6.3, together with the supply chain of different sub-components and materials which is described in Section 6.6.1. The goal of the production plan is to provide an efficient strategy to minimise the manufacturing cost of one aircraft. This is done by following the principles of lean manufacturing [39]. Lean manufacturing is defined as a customer-focused process, through which all employees continuously eliminate waste with the goal of creating value. This means that all actions that contribute no value to the customer are eliminated or reduced to a minimum. This includes for example time spent on moving components from one machine to another. Other elements in which waste should be minimised in order to reduce cost are:

- Man hours
- Materials

	Fuselage	Wing	HT	VT	Engine	Fuel	Pilot	Landing Gear	Total
$I_{xx}$ [kg · m <sup>2</sup> ]	6.46	634.89	3.39	10.59	9.55	0.005	4.44	12.6	682.9
$I_{yy}$ [kg · m <sup>2</sup> ]	82.7	34.14	221.1	496.1	304.2	6.92	38.9	23.1	1232
$I_{zz}$ [kg · m <sup>2</sup> ]	83.9	669	217.7	506.13	310.1	6.9	34.43	10.55	1862.9
$I_{xz}$ [kg · m <sup>2</sup> ]	1.3	0.17	-14.8	-11.59	-2.39	-0.19	-12.4	-11.52	-47.79

Table 6.10: Mass moments of inertia of the most important components as well as the total moments of inertia.

- Space
- Tooling & Equipment
- Energy

During the manufacturing process extra care is given to ensure employees do not have to work in hazardous or unsafe environments.

### 6.6.1 Part Manufacturing

The key component that drives the decisions for the production plan are the expected number of produced aircraft. While it could be beneficial to invest in a highly automated production line when it is expected that a lot of aircraft are sold, for low quantity production it will actually be more beneficial to keep the tooling cost as low as possible. This will increase the number of man hours needed to manufacture one aircraft, but will limit the initial investment. As discussed in Section 6.1, the aircraft will be almost exclusively be produced out of composites. The main advantages composites have in manufacturing is the low initial investment needed for tooling and the minimal amount of scrap material. The manufacturing technique that will be used is *tape laying*. This technique involves manually laying layers of prepreg composite sheets in a one sided mold and letting it cure as can be seen in Figure 6.21. Advantages of this method of this method over, for example, vacuum infusion is that the direction of the fibres is not able the shift after the positioning of the sheets. The disadvantage of this method is however that working with composites requires some skill level of the workers and thus people need to be trained. The work flow of generating a part can be found in Figure 6.22.



Figure 6.21: Hand lay up of prepreg composite sheets [46].

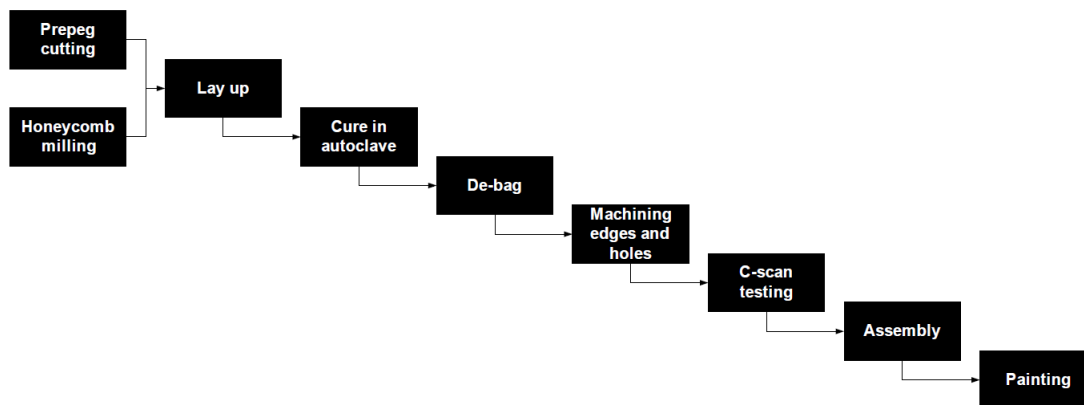


Figure 6.22: Work flow diagram of the manufacturing procedure of carbon components [39].

### 6.6.2 Assembly

The production of the aircraft is divided in several structural divisions that are assembled later on to increase production efficiency. By splitting the work up in portions, it is easier to work on multiple parts at the same time, thus improving efficiency. Other reasons for this are the ability to change parts for maintenance and to

increase the ease of production by avoiding the handling of large parts [39]. The *StefX* will be divided in the following structural components:

- Fuselage
- Single main wings
- Horizontal stabilisers
- Vertical stabiliser
- Propulsion system

Those structural components will be produced by different manufacturing divisions. The divisions are divided in equally sized work packages, making sure that each structural component takes an equal time to produce. This reduces the average amount of time components have to be stored, thus reducing the space needed, thus reducing cost. The general work flow of the assembly is shown in 6.23. As carbon composites handle peak loads induced through holes quite poorly, nearly all components will be bonded with adhesives. This poses a challenge to the assembly of the components as adhesives, contrary to for example riveting, require great accuracy. Due to this accuracy constraints, parts shall be produced with low tolerances. This also increases the requirement on the stiffness and precision of the assembly jigs. If bolts or rivets have to be used however, it is made sure that they are all standardised sizes.

The propulsion system is ordered in large batches as most of those components have to be manufactured by third parties. Ordering relatively large quantities at ones often result in lower prices due to the quantity discount factor [39]. The structural components will be manufactured in line production. This means assembly line consists of multiple stations. At each station the same crew performs the same tasks at subsequent aircraft over and over again. The allocated time for these tasks is fixed and is the same for all stations, the delivery interval. When the time of the delivery interval is reached, all components move to the next station. The advantages of this production strategy is minimal transport, simple planning, good indication of progress, maximal equal shaped products and maximal routine forming per crew [39].

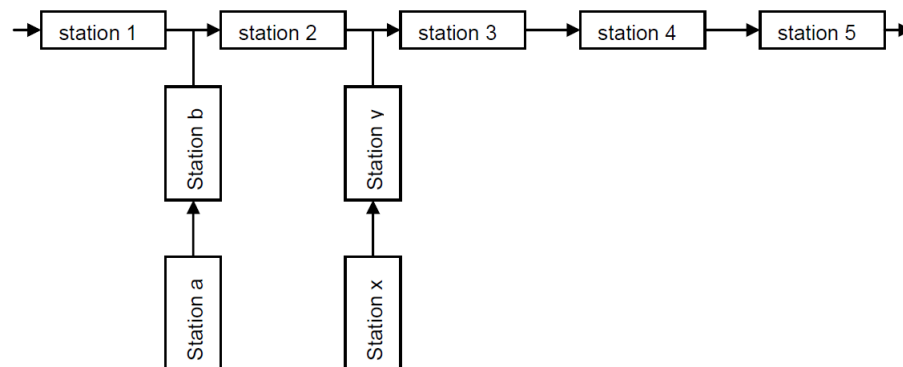


Figure 6.23: Work flow diagram of the assembly procedure of the sub-components [46].

### 6.6.3 Supply Chain

The choice for composites also effects the supply chain of the project. For example, the used composites come in prepreg form and have therefore a certain shelf life. Composites are also notorious for their material price. Those two factors combined complicates the logistics of the manufacturing, as the material can not be ordered all at ones in a large bulk, but instead have to be ordered with a time interval, reducing the time the prepreg composites have to be stored.

Not only the materials have to ordered, but also components produced by third parties, such as the avionics and propulsion systems. As mentioned in Section 6.6.2, those components have to ordered in batches in order to gain a quantity discount factor. However, it should be noted that the right balance is needed between the batch size of those components and the delivery interval of the aircraft, as storing costs can rise to a substantial amount when to large batches are ordered.

The manufacturing and the assembly of all the components take place at one location in the Netherlands to reduce the waste of resources for transportation. This decision is not only made from an economical perspective, but also to increase the sustainability of the project. Producing the whole aircraft at one location also makes quality insurance easier and increases the similarity between all produced aircraft.

# Chapter 7

## Cost

To ensure the *StefX* will be profitable a cost and market analysis was done. First in Section 7.1 a market analysis was done. After this the unit price was estimated in Section 7.2. Also the operational costs were analysed in Section 7.3

### 7.1 Market Analysis

As the *StefX* is designed as a highly competitive aircraft for the unlimited category of the FAI World Aerobatic Championships it is expected that the costumers of the aircraft will primarily consist of the teams of UACs (Unlimited Aerobatic Competition). Those costumers will pay the premium for an aircraft, as long as it is a clear improvement.

**Comparison to EXTRA 330SC** On request of the Communication Manager, EXTRA Aircraft provided documentation on the number of aircraft they have built so far (January 2018), presented in Table 7.1. Since the EXTRA 330SC started production in 2009, they have built an average of 8.1 aircraft per year. Since EXTRA 330SC has a 70 % market share, the total market is assumed to be 11.6 aircraft per year. If the *StefX* would be a success and would obtain a 70 % market share in a period of 8 years it can be estimated that 65 aircraft will be sold. Since EXTRA also obtained this market share in this time span, 65 aircraft in eight years will be used.

**Business Model** An often used business model of aerobatic aircraft manufacturers is to design a double-seater as well as a single-seater aircraft with a very similar design. Despite the fact that the double-seater has lesser performance than the single-seater, it is sold more. All the EXTRA models shown in Table 7.1, except the 330SC, are double-seater aircraft. Double-seater aircraft are often preferred over single-seater aircraft due to their ability to be used as training aircraft and the option to bring a passenger. It is decided that after the single-seater version of the *StefX* has been designed, also a double-seater version should be manufactured to enter a bigger market and reach the break even point earlier. The additional development costs by designing a double-seater variant of the aircraft are very small in comparison by the market size.

In order to estimate the number of aircraft sold, both the single-seater and the double-seater version will be combined, due to the relatively low amount of resources needed to develop the double-seater version and high level of similarities between those to versions. Based on the sales numbers of EXTRA Aircraft it is estimated that in eight years time 240 versions of the *StefX* will be sold, with around 65 single-seaters and 175 double-seaters. In addition to this, the aircraft might be sold as a military trainer as it is a safe aircraft with extreme manoeuvrability.

Type	330SC	330LX	330LT	300L	300
Number built	73	75	45	326	68

Table 7.1: Number of EXTRA 300 and 330 aircraft build until January 2018 [34].

### 7.2 Unit Price Estimation

The unit price estimation consist of multiple parts. These parts can be subdivided in fixed cost and the unit cost. The fixed cost is only payed once, and has to do with the design of the aircraft. The unit cost has to be payed for every aircraft which is produced, and has to do with the production and manufacturing of the aircraft.

**Fixed Cost** The fixed cost includes the engineering cost, the development support cost, the flight test cost, and the tooling cost. This cost is the initial investment and will only be necessary once. These were estimated using relations suggested in [22]; for example, the development support was estimated by

$$C_{DEV} = 0.06458 \cdot W_{airframe}^{0.873} \cdot V_H^{1.89} \cdot N_p^{0.346} \cdot CPI_{2012} \cdot F_{CERT} \cdot F_{CF} \cdot F_{COMP} \cdot F_{PRESS} \quad (7.1)$$

This cost depends on the weight of the airframe ( $W_{airframe}$ ), the maximum level airspeed ( $V_H$ ), the number of prototypes to be constructed ( $N_p$ ), a correction factor for inflation ( $CPI_{2012}$ ), the type of certification (CFR 23 or LSA) ( $F_{CERT}$ ), if the aircraft includes a complex flap system ( $F_{CF}$ ), the fraction of composites used in the aircraft ( $F_{COMP}$ ), and if the aircraft includes a pressurised cabin ( $F_{PRESS}$ ). Similar relations exist for the other the other fixed costs; their results are shown in Table 7.2.

**Variable Cost** The unit cost is calculated per batch over five years; it is assumed that 30 aircraft will be produced per year. The variable cost consists of the manufacturing cost, the cost of quality control, the cost of materials, the cost of a retractable landing gear, the cost of avionics, the cost of the engine, the cost of the propeller and the insurance cost. Estimation relationships exist for all of these, similar to Equation (7.1), and the results are listed in Table 7.2. In order for the aircraft to be successful and economically feasible, it has to break even after eight years of production. the production of 30 aircraft per year leads to 240 aircraft in eight years. From this number, the unit cost, and the fixed cost, a final minimum price can be assigned to each aircraft. This cost is stated in Figure 7.1 per part of the cost. It should be noted that the aircraft can also be sold at the maximum allowable price of \$325,000. If this price is used, the aircraft will break even after 200 aircraft instead of 240.

### 7.3 Operational Cost

A large factor in the accessibility of an aircraft are the operational costs that come with it. The airport fees and the fuel consumption are significant factors in the operational costs, as well as the maintenance costs. Every aircraft also needs to be insured. The insurance cost is nebulous value that is disclosed by insurance companies on an individual bases. A calculation of the operational cost is performed for all concepts, will result in the average cost per flight hour. Once again, this is done based on the statistical relation described in *General Aviation Aircraft Design* [22], which describe the maintenance cost, airport fees, fuel cost, insurance cost, and loan payments. The results are shown in Table 7.2. Based on an interview with Stijn De Jaeghere it is estimated that competitive unlimited aerodynamic pilots fly their aircraft around 200 hours a year. The cost per flight hour was determined by dividing the total annual operating cost by the hours flown per year. It should be noted that many of the values used in this calculation are based on the Netherlands and could vary for other countries. If the aircraft is for instance owned in the United States, the landing fees are non-existent, and the fuel is cheaper. This puts the operational cost per 5 years at a mere \$201,700. Another difference will be the insurance which is strongly dependent on the pilots, and can vary greatly.

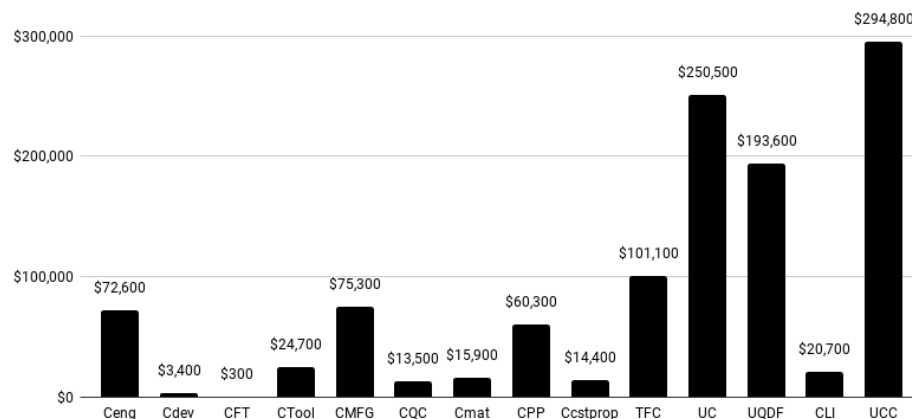


Figure 7.1: The unit price divided in the different parts.

Output	$C_{eng}$	$C_{dev}$	$C_{FT}$	$C_{Tool}$	$TFC$
Name	Engineering cost	Development support cost	Flight test operations cost	Tooling cost	Total fixed cost
Input	$H_{ENG}, R_{ENG}, CPI_{2012}$	$W_{airframe}, V_H, N_P, CPI_{2012}, F_{CERT}, F_{CF}, F_{COMP}, F_{PRESS}$	$W_{airframe}, V_H, N_P, CPI_{2012}, F_{CERT}$	$H_{TOOL}, R_{TOOL}, CPI_{2012}$	$C_{ENG}, C_{DEF}, C_{FT}, C_{TOOL}$
Value	\$17,430,400	\$827,500	\$76,700	\$5,937,700	\$24,272,300

Output	$C_{MFG}$	$C_{QC}$	$C_{mat}$	$C_{PP}$	$C_{cstprop}$	$UC_{Pre}$
Name	Manufacturing cost	Quality control cost	Materials cost	Power plant cost	Constant speed propeller cost	Preliminary unit cost
Input	$H_{mfg}, R_{mfg}, CPI_{2012}$	$C_{MFG}, F_{CERT}, F_{COMP}$	$W_{airframe}, V_H, N, CPI_{2012}, F_{CERT}, F_{CF}, F_{PRESS}$	$N_{PP}, P_{BHP}, CPI_{2012}$	$N_{PP}, CPI_{2012}, D_P, P_{SHP}$	$C_{MFG}, C_{QC}, C_{mat}, C_{PP}, C_{cstprop}$
Value	\$18,081,300	\$3,232,000	\$3,814,800	\$60,300	\$14,400	\$250,500

Output	$H_{eng}$	$H_{tool}$	$H_{mfg}$	$UC_{QDF}$	$C_{LI}$	$UC$
Name	Engineering hours	Tooling hours	Manufacturing hours	Unit cost with QDF	Liability insurance cost	Unit cost
Input	$W_{airframe}, V_H, N, F_{CERT}, F_{CF}, F_{COMP}, F_{PRESS}$	$W_{airframe}, V_H, N, Q_m, F_{TAPER}, F_{CF}, F_{COMP}, F_{PRESS}$	$W_{airframe}, V_H, N, F_{CERT}, F_{CF}, F_{COMP}$	$UC_{Pre}, QDF$		$UC_{QDF}, C_{LI}$
Value	97,600	83,100	379,700	\$193,600	\$20,700	\$294,800

Output	$C_{AP}$	$H_{FM}$	$C_{stor}$	$C_{fuel}$	$C_{ins}$
Name	Annual maintenance cost	Flight to man-hours ratio	Storage cost	Fuel cost	Insurance cost
Input	$H_{MF}, R_{AP}, Q_{FLGT}$		$R_{STOR}$	$FF, Q_{FLGT}, R_{FUEL}$	$C_{AC}$
Value	\$7,300.00	0.39	\$3,000.00	\$50,700.00	\$5,400.00

Output	$C_{insp}$	$C_{cover}$	$C_{year}$	$C_{HR}$	$C_{5Y}$
Name	Inspection cost	Overhaul cost	Yearly cost	Hourly cost	5 yearly cost
Input		$N_{PP}, Q_{FLGT}$	$C_{AP}, C_{STOR}, C_{FUEL}, C_{INS}, C_{INSP}, C_{COVER}$	$C_{year}$	$C_{year}$
Value	\$500.00	\$2,900.00	€63,300.00	\$370.00	\$372,500.00

Table 7.2: Unit cost estimation and operational cost estimation.

# Chapter 8

## Reliability, Availability, Maintainability, and Safety

In this chapter a Reliability, Availability, Maintainability, and Safety (RAMS) analysis is performed for *StefX*. The RAMS analysis is executed by analysing the four different components in four different sections. In Section 8.1 the reliability of the concept is analysed qualitatively as well as a brief quantitative analysis. In Section 8.2 the availability and the lack of it due to maintenance is analysed. In Section 8.3 the maintainability of the *StefX* is discussed and in Section 8.4 an analysis of the safety of the concepts, together with potential hazards, is performed.

### 8.1 Reliability

Reliability in the RAMS analysis describes the probability that a system will perform in a satisfactory manner for a given period of time when used under specified operating conditions[19]. To calculate such probabilities, the reliability or failure function of different components is needed. Therefore, to calculate the probability that a component will survive up to a certain time is based on general statistical data and several assumptions.

First, to calculate the reliability of the aircraft, an analysis is done to identify which components are most likely to fail. For this statistical analysis of this reliability calculation it is determined that the aircraft has not performed in a satisfactory manner once an accident has occurred, due to a failure of one or multiple components. The definition of an accident in aviation is when a person is seriously injured while in contact with the aircraft or when the aircraft sustains damage or structural failure,<sup>1</sup>. This choice is made as there is not enough data available for failures that not lead to an accident, partly because it is not always mandatory to report these small failures.

To calculate the probability that the *StefX* will perform in a satisfactory manner for a given period of time, a negative exponential distribution is used. A negative exponential distribution assumes a constant failure rate, which is representative for random failures. This is for example, often the case in components with a large number of components[19]. In [30] it is stated that there are 0.86 accidents per 100,000 flight hours due to mechanical failure in 2014 for fixed wing general aviation aircraft, which is equal to 161 accidents. This means that the mean time to failure (MTTF) equals 116,279 hours on average for general aviation aircraft. There is no reason to believe the design will defer from this value.

### 8.2 Availability

The availability in the RAMS analysis is defined as the percentage of the amount of time that a system will be ready or available when required for use [19]. This consists both at the amount of time the aircraft needs maintenance and the amount of days the aircraft is able to fly during the year due to weather conditions. In FAR 91.409 the minimum requirements pertaining to annual and 100 hour inspection are stated<sup>2</sup>. The annual inspection must be performed within twelve months. An aircraft used to carry passengers or for flight instruction must be inspected within each 100 hours. The annual inspection is acceptable as a 100-hour inspection, but the reverse is not true. This 100 hour inspection should therefore only be necessary if the double seater version of the winning concept would be used for aerobatics training, but not mandatory for the single seater that will compete in the unlimited competition.

It is estimated that an aircraft is unavailable for approximately a few working days for the annual inspection or the 100 hour inspection. It is estimated that the aircraft will make approximately 200 flight hours per year. That means that one (optional) 100 hour inspection and one annual inspection will be performed annually. Therefore this will account for at least 10 days of maintenance. As the TBO of the chosen Lycoming engine equals 1400 flight hours, a engine overhaul has to be performed once every seven years. With one

---

<sup>1</sup>URL <https://www.skybrary.aero/index.php/Accident>

<sup>2</sup>URL <https://www.lycoming.com/content/basics-maintenance-general-aviation>

overhaul taking between two to three weeks<sup>3</sup>, this totals the unavailability due to maintenance to approximately 8 working days per year. This results in an availability percentage of approximately 98%. However, if maintenance is planned during seasons with frequently occurring bad weather, the availability is almost 100%.

### 8.3 Maintainability

The maintainability part analyses the ease, accuracy, safety and economy in the performance of maintenance actions. The ease of the maintenance will be taken into account in designing the detailed components. Parts will be categorised based on how likely they are to be replaced. Parts that will be replaced often, will be made easy to access and will be fastened with mechanisms that require low time to detach and attach, such as bolts. The level of accuracy and safety of the maintenance will be inline with the requirements from the aviation authorities.

### 8.4 Safety

Safety is an important driving factor in the development of general aviation. In 2014 there were 1017 accidents with fixed wing general aviation aircraft, of which 207 accidents were fatal [30]. 75% of both the accidents as the fatalities happened due to a pilot error. It should be noted however that accident data of general aviation may not be valid for aerobatics, as general aviation includes many other types of airplanes than aerobatic aircraft. Accidents in aerobatics are rare, but severe when they happen. In 2014 four accidents happened while performing aerobatics of which all were fatal. Although it is not found how many of these accidents were due to a mechanical failure, it is known that at least one of them was due to alcohol abuse by the pilot. Based on this figures it can be concluded that the biggest hazard of aerobatics is a pilot error. Although this is partially preventable by the design of the aircraft, by a clear cockpit lay out and well balanced controls, a large part of those accidents can not be prevented by certain design choices.

It is in the very nature of aerobatics to be risky, but the aircraft should be designed with such tolerances, such that the risk of an accident due to mechanical failure is minimised as is done in Chapter 6. Furthermore design choices are made such that the crash characteristics of the aircraft are optimised. For example when designing the fuel system, the fuel tank will always be in front of the pilot, such that in case of a hard deceleration during a crash landing, the pilot will not get crushed by the fuel tank or be drained in fuel due to a rupture.

A major advantage of the design *StefX* over its competitors regarding safety is the fact that *StefX* has a significantly lower stall speed due to its high lift devices. The lower stall speed results in a lower landing distance as explained in Section 9.2. This greatly improves the odds of surviving an emergency landing, for example due to an engine failure, as it increases the number of fields that can be used as emergency landing spots.

---

<sup>3</sup>URL [http://www.victor-aviation.com/Frequently\\_Asked\\_Questions.php#how\\_long](http://www.victor-aviation.com/Frequently_Asked_Questions.php#how_long)

## 8.5 Sustainable Development Strategy

The sustainable development strategy aims at implementing sustainability in the design phase for the entire life cycle of the *StefX* aerobatic aircraft. During the design of *StefX*, attention is paid to the influence of the design choices to the sustainability of the aircraft. The sustainable development strategy has been updated with respect to the Midterm Report [3], more detail is added where possible.

The tools selected for sustainable development are CES Edupack and the Sustainability Checklist. CES Edupack is a software tool available to TU Delft students that allows calculations on the carbon footprint and energy used for production, transport, use and disposal of a certain product. It has a dedicated aerospace materials database which makes this tool applicable for this project. The Sustainability Checklist is a tool for the Sustainability Manager to overview the areas and aspects where sustainability can be applied. This helps the Sustainability Manager to check the efforts towards sustainability of the design team. More information on the sustainability checklist as well as a more detailed definition of sustainability and more information on organisational approach for sustainability can be found in the Project Plan [1].

As described in the approach to sustainability in the Project Plan [1], the Sustainability Manager made sure that sustainability would be a trade-off criterion in the Midterm phase [3], but also in the material selection for this phase of the design 6.1. Sustainability can be applied to a certain extent for the manufacturing of the *StefX* aircraft. Requirements on energy and material usage and origin were made and can be found in the baseline report [2].

The team will try to improve product sustainability by improving the lifetime of the aircraft by considering durable materials for all parts of the aircraft. The team will investigate if it is for example more sustainable to use more sustainable materials that need to be replaced after a certain moment in time or to use a 'less' sustainable material that lasts much longer. The team will also make an effort to increase the number of flying hours before maintenance has to take place. Since maintenance often requires replacement of certain parts or fluids, increasing the flying hours in between maintenance implies less replacements of parts and fluids.

In the final design phase, the tools will be used to select sustainable materials if they meet the performance requirements. Furthermore, in the selection of the manufacturing processes, attention is paid to sustainability as well. Data found on the carbon footprint, energy and water usage can be found in Table 8.1, the mass part is present in this table since the carbon footprint, energy and water usage are directly related to the mass of the aircraft part. It was chosen to use tape laying as the production method for the *StefX*. Compared to production methods for aluminium alloys very little energy is needed, less expensive tooling is needed and less waste is being generated. The weight of each of the parts can be found in Chapter 6. The requirements on emission and noise will be validated using data obtained from the engine manufacturer.

The total values in Table 8.1 for the energy usage can be compared to an average household. An average household uses 4000 kWh in one year<sup>4</sup>. This would mean the production of one *StefX* aircraft will have the same energy usage as 2.57 households. A similar analysis can be made for the carbon footprint. The production of 1 kg of cattle meat produces 9.5 kg of CO<sub>2</sub><sup>5</sup>. This would mean that the carbon footprint of the production of one *StefX* would be the same as the carbon footprint of the production of 266 kg of cattle meat. Finally the water usage can also be analysed and is compared to the volume of water in an Olympic swimming pool, which holds 2500000 l. The production of one *StefX* would only use 7.47 % of this volume.

During the selection of production process, attention will be paid to the amount of energy used for a certain process. This will be a selection criterion for the production process.

The production facility will be equipped with solar panels to produce a part of the used energy of the facility. The other electricity needed will be provided by a known energy supplier of green energy (wind energy, etc.). Measures will be taken to limit the unnecessary use of energy, such as a central system turning of machines, lights and computer that do not need to work overnight.

Considering the production phase of the aerobatic aircraft, an effort will be made to produce most parts, if not all, in the same location to minimise transportation of parts. The chosen production method will also allow this, see Section 6.6. The company which supplies the raw materials will be located within Europe. The

<sup>4</sup> <https://www.ovoenenergy.com/guides/energy-guides/how-much-electricity-does-a-home-use.html>

<sup>5</sup> [https://www.researchgate.net/publication/278730159\\_Carbon\\_Footprint\\_of\\_Beef\\_Cattle](https://www.researchgate.net/publication/278730159_Carbon_Footprint_of_Beef_Cattle)

	Total Mass	Energy Usage [MJ]		
	[kg]	Primary production	Manufacturing	Total
Main Wing	88	23144	293	23437
Horizontal Tail	7.60	1998	25.30	2023.6
Vertical Tail	2.83	744	9.42	753.4
Fuselage	40	10520	133.2	10653.2
Landing Gear	2	193	19.42	212.22
Total	140.4	36599	480	37079
	Total Mass	CO2 footprint [kg]		
	[kg]	Primary production	Manufacturing	Total
Main Wing	88	1575	23.41	1599
Horizontal Tail	7.60	136	2.02	138
Vertical Tail	2.83	50.64	0.753	51.4
Fuselage	40	716	10.6	727
Landing Gear	2	10.82	1.55	12.37
Total	140.4	2488	38.38	2527
	Total Mass	Water Usage [l]		
	[kg]	Primary Production	Manufacturing	Total
Main Wing	88	117920	555	118475
Horizontal Tail	7.60	10181	47.94	10229
Vertical Tail	2.83	3791	17.85	3808
Fuselage	40	53600	252	53852
Landing Gear	2	398	17	415
Total	140.4	185890	891	186782

Table 8.1: Carbon footprint, energy and water usage for the production of the *StefX*.

transportation will happen by rail or sea freight.

The structural engineers aimed to minimise the environmental impact of the disposal of the aerobatic aircraft at the end-of-life phase, by selecting materials and parts that can be downcycled. The aerodynamics department minimised drag without sacrificing performance, this results in less fuel consumption, which is beneficial for both an economic and ecologic point-of-view. The propulsion department chose for a composite prop since it is way lighter and not susceptible to corrosion. This will allow the propeller to be used for an increased amount of time.

The employees of *StefX* will be enforced to use sustainable initiatives such as Ecosia. This is a search engine from which all profits This is a passive method to support the environment.

# Chapter 9

## Performance

This chapter discusses the performance of the *StefX*. It states the regulatory V-speeds in Section 9.1. The airfield performance is discussed in Section 9.2. Moreover, the climb and cruise performance are discussed in Section 9.3. The flying and handling qualities are stated in Section 9.4. Section 9.5 discusses the manoeuvrability of *StefX* in terms of angular rates. Section 9.6 discusses the effectiveness of the control surfaces during stall.

### 9.1 Regulatory V-speeds

Two requirements were set for the stall speed. The stall speed of the *StefX* for clean configuration and fully deployed HLD configuration has been determined using the lift equation. The stall speeds can be found in Table 9.1. In addition, the manoeuvring speeds are presented. The manoeuvring speeds were determined by multiplying the stall speed by  $n_{max}$ . The stall speed and manoeuvring speed were needed for various calculations in this report. The design cruise speed was determined in Section 5.6. From the design cruise speed, the never exceed speed was calculated according to CS23.1505 [4].

V- speed	
$V_{stall_{clean}}$	27.7 m/s
$V_{stall_{HLD}}$	20.1 m/s
$V_{A_{clean}}$	87.6 m/s
$V_{A_{HLD}}$	63.6 m/s
$V_{C_{design}}$	82.8 m/s
$V_{NE}$	115.5 m/s

Table 9.1: *StefX* V-speeds

### 9.2 Airfield Performance

The airfield performance consists of take-off, landing and taxi performance. The methodology for the analyses on these performance are explained in this section. As well as the performance of *StefX*.

**Take-off Performance** The take-off distance for the *StefX* has been calculated. This was done to confirm that the *StefX* meets the requirement for a take-off distance of 400 m. The take-off consists of a ground run and an airborne phase. The aircraft becomes airborne at a speed of  $V_{LOF}$ . This speeds has to be at least 1.05  $V_{s_{tall}}$  [4]. The take-off is completed when the aircraft has reached the screen height. For aerobatic aircraft the screen height is 15 m [4].

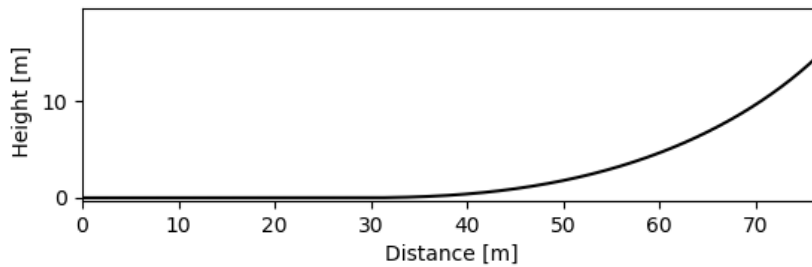
The time to accelerate from a stand still to  $V_{LOF}$  is a measure for the time for the ground roll of the take-off. During the take-off, maximum thrust will be applied and the slats and flaps will be extended. The reduction of the normal force on the tires because of the production of lift, and thus the ground friction, is not incorporated. By using this assumption the time and distance needed for the ground run will be longer than in reality. In addition, no wind has been assumed. A rolling friction coefficient of 0.04 has been used for the calculation of the ground run [48].

For the analysis of the aircraft after lift-off until screen height, the equations of motion have been used as shown in Equation (9.1). At this phase of the take-off, full thrust will still be applied and the aircraft will have an angle of attack corresponding with the maximum lift coefficient.

The sum of the distance covered during the ground roll and airborne phase, is the total take-off distance. For maximum take-off performance HLDs will be deployed. For this condition the take-off distance of the *StefX* is shown in Table 9.2. In addition, the time required for take-off is shown as well as the rotational speed and velocity at screen height. The take-off trajectory of the *StefX* is visualised in Figure 9.1.

$$T \cos(\alpha) - D - W \sin(\gamma) = m(\dot{V}) \quad L - W \cos(\gamma) + T \sin(\alpha) = mV\dot{\gamma} \quad (9.1)$$

Performance parameter	Value <i>StefX</i>
Take-off distance	77 m
Take-off time	5 s
Rotational speed	21 m/s
Velocity at screen height	25 m/s

Table 9.2: Summary of the *StefX* take-off performance.Figure 9.1: The *StefX* take-off trajectory.

**Landing Performance** A landing distance requirement of 550 m had been set. Similarly to the take-off, the landing consists of different phases. The first phase starts at screen height, which is 15 m [4]. At this height, the aircraft should have a speed of at least  $1.3 V_{SO}$ . The next phase is the flare. The radius of the flare depends on the normal force at touchdown, the equation for the radius of the flare can be seen in Equation (9.2) together with the equation for the flare height. After the touchdown the aircraft has to slow down, this phase is the ground run. In this phase a braking force will be applied increasing the ground friction to 0.4 taken from [18]. Furthermore, not thrust will be applied. The total distance covered in these three phases is the landing distance. A summary of the landing performance can be seen in Table 9.3. The landing trajectory of the *StefX* is visualised in Figure 9.2.

$$R = \frac{V^2}{g(n-1)} \quad h_f = R - \cos(\gamma_a) \quad (9.2)$$

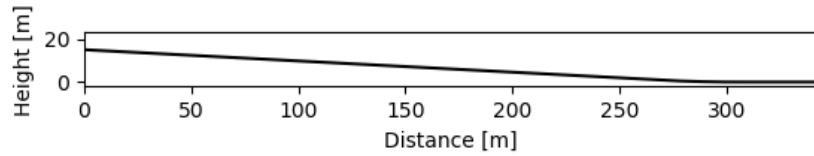
Performance parameter	Value <i>StefX</i>
Velocity at screen height	26 m/s
Landing distance	345 m
Landing time	20 s

Table 9.3: Summary of *StefX* take-off performance.

**Taxi Performance** To ensure that the *StefX* is able to do a  $180^\circ$  turn on a runway during taxiing, a requirement was set that the *StefX* shall be able to have a turn rate of  $15^\circ/s$  during taxi with a velocity of 5 kts. With Equation (9.3) it was calculated that the tail wheel deflection required to get a turn rate of  $15^\circ/s$  is almost  $30^\circ$ .

$$\dot{\psi} = \frac{V}{l_{wheelbase}} \tan(\delta_{tailwheel}) \quad (9.3)$$

However this does not take into account any effect of wheel slip. To take this into account a python program was made, which would calculate the forces generated by the tires at each time step. To calculate the

Figure 9.2: The *StefX* landing trajectory.

forces generated by the tire due to side slipping of the tire Equation (9.4) [20] was used in which the cornering stiffness coefficient was calculated using [25] to be 0.15. As [25] claims to have an error margin of 30 % the turn rate was calculated for this range to check if it would still meet the requirements.

$$F_y = C_{c_{tail}} \cdot N_{tail} \cdot \cos(\delta_{tailwheel}) \quad (9.4)$$

From the simulation it became clear that the *StefX* will reach the required turn rate at two seconds after deflecting the tail gear, in which it was assumed that the tail wheel would be fully deflected within half a second. To check if this is fast enough to meet the requirement, the turn radius was also calculated, which was determined (at the worst case of the cornering stiffness coefficient) to be 7 m which is less than half of most runways, and therefore it was concluded that the *StefX* will meet this requirement.

### 9.3 Climb and Cruise

**Sustained Climb** The customer had a requirement for a minimum sustained climb angle. This angle should at least be 45 deg. The climb angle indicates how many horizontal distance is needed for a vertical displacement as shown in Equation (9.5). If the climb angle is sustained, the angle and the velocity stay constant. Moreover, the angle of attack was assumed to be small. This makes it possible to rewrite the equations of motion to Equation (9.6). The maximum climb angle that can be sustained depends on the power available and the lift coefficient. The required angle of attack and thrust for an arbitrary climb angle can be calculated by Equation (9.7). If the required angle of attack is higher than the stall angle of attack, the climb angle can not be sustained. The same holds for the required thrust. If the required thrust is higher than the maximum thrust, the angle can not be sustained. Table 9.4 summarises the climb performance. The maximum sustained climb angle is achieved just above stall speed at a velocity of 21 m/s, with HLD deployed and having 15 kg of fuel left. The lower the fuel level, the higher the possible sustainable climb angle. After take-off with a mass equal to the MTOW, a climb angle of 39° can be sustained. The maximum sustained climb angle at each speed between  $V_{stall}$  and  $V_A$  is displayed in Figure 9.3. Note that this graph is not smooth due to floating point errors.

$$\dot{h} = V \sin(\gamma) \quad \dot{x} = V \cos(\gamma) \quad (9.5)$$

$$T - D - W \sin(\gamma) = 0 \quad 0.5\rho V^2 SC_{L\alpha} \alpha - W \cos(\gamma) = 0 \quad (9.6)$$

$$\alpha_{req} = \frac{W \cos(\gamma)}{0.5\rho V^2 SC_{L\alpha}} \quad T_{req} = D + W \sin(\gamma) \quad (9.7)$$

Performance parameter	Value <i>StefX</i>
Maximum sustained climb angle	45°
	21 m/s
Maximum sustained climb angle after take-off	37°

Table 9.4: Summary of the *StefX* climb performance.

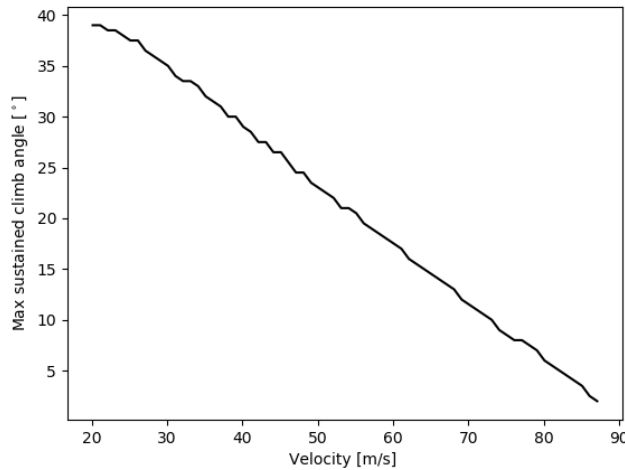


Figure 9.3: Maximum sustained climb angle at speeds between  $V_{stall}$  and  $V_a$  at MTOW and HLD deployed.

	Value	Unit
Center fuel tank volume	75	L
Wing tanks volume	207	L
Total fuel volume	282	L
Endurance at full power	71	min
Maximum range	1417	km

Table 9.5: Fuel volumes, range and endurance

**Ferry Range** The fuel volumes and corresponding range and endurance are presented in Table 9.5. Note that the range takes into account legally required reserves.

**Cruise Speed** The design cruise speed was determined in Section 5.6 to be 161 kts. This is consistent with the requirements on design cruise speed in CS23.335, which states that the design cruise speed in knots may not be less than  $36\sqrt{W/S}$  for aerobatic aircraft, where  $W/S$  is the wing loading in  $lb/ft^2$ . Using a wing loading of  $596 N/m^2$  ( $12.4 lb/ft^2$ ), the minimum cruise speed is 127 kts.

## 9.4 Flying and Handling

The flying qualities were calculated in Section 3.1. In Table 9.6 the level of flying quality of each eigenmotion, as well as the CAP can be found.

Motion	Level
CAP	Level 1
Short Period	Level 1
Phugoid	Level 2
Aperiodic roll	Level 1
Dutch roll	Level 2
Spiral	Level 1

Table 9.6: Level of flying qualities

As can be seen in Table 9.6 the flying qualities of the *StefX* are of level 1 for each part, except for the Phugoid and Dutch roll. This is not a problem for meeting the requirements, as these motions span a long time, and are therefore of less importance for aerobatic flying. For the system requirements it was deemed enough to have those eigenmotions stable, which they are.

## 9.5 Manoeuvrability

With the size of the entire aircraft, the weight and the c.g. location known, the performance in roll, pitch and yaw can be simulated using the simulation as described in Section 3.2.1. The simulations were performed starting from trim condition at manoeuvring speed and sea-level density. The three angular velocities were individually analysed and pure motions were assumed. That is, a pure roll motion is assumed to generate no yaw motion and a pure yaw is assumed to generate no roll motion. Finally, no wind or other disturbances were included.

**Roll** Figure 9.4 shows the roll rate for an aileron deflection of  $30^\circ$  after one second. The maximum sustained roll rate  $463^\circ/\text{s}$ . The instantaneous roll acceleration is  $9.690^\circ/\text{s}^2$ . It should be noted that this roll acceleration will not be achieved in the real aircraft since the aileron deflection is a instantaneous step input. The additional yawing moment created due to this roll motion is  $2.390\text{ N}$  and should be balanced with a rudder input.

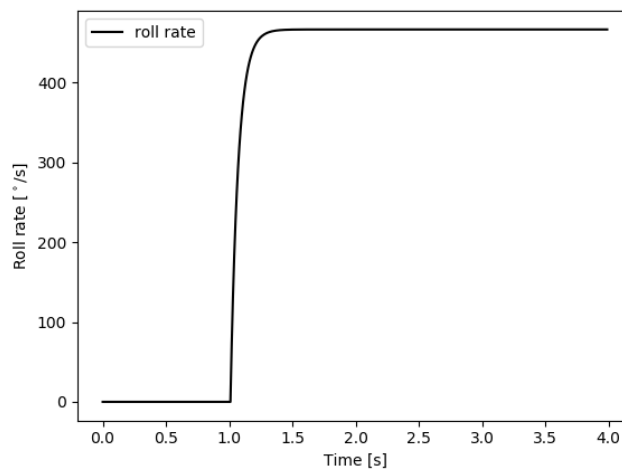


Figure 9.4: Roll rate for  $\delta_a = 30^\circ$  at 1 s.

**Pitch** Figure 9.5 shows the pitch rate for an elevator deflection of  $-25^\circ$  after two seconds. The initial pitch rate is  $66^\circ/\text{s}$  and the maximum sustained pitch rate  $25^\circ/\text{s}$ . The instantaneous pitch acceleration is  $1.286^\circ/\text{s}^2$ . It should be noted that this pitch acceleration will not be achieved in the real aircraft since the elevator deflection is a instantaneous step input.

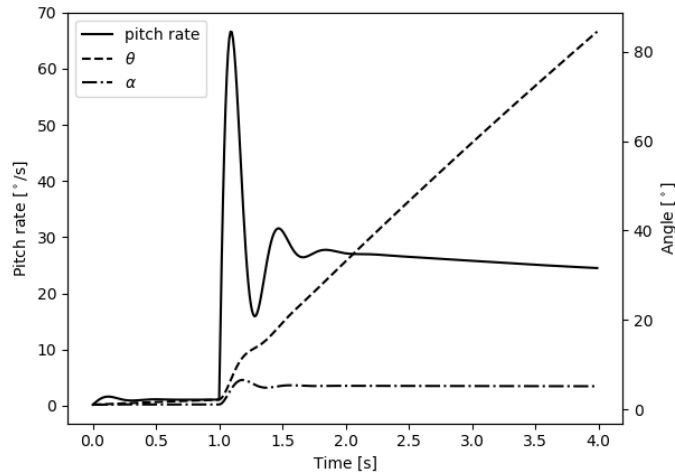
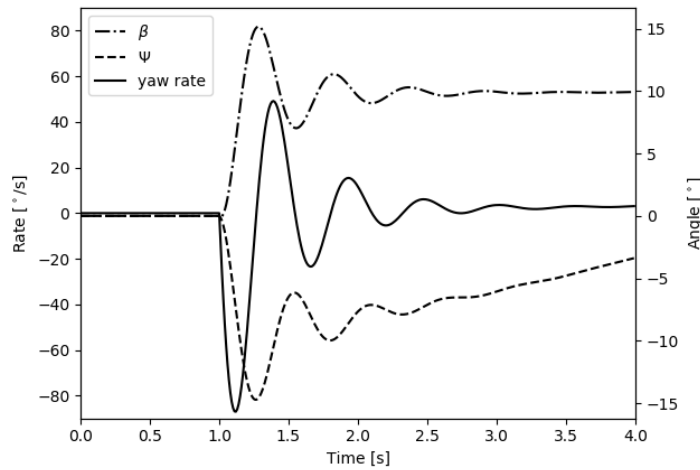
**Yaw** Figure 9.6 shows the yaw rate for a rudder deflection of  $25^\circ$  after two seconds. The maximum initial yaw rate is  $-87^\circ/\text{s}$ . The instantaneous roll acceleration is  $-23^\circ/\text{s}^2$ . The rudder deflection necessary to counteract to addition yaw moment created due to roll is only  $3^\circ$ .

## 9.6 Control Effectiveness during Stall

During stall, the aircraft losses a big part of its control effectiveness since the control areas are no longer immersed in the airflow. *StefX* however has a propeller in front of the aircraft, and this propeller also produces some airflow over the wing and empennage. In this section, the control effectiveness *StefX* has in stall due to the propeller flow was calculated.

As a first step, the area of control surface immersed in the propeller slipstream is determined. The radius of this contracted slipstream is found using Equation (9.8) [40].

$$R_s = R_p \sqrt{\frac{1+a}{1+a\left(\frac{x}{\sqrt{R_p^2+x^2}}\right)}} \quad (9.8)$$

Figure 9.5: Pitch rate for  $\delta_e = -25^\circ$  at 1 s.Figure 9.6: Yaw rate for  $\delta_r = 25^\circ$  at 1 s.

Here,  $V_0$  is the speed of the manoeuvre, which will be equal or less than the stall speed and  $a$  is the ratio of propeller induced axial velocity over  $V_0$ . The slipstream radius varies with distance from the propeller in axial direction (x-direction).

Based on this varying slipstream radius  $R_s$ , the immersed control surface area is calculated using a python script. The results can be found in Table 9.7.

With the effective areas during stall and the experienced velocity, the flight dynamic simulation could be ran for a stall condition. The aileron loses a great part of its effective area during stall. The roll rate that can be obtained is neglectable small compared to the roll rates that can be obtained during normal flight. The rudder stays fully effective during a stall but the experienced velocity is greatly reduced. During a low speed stall, an instantaneous yaw rate of  $11^\circ/\text{s}$  could be obtained. In this case, the aircraft would convert to a sideslip angle of  $-1.8^\circ$ .

## 9.7 Propulsion

The propeller converts the engine power to thrust. This is dependent on parameters like speed, power output, and propeller pitch. The propeller itself was designed in Section 3.3, and also the method can be found here.

Stall	$V_0$ [ms <sup>-1</sup> ]	$V_a$ [ms <sup>-1</sup> ]	$R_s$ range[m]	$S_{a_s}$ [m <sup>2</sup> ]	$S_{e_s}$ [m <sup>2</sup> ]	$S_{r_s}$ [m <sup>2</sup> ]
	30	21.77	0.8 - 0.95	0.27	0.64	0.57
Full control surface	$V_0$ [ms <sup>-1</sup> ]	$V_a$ [ms <sup>-1</sup> ]	$R_s$ range[m]	$S_a$ [m <sup>2</sup> ]	$S_e$ [m <sup>2</sup> ]	$S_r$ [m <sup>2</sup> ]
	94	2.67	0.93 - 0.95	2.677	1.31	0.57

Table 9.7: Control surface immersed in propeller slipstream during stall with comparison to full control surface areas.

**Static Thrust** All the geometry is now set, and the analysis can be done. The static thrust is first calculated. This is done using the Rankline-Froude Momentum Theory from [22]. The maximum static thrust is calculated from an empirical adaptation from the formula to calculate the maximum static thrust. The maximum static thrust is 5902 N. This value is used to verify the BET at low speeds. The thrust value at low speeds has to be comparable to, but lower than, the maximum static thrust. The static thrust can be calculated from the Formula (9.9) from [22].

$$T_{Static} = 0.85P^{2/3}(2\rho A_{Disk})^{1/3}\left(1 - \frac{A_{Spinner}}{A_{Disk}}\right) \quad (9.9)$$

**Results** The next part is to calculate the lift and drag of the airfoil. To do this the induced angle of attack has to be calculated. This is done using the Newton method for iteration. When the induced velocity converges, the efficiency, thrust, power needed, and the torque can be calculated. This is then done for a range of pitch angles, until the highest possible power value is reached of 235 kW for the engine. As can be seen from the results in Figure 9.7a, the thrust at low speeds comes close to the value for static thrust. Furthermore, the faster the aircraft flies, the smaller the thrust values becomes. The efficiency, however, becomes larger as the airspeed increases until it reaches a maximum value, as seen in Figure 9.7c. This relates the forward speed with the rotational speed, while the thrust and power coefficient relate quadratic to the airspeed. As can also be seen, there is an optimal speed setting where the efficiency is highest. This is the preferred cruise speed.

Figure 9.7b shows the torque of the aircraft at different air speeds. This torque is almost constant with only some small variations. This is as expected because the analysis is done at maximum power, at which the engine will deliver maximum torque. The torque will be used to evaluate the gyro effect the propeller induces. Figure 9.7d shows at which pitch angle the maximum power needed is achieved. This pitch angle is the pitch at the hub of the propeller. The pitch decreases towards the tip of the propeller, which is in a more flat position. The faster the aircraft flies, the more the propeller is able to turn into the wind. This can be used as an indication of optimal pitches at different air speeds. In addition to these values, some additional values can be calculated from this method. The BET relies on calculating the induced angle of attack in order to make the results more accurate. This induced angle of attack can then be used to compute the induced velocity in the airflow. The induced velocity of the propeller at the tip and at the hub are plotted in both the direction of the free stream, and perpendicular to it in Figure 9.8. The propeller can be analysed further in order to create the throttle control for every speed, and create a pitch range for every speed, but that is deemed out of the scope of this project.

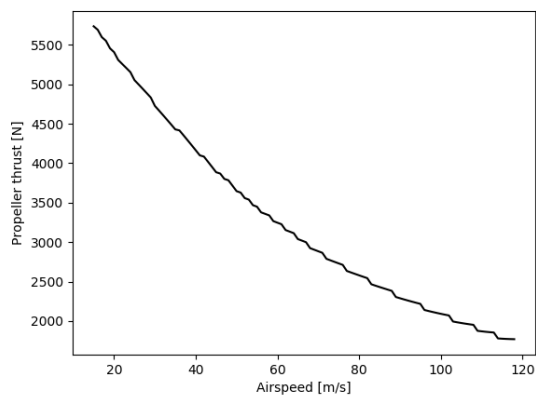
## 9.8 Gyroscopic Effects

The propeller of an aircraft is a rapidly rotating object with a significant mass moment of inertia. This makes it behave like a gyroscope, which introduces unexpected behaviour in both the structural loading and the handling of the aircraft. This effect is relatively large in aerobatic aircraft, which are very lightweight and have a relatively large propeller.

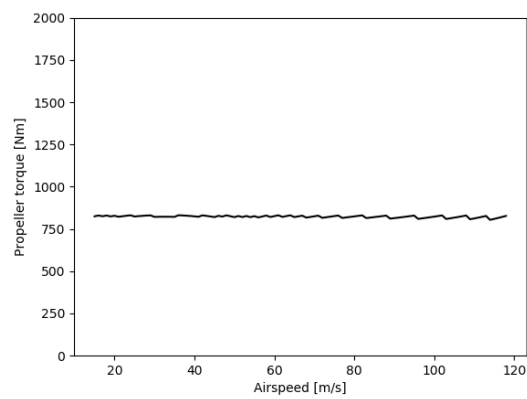
To calculate the gyroscopic effects, equations were derived from the general equations of motion for rigid bodies in three dimensions, Equations 9.10 [26].

$$\begin{cases} \sum M_x = I_x \dot{\omega}_x - I_y \Omega_z \omega_y + I_z \Omega_y \omega_z \\ \sum M_y = I_y \dot{\omega}_y - I_z \Omega_x \omega_z + I_x \Omega_z \omega_x \\ \sum M_z = I_z \dot{\omega}_z - I_x \Omega_y \omega_x + I_y \Omega_x \omega_y \end{cases} \quad (9.10)$$

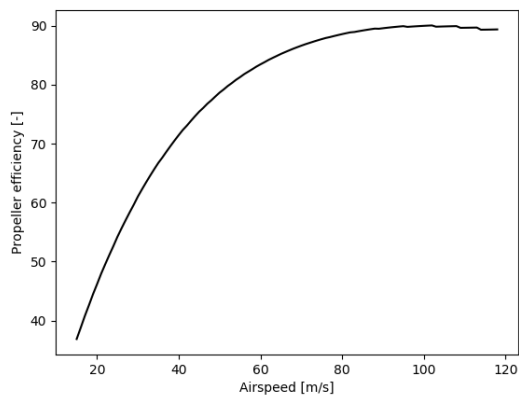
These equations were then applied to 2 objects (the propeller and the rest of the aircraft), see Equations 9.11. The subscript  $p$  stands for propeller, the subscript  $a$  stands for aircraft.



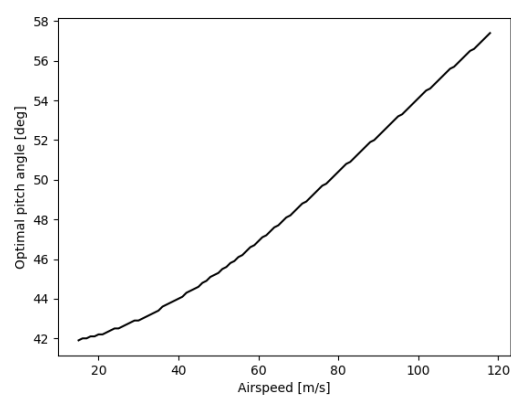
(a) Propeller thrust vs. free stream velocity.



(b) Propeller torque vs. free stream velocity.

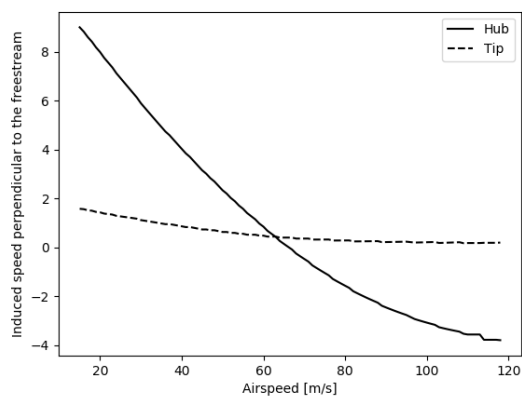


(c) Propeller efficiency vs. free stream velocity.

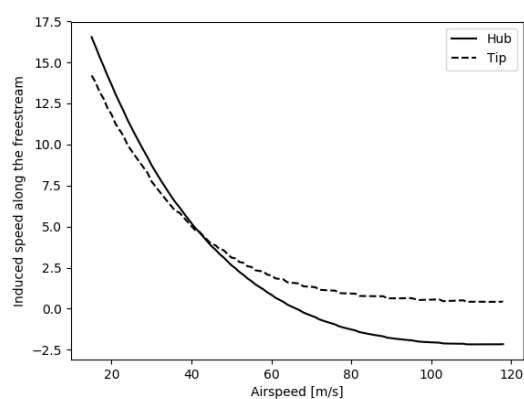


(d) Optimal propeller pitch vs. free stream velocity.

Figure 9.7: Comparison of both propeller airfoils.



(a) Induced airspeed perpendicular to the freestream velocity.



(b) Induced airspeed along the freestream velocity.

Figure 9.8: Induced velocities at the hub and tip of the propeller.

$$\begin{cases} \sum M_x = I_{x_p} \dot{\omega}_{x_p} - I_{y_p} \Omega_{z_p} \omega_{y_p} + I_{z_p} \Omega_{y_p} \omega_{z_p} + I_{x_a} \dot{\omega}_{x_a} - I_{y_a} \Omega_{z_a} \omega_{y_a} + I_{z_a} \Omega_{y_a} \omega_{z_a} \\ \sum M_y = I_{y_p} \dot{\omega}_{y_p} - I_{z_p} \Omega_{x_p} \omega_{z_p} + I_{x_p} \Omega_{z_p} \omega_{x_p} + I_{y_a} \dot{\omega}_{y_a} - I_{z_a} \Omega_{x_a} \omega_{z_a} + I_{x_a} \Omega_{z_a} \omega_{x_a} \\ \sum M_z = I_{z_p} \dot{\omega}_{z_p} - I_{x_p} \Omega_{y_p} \omega_{x_p} + I_{y_p} \Omega_{x_p} \omega_{y_p} + I_{z_a} \dot{\omega}_{z_a} - I_{x_a} \Omega_{y_a} \omega_{x_a} + I_{y_a} \Omega_{x_a} \omega_{y_a} \end{cases} \quad (9.11)$$

The axis system used is fixed to the aircraft. The x-axis is placed at the centre of the propeller, pointing rear through the driveshaft. The y-axis is pointed up and the z-axis left, both for an aircraft in level upright attitude. Using this axis system, the following simplifications can be applied:

$$\begin{aligned} \omega_{y_p} &= \omega_{y_a} = \omega_y \\ \omega_{z_p} &= \omega_{z_a} = \omega_z \\ \dot{\omega}_{y_p} &= \dot{\omega}_{y_a} = \dot{\omega}_y \\ \dot{\omega}_{z_p} &= \dot{\omega}_{z_a} = \dot{\omega}_z \\ \Omega_{y_p} &= \Omega_{y_a} = \Omega_y \\ \Omega_{z_p} &= \Omega_{z_a} = \Omega_z \\ \Omega_y &= \omega_y \\ \Omega_z &= \omega_z \\ \Omega_{x_p} &= \Omega_{x_a} = \omega_{x_a} \end{aligned}$$

Additionally, the propeller is assumed to be symmetric about both the y- and z-axes, therefore:

$$I_{y_p} = I_{z_p} = I_p$$

This reduces Equations 9.11 to Equations 9.12:

$$\begin{cases} \sum M_x = I_{x_p} \dot{\omega}_{x_p} + I_p (\omega_y \omega_z - \omega_z \omega_y) + I_{x_a} \dot{\omega}_{x_a} - I_{y_a} \omega_z \omega_y + I_{z_a} \omega_y \omega_z \\ \sum M_y = I_p \dot{\omega}_y - I_p \omega_{x_a} \omega_z + I_{x_p} \omega_z \omega_{x_p} + I_{y_a} \dot{\omega}_y - I_{z_a} \omega_{x_a} \omega_z + I_{x_a} \omega_z \omega_{x_a} \\ \sum M_z = I_p \dot{\omega}_z - I_{x_p} \omega_y \omega_{x_p} + I_p \omega_{x_a} \omega_y + I_{z_a} \dot{\omega}_z - I_{x_a} \omega_y \omega_{x_a} + I_{y_a} \omega_{x_a} \omega_y \end{cases} \quad (9.12)$$

Grouping terms and using  $I_p + I_{y_a} = I_{y_{total}} = I_y$  and  $I_p + I_{z_a} = I_{z_{total}} = I_z$ :

$$\begin{cases} \sum M_x = I_{x_p} \dot{\omega}_{x_p} + I_{x_a} \dot{\omega}_{x_a} + (I_{z_a} - I_{y_a}) \omega_z \omega_y \\ \sum M_y = I_y \dot{\omega}_y + (I_{x_a} - I_z) \omega_{x_a} \omega_z + I_{x_p} \omega_z \omega_{x_p} \\ \sum M_z = I_z \dot{\omega}_z + (I_y - I_{x_a}) \omega_{x_a} \omega_y - I_{x_p} \omega_y \omega_{x_p} \end{cases} \quad (9.13)$$

Furthermore, assuming a perfect propeller governor,  $\dot{\omega}_{x_p} = 0$ :

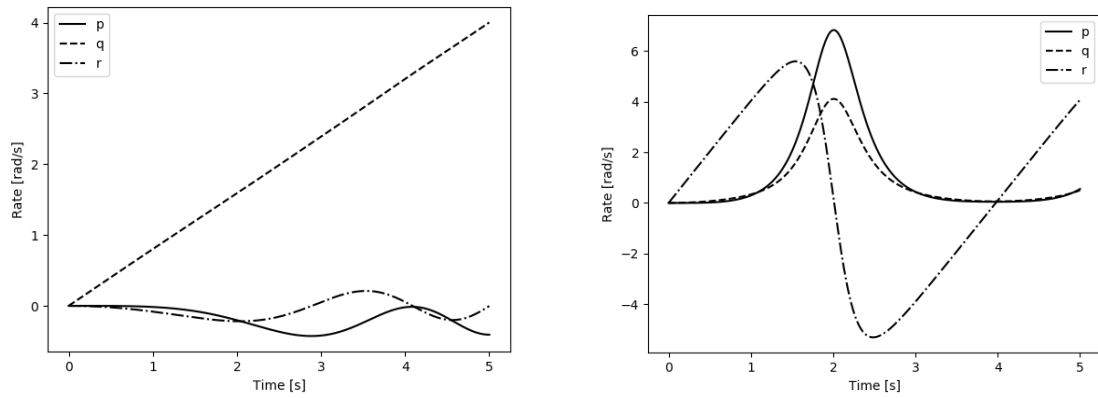
$$\begin{cases} \sum M_x = I_{x_a} \dot{\omega}_{x_a} + (I_{z_a} - I_{y_a}) \omega_z \omega_y \\ \sum M_y = I_y \dot{\omega}_y + (I_{x_a} - I_z) \omega_{x_a} \omega_z + I_{x_p} \omega_z \omega_{x_p} \\ \sum M_z = I_z \dot{\omega}_z + (I_y - I_{x_a}) \omega_{x_a} \omega_y - I_{x_p} \omega_y \omega_{x_p} \end{cases} \quad (9.14)$$

Since this is a nonlinear system of equations, it cannot be solved in a straightforward way. Therefore, a Python package supporting nonlinear dynamic simulation was used [24]. Using Equations 9.14 as input, time responses were simulated for a constant moment of 1500 Nm for the elevator and 5000 Nm for the rudder. These values were checked by simulating the control surfaces using only the propeller slipstream discussed in Section 9.6. The time responses are shown in Figures 9.9 in terms of the angular rates  $p$ ,  $q$  and  $r$ .

It should be noted that these simulations do not take into account gravity or aerodynamic effects such as yaw- roll- and pitch damping. However, it can be concluded that a strong effect is present after a relatively short time, especially when using the rudder. This is an indication that the aircraft is suitable for tumble manoeuvres, however, in further development this simulation should be combined with the model for the flight dynamics presented in Section 3.2.1 to include aerodynamic and gravity effects.

For determining the load introduced by the gyroscopic effect on the fuselage structure, a highly simplified model is used using the following assumptions:

- Aircraft rotations are constant
- Roll rate is zero
- No moments are present in roll



(a) Time response for 1500 Nm constant elevator input      (b) Time response for 5000 Nm constant rudder input

Figure 9.9: Gyroscopic time responses

This simplifies Equations 9.13 to Equations 9.15:

$$\begin{cases} \sum M_y = I_{x_p} \omega_z \omega_{x_p} \\ \sum M_z = I_{x_p} \omega_y \omega_{x_p} \end{cases} \quad (9.15)$$

For the ultimate load case of a 10G pull up, a moment of 207 Nm in yaw was calculated using the following inputs:

- $I_{x_p} = 0.9 \text{ kgm}^2$  (found for a similar propeller <sup>1</sup>)
- $\omega_z = 60^\circ/\text{s}$  (calculated for a 10G pullup at manoeuvring speed)

<sup>1</sup><https://www.mt-propeller.com/pdf/datsheet/mtv-23.pdf>

# Chapter 10

## Compliance

This chapter discusses the compliance matrix. The matrix shows the system requirements. All of the requirements, except for a few, have been discussed previously in the report. The matrix shows where in the report the requirement is discussed. Requirements with a ✓-symbol are met, requirements with a ✖-symbol are considered to be beyond the scope of this design phase and are elaborated upon below.

Identifier	Requirement	Discussed in	Requirement met?
<b>Mass</b>			
STX-SYS-01	The maximum take off mass shall be 1000 kg for the utility category.	Section 6.5	✓
STX-SYS-02	The maximum take off mass shall be 850 kg for the unlimited category.	Section 6.5	✓
<b>Stall</b>			
STX-SYS-03	The aircraft shall have a stall speed that is at least as high as to be determined in CS23.49.	Section 9.1	✓
STX-SYS-04	The aircraft shall have a stall speed of less than 65 kts.	Section 9.1	✓
<b>Speed</b>			
STX-SYS-05	The aircraft shall have a rotation speed ( $V_R$ ) greater than $V_{S1}$ .	Section 9.2	✓
STX-SYS-06	The aircraft shall have a speed at 15 m above the take-off surface of $1.2 V_{S1}$ .	Section 9.2	✓
STX-SYS-07	The reference landing approach speed, $V_{REF}$ shall be at least 1.3 times $V_{S0}$ .	Section 9.2	✓
STX-SYS-08	The minimum control speed, $V_{MC}$ for take-off shall be no more than $1.2 V_{S1}$ .	Section 9.2	✓
STX-SYS-09	Design cruising Speed, $V_C$ shall be in the range specified in CS23.335.	Section 9.3	✓
<b>Performance</b>			
STX-SYS-10	The aircraft shall be able to turn at least $15^\circ/s$ during taxiing with a speed of 5 kts.	Section 9.2	✓
STX-SYS-11	STX-SYS-11: The aircraft shall have at least a steady gradient of climb of 3.3 % in landing configuration.	Section 9.3	✓
STX-SYS-12	The aircraft shall be able to climb at a sustained climb angle of at least $45^\circ$ .	Section 9.3	✓
STX-SYS-13	The ferry range shall not be less than 750 km.	Section 9.3	✓
STX-SYS-14	The aircraft shall have a fly time of at least 30 minutes in aerobatic flight.	Section 5.6	✓
STX-SYS-15	The aircraft shall be able to obtain a roll rate of at least $450^\circ/s$ .	Section 9.5	✓
STX-SYS-16	The pitch rate shall not be less than $20^\circ/s$	Section 9.5	✓
STX-SYS-17	The yaw rate shall not be less than $40^\circ/s$ while flying at 40 kts in a vertical line up.	-	✖
STX-SYS-18	The take-off distance of the aircraft shall be no more than 400 m at sea level.	Section 9.2	✓
STX-SYS-19	The landing distance of the aircraft shall be no more than 550 m at sea level.	Section 9.2	✓
STX-SYS-20	The aircraft shall be able to withstand a $\pm 10$ G limit load.	Section 6.2	✓

STX-SYS-21	The seat shall be able to withstand a 20 G load.	Section 5.1	✓
<b>Control Stability</b>			
STX-SYS-22	The aircraft shall be able to establish a zero rate of descent while at an attitude suitable for a controlled landing and without the use of the primary longitudinal control system.	Section 3.2	✓
STX-SYS-23	The aircraft shall be safely controllable without the use of the primary lateral control system.	Section 3.2	✓
STX-SYS-24	The aircraft shall maintain lateral and directional trim in level flight, in clean configuration.	Section 9.5	✓
<b>Cost</b>			
STX-SYS-25	The maximum unit price of the aircraft shall be \$ 325,000.	Section 7.2	✓
STX-SYS-26	The production of the aircraft shall break even after 8 years of production.	Section 7.1	✓
<b>Additional</b>			
STX-SYS-27	The possibility of egress by parachute shall exist.	Section 5.1	✓
STX-SYS-28	The aircraft shall use an off-the-shelf engine.	Section 2.4	✓
STX-SYS-29	The aircraft shall use a piston engine.	Section 2.4	✓
STX-SYS-30	The span of the aircraft shall be less than 12 m.	Section 2.11	✓
STX-SYS-31	The noise level in the cockpit shall be less than 90 dB.	-	✱
STX-SYS-32	The aircraft shall have a CO <sup>2</sup> emission evaluation metric that conforms with CS23 [5].	Section 5.6	✓
STX-SYS-33	The aircraft shall be limited to 102 EPNdB at measuring points defined in 14 CFR 36.	-	✱
STX-SYS-34	The aircraft shall use standardised rivets and bolts for manufacturing.	Section 6.6	✓
STX-SYS-35	The workers shall not be exposed to hazardous materials during manufacturing.	Section 6.6	✓
<b>Handling Characteristics</b>			
STX-SYS-36 - STX-SYS-41	Requirements STX-SYS-36 upto and including STX-SYS-41 are discarded. In return, the requirements on handling qualities are stated in STX-SYS-44 to STX-SYS-52.		
<b>Pilot</b>			
STX-SYS-42	A pilot of 193 cm or less shall be able to fit in the aircraft.	Section 5.1	✓
STX-SYS-43	The aircraft shall be able to carry a pilot of at least 100 kg.	Section 6.5	✓
<b>Flying and Handling Qualities</b>			
STX-SYS-44	The aperiodic roll shall be of level 1 flying and handling quality.	Section 9.4	✓
STX-SYS-45	The short period shall be of level 1 flying and handling quality.	Section 9.4	✓
STX-SYS-46	The spiral shall be of level 1 flying and handling quality.	Section 9.4	✓
STX-SYS-47	The CAP shall be of level 1 flying and handling quality.	Section 9.4	✓
STX-SYS-48	The dutch roll shall be stable.	Section 9.4	✓

STX-SYS-49	The phugoid shall be stable.	Section 9.4	✓
STX-SYS-50	The aileron control force shall be of level 1 flying and handling quality.	Section 5.2	✓

Requirement STX-SYS-17: This requirements was set-up to verify the proper execution of a hammer-head manoeuvre close to stall speed. The performance analysis of the aircraft with detailed stall characteristics in aerobatic figures have been identified to be outside of the scope of this design phase. Therefore, this requirement could not be checked for compliance.

Requirement STX-SYS-31: This requirement was set-up to avoid hearing damage to the pilot when exposed to the noise of the engine for a period of two hours. The acoustic analysis of the noise generated by the engine which is damped by the canopy has been identified to be outside of the scope of this design phase. Therefore, this requirement could not be checked for compliance. However, reference aircraft with similar engines have proven to meet noise regulations when the pilot is wearing proper headphones.

Requirement STX-SYS-33: This requirement, similar to requirement STX-SYS-31, could not be checked for compliance since an acoustic analysis of the engine noise has been identified to be outside the scope of this design phase.

These three requirements which cannot be checked for compliance raise a development risk which is elaborated upon in Section 12.2.

# Chapter 11

## Sensitivity Analysis

To check if the final design will still meet all the requirements if some of the input values of the analysis change.

For the sensitivity analysis the effect of a change in the mass of the *StefX*, the location of the c.g. and a change in thrust of the aircraft is analysed. At the end also the effect of designing a two seater variant of the aircraft is designed.

### 11.1 Effect on Flying Qualities

First the MTOW was changed from 715 kg to 800 kg and the flying qualities were completely analysed, the same was done from moving the c.g. from 1.65 m to 1.2 m and 1.8 m, the results of these changes can be found in Table 11.1.

	MTOW to 800 kg	c.g. to 1.2 m	c.g. to 1.8 m
CAP	3.9	7.7	2.95
$\zeta_{shortperiod}$ [-]	0.12	0.14	0.087
$\zeta_{phugoid}$ [-]	0.010	0.005	0.004
$T_{caperiodicroll}$ [s]	0.07	0.07	0.07
$\zeta_{dutchroll}$ [-]	0.067	0.073	0.062
$T_{2spiral}$ [s]	108.5	119	117

Table 11.1: Effects of change in mass and c.g. location on the flying qualities of the *StefX*

As can be seen in Table 11.1 is that a c.g. located more to the front then determined at this point in the design process, would be detrimental for the flying qualities of the *StefX*, where a c.g. location that is more aft would actually slightly benefit the flying quality of the *StefX*. A higher maximum take off weight would slightly decrease the flying quality, but would still be manageable. Therefor it is important for the later stages in the design process to still keep close track of the weight and c.g. location. Also measures should be taken to prevent the c.g. moving forward. As a c.g. location moving to the front could prevent the *StefX* of meeting the requirements. A change in thrust and LEHLD effectiveness is not mentioned in Table 11.1 as they do not have a influence on the flying qualities.

Another interesting analysis, is to analyse for what values the *StefX* still meets the requirements. For the CAP to still be level 1, the mass can increase to 780 kg, Ceteris Paribus, to have a CAP that is still within level 1 flying quality. Another boundary for a CAP of level 1 is the c.g. location, as long as it moves no further to the front then to 1.55 m from the nose, the CAP will be still level 1. For the eigenmotions the boundaries for meeting the requirements were not analysed, as even for the value changes in Table 11.1 the *StefX* is still meeting the requirements.

### 11.2 Effect on Performance

After the effects of changing the mass and c.g. location were analysed for the flying qualities, the same was done for the performance of the *StefX*, in this analysis also a change in available thrust and HLD effectiveness was analysed, the results of this can be found in Table 11.2.

As can be seen in Table 11.2 is the maximum climb rate quite sensitive for changes in mass, thrust or HLD effectiveness. This is a requirement that during further design should be watched closely as their is a large risk of not meeting this requirement. Furthermore could a decrease in HLD effectiveness make it difficult to meet requirement STX-SYS-, however after further analysis it became clear, that without any HLD deployed, the landing distance is 540 m, and therefor it would still meet the requirements. The maximum mass the climb rate of 45°/s can be obtained is at a mass of 680 kg, therefor to meet requirement STX-SYS-43, and STX-SYS-12 at the same time, the OEW of the aircraft can only increase with 15 kg, however it could be argued that

	MTOW to 800 kg	c.g. to 1.2 m	c.g. to 1.8 m	Thrust -10 %	$\delta C_{L_{HLD}}$ to 0.2
Climb rate [°/s]	31	45	45	38	37
Take-off distance [m]	142	115	115	121	115
Landing distance [m]	402	380	380	385	520
Max Roll rate [°/s]	460	460	460	460	460
Max Yaw rate [°/s]	82	84	86	87	87
Max pitch rate [°/s]	65	54	75	66	66
Sustained pitch rate [°/s]	20	15	30	25	25

Table 11.2: Effects of change in parameters to the performance of the *StefX*

STX-SYS-12 does not have to be met while flying with a pilot of 100 kg, and that way the OEW could increase more.

### 11.3 Effect of a Two-seater Variant

To give a better estimate if a two-seater variant of the *StefX* is possible, and to estimate what effects it will have on the performance of this variant. For this estimation the extra weight of the extra pilot, as well as the weight of the extra instrumentation, and weight of the longer fuselage is taken into account, as well as the overall effect of the longer fuselage. For this it was assumed the fuselage would be elongated with 1 m and the MTOW (for aerobatics) would increase to 890 kg

	<i>StefX</i>	Two-seater variant
CAP	3.53	6.1
$\zeta_{shortperiod}$ [-]	0.96	0.11
$T_{caperiodicroll}$ [s]	0.067	0.067
Climb rate [°/s]	45	26
Take-off distance [m]	77	164
Landing distance [m]	345	412
Max Roll rate [°/s]	460	455
Max Yaw rate [°/s]	87	83
Max pitch rate [°/s]	66	64
Sustained pitch rate [°/s]	25	21

Table 11.3: Effects of making a two-seater variant on the performance of this variant

As can be seen in Table 11.3 the two seater variant will still be a capable aircraft that has good flying qualities. The two-seater variant shall probably not win in the ultimate category of aerobatic flying, but that is not the point of this variant. However this version will fly good enough to be used as a training aircraft, or to compete in lower category aerobatic competitions. Therefore a two-seater variant is deemed to be a feasible extra variant to enlarge the market for the *StefX*.

# Chapter 12

## Risk

In this chapter, the updated technical budget management will be discussed in Section 12.1. A detailed risk analysis for the post-DSE phase of the project has been performed as well as the identification of the individual risks related to the different subsystems of the *StefX*. A list of the general possible risks can be found in Table 12.2. For some risks, a mitigation strategy has been worked out which can be consulted in Table 12.4. The risks maps before and after applying the risk mitigation strategies are shown in Table 12.3 and Table 12.5.

### 12.1 Technical Budget Management

The technical budgets of the aircraft were determined during a earlier stage of the project. Table 12.1 shows the previously determined values, together with the current values.

	MTOW	Stick force gradient	Roll rate	Yaw rate	c.g. - pilot	Range	Unit cost
First value	850 kg	5kg/G	450 °/s	40 °/s	0.5 m	750 km	\$325,000
Real value	714 kg	5kg/G	463 °/s	87 °/s	0.8 m	1417 km	\$294,800

Table 12.1: Technical budgets as determined at the start of the project.

Some differences can be noted. Most values are better than the first set budgets. Only the distance between the pilot and the c.g. is worse. However, this budget has been adapted because the first value was too small. The maximum distance between pilot and c.g. is now 1 m. The first value of 0.5 m was obtained from interviews with pilots, in which Stijn de Jaeghere mentioned that the distance from the c.g. in the EXTRA was the limit, and that it was 0.5 m, however after more research it became clear that the actual distance between the pilot and the c.g. of the EXTRA 330SC was about 1 m, and therefore the budget was changed. Furthermore, the value for the maximum stick force per G is used as input for the aerodynamic balancing. The range has significantly increased with respect to the first value. This is caused by design choices as stated in Section 5.6. The technical budget is and not crossed. This means the values for the technical budget will be kept the same for the final design phase after the DSE is completed.

### 12.2 Post-DSE risks

In Table 12.3 the risk map can be found. Events 2, 3 and 5 have a catastrophic impact and the TRL is determined to be 5 - 6, and they should thus definitely be mitigated. Events 1 and 15 have a critical impact on the design and the TRL is also determined to be 3 - 4, as a result they should also mitigated. The mitigation strategies associated with these events can be found in table 12.4. Only the events with the highest probability of occurrence and severity are mitigated, since only limited resources and time are available. Some events cannot be mitigated since they are completely external, these events are event 6 and 14.

In Table 12.5, the risk map can be seen after the risk mitigation has occurred. The before mentioned risk mitigation strategies are mentioned during a team meeting and implemented in the DSE. All team members are now aware of these strategies and know how to apply them.

### 12.3 Subsystem Risk

#### 12.3.1 HLDs

Incorporating deployable high lift devices (HLDs) into the design will impose some additional risks due to the addition of a new subsystem. In Table 12.6, these risks are tabulated. However, the HLDs will also reduce the severity of injuries during a forced landing because of the greatly reduced stall speed that can be accomplished when these are deployed. Since the kinetic energy at landing is proportional to the velocity squared, even a slightly lower stall speed will decrease the probability of injuries considerably.

ID	Event	TRL	Severity
1	Unavailability of off-the-shelf parts used in design.	3 - 4	Critical
2	Design does not meet the target audience's requirements	5 - 6	Catastrophic
3	Design is not cost effective to produce	5 - 6	Catastrophic
4	New competitive design steals market share	5 - 6	Critical
5	Prototype aircraft fails to comply with CS23 certification requirements	5 - 6	Catastrophic
6	Data used from external sources is not reliable and/or inaccurate	5 - 6	Critical
7	Cost analysis methods are inaccurate	7 - 8	Critical
8	Time to market underestimated	3 - 4	Marginal
9	Supplier or subcontractor unable to supply the sub components in a timely manner	5 - 6	Critical
10	Contingencies are underestimated	7 - 8	Catastrophic
11	Design has not been fully optimised	1 - 2	Marginal
12	Design is very sensitive to changing requirements	5 - 6	Critical
13	Risk has not been identified	1 - 2	Critical
14	Two-seater version concept is unfeasible	7 - 8	Critical
15	National regulation not met which decreases market size	3 - 4	Critical

Table 12.2: List of possible technical risks before mitigation.

TRL	Colour			
1 - 2	Negligible	Marginal	Critical	Catastrophic
3 - 4				
5 - 6				
7 - 8				
9				

Table 12.3: Technical risk map before mitigation.

In order to mitigate these risks, some extra measures or operating procedures should be established. Some possible mitigation strategies include making sure the pilot is aware of the operational limitations of the system and verify routine checks of the mechanism are carried out during maintenance.

**Avionics** During the operation of the aircraft it is vital to have reliable indications of key flight and engine parameters such as altitude, airspeed, acceleration (G-load), engine pressures and temperatures, ... In order to guarantee the operation and accuracy of these instruments, care should be taken to keep them well maintained and calibrated. For the electronic flight instruments a backup battery is present such that in case of a failure of the electrical system the instruments can still function for a limited time frame.

**Powerplant** One of the biggest risks is the failure of the powerplant. Since the *StefX* is a single engined aircraft, a forced landing will be necessary if the engine can not be restarted. Mitigation strategies include regularly scheduled engine inspection and maintenance, performing proper run-ups and engine checks before each flight and respecting the engine's operational limitations by monitoring the engine instruments during flight. This task is facilitated by including a state-of-the-art engine monitoring system (see Section 5.5) which can monitor every cylinder independently. This will increase the chances of spotting problems early on which will decrease the probability of sudden engine stoppage.

**Airframe structure** Care should be taken not to overstress the airframe during aerobatic manoeuvres. In particular, the 10G limit should be respected as well as the max airspeed limitations. With proper monitoring and energy management during the manoeuvres as well as regular checks of the aircraft structure these risks can be mitigated. This is further facilitated by the two G-meters placed in the cockpit one of which is in the peripheral vision of the pilot while he or she is looking outside. (see Section 5.5)

ID	Reduce Probability of Occurrence	Reduce Severity
1	In order to reduce the probability of this event occurring, reputable suppliers who have a large stock should be chosen. Care should be taken (if possible) not to use obscure or end-of-life components which might be difficult to obtain.	To reduce the severity, an internal production stock system should be established. If a part is known to be unavailable from time to time, a larger buffer stock should be present.
2	A detailed market study has been preformed before the design was finalised. If the market analysis is continuously updated and, where possible, the design is improved to comply with the new demands, the probability of this risk occurring can be reduced. If some details need to be changed after the final design phase due to customer demands, they should be implemented in a timely and cost effective manner.	
3	The reduce the probability of this event occurring, proper production techniques should be chosen that are coherent with the production volume. Other materials should be used where possible if no cost effective production method exists.	
5	The probability of this risk occurring can be reduced by applying proper V&V procedures and by checking if the design complies with all CS23 requirements by for instance using a compliance matrix (see Chapter 10).	
15	This probability can be reduced by using larger margins than the bare minimum values specified by the CS23 requirements. A good example of this is for instance the increased reserve fuel tank volume which is explained in Section 5.6.	

Table 12.4: Risk mitigation strategies.

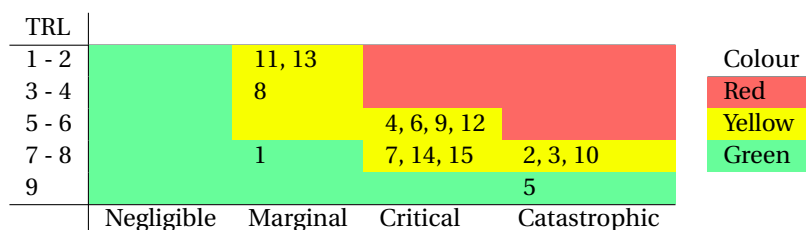


Table 12.5: Technical risk map after mitigation.

ID	Event	TRL	Severity
1	Motion disharmony during extension	3-4	Negligible
2	Unexpected deployment	5-6	Critical
3	Stuck actuator(s)	5-6	Marginal
4	Asymmetric deployment	5-6	Marginal
5	Structural failure due to pilot error	7-8	Catastrophic

Table 12.6: Deployable HLDs risks.

# Chapter 13

## Recommendations

In this chapter, an overview will be given of the recommendations and plans for further development of the *StefX*. This overview can also be seen in the project development logic diagram and post DSE Gantt chart in Appendix A.

**Structural Design** In the post-DSE phase still a lot of work should be spend on the structural design of the *StefX*. A lot of components are not yet designed, such as the engine mounts, engine cowling, ... A more detailed structural analysis of the fuselage, landing gear, etc. will still need to be performed. For the structural analysis of the wing, buckling was not taken into account yet, this should also be incorporated in the final design of the *StefX*. Smaller cutouts in the wing and fuselage are neglected until now, but will be analysed in the next phase.

It was now assumed that that the material will use a quasi-isotropic lay-up. It was chosen to do this, to make sure the structure will not fail due to any forces that are not taken into account. If the wing box is built a destructive test can be performed. Using the data obtained from strain gauges from the destructive test, a more precise and correct strain distribution will be obtained. This data can then be used to alter the fibre orientation in the material, which will allow the weight of the structure to decrease.

A more detailed analysis of the landing gear is needed. In this report the structural strength of the landing gear is calculated by assuming a certain deceleration experienced by the plain in case of a hard landing. To more accurately analyse if the landing gear is strong enough, the landing should be designed based on the maximum vertical velocity the plane is allowed to have at landing by regulations.

Furthermore, a thorough analysis of shock absorbing structures and materials will be performed for the design of a crash worthy seat for the pilot.

**Aerodynamic Design** In Section 4.4, a vortex ring method was used to simulate the flow around the wing. This model is relatively elementary still, although a clear plan may be laid out in order to improve the accuracy of the model:

1. The fuselage may be modelled relatively easily, using e.g. source panels.
2. The aircraft may be integrated as a whole, that is, simulating the aerodynamic surfaces and the fuselage simultaneously, so that their interference effects become clear.
3. Spades may be added to the aileron, so that aerodynamic balancing of the aileron becomes possible without shifting the hingeline as much aft.
4. Vortex wake roll-up may be simulated, as this would increase the accuracy with regards to the interference between the main wing and the empennage.
5. The aerodynamic surfaces may be modelled as thick surfaces, rather than the current assumptions of them having negligible thickness.
6. Unsteady flow effects may be added relatively straightforwardly: an ansatz has already been provided with the work performed on the unsteady airfoil simulation of Subsection 4.4.2; this can relatively straightforwardly be extended to 3D, and significant work has already been performed in this respect, although due to limited resources it was not ready for integration into the design process so far. Nonetheless, it shows extremely promising characteristics: once the pressure forces over the entire aircraft are known based on the unsteady flowfield, it is trivial to compute the moments and forces acting on it, after with simple kinetics and kinematics, the flowfield at the next timestep may be computed. This way, a very detailed analysis of the flight dynamics of the entire aircraft in six degrees of freedom may be obtained.
7. Propeller flow may be added to the simulation.

The aforementioned proposals are all relatively straightforward to implement. More challenging is the implementation of viscous effects, although several proposals have been mentioned in Chapter 15 of [28]. It may be appropriate to instead use already existing CFD software, such as ANSYS. Such a CFD analysis will also be used to optimise the fuselage shape for better aerodynamic properties. Furthermore, the CFD analysis

---

will allow detailed calculation of the forces acting on the slat system. These forces on their turn are needed to size and design the slat actuation system.

**Control and Stability** A CFD analysis could improve the accuracy of the stability derivatives, and therefore the estimation of the flying qualities. The aerobatic figures could be analysed by coupling the equations of motion in order to have a full dynamic model of the aircraft. A more accurate model for the stall characteristics of the wings could be implemented to simulate complete aerobatic manoeuvres, for which the control surfaces could be optimised.

**Aircraft Systems** For the design to mature to production, a lot of detailing is needed in the aircraft systems department. This work includes detailed design of the control linkage parts (e.g. sizing bell-cranks and choosing bearing sizes), choosing suitable actuators for the HLDs, making wiring diagrams, choosing suppliers for parts for several subsystems and detailed design of the engine mount structure.

# Chapter 14

## Conclusion

The goal of this project was to design an aerobatic aircraft that is better than everything currently out there. The *StefX* has been designed to win the Unlimited Aerobatic competition. After this final design phase and elaborate analysis of the performance of the *StefX*, it can be shown that the *StefX* beats the competition and is thus able to win Unlimited Aerobatic Championships.

The *StefX* distinguishes itself from all other aerobatic aircraft by the innovative use of HLDs. The main wing is equipped with both leading and trailing edge HLDs. A system was designed to allow use of the aileron as flaps, and thus flaperons were created. Furthermore, a double slat system is installed in the leading edge, that can be used both in normal as in inverted flight. Together, a lift coefficient increase of 1.098 can be obtained in flight. This reduces the stall speed to 20.1 m/s.

Based on the analysis of control and manoeuvrability of the *StefX*, it can also be concluded that the *StefX* meets all requirements set up in the beginning of the project. Many of these requirements were set to have a better performance compared to the EXTRA 330SC. Meeting the requirements thus implies a better performance than the EXTRA 330SC. The *StefX* has maximum sustained climb angle of 45°, level 1 flying qualities for the CAP, short period, aperiodic roll and spiral and level 2 flying qualities for the phugoid and Dutch roll which proofs exceptional performance. The manoeuvrability of the *StefX* gives a roll rate of 463 °/s, and initial pitch rate of 66 °/s and maximum sustained pitch rate of 25 °/s and a yaw rate of 87 °/s.

The *StefX* has a carbon structure, including a fully carbon monocoque fuselage. The *epoxy/carbon fiber uni-directional prepreg with quasi-isotropic lay-up* is used for the majority of the structure and allows a strong and stiff structure certified for  $\pm 10$  G. The carbon structure is also light, weighing just 140.4 kg. With the Lycoming IO-580 engine and all aircraft systems installed, an OEW of 557 kg and MTOW of 714 kg is obtained.

Based on the performed market analysis, it is estimated that *StefX* will sell 240 aircraft in eight years time. 175 of them will be two-seaters, that will be designed in a next stage. To break even in those 8 years, a unit price of the single seater of \$ 294,800 is estimated.

# Bibliography

- [1] DSE Group 23. Project plan ultimate unlimited aerobatic aircraft. Technical report, TU Delft, May 2018.
- [2] DSE Group 23. Baseline report. Technical report, Delft University of Technology, May 2018.
- [3] DSE Group 23. Midterm report. Technical report, Delft University of Technology, May 2018.
- [4] European Aviation Safety Agency. Certification specifications and acceptable means of compliance for normal, utility, aerobatic, and commuter category aeroplanes cs23. Technical report, European Aviation Safety Agency, July 2015.
- [5] European Aviation Safety Agency. Notice of proposed amendment 2017-01. Technical report, European Aviation Safety Agency, July 2017. <https://www.easa.europa.eu/sites/default/files/dfu/NPA%202017-01.pdf>.
- [6] David Allerton. *PRINCIPLES OF FLIGHT SIMULATION*. John Wiley & Sons, 2009.
- [7] Ever Barbero and John Tomblin. Euler buckling of thin-walled composite columns. *Thin-Walled Structures*, 17(4):237 – 258, 1993. ISSN 0263-8231. doi: [https://doi.org/10.1016/0263-8231\(93\)90005-U](https://doi.org/10.1016/0263-8231(93)90005-U). URL <http://www.sciencedirect.com/science/article/pii/026382319390005U>.
- [8] W. Bihrlé. A handling quality theory for precise flight path control. Technical report, June 1966.
- [9] J.P. Campbell and M.O. McKinney. Summary of methods for calculating dynamic lateral stability and response and for estimating lateral stability derivatives. Technical Report NACA TN-1098, Januari 1952.
- [10] Alan Cassidy. *Better Aerobatics*. Freestyle Aviation Books, 18 Woodhurst Road, Maidenhead, SL6 8TF, England, 1 edition, 2012. ISBN 0954481402.
- [11] Douglas Aircraft Company, D.E. Hoak, and R.D. Finck. *USAF Stability and Control DATCOM*. USAF Stability and Control Datcom. National Technical Information Service, 1975.
- [12] The Goodyear Tire & Rubber Company. *Global Aviation Tires*. 2016.
- [13] Michael V. Cook. *Flight Dynamics Principles*. Elsevier, 2013.
- [14] Granta Design. Ces edupack 2017 version: 17.1.0, 2017.
- [15] R.J. Woodcock D.J. Moorhouse. Military specification: Flying qualities of piloted airplanes. Technical Report MIL-F-8785C, July 1982.
- [16] Lycoming Engines. Io-580-b1a operation and installation manual. Technical report, Lycoming, June 2007.
- [17] T. Yakovich et al. *Exhaust Emissions from In-Use General Aviation Aircraft*. Transportation Research Board, 2016.
- [18] Jonathan Gerthoffert. Modelling of aircraft braking coefficient from imag friction measurements. Technical report, 2014.
- [19] E.K.A. Gill. Slides from ae3211-i systems engineering & aerospace design (2017/18 q3). TU Delft, 2017.
- [20] T.D. Gillespie. *Fundamentals of Vehicle Dynamics*. Society of Automotive Engineers, Inc, 1992.
- [21] W. Gracey. Measured moments of inertia of 32 airplanes. Technical Report NACA TN-780, October 1940.
- [22] S. Gudmundsson. *General Aviation Aircraft Design: Applied Methods and Procedures*. Butterworth-Heinemann, 2013.
- [23] P. H. HAWL. A set of flight dynamic equations for aircraft simulation. Technical report, June 1982.

- [24] John D. Hedengren, Reza Asgharzadeh Shishavan, Kody M. Powell, and Thomas F. Edgar. Nonlinear modeling, estimation and predictive control in APMonitor. *Computers & Chemical Engineering*, 70:133 – 148, 2014. ISSN 0098-1354. doi: <http://dx.doi.org/10.1016/j.compchemeng.2014.04.013>. URL <http://www.sciencedirect.com/science/article/pii/S0098135414001306>. Manfred Morari Special Issue.
- [25] P. Hewson. Method for estimating tyre cornering stiffness from basic tyre information. *Proceedings of The Institution of Mechanical Engineers Part D-Journal of Automobile Engineering - PROC INST MECH ENG D-J AUTO*, 219:1407–1412, 12 2005.
- [26] R. C. Hibbeler. *Engineering mechanics. Dynamics*. Pearson/Prentice Hall, Upper Saddle River :, 12th ed. edition, 2010.
- [27] A.C. in 't Veld. Project guide design synthesis exercise: The ultimate unlimited aerobatic competition aircraft. Technical report, 2018.
- [28] J. Katz and A. Plotkin. *Low-Speed Aerodynamics*. Cambridge Aerospace Series. Cambridge University Press, 2001. ISBN 9780521665520. URL <https://books.google.nl/books?id=rAS1DmBRLo8C>.
- [29] Shuguang Li. The tsai-wu failure criterion rationalised in the context of ud composites. *Composites Part A: Applied Science and Manufacturing*, 102:207 – 217, November 2007. <https://doi.org/10.1016/j.compositesa.2017.08.007>.
- [30] R.G. McSpadden. 26th joseph t. nall report, general aviation accidents in 2014. Technical report, AOPA Air Safety Institute, 2014.
- [31] T.H.G. Megson. *Aircraft Structures for Engineering Students*. Elsevier Ltd., 2012.
- [32] J. Molenbroek. Dined database, 2017. URL <https://dined.io.tudelft.nl/en>.
- [33] T. Mutluay. The development of an inertia estimation method to support handling quality assesment. Technical Report 042#15#MT#FPP, TU Delft, September 2015.
- [34] Extra Aerobatic Planes. General description extra aircraft aerobatics essentials, 2018.
- [35] E.C. Polhamus and W.C. Sleeman Jr. The rolling moment due to sideslip of swept wings at subsonic and transonic speeds. Technical Report NACA RM L54L01, March 1955.
- [36] P.K.C. Rudolph. High-lift systems on commercial subsonic airliners. Technical report, September 1996.
- [37] E. Seckel and J.J. Morris. The stability derivatives of the navion aircraft estimated by various methods and derived from flight test data. Technical Report FAA-RD-71-6, January 1971.
- [38] Michael S. Selig. Real-time flight simulation of highly maneuverable unmanned aerial vehicles. *Journal of Aircraft*, 51(6):1705 – 1724, 2014. doi: <https://doi.org/10.2514/1.C032370>.
- [39] J. Sinke. Ae3211-ii: Production of aerospace systems. TU Delft, 2018.
- [40] T. Theodorson. The theory of propellers iii: The slipstream contraction with numerical values for two-blade and four-blade propellers. Technical Report NACA-ACR-L4J10, November 1944.
- [41] T.A. Toll and M.J. Queijo. Approximate relations and charts for low-speed stability derivatives of swept wings. Technical Report NACA TN-1581, May 1948.
- [42] Egbert Torenbeek. *Synthesis of subsonic airplane design: an introduction to the preliminary design of subsonic general aviation and transport aircraft, with emphasis on layout, aerodynamic design, propulsion and performance*. Springer Science & Business Media, 2013.
- [43] E.J. van Kampen. Ae4301: Automatic flight control system design, lecture 8. TU Delft, 2016.
- [44] J.A. Mulder & W.H.J.J. van Staveren & J.C. van der Vaart & E. de Weerd & C.C. de Visser & A.C. In 't Veld & E. Mooij. Lecture notes ae3202 flight dynamics. Technical report, Delft University of Technology, March 2013.
- [45] Leo L.M. Veldhuis. Manual for low speed windtunnel test ae2130-ii, October 2016.

- 
- [46] J. Verbeek. Ae4454: Life cycle analysis and production. TU Delft, 2017.
- [47] R. Vos. Ae4245: Advanced aircraft design ii. TU Delft, 2018.
- [48] J. W. WETMORE. The rolling friction of several airplane wheels and tires and the effect of rolling friction on take-off. Technical report, March 1937.
- [49] Serkan Özgen. Aeronautical engineering design i landing gear sizing and placement. Middle East Technical University, 2015.

# Appendix A

## FFBD, FBS and Project Design & Development Diagram

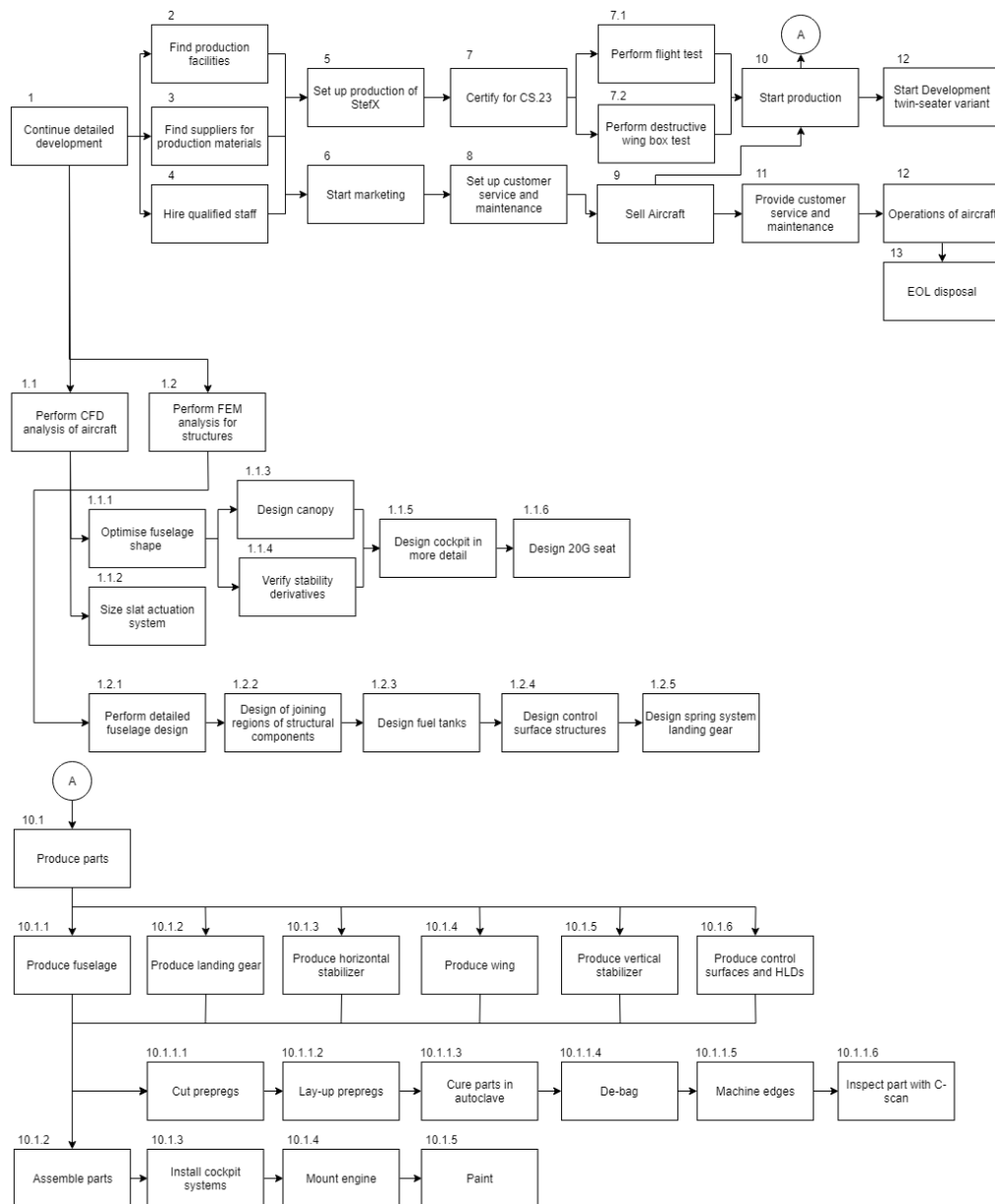


Figure A.1: Project Development Diagram.

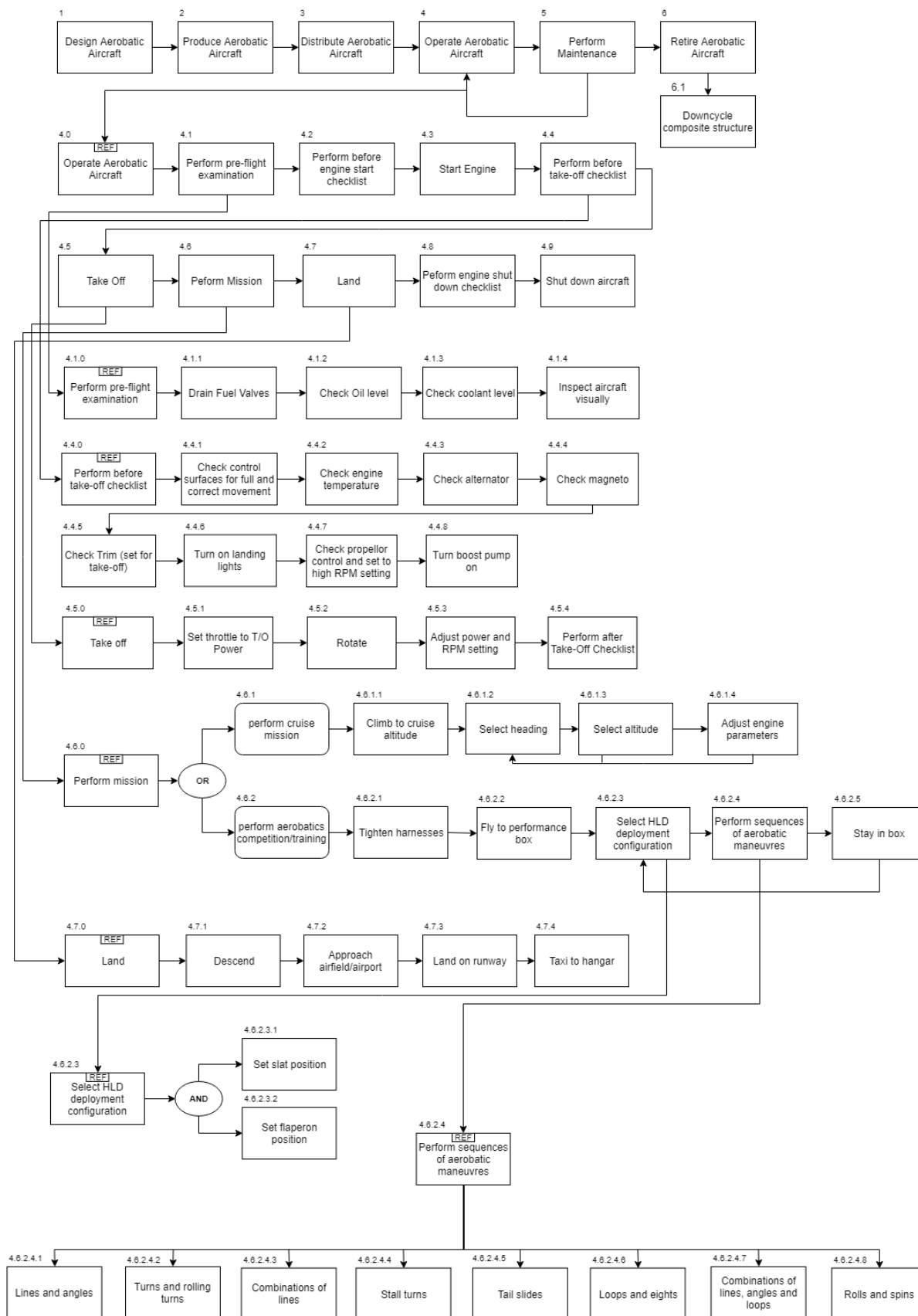


Figure A.2: Function Flow Block Diagram.

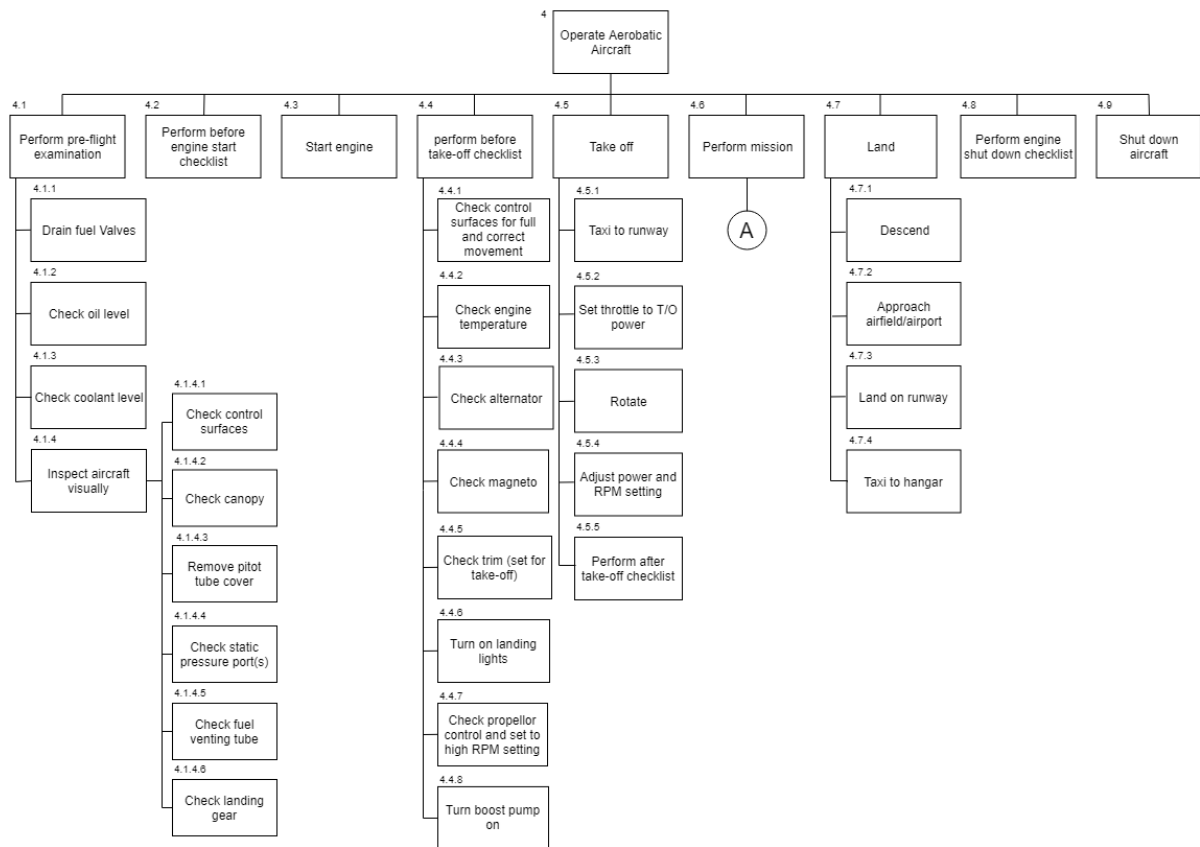


Figure A.3: Functional Breakdown Structure.

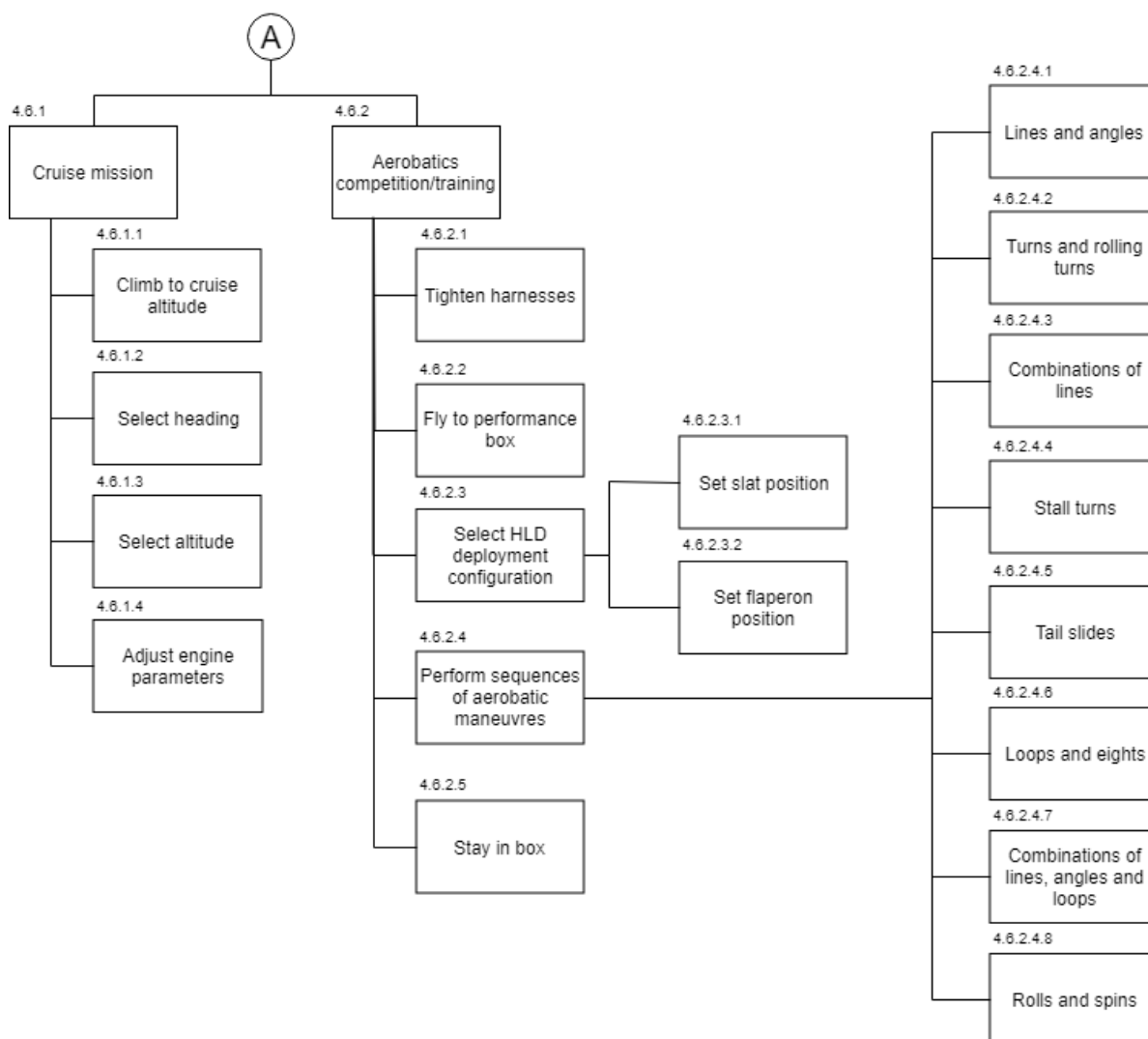


Figure A.4: Functional Breakdown Structure of mission.

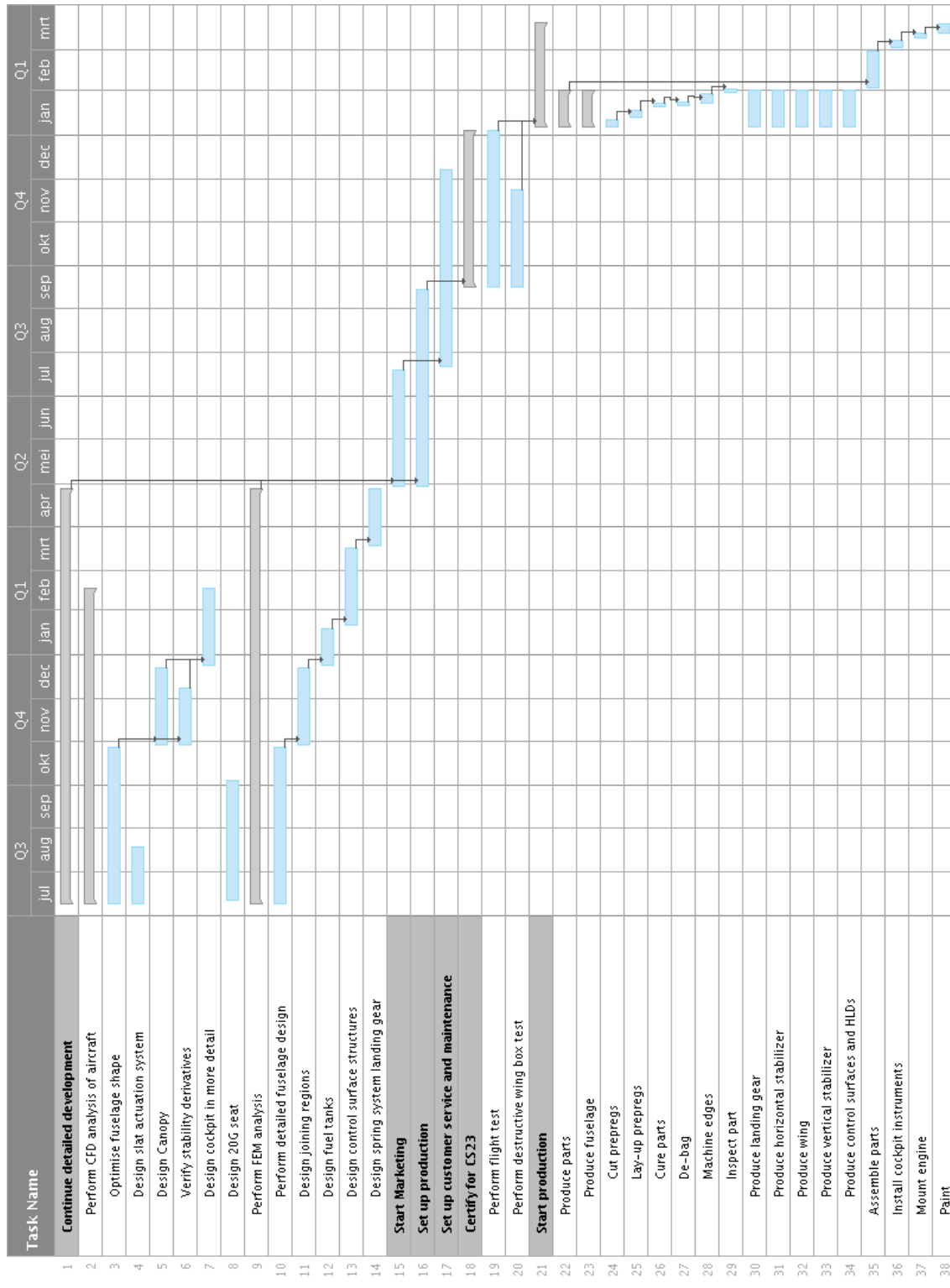


Figure A.5: Post-DSE Gantt Chart

**Appendix B**  
**Technical Drawings**

4

3

2

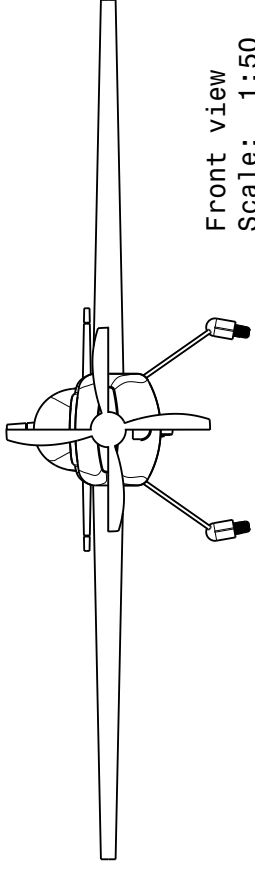
1

4

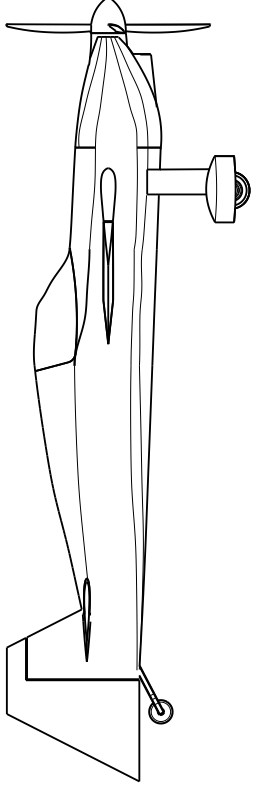
3

2

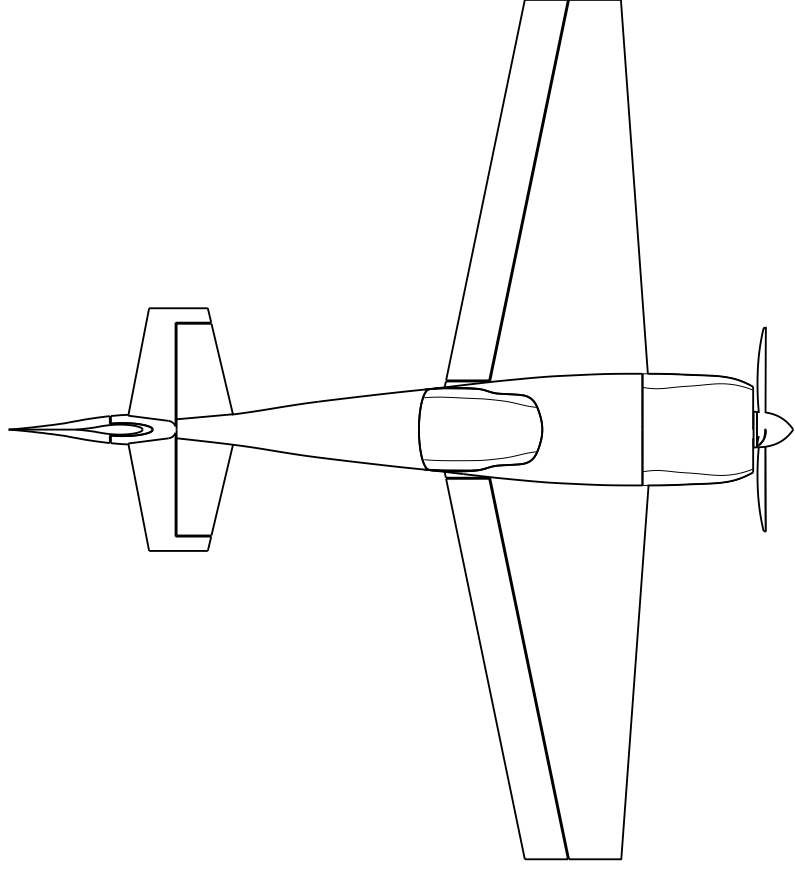
1



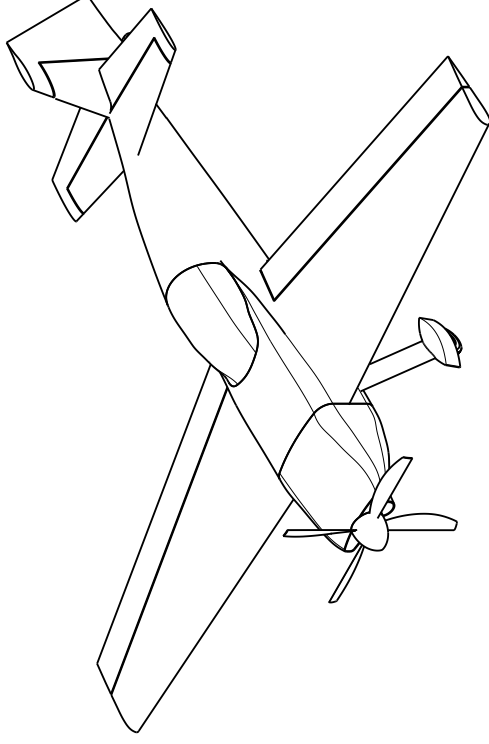
Front view  
Scale: 1:50



Right View  
Scale: 1:50



Top view  
Scale: 1:50



Isometric view  
Scale: 1:50

This drawing is our property.  
It can't be reproduced  
or communicated without  
our written agreement.

<b>DRAWN BY</b>	<b>DATE</b>
T. Haegens	02-Jul-18
<b>CHECKED BY</b>	<b>DATE</b>
M. Gossye	02-Jul-18
<b>DESIGNED BY</b>	<b>DATE</b>
DSE 23	02-Jul-18

<b>Stefx Aircraft</b>			
<b>DRAWING TITLE</b>			
<b>DRAWN BY</b>		<b>DATE</b>	
T. Haegens		02-Jul-18	
<b>CHECKED BY</b>		<b>DATE</b>	
M. Gossye		02-Jul-18	
<b>DESIGNED BY</b>		<b>DATE</b>	
DSE 23		02-Jul-18	
<b>DRAWING NUMBER</b>		<b>REV</b>	
StefX 1		X	
<b>SIZE</b>	<b>DRAWING NUMBER</b>	<b>SCALE</b>	<b>WEIGHT (kg)</b>
A3	Assembly	1:50	557
<b>SHEET</b>		<b>1/1</b>	

H

G

F

E

D

C

B

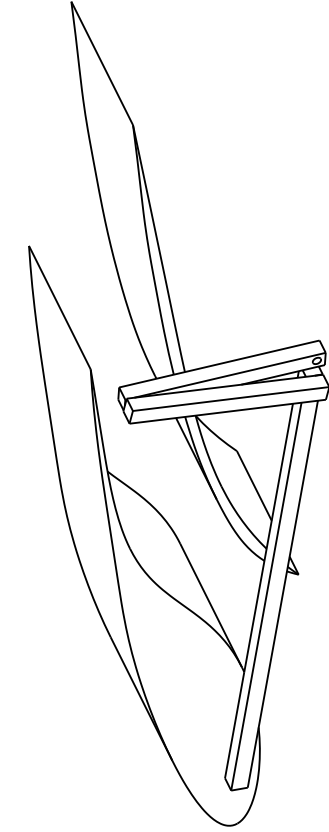
A

4 3 2 1

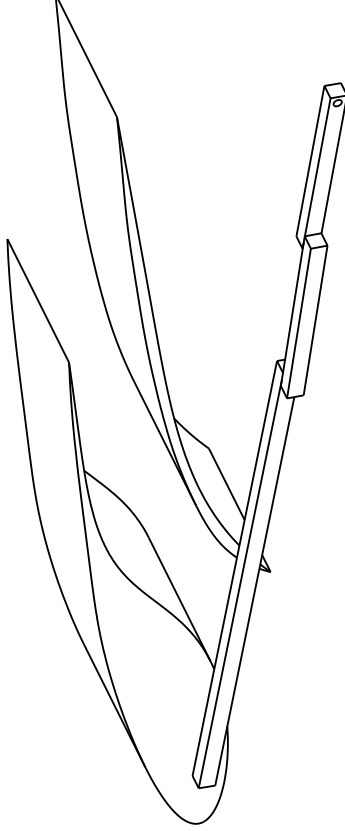
A B C D E F G H

H G F E D C B A

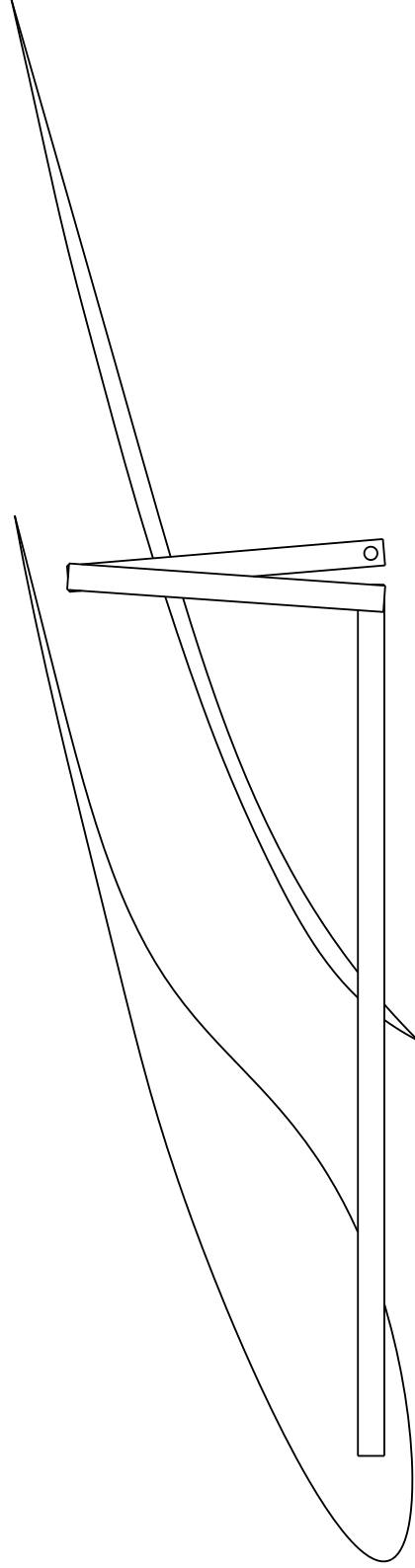
4 3 2 1



Isometric view  
Scale: 2:3



Isometric view  
Scale: 2:3



Front view  
Scale: 1:1

This drawing is our property.  
It can't be reproduced  
or communicated without  
our written agreement.

DRAWN BY	DATE
Gijs	26-6-2018
CHECKED BY	DATE
XXX	xxx
DESIGNED BY	DATE
XXX	xxx

# DASSAULT SYSTEMES

DRAWING TITLE

Leading Edge High Lift Device

SIZE	DRAWING NUMBER	REV
A3	Product1	X

SCALE	1:1	WEIGHT (kg)	5,86	SHEET	1/1
-------	-----	-------------	------	-------	-----

H G F E D C B A